

Nuclear Lattice Investigations of Fundamental Symmetries

Dissertation
zur
Erlangung des Doktorgrades (Dr. rer. nat.)
der
Mathematisch-Naturwissenschaftlichen Fakultät
der
Rheinischen Friedrich-Wilhelms-Universität Bonn

von
Christopher Körber
aus
Bochum

Bonn, November 2017

Dieser Forschungsbericht wurde als Dissertation von der
Mathematisch-Naturwissenschaftlichen Fakultät der Universität Bonn angenommen
und ist auf dem Hochschulschriftenserver der ULB Bonn
http://hss.ulb.uni-bonn.de/diss_online elektronisch publiziert.

1. Gutachter: Prof. Dr. Thomas Luu
2. Gutachter: Prof. Dr. Ulf-G. Meißner

Tag der Promotion: March 2018
Erscheinungsjahr: 2018

Abstract

Fundamental symmetries (and their violations) play a significant role in active experimental searches of Beyond the Standard Model (BSM) signatures. An example of such phenomena is the neutron Electric Dipole Moment (EDM), a measurement of which would be evidence for Charge-Parity (CP) violation not attributable to the basic description of the Standard Model (SM). Another example is the strange scalar quark content of the nucleon and its coupling to Weakly Interacting Massive Particles (WIMPs), which is a candidate model for Dark Matter (DM). The theoretical understanding of such processes is fraught with uncertainties and uncontrolled approximations. On the other hand, methods within nuclear physics, such as Lattice Quantum Chromodynamics (LQCD) and Effective Field Theories, are emerging as powerful tools for calculating non-perturbatively various types of nuclear and hadronic observables. This research effort will use such tools to investigate phenomena related to BSM physics induced within light nuclear systems.

As opposed to LQCD which deal with quarks and gluons, in Nuclear Lattice Effective Field Theory (NLEFT) individual nucleons—protons and neutrons—form the degrees of freedom. From the symmetries of Quantum Chromodynamics (QCD), one can derive the most general interaction-structures allowed on the level of these individual nucleons. In general, this includes an infinite number of possible interactions. Utilizing the framework of EFTs, more specifically for this work Chiral Perturbation Theory (χ PT), one can systematically expand the nuclear behavior in a finite set of relevant nuclear interactions with a quantifiable accuracy. Fundamental parameters of this theory are related to experiments or LQCD computations. Using this set of effective nuclear interaction-structures, one can describe many-nucleon systems by simulating the quantum behavior of each involved individual nucleon. The ‘*ab initio*’ method NLEFT introduces a spatial lattice which is finite in its volume (FV) and allows to exploit powerful numerical tools in the form of statistical Hybrid Monte Carlo (HMC) algorithms. The uncertainty of all three approximations—the statistical sampling, the finite volume and the discretization of space—can be analytically understood and used to make a realistic and accurate estimation of associated uncertainty.

In the first part of the thesis, χ PT is used to derive nuclear interactions with a possible BSM candidate up to Next-to-Leading Order (NLO) in the specific case of scalar interactions between DM and quarks or gluons. Following this analysis, Nuclear Matrix-Elements (NMEs) are presented for light nuclei (^2H , ^3He and ^3H), including a complete

uncertainty estimation. These results will eventually serve as the benchmark for the many-body computations.

In the second part of this thesis, the framework of NLEFT is briefly presented. It is shown how one can increase the accuracy of NLEFT by incorporating few-body forces in a non-perturbative manner. Finite-Volume (FV) and discretization effects are investigated and estimated for BSM NMEs on the lattice. Furthermore, it is displayed how different boundary conditions can be used to decrease the size of FV effects and extend the scope of available lattice momenta to the range of physical interest.

The following articles were published during the progression of this thesis

- [1] C. Körber and T. Luu,
Applying Twisted Boundary Conditions for Few-body Nuclear Systems, *Physical Review C* 93, no. 5, 054002 (2015), arXiv: 1511.06598.
- [2] C. Körber, A. Nogga, and J. de Vries,
First-principle calculations of Dark Matter scattering off light nuclei, *Physical Review C* 96, no. 3, 035805 (2017), arXiv: 1704.01150.
- [3] C. Körber, E. Berkowitz, and T. Luu,
Sampling General N-Body Interactions with Auxiliary Fields, *Europhys. Lett.* 119, no. 6, 60006 (2017), arXiv: 1706.06494.
- [4] C. Körber, E. Berkowitz, and T. Luu,
Hubbard-Stratonovich-like Transformations for Few-Body Interactions, *Submitted to PoS* (2017), arXiv: 1710.03126.
- [5] E. Berkowitz, C. Körber, S. Krieg, P. Labus, T. A. Lähde, and T. Luu,
Extracting the Single-Particle Gap in Carbon Nanotubes with Lattice Quantum Monte Carlo, *Submitted to PoS* (2017), arXiv: 1710.06213.

Publications [1-3] are the basis for this cumulative thesis.

Contents

1	Introduction	1
1.1	Motivation	1
1.2	Dedication of this work	4
1.3	How to measure Dark Matter	5
1.4	Organization of the thesis	8
2	First-principle calculations of Dark Matter scattering off light nuclei	9
2.1	Introduction	12
2.2	Scalar Dark Matter currents and the chiral effective field theory framework	14
2.2.1	Currents for isoscalar and isovector DM-quark interactions	16
2.2.2	Currents for DM-strange and DM-gluon interactions	20
2.3	Generation of nuclear wave functions and scattering matrix-elements	21
2.3.1	Matrix-elements	21
2.3.2	Nuclear wave functions	24
2.3.3	Chiral expansion and uncertainty estimation	29
2.4	Results and discussion	31
2.4.1	Convergence and uncertainty estimates	31
2.4.2	Discussion	34
2.4.3	The remaining DM interactions	38
2.4.4	Suppressing the leading order contributions	40
2.5	Summary and outlook	43
3	Nuclear Lattice Effective Field Theory	47
3.1	Introduction	47
3.2	The NLEFT formalism	50
4	Sampling general N-body interactions with auxiliary fields	57
4.1	Introduction	60
4.2	Formalism	61
4.3	Numerical results	64
4.4	Summary and discussion	67
5	Currents within a box	69
5.1	Introduction	69

5.2	Analytical solutions to separable potentials	72
5.2.1	Two-body solutions to separable potentials	72
5.2.2	Specific choice of potential	73
5.3	Currents within the box	75
5.3.1	Living within a box	75
5.3.2	Estimation of discretization errors	77
5.3.3	Estimation of Finite-Volume errors	78
5.4	Results	79
5.5	Summary and conclusion	83
6	Applying Twisted Boundary Conditions for few-body nuclear systems	85
6.1	Introduction	88
6.2	Implementation of Twisted Boundary Conditions for N-body systems . .	89
6.3	Non-relativistic Finite-Volume effects	93
6.4	Applying twists within the NLEFT formalism	97
6.4.1	Twists on the transfer matrix	97
6.4.2	Identification of systematic errors and description of error analysis	100
6.5	Two-body system: the deuteron	102
6.6	Three-body case: the triton	106
6.7	Comment on discretization effects	112
6.8	Conclusion	114
6.9	Acknowledgments	115
7	Conclusion	117
	Appendix	123
A	Scattering currents and recoil rates	123
A.1	Bound state matrix-elements	124
A.1.1	Two body bound states	125
A.2	Recoil rates	129
B	Operator partial wave decomposition	133
B.1	The idea	133
B.2	Partial wave basis of nuclear states	134
B.2.1	Two-nucleon states	134
B.2.2	Three-nucleon states	135
B.3	Advantage of operator decomposition	136
B.4	Example: Dark Matter two-nucleon operator	138
B.5	Current normalization	140
C	NLEFT on GPUs	143
C.1	Hybrid Monte Carlo integration	144

C.2	Hybrid Monte Carlo implementation for NLEFT	148
C.2.1	Computational details	148
C.2.2	Hybrid Monte Carlo workflow	150
C.3	Implementation on GPUs and intermediate results	152
C.3.1	A trial implementation	154
	Bibliography	157
	Acronyms	175

Introduction

1.1 Motivation

The Standard Model (SM) of particle physics is currently the most accurate and precise theory describing fundamental physics and drives research at a global level. As the discovery of the Higgs particle further confirmed the SMs applicability, it also denied the existence of new physics—physics Beyond the Standard Model (BSM)—up to the TeV scale. This absence of new *microscopic* signals is challenging as current theories cannot explain *macroscopic* observations like the asymmetry between matter and antimatter or the existence of Dark Matter (DM). The essential question is, therefore: *where does one expect signals beyond the Standard Model on a microscopic level and how can one describe this?*

Fundamental symmetries, as well as their violations, play a substantial role in active experimental searches of BSM physics. Examples of such phenomena are hadronic Electric Dipole Moments (EDMs) such as the neutron EDM [6]. A measurement of this quantity would be clear evidence for Charge-Parity (CP) violation [7] not attributable to the SM¹ which could help to resolve the matter-antimatter puzzle [9]. A further illustration of such phenomena is the Neutrinoless Double β Decay ($0\nu\beta\beta$ -decay) [10]—a confirmation of a non-zero decay rate would provide an additional amount of lepton number violation and indicates that neutrinos may be their antiparticles. This supports a solution to the matter-asymmetry puzzle known as leptogenesis. Another example is the strange scalar quark content of the nucleon and its coupling to Weakly Interacting Massive Particles (WIMPs), which is a candidate model for DM.

The variety of possible BSM theories proposes different scenarios for the description of such effects which lead to distinctive BSM phenomena. Linking these experiments to the fundamental level is of relevance for two reasons:

¹ In principal, the ‘so-called’ θ_{QCD} -term, which is allowed by the SM or more precisely Quantum Chromodynamics, could also contribute to a hadronic EDM. However, thus far, no non-zero hadronic EDM has been measured and therefore the θ_{QCD} -term is anomalously small if not zero. This puzzling (potential) fine-tuning of Quantum Chromodynamics is known as the strong CP problem and could be explained by the Peccei–Quinn formalism [8], which introduces a new pseudoscalar particle: the axion.

- While a non-vanishing experimental signal would confirm the existence of BSM structures and might explain the unresolved macroscopic observations, to identify the true origin of these signals, one needs to propagate the signal from the experimental target back to the level of the fundamental theory.
- Once one can accurately propagate possible BSM interactions to the level of experimental systems, it might be possible to identify *special* systems which feature a coherent enhancement or suppression of such interactions. Moreover, even if one is not able to guide experimental efforts, the reduction of theoretical uncertainties is equally important as improving on detection uncertainties and therefore has the potential to reduce the costs of required detectors drastically.

Complementary to the collider investigations of BSM signatures that take place at the high-energy frontier, it is also possible to probe for these signals with experiments at low energy via precision measurements. Sensitive low-energy tests of BSM physics include searches for nucleon, electron, and atomic EDMs and efforts to directly detect DM through its scattering off atomic nuclei. Though there is a variety of ideas on how to detect such signals, the common aspect of these low-energy experiments is the measurement of BSM signals on a nuclear level—ranging from large nuclear cores such as Xenon [11, 12] to planned experiments on light nuclei like Helium [13, 14]. Thus far, there is no scientific consensus that such measurements have detected a positive signal yet. However, such experiments have already reached a sensitivity which can rule out different BSM theories and will confront multiple further scenarios within the next years.

The theoretical descriptions of such Nuclear Matrix-Elements (NMEs) still suffer from significant uncontrolled uncertainties—mostly associated with the nuclear many-body methods or an inadequate treatment of relevant interactions. In case of $0\nu\beta\beta$ -decay computations, the method-dependent extrinsic uncertainties have improved by several factors but still can be as big as 100% [15, 16]. These uncertainties are troublesome for multiple reasons. Because it is the ultimate goal to understand the fundamental origin of these signals, one must eventually compare different measurements, and for this, an accurate and precise description is needed to discriminate between different theoretical BSM interaction structures. Therefore it is essential to understand the uncertainties of all relevant aspects associated with the propagation of scales.

Effects of SM or BSM interactions, at the level of individual nucleons, can be described through non-perturbative methods like Effective Field Theories [17–30] and Lattice Quantum Chromodynamics (LQCD) [31]. The form of the fundamental BSM interactions hereby constrain the number of possible nucleon-BSM contributions. Because the infinite set of possible interactions at the nuclear level comes with de-facto unknown coefficients—which describe their respective interaction strength—it is essential to relate the (finite) parameters at the fundamental BSM level to the (infinite) set of parameters on the nuclear level. This relation between the BSM model and effective nuclear description enables the ordering of the nuclear interactions by their relevance and thus allows a systematic computation. The whole process associated with the propagation of scales is illustrated in [fig. 1.1](#).

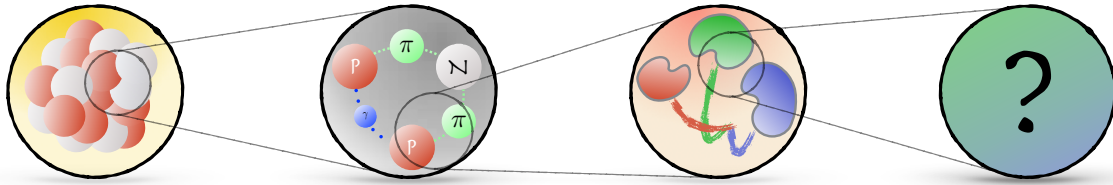


Figure 1.1: Illustration of the propagation of scales. While BSM experiments utilize large nuclear targets (left diagram), such targets are described through the interactions between individual nucleons (second diagram). Individual nucleons themselves are described through quarks and gluons (third diagram) which are linked to the BSM physics (right diagram).

Due to the complexity of many-body quantum systems and limitations of computational resources, an accurate *traditional* description cannot be extended to nuclear cores containing more than four nucleons and thus cannot establish a direct link to experiments—if one uses these methods only. For this reason, one must systematically compute effective nucleon-BSM interactions which are the starting point for many-body calculations. Recently Nuclear Lattice Effective Field Theory (NLEFT) [32–36] has proven to be a viable candidate for pushing the borders of nuclear physics in the low-energy regime and has enabled the computation of nuclear matrix-elements for large systems. In NLEFT, similar to LQCD, space and time are discretized on a lattice. Different to LQCD, however, is that in NLEFT individual nucleons—protons and neutrons—form the degrees of freedom. From the symmetries of Quantum Chromodynamics (QCD), one can derive the most general interaction structures allowed on the level of these individual nucleons. In general, this includes an infinite number of possible interactions. Utilizing the framework of EFTs, and more specifically for this work Chiral Perturbation Theory (χ PT), one can systematically expand the nuclear behavior in a finite set of relevant nuclear interactions with a quantifiable accuracy. The fundamental parameters of this theory must be determined from experiments or LQCD computations. Using this set of nuclear interaction structures, NLEFT can describe many-nucleon systems by simulating the quantum behavior of each involved nucleon. Lattice stochastic methods are used to calculate, for example, the binding energies of nuclei as large as Silicon [37, 38]. To put it in a simple way, the cost of the extended application range in the number of nucleons is given by discretization and Finite-Volume (FV) effects (both extrinsic uncertainties) and statistical fluctuations due to stochastic algorithms. An advantage of NLEFT compared to other many-body methodologies is the capability of quantifying related uncertainties.

1.2 Dedication of this work

The primary focus of this work is the analysis of hypothetical interactions between possible candidates for DM and SM-particles with the objective of helping to make accurate predictions at the level of experimental systems. Because the focus is less on the nature or ideas behind the postulated BSM theories, this work uses an EFT point of view. The fundamental descriptions are expressed by their most general form constrained by symmetries and a hierarchical relevance. More precisely, the starting point of this work are scalar interactions—interactions which do not depend on any spin or other quantum numbers—between DM and up (u), down (d) and strange (s) quarks as well as gluons (incorporated by the field-strength tensor $G_{\mu\nu}^a$)

$$\mathcal{L}_\chi = \left(c_u m_u \bar{u}u + c_d m_d \bar{d}d + c_s m_s \bar{s}s + c_G \alpha_s G_{\mu\nu}^a G^{\mu\nu a} \right) \bar{\chi}\chi, \quad (1.1)$$

where $\bar{\chi}\chi$ denotes the scalar DM bilinear. The masses m_q and the strong coupling α_s are inserted for convenience and could be absorbed in the unknown DM-SM couplings c_i . These unknown effective parameters c_i are constrained by the parameters of a more fundamental theory and thus must be eventually matched. As an example, these scalar interaction structures can be motivated via the Higgs-Portal DM [25, 39, 40]. Not restricting computations to fixed values of the c_i parameters allows one to make more general predictions and thus cover a larger field of possible scenarios.

Nevertheless, there are multiple reasons for choosing this particular set of interaction structures—the interactions of a scalar DM candidate—as the starting point for the analysis of this work

1. Because it is the goal of this thesis to help establish an accurate connection between fundamental symmetries and experiments, as the final step one has to accurately build the connection between the description of individual nucleons and the prediction for experimental systems. This prescription remains the same for the few- and many-body systems of interest. As one of the first analysis of this kind, it makes more sense to reduce the starting point to its most basic form—scalar interactions—and, once the framework is established, build on top of that.
2. Only experiments can confirm the existence of possible BSM candidates. However, the interpretation of such experiments is a consequence of more fundamental theories. Often, there is more than just one notion for BSM theories which provides different characteristics in describing the interaction between SM and BSM candidates. For example, are the SM-BSM interactions spin-dependent? How important are collective interactions compared to isolated interactions? To eventually identify the fundamental source for BSM candidates, one has to compare complementary measurements and predictions. Specifically in the case of scalar DM interactions, collective two-nucleon phenomena are predicted to be more relevant than in the case of spin-dependent interactions. Thus, from a theoretical point of view, a pos-

sible entanglement of different DM scenarios would be most dominant in the case of scalar DM interactions.

3. Collective scalar DM two-nucleon interactions have a nearly identical theoretical shape as interactions in another test of fundamental symmetries: the $0\nu\beta\beta$ -decay. Therefore, if one successfully implements the framework with such interactions, one can describe another process of interest with a minimal amount of further modifications.
4. Though the theoretical understanding of hypothetical DM scattering processes is an exciting and ongoing field of work, the aspect of high-accuracy nuclear descriptions is a relatively new to it. Because of this, the focus of the community has been rather the accessibility of an *a priori* description of experimental targets than systematically quantifying all uncertainties—especially coming from the nuclear description and many-body framework of use. Thus, a more systematic approach, which can provide realistic uncertainty estimations, will complement existing studies and might be able to provide an answer to the question if one can theoretically distinguish different BSM scenarios and would signalize where to improve the description in case one is not.
5. Though the majority of low-energy DM experiments utilize large nuclear targets like Xenon, there are also notions for setups using lighter targets like Helium. Such lighter targets would have a higher sensitivity in case of light DM candidates. From a theoretical perspective, such light systems are easier to describe and therefore, by establishing this high-accuracy framework, one could also make direct connections from experiment to fundamental symmetry.
6. And last but not least, understanding the nature of the unknowns in our galaxy like DM was one of my motivations to study physics. After I found myself more and more interested in quantum physics and specifically nuclear physics as one of its manifestations, this project was the perfect opportunity to work on both fields at the same time—an example of overlaps and thus synergies between different fields within fundamental research.

1.3 How to measure Dark Matter

There are several ideas on how to detect possible candidates for DM. These ideas can be categorized into DM-production, e.g., in high-energy collider investigations, or through indirect detection of DM such as the observation of galactic gamma-ray spectra, or direct detection experiments [see [fig. 1.2](#)]. Relevant for this work are the direct detection precision experiments which analyze potential scattering processes with the normal matter at low energies [41]. Choosing low-energy observables allows to describe observables using the theoretical low-energy framework of χ PT and NLEFT.

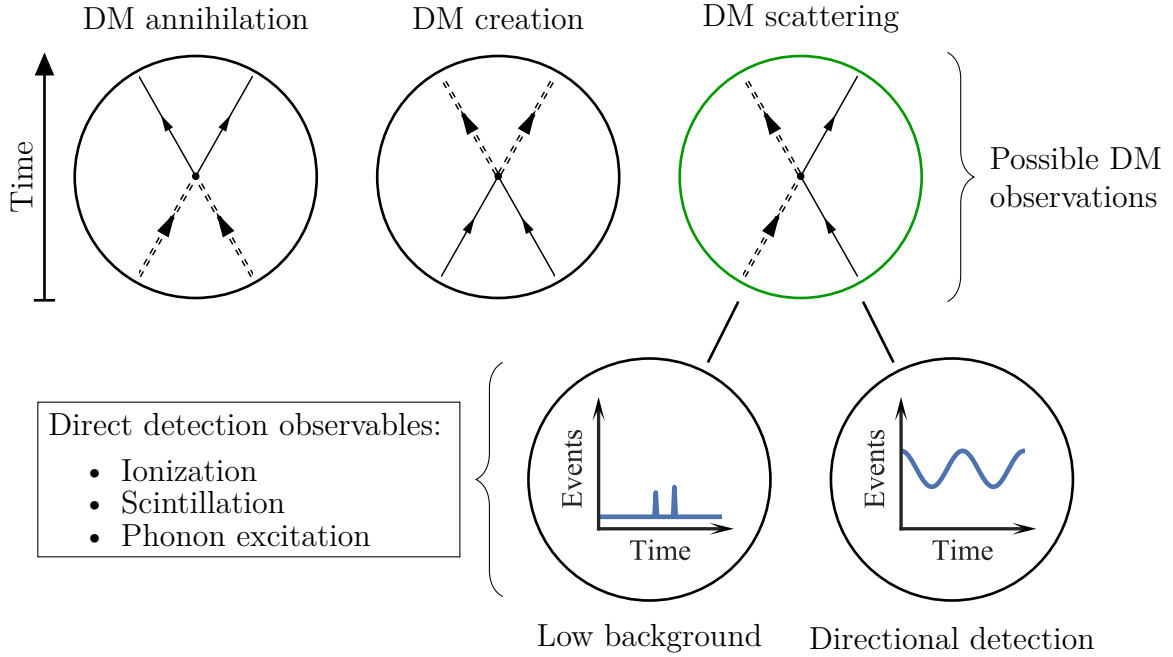


Figure 1.2: Different categories for DM detection experiments. The first row presents three possible but different kinds of observations for interactions between DM (double dashed lines) and regular matter (solid lines). The exact form of interactions and the type of DM is not known. Thus, the exact DM-matter vertices could be different. This work focuses on the direct detection of DM through scattering observables, which can be further categorized into experiments measuring absolute scattering event rates or temporal variations of the scattering rate. For more details, see the paragraphs below.

Through analysis of our galaxy one can infer a DM velocity distribution which eventually results in an expected DM interaction rate of less than 0.01 event per kg of detector material per day [42]—much lower than background signals coming from, e.g., cosmic rays or radioactivity in detector materials. For example, the event rate of cosmic neutrons at 15m water equivalent is 1 per kg per second. For this reason, one has to either eliminate or account for background events. Most of the direct detection experiments are placed well below the surface to protect detectors from cosmic radiation while using as little radioactive material as possible. Other effects are isolated by active (e.g., scintillating panels) and passive shielding (e.g., like hydrocarbon materials to absorb neutrons or copper to absorb photons). Last but not least, one subtracts further non-absorbed background events (e.g., beta decays) by analysis techniques which try to discriminate between background and signal.

One can further categorize direct detection experiments into two strategies: experiments which try to characterize and account for all relevant background events to highlight DM scattering only and experiments which look for variations in the total event rate or the event direction. While, as an advantage, the latter experiments do not need to know the

specifics of the background rates themselves, this technique requires a temporal constant event background to work. It also requires large detector volumes.

Detector materials for such elements can be classified as crystals, superheated fluid and gels like CF_3I (COUPP [43]) or C_4F_{10} (PICASSO [44]) and liquid novel gasses like Argon and Xenon (e.g. LUX [11], PANDAX [12] and XENON [45]). A few examples for crystal detector experiments are CoGeNT [46, 47], CDMS [48], SuperCDMS [49, 50] or EDELWEISS [51], which utilize Germanium and/or Silicon crystals, or CRESST [52, 53] (CaWO_4).

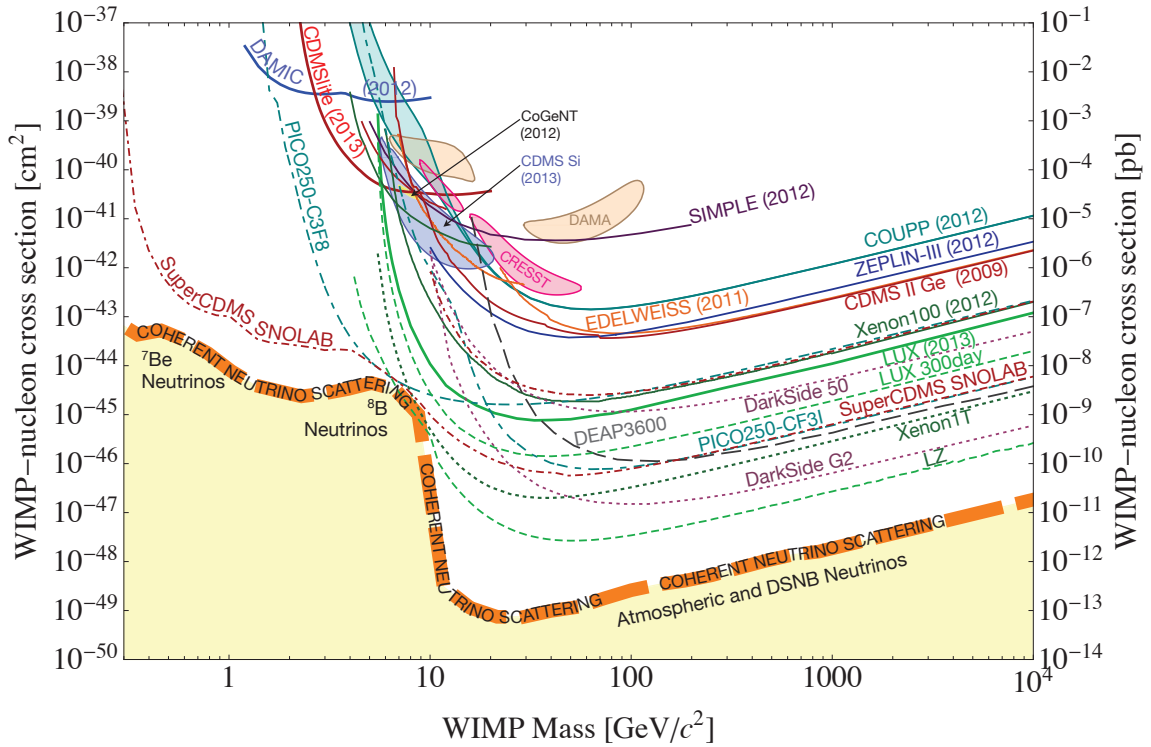


Figure 1.3: Mass projections for spin-independent WIMP-nucleon cross sections. Solid lines correspond to upper bounds of current direct detection experiments, dashed lines to planned experiments. Shaded areas display experiments which hint a WIMP signal. The lower band is the approximate region in which coherent neutrino scattering from supernova, solar or atmospheric events will dominate. Figure taken from [54].

All of these experiments measure nuclear recoil rates in the form of three observable interactions: ionization, phonon excitations in crystals and scintillations. These experiments usually measure one or two of such observables, where a second observation can

be used to distinguish background events from scattering events, for example, by identifying electron-only recoils. The recoil rates can be used to compute DM-nucleon cross sections depending on the unknown DM mass by integrating over the local DM velocity distribution. Positive indications of DM signals form colored areas in the mass-cross section diagram [fig. 1.3](#), while DM recoil rates consistent with zero form upper bounds on the cross section. Current generations of experiments are in principle able to account for all systematic sources of background signals, but the next generation of experiments will reach the region where one expects background signals from coherent neutrino scattering. Finally, direct detection experiments are constrained to particular sizes of DM mass values because its influence on the recoil energy transfer during scattering and the detectors energy resolution.

1.4 Organization of the thesis

This cumulative thesis is organized in seven chapters. In this chapter, the general notion and motivation of the thesis is presented. The following [chapter 2](#) is published in Physical Review C [\[2\]](#) and describes the scattering of scalar DM off light nuclei. The nuclear interactions with BSM sources are derived up to Next-to-Leading Order (NLO) in the case of scalar interactions between DM and quarks and gluons and first of its kind NMEs are presented for light-nuclei (^2H , ^3He and ^3H) which include a complete uncertainty estimation. These results are dedicated to serve as the benchmark for an eventual NLEFT computation. [Chapter 3](#) briefly introduces NLEFT, explains the basic idea behind overcoming the exponential scaling regarding the system size, draws the connection between NLEFT and Chiral Effective Field Theory (χEFT) and motivates the inclusion of few-body forces. The next chapter, [chapter 4](#), has been accepted for publication in European Physics Letters [\[3\]](#) and describes how one can include general N -body contact interactions in stochastic lattice algorithms by generalizing the so-called Hubbard-Stratonovitch (HS) transformation. [Chapter 5](#) presents how external current matrix-elements, such as scalar DM-scattering observables, could be incorporated in nuclear lattice computations. It is presented that the computation of physically interesting observables limits the available parameter space of computations. As the prime consequence of this section, the opposing constraints from the parameter space and from the feasibility demands of lattice computations are contrasted. A possible solution to the parameter space constraints is the extension of the (momentum-)range for the lattice computations by the introduction of Twisted Boundary Conditions (TBCs). This extension, described in [chapter 6](#) was introduced and published in Physics Review C [\[1\]](#). Finally, the thesis is concluded in [chapter 7](#).

First-principle calculations of Dark Matter scattering off light nuclei

The following chapter is published in Physical Review C [2].

First-principle calculations of Dark Matter scattering off light nuclei

C. Körber^a, A. Nogga^{a,b}, J. de Vries^c

^a *Institute for Advanced Simulations 4, Institute für Kernphysik 3, Jülich Center for Hadron Physics, and JARA-High Performance Computing, Forschungszentrum Jülich, D-52425 Jülich, Germany*

^b *Department of Physics and Astronomy, Ohio University, Athens, OH 45701, USA*

^c *Nikhef, Theory Group, Science Park 105, 1098 XG, Amsterdam, The Netherlands*

We study the scattering of Dark Matter particles off various light nuclei within the framework of Chiral Effective Field Theory. We focus on scalar interactions and include one- and two-nucleon scattering processes whose form and strength are dictated by chiral symmetry. The nuclear wave functions are calculated from Chiral Effective Field Theory interactions as well, and we investigate the convergence pattern of the chiral expansion in the nuclear potential and the Dark Matter-nucleus currents. This combined effective treatment allows us to provide a systematic uncertainty estimate of our calculations. We provide results for ^2H , ^3H , and ^3He nuclei which are theoretically interesting, and the latter is a potential target for experiments. We show that two-nucleon currents can be systematically included but are smaller than predicted by power counting and suffer from significant theoretical uncertainties even in light nuclei. We demonstrate that accurate high-order wave functions are necessary to incorporate two-nucleon currents.

2.1 Introduction

Despite the lack of a conclusive signal in a direct, indirect, or accelerator experiment, the astrophysical and cosmological evidence for Dark Matter (DM) remains solid [55]. Direct detection experiments have greatly improved in recent decades [11, 12] and are expected to improve even further in the near future [45, 56]. These experiments have great potential to not only discover the existence of DM but also to unravel its nature. The interpretation of a signal (or lack thereof) however, requires input from hadronic and nuclear physics [42] to connect the experimental results to more fundamental interactions between DM and Standard Model (SM) particles.

The nuclear physics aspects of DM direct detection has recently been discussed in several Effective Field Theory (EFT) frameworks [23–29]. For instance, Ref. [24] constructed an EFT description at the DM-nucleon level by constructing all possible interactions up to a certain order in momentum transfer and performed shell-model calculations of the associated nuclear responses for different target nuclei. A different approach includes the consequences of spontaneous breaking of chiral symmetry and the associated pions as pseudo-Goldstone bosons. Starting from a given set of interactions between DM and SM fields (in particular light quarks and gluons), this Chiral Effective Field Theory (χ EFT) approach allows for the systematic derivation of DM-hadron interactions. In this approach, DM-nucleus scattering does not solely arise from DM-nucleon interactions but also from two-nucleon currents arising from DM-pion interactions [25, 26, 28, 39]. The χ EFT power counting predicts a hierarchy of different terms which can be systematically included. For example, Refs. [26, 40] investigated in detail several two-nucleon interactions and performed shell-model calculations of the associated structural factors.

The effects of multi-nucleon interactions are particularly interesting as these can potentially lead to a very distinct dependence of the DM-nucleus cross section on A (the atomic number) and Z (number of protons) of the target nucleus concerning the regular DM-nucleon contributions. For instance, scalar DM-quark or DM-gluon interactions lead to similar DM-nucleon interactions but quite distinct two-nucleon interactions. If two-nucleon contributions can be probed by experiments on different target nuclei, it might, therefore, be possible to unravel different DM-quark/gluon interactions even if they both lead to spin-independent scattering processes. Two-nucleon corrections for spin-independent scattering were studied in several previous works [25, 26, 28, 39, 57]. In general, the corrections are found to be relatively small. Reference [40] found $\mathcal{O}(10\%)$ corrections for ^{132}Xe and somewhat smaller for light nuclei [57], but they can become much more important in specific scenarios where the one-body contributions are suppressed [25, 39, 58].

The above statements depend crucially on the accuracy of the nuclear calculations, which we investigate in this work. We also apply the χ EFT framework for DM scattering, but we wish to simultaneously describe the nuclear wave functions within the same χ EFT approach. This allows for a first-principle calculation, i.e. starting from an assumed (set of) DM-SM interaction(s), of the DM-nucleus cross sections. The complexities of

many-body nuclear physics limits this approach to light nuclei, and here we perform calculations of DM scattering of the first few bound nuclei. Such nuclei are interesting for both theoretical and experimental reasons. Theoretically, light nuclei are great testing laboratories as they can be described from first principles to high accuracies. On the other hand, for example, helium isotopes are potential experimental targets [13, 14] as they are sensitive to relatively light DM (below 10 GeV) [59] and they can potentially be used for directional detection purposes [60, 61]. Our calculations provide direct input for the interpretation of these experiments. Very recently, Ref. [61] performed an analysis of DM scattering of light nuclei in a similar spirit to our work but extended to the ${}^4\text{He}$ case. The main difference in the applied method to our work is that Ref. [61] applies chiral wave functions at fixed chiral order [Next-to-Next-to-Leading Order (N²LO)] obtained from the no-core shell model, in combination with one-nucleon currents not derived from chiral perturbation theory but taken from Ref. [24].

In this work, we wish to investigate several essential questions: How dependent are DM scattering cross sections on the nuclear potential and the resulting nuclear wave functions? That is, how significant are the intrinsic nuclear uncertainties? How vital are two-nucleon operators compared to standard one-body interactions and, crucially, how accurately can we calculate such contributions? As mentioned, we focus on scattering off the deuteron (${}^2\text{H}$), triton (${}^3\text{H}$), and helium isotope ${}^3\text{He}$, while results for ${}^4\text{He}$ are presented in upcoming work. These are nuclei for which we can solve the bound-state equations with direct methods for a given nuclear potential [including Three-Nucleon Forces (TNFs)]. We use these nuclei as theoretical laboratories and aim to extend our framework to heavier nuclei with more sophisticated many-body techniques. Tremendous progress has been made in recent years in first-principle calculations of medium-heavy nuclei by use of nuclear quantum Monte Carlo methods [62] and Nuclear Lattice Effective Field Theory (NLEFT) [38]. Anticipating similar progress for DM direct detection, our calculations perform a benchmark for such future studies.

This paper is organized as follows. In [section 2.2](#) we introduce the DM interactions we focus on and introduce the chiral EFT framework. We derive the one- and two-nucleon currents and discuss the power counting. In [section 2.3](#) we describe the calculation of the nuclear wave functions and the scattering cross section. We explain how we estimate the theoretical uncertainties associated with our calculations. We present our main results in [section 2.4](#), where we also discuss scenarios where leading order cross sections are suppressed, and subleading effects become dominant. Finally, we summarize and give an outlook for future work in [section 2.5](#).

2.2 Scalar Dark Matter currents and the chiral effective field theory framework

In this work we focus on scalar interactions between DM and light quarks and gluons. We assume the mediator of the interactions to be heavy with respect to the typical momentum exchange in the DM-nucleus scattering process and use the following effective interactions

$$\mathcal{L}_\chi = \bar{\chi}\chi \left(c_u m_u \bar{u}u + c_d m_d \bar{d}d + c_s m_s \bar{s}s + c_G \alpha_s G_{\mu\nu}^a G^{\mu\nu a} \right), \quad (2.1)$$

in terms of a massive DM spin-1/2 Dirac fermion χ with typical mass m_χ in the GeV to TeV range (the cases of scalar, vector, or Majorana DM particles are almost identical for the scalar interactions under consideration). Furthermore, u , d , and s denote the light quark fields, $G_{\mu\nu}^a$ denotes the gluon field strength, α_s denotes the strong coupling, and the three coupling constants $c_{u,d,s,G}$, of mass dimension (-3) , parametrize the strength of the DM-SM interactions. For convenience, we have assumed the DM-quark operators to scale with the quark masses, $m_{u,d,s}$. The Lagrangian in eq. (2.1) is taken at a scale around 1 GeV, and at lower energies, we match to effective DM-hadron interactions. The coefficients $c_{u,d,s,G}$ include contributions from potential couplings to heavier quarks which have been integrated out [63].

We focus on scalar interactions as these are well motivated, for instance via Higgs-portal DM, and have interesting two-nucleon currents [25, 39, 40]. There can be other interactions, e.g., vector, axial-vector, or tensor interactions, but in these cases, two-nucleon currents are expected to be more suppressed compared to single-nucleon contributions than for scalar interactions [28]. We, therefore, leave the more general case for forthcoming work.

We wish to describe the scattering process between DM and light nuclei completely within the framework of chiral EFT. Our starting point is the Quantum Chromodynamics (QCD) Lagrangian supplemented by the DM interactions in eq. (2.1). By constructing the most general Lagrangian that incorporates the symmetries of the microscopic theory (QCD supplemented with DM interactions) and their explicit and spontaneous breaking, in terms of the relevant low-energy degrees of freedom (DM fields, pions, nucleons, and, in principle, heavier hadrons), we obtain Chiral Perturbation Theory (χ PT), which is the low-energy equivalent of QCD. The power of χ PT is that it can be used to calculate hadronic and nuclear observables in perturbation theory where p/Λ_χ is the expansion parameter depending on p , the low-momentum scale of the process, and $\Lambda_\chi \simeq 1$ GeV on the chiral-symmetry-breaking scale.

While χ PT allows for the derivation of the form of the interactions, each term is associated with a Low-Energy Constant (LEC) that captures the non-perturbative nature of low-energy QCD. These LECs need to be fitted to data or calculated with non-perturbative methods such as lattice QCD. χ PT has been extended to the multi-nucleon

sector where it is usually called χ EFT and this has led to the derivation of the strong nucleon-nucleon (NN) potential up to Next-to-Next-to-Next-to-Next-to-Leading Order (N^4 LO) [22]. Throughout this work we apply $SU(2)$ χ PT instead of $SU(3)$ χ PT as the extension of the latter theory to include nuclear forces has not been developed to the same accuracy as for the $SU(2)$ case. We, therefore, do not include dynamical effects of the strange pseudo-Goldstone bosons: kaon- and η -mesons.

Pions play an important role in χ PT as they emerge as Goldstone bosons of the spontaneously broken chiral symmetry of QCD to the subgroup of isospin $SU(2)_L \times SU(2)_R \rightarrow SU(2)_I$. Because chiral symmetry is only an approximate symmetry, being violated by quark masses and charges and, in our case, the DM-quark scalar interactions, the pions obtain a small mass $m_\pi^2 \sim m_q$. The smallness of the symmetry-breaking terms, fortunately, ensures that the chiral-symmetry-breaking sources can be incorporated in the chiral expansion. The χ EFT Lagrangian is then obtained by adding to all chiral-invariant interactions, all interactions that break chiral symmetry in the same way as the quark level chiral-symmetry-breaking sources. The infinite numbers of terms can be ordered by the chiral index $\Delta = d + n/2 - 2$, where d counts the number of derivatives and quark mass insertions (a quark mass insertion increases d by 2 because $m_q \sim m_\pi^2 \sim p^2$) and n is the number of nucleon fields [17, 18]. Since we are interested in processes where a single DM particle scatters off a nucleus, we will only consider chiral interactions that are linear in the couplings $c_{u,d,s,G}$. In what follows, we introduce $Q = p/\Lambda_\chi$ as the expansion parameter.

To obtain the nuclear wave function we require the strong nucleon-nucleon potential. At Leading Order (LO) [$\mathcal{O}(Q^0)$] the potential consists of a One-Pion Exchange (OPE) diagram and two short-range nucleon-nucleon interactions [19]. At Next-to-Leading Order (NLO) [$\mathcal{O}(Q^2)$] one finds corrections to the OPE diagrams, several Two-Pion Exchange (TPE) diagrams, and subleading contact interactions [20]. At N^2 LO [$\mathcal{O}(Q^3)$] additional TPE diagrams appear that arise from $\pi\pi$ -nucleon interactions with chiral index $\Delta = 1$, the c_i interactions [21], which also give rise to TNFs. The number of terms grows at even higher order [22], although how many terms are relevant depends on the process under investigation.

The LECs appearing in the potential are fitted to pion-nucleon scattering data (see, e.g., Ref. [64]) and the few-nucleon database and then other nuclear observables can be predicted. The scattering and bound-state equations are typically divergent, and a coordinate-space cutoff is applied to regulate the integrals. Of course, observables should not depend on the chosen cutoff, but in numerical calculations, explicit cutoff independence is lost. The LECs appearing in the nucleon-nucleon potential are fitted (at each order) for different values of the applied cutoff. By varying the chiral order of the potential and the cutoff, we can test both the chiral convergence and the cutoff dependence of our results, allowing for a well-defined uncertainty estimate. We provide more details of this procedure below.

2.2.1 Currents for isoscalar and isovector DM-quark interactions

The second part of the calculation involves the chiral expansion of DM-hadron interactions. For the scalar interactions under consideration, this has been studied in detail in, for example, Refs. [25, 29, 40]. Here we repeat the analysis for completeness and add a few comments about higher order corrections. We begin by considering scalar interactions involving up and down quarks. These can be treated in χ PT as ordinary quark mass terms by replacing the usual spurion field χ ,

$$\chi = 2B\mathcal{M} \rightarrow 2B[\mathcal{M} - \text{diag}(m_u c_u \bar{\chi}\chi, m_d c_d \bar{\chi}\chi)], \quad (2.2)$$

where $\mathcal{M} = \text{diag}(m_u, m_d)$ is the quark mass matrix. The leading terms in the DM chiral Lagrangian are then given by

$$\mathcal{L}_{\chi,q} = \frac{f_\pi^2}{4} \text{Tr}[U^\dagger \chi + U \chi^\dagger] + c_1 \text{Tr}(\chi_+) \bar{N}N + c_5 \bar{N} \hat{\chi}_+ N, \quad (2.3)$$

where $N = (p, n)^T$ is the nucleon isospin doublet containing proton (p) and neutron (n) fields, the Goldstone bosons are parametrized by

$$U(\pi) = u(\pi)^2 = \exp\left(\frac{i\boldsymbol{\pi} \cdot \boldsymbol{\tau}}{f_\pi}\right), \quad (2.4)$$

where $\boldsymbol{\pi}$ is the pion triplet, $\boldsymbol{\tau}$ are the Pauli matrices, $f_\pi = 92.4$ MeV is the pion decay constant, and $c_{1,5} \sim \mathcal{O}(1/\Lambda_\chi)$ are LECs associated to the nucleon σ -term and strong proton-neutron mass splitting. A hat denotes the traceless component of a chiral structure, e.g., $\hat{\chi} = \left(\chi - \frac{1}{2} \text{Tr}(\chi)\right)$, and $\chi_\pm = u^\dagger \chi u^\dagger \pm u \chi^\dagger u$.

We can now read off the relevant interactions beginning with DM-pion interactions

$$\mathcal{L}_{\chi,q}^\pi = c_q^\pi \boldsymbol{\pi}^2 \bar{\chi}\chi, \quad c_q^\pi = \frac{m_\pi^2}{4} [c_u(1 - \varepsilon) + c_d(1 + \varepsilon)] \equiv \frac{m_\pi^2}{2} \bar{c}_{q^{(\text{is})}}, \quad (2.5)$$

where $\varepsilon = (m_d - m_u)/(m_d + m_u) = 0.37 \pm 0.03$ [65], and we defined the effective isoscalar DM coupling $\bar{c}_{q^{(\text{is})}}$. Similarly we can read off the tree-level DM-nucleon interactions [66]

$$\begin{aligned} \mathcal{L}_{\chi,N} &= c_q^{N,(\text{is})} \bar{N}N \bar{\chi}\chi + c_q^{N,(\text{iv})} \bar{N} \tau^3 N \bar{\chi}\chi, \\ c_q^{N,(\text{is})} &= -4m_\pi^2 c_1 \bar{c}_{q^{(\text{is})}}, \\ c_q^{N,(\text{iv})} &= B(m_d - m_u) c_5 \left[c_u \left(1 - \frac{1}{\varepsilon}\right) + c_d \left(1 + \frac{1}{\varepsilon}\right) \right] \equiv B(m_d - m_u) c_5 \bar{c}_{q^{(\text{iv})}}, \end{aligned} \quad (2.6)$$

where $c_q^{N,(\text{is})}$ and $c_q^{N,(\text{iv})}$ are, respectively, the coupling strengths of the isoscalar and isovector DM-nucleon interactions, and we defined the effective isovector DM coupling $\bar{c}_{q^{(\text{iv})}}$.

Power counting

The DM-nucleon interactions contribute to DM-nucleus scattering via [fig. 2.1\(a\)](#), while the DM-pion interactions contribute via one-nucleon and two-nucleon interactions via [figs. 2.1\(b\)](#) and [2.1\(c\)](#), respectively. A power-counting scheme is necessary to determine the relative order of these and other contributions. We count powers of the generic momentum p , where p is determined from the nuclear binding momentum which for typical nuclei is of the order $p \sim m_\pi$ as usual in χ PT. In addition, we have the momentum transfer, q , between DM and the nucleus, which for scattering off light nuclei is expected to be somewhat smaller, but for simplicity we treat $q \sim p$.

Weinberg showed [19] that the usual χ PT power counting needs to be adapted for $A \geq 2$ intermediate states that contain only propagating nucleons. A diagram can then be separated into two parts which do not contain such states (the irreducible part) and a part which does (the reducible part). Inside an irreducible subloop, the contour integration over the time component of the loop momentum can always be done in such a way that the nucleon pole is avoided and the nucleon energy is of order $\sim p$ as in standard χ PT. An irreducible diagram can then be counted via the rules: $p^4/(4\pi)^2$ for each loop, $1/p$ for each nucleon propagator, $1/p^2$ for a pion propagator, and the product of the LECs associated to the relevant interactions. In irreducible diagrams, however, the nucleon poles cannot be avoided, and the nucleon energy becomes $\sim p^2/m_N$ instead of $\sim p$. For such reducible diagrams we use the modified rules: $p^5/[(4\pi)^2 m_N]$ for each loop, m_N/p^2 for each nucleon propagator, $1/p^2$ for a pion propagator, and the product of the LECs associated to the relevant interactions. Typically p/m_N is counted as $p^2/\Lambda_\chi^2 \sim Q^2$, indicating a suppression of two orders in the chiral counting [67].

We can apply these rules to determine the hierarchy of the diagrams in [fig. 2.1](#). We use $\bar{c}_{q^{(is)}}$ and $\bar{c}_{q^{(iv)}}$ defined in [eqs. \(2.5\)](#) and [\(2.6\)](#) instead of c_u and c_d , as the former have a simpler power counting. As we do not know the (relative) sizes of $\bar{c}_{q^{(is)}}$, $\bar{c}_{q^{(iv)}}$, c_s , and c_G , we have to determine the power counting for each DM interaction at the quark-gluon level separately. For each DM interaction we denote the dominant contribution by (0), the NLO by (1), and so on.

We begin with the isoscalar DM interactions. [Figure 2.1\(a\)](#) is counted as $c_q^{N,(is)} \sim m_\pi^2 c_1 \bar{c}_{q^{(is)}} \sim \bar{c}_{q^{(is)}} (m_\pi^2/\Lambda_\chi)$, where we took into account an overall normalization common to all diagrams. This contribution forms the LO structure at order (0).

[Figure 2.1\(b\)](#) contains an additional irreducible loop, one nucleon propagator, two pion propagators, and two strong pion-nucleon vertices such that the relative scaling becomes

$$\mathcal{A}_b \sim c_q^\pi \left(\frac{p^4}{(4\pi)^2} \right) \left(\frac{1}{p} \right) \left(\frac{1}{p^2} \right)^2 \left(\frac{g_A p}{f_\pi} \right)^2 \sim c_q^\pi \frac{g_A^2 p}{(4\pi f_\pi)^2} \sim \bar{c}_{q^{(is)}} \frac{m_\pi^2}{\Lambda_\chi} \times \frac{p}{\Lambda_\chi}, \quad (2.7)$$

where we identified $4\pi f_\pi \sim \Lambda_\chi$ and counted $g_A \sim 1$. We obtain the familiar result [25, 39] for the isoscalar DM-quark interaction that the pion loop is suppressed by $p/\Lambda_\chi \sim Q$

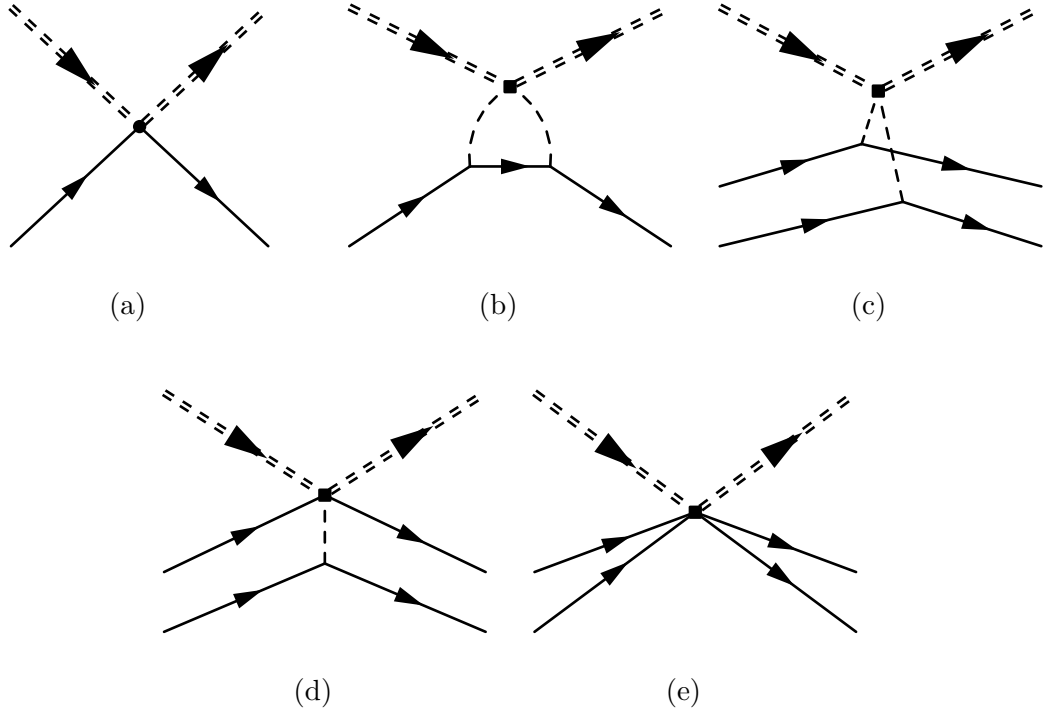


Figure 2.1: Diagrams contribution to DM-nucleus scattering. Solid lines correspond to nucleons, single dashed lines correspond to pions, and double-dashed lines correspond to DM. Our analysis focuses on the diagrams in the first row, while those in the second row only appear at higher order.

and is therefore one order down in the chiral power counting. This contribution therefore appears at order (1).

We now turn to [fig. 2.1\(c\)](#) which, compared to [fig. 2.1\(a\)](#), has an additional reducible loop, one nucleon propagator, two pion propagators, and two strong pion-nucleon vertices. The power-counting predicts

$$\mathcal{A}_c \sim c_q^\pi \left(\frac{p^5}{(4\pi)^2 m_N} \right) \left(\frac{m_N}{p^2} \right) \left(\frac{1}{p^2} \right)^2 \left(\frac{g_A p}{f_\pi} \right)^2 \sim \bar{c}_{q^{(is)}} \frac{m_\pi^2}{\Lambda_\chi} \times \frac{p}{\Lambda_\chi}, \quad (2.8)$$

such that this diagram appears at order (1) as well. higher order corrections are discussed in the next subsection.

We can perform a similar counting for isovector DM interactions. [Figure 2.1\(a\)](#) is counted as $c_q^{N,(iv)} \sim B(m_d - m_u) c_5 \bar{c}_{q^{(iv)}} \sim \bar{c}_{q^{(iv)}} (\varepsilon m_\pi^2 / \Lambda_\chi)$, which provides the leading (0) contribution. It is tempting to argue that isovector DM interactions lead to small one-nucleon currents with respect to isoscalar DM because of the additional factor ε appearing in the scaling of the diagram. However, such a comparison depends also on the ratio of $\bar{c}_{q^{(iv)}} / \bar{c}_{q^{(is)}}$ which depends on unknown parameters in the underlying DM model and can therefore be enhanced (see e.g. Ref. [68]). We therefore cannot compare contributions

from different DM operators in a model-independent way.

Since isospin-violating DM interactions do not lead to the DM-pion interactions in eq. (2.5), figs. 2.1(b) and 2.1(c) do not appear at order (1), but only at higher orders in the power counting. For instance, operators like $\bar{\chi}\chi\pi_3^2$ appear after an additional insertion of the quark mass difference and are therefore suppressed by two powers in the chiral counting. Contributions from the diagrams with topology analogous to figs. 2.1(b) and 2.1(c) therefore only appear at order (3).

LO and NLO currents for isoscalar and isovector DM-quark interactions

The calculation of the first two diagrams in fig. 2.1(b) is straightforward. We consider a nucleon of incoming (outgoing) momentum p (p') and define $\mathbf{q} = \mathbf{p} - \mathbf{p}'$. Up to order (1), the nucleon-DM current can be written as

$$J_{q^{(\text{is}+\text{iv})}}(\mathbf{q}) = \left[\left(-4m_\pi^2 c_1 - \frac{9g_A^2 \pi m_\pi^3}{4(4\pi f_\pi)^2} \right) - \frac{9g_A^2 \pi m_\pi^3}{4(4\pi f_\pi)^2} F\left(\frac{|\mathbf{q}|}{2m_\pi}\right) \right] \bar{c}_{q^{(\text{is})}} + B(m_d - m_u) c_5 \bar{c}_{q^{(\text{iv})}} \tau_i^3, \quad (2.9)$$

where τ_i^3 acts on the isospin of the interaction nucleon and we defined a function of the momentum transfer

$$F(x) = \frac{-x + (1 + 2x^2) \arctan x}{3x}, \quad (2.10)$$

which for small momentum transfer becomes $F(x) \simeq \frac{5}{9}x^2 + \dots$. As noted in Ref. [66], the momentum-independent part of the isoscalar current can be identified as the first two terms in the chiral expansion of the nucleon σ -term $\sigma_{\pi N} = \bar{m}(dm_N/d\bar{m})$ where $\bar{m} = (m_u + m_d)/2$ is the average light quark mass. Similarly, the isovector current can be identified as the strong proton-neutron mass splitting $(m_n - m_p)^{\text{strong}} \equiv \delta m_N = -4Bc_5(m_d - m_u)$. We can therefore resum higher chiral orders [66] by writing

$$J_{q^{(\text{is}+\text{iv})}}(\mathbf{q}) = \left[\sigma_{\pi N} - \frac{9g_A^2 \pi m_\pi^3}{4(4\pi f_\pi)^2} F\left(\frac{|\mathbf{q}|}{2m_\pi}\right) \right] \bar{c}_{q^{(\text{is})}} - \frac{\delta m_N}{4} \bar{c}_{q^{(\text{iv})}} \tau_i^3. \quad (2.11)$$

A big advantage of the resummation is that the nucleon σ -term and mass splitting have been precisely determined

$$\sigma_{\pi N} = (59.1 \pm 3.5) \text{ MeV}, \quad \delta m_N = (2.32 \pm 0.17) \text{ MeV}, \quad (2.12)$$

from, respectively, a Roy-Steiner analysis of pion-nucleon scattering [69] and Lattice Quantum Chromodynamics (LQCD) calculations [70]. Recent LQCD calculations [71] find a smaller number for the nucleon σ -term than the Roy-Steiner analysis. The chiral prediction for the slope of the scalar form factor, the coefficient of \mathbf{q}^2 , is smaller by roughly 40% than a determination based on a dispersive analysis [72], indicating that higher order effects can be relevant for the momentum-dependent interactions.

We now turn to the two-nucleon current depicted in [fig. 2.1\(c\)](#) which becomes

$$J_{q^{(\text{is})},2b}(\mathbf{q}) = -m_\pi^2 \left(\frac{g_A}{2f_\pi} \right)^2 \frac{(\boldsymbol{\sigma}_1 \cdot \mathbf{q}_1)(\boldsymbol{\sigma}_2 \cdot \mathbf{q}_2)}{(\mathbf{q}_1^2 + m_\pi^2)(\mathbf{q}_2^2 + m_\pi^2)} \tau_1 \cdot \tau_2 \bar{c}_{q^{(\text{is})}}, \quad (2.13)$$

where $\mathbf{q}_i = \mathbf{p}'_i - \mathbf{p}_i$ is the difference between the outgoing and incoming momentum of nucleon i , and σ_i (τ_i) the spin (isospin) of nucleon i .

At the next order in the chiral expansion, i.e. order (2), there appear several new contributions. For instance, the isoscalar and isovector one-nucleon currents can be dressed by pion loops. However, all such contributions can be absorbed in the resummation of $\sigma_{\pi N}$, δm_N , and the radius corrections [[73](#)]. That is, there appear no genuinely new topologies. At order (3), several new contributions appear. Particularly interesting for the isoscalar DM interactions are new two-nucleon contributions that arise, for example, from two-derivative DM-pion-pion interactions (e.g., LEC l_4 in Ref. [[18](#)]), DM-nucleon-pion interactions (e.g. LEC d_{16} in Ref. [[74](#)]), and DM-nucleon-nucleon contact interactions. The relevant topologies of the latter two contributions are shown in [figs. 2.1\(d\)](#) and [2.1\(e\)](#). For the isovector DM interactions, the first two-nucleon corrections appear as well as discussed at the end of [section 2.2.1](#). The corrections at this order have not been fully calculated and will not be considered here.

2.2.2 Currents for DM-strange and DM-gluon interactions

As the interactions between DM and strange quarks and gluons in [eq. \(2.1\)](#) are invariant under $SU(2)$ chiral-symmetry transformations, the hierarchy of hadronic interactions will be different compared to those arising from the couplings to light quarks. In particular, the interaction between DM and pions¹ only arises at higher order and the main contributions arise from DM-nucleon interactions. These have been studied in many papers, see e.g. Refs [[27](#), [29](#)] and references therein, and here we summarize the results. For the interactions to strange quarks, the relevant matrix-element is the strange σ -term $\sigma_s = m_s(dm_N/dm_s) = 40 \pm 10$ MeV from an average of LQCD calculations [[75](#)]. For the momentum-dependent term, which cannot be obtained from $SU(2)$ χ PT but instead requires $SU(3)$ χ PT, we follow Ref. [[40](#)] and use a dispersive extraction [[72](#)]. This gives for the one-nucleon current

$$J_s(\mathbf{q}) = (\sigma_s - \dot{\sigma}_s \mathbf{q}^2) c_s, \quad (2.14)$$

where $\dot{\sigma}_s = 0.3 \pm 0.2 \text{ GeV}^{-1}$ which, by comparison to the numerical value of the radius correction in [eq. \(2.11\)](#), we label as an NLO correction. Isovector currents and two-

¹ In $SU(3)$ χ PT the strange interactions would lead to DM-kaon and DM- η vertices [[25](#)]. However, including dynamical strange mesons is not consistent with the χ EFT expansion of nuclear forces that we apply here.

nucleon currents only appear at Next-to-Next-to-Next-to-Leading Order (N³LO) and are neglected.

For the gluonic interaction in eq. (2.1), the trace anomaly gives [63]

$$J_G(\mathbf{q}) = c_G^{N,(\text{is})} = -c_G \frac{8\pi}{9} [m_N - \sigma_{\pi N} - \sigma_s], \quad (2.15)$$

where the $\sigma_{\pi N}$ and σ_s are formally order (2) corrections which we absorb into $m_N^G \equiv m_N - \sigma_{\pi N} - \sigma_s$.

As for the interactions with strange quarks, momentum-dependent, isovector, and two-nucleon contributions only appear at order (3). However, it was noticed in Ref. [40] that two-nucleon currents provide numerically significant contribution to the nuclear structure functions of ¹³²Xe. These two-nucleon corrections arise from the DM-pion interactions

$$\mathcal{L}_{\chi,G}^\pi = c_G \frac{8\pi}{9} \bar{\chi} \chi \left[(\partial_\mu \boldsymbol{\pi})^2 - \frac{3}{2} m_\pi^2 \boldsymbol{\pi}^2 \right], \quad (2.16)$$

where the LECs are fixed by a comparison of the QCD and χ PT energy-momentum tensor [29]. The power-counting rules outlined in section 2.2.1 indicate that the resulting two-nucleon terms are indeed suppressed by three orders in the chiral expansion compared to the one-body contributions in eq. (2.15). Nevertheless, we investigate the resulting two-nucleon contributions to estimate the size of the missing order (3) terms and to study the numerical enhancement found in Ref. [40]. We obtain for the two-nucleon current

$$J_{G,2b}(\mathbf{q}) = -c_G \frac{8\pi}{9} \left(\frac{g_A}{2f_\pi} \right)^2 \frac{(\boldsymbol{\sigma}_1 \cdot \mathbf{q}_1)(\boldsymbol{\sigma}_2 \cdot \mathbf{q}_2)}{(\mathbf{q}_1^2 + m_\pi^2)(\mathbf{q}_2^2 + m_\pi^2)} \boldsymbol{\tau}_1 \cdot \boldsymbol{\tau}_2 (2\mathbf{q}_1 \cdot \mathbf{q}_2 - 3m_\pi^2), \quad (2.17)$$

where it should be stressed that there appear additional contributions at this order. In fact, in the limit of $|\mathbf{q}_{1,2}| \gg m_\pi$ the two-nucleon current approaches a DM-nucleon-nucleon contact interaction which appears at the same order in the chiral counting and is, in general, necessary to absorb the divergence and associated cutoff dependence of eq. (2.17). This implies that the calculation of the contribution from eq. (2.17) only provides a rough estimate of the size of higher order corrections.

2.3 Generation of nuclear wave functions and scattering matrix-elements

2.3.1 Matrix-elements

We consider scattering processes of the type $\chi(\mathbf{p}_\chi) + T(\mathbf{p}_T) \rightarrow \chi(\mathbf{p}'_\chi) + T(\mathbf{p}'_T)$, where T denotes the target nucleus of mass m_T consisting of A nucleons. We express the

spin-independent cross sections in the non-relativistic limit as [76]

$$\frac{d\sigma}{d\mathbf{q}^2} = \frac{1}{64\pi} \frac{|\mathcal{M}_A(\mathbf{q}^2)|^2}{m_T^2 m_\chi^2 v_\chi^2}, \quad (2.18)$$

where $\mathbf{q} = \mathbf{p}_\chi - \mathbf{p}'_\chi$ is the momentum transfer from DM to the target nucleus, v_χ is the DM velocity, and \mathcal{M}_A is the spin-independent scattering matrix-element. We compute the scattering matrix depending on the DM current \hat{J} and the wave function of the target nucleus $|\Psi_T, jm_j\rangle$ – with distinct total spin j and spin polarization m_j

$$|\mathcal{M}_A(\mathbf{q}^2)|^2 = \frac{(2m_T)^2(2m_\chi)^2}{2j+1} \sum_{m_j, m'_j=-j}^j |\langle \Psi_T, jm'_j | \hat{J}(\mathbf{q}^2) | \Psi_T, jm_j \rangle|^2. \quad (2.19)$$

The mass factors arise from the normalization of the relativistic particle states. In the following, we use that the internal properties of the wave functions are independent of the polarization m_j . The spin averaging guarantees that the matrix-element is spherically symmetric such that we are free to choose the direction of the momentum transfer \mathbf{q} . For convenience, we pick $\mathbf{q} = q\hat{e}_z$. As a consequence, m_j is conserved and the scattering process is independent of the value of m_j . Hence, the sum cancels against the spin averaging. We denote $|\Psi_T\rangle = |\Psi_T, jm_j\rangle$ from now on. The properties of the applied wave functions are described in [section 2.3.2](#).

To obtain the differential recoil rates measured in experiments, we have to convolve the cross section with the DM velocity distribution in the Earth frame

$$\frac{dR}{d\mathbf{q}^2} = \frac{1}{m_T m_\chi} \rho_\chi \int_{v_\chi^{(\min)}}^{v_\chi^{(\text{esc})}} d^3\mathbf{v}_\chi |\mathbf{v}_\chi| f(|\mathbf{v}_\chi|) \frac{d\sigma}{d\mathbf{q}^2}(\mathbf{v}_\chi), \quad (2.20)$$

where ρ_χ is the local DM density, and $v_\chi^{(\text{esc})} \approx 550$ km/s [77] is the maximal (escape) velocity which can be inferred from galaxy velocity distributions. The momentum transfer \mathbf{q} , in the non-relativistic limit, is constrained through energy conservation by a product of the minimal DM velocity $v_\chi^{(\min)}$ and the reduced mass of the colliding system, $\mu_T = m_T m_\chi / (m_T + m_\chi)$, times two. Hence, the upper bound for the momentum transfer is given by

$$|\mathbf{q}| \lesssim 2\mu_T v_\chi^{(\text{esc})} \lesssim A \times 2.5 \text{ MeV}, \quad (2.21)$$

for DM masses ≥ 1 GeV and for the light nuclei we consider here. For large nuclei the momentum transfer can become of the order of the pion mass and \mathbf{q}^2 corrections become more important. Since one of our primary goals is to estimate the accuracy of DM-nucleus cross sections, we present cross sections for larger \mathbf{q}^2 than relevant for scattering off light nuclei, assuming the expected DM velocity distributions, in order to test whether the accuracy of our results depends on the momentum transfer.

The scattering matrix-element can be expressed in terms of a sum over different nuclear

response functions $\mathcal{F}_{i,a}^{(\nu)}$

$$\left| \mathcal{M}_A(\mathbf{q}^2) \right|^2 = (2m_T)^2 (2m_\chi)^2 \sigma_N^{(\text{is})} \frac{\pi A^2}{\mu_N^2} \left| \sum_{i,a,\nu} \alpha_i \mathcal{F}_{i,a}^{(\nu)}(\mathbf{q}^2) \right|^2, \quad (2.22)$$

where we factored out A^2 and the LO isoscalar cross section of a DM-nucleon scattering process at zero momentum transfer

$$\sigma_N^{(\text{is})} = \frac{\mu_N^2}{\pi} |\sigma_{\pi N} c_\chi|^2. \quad (2.23)$$

We have set here $\bar{c}_{q^{(\text{is})}} = c_\chi$ and $\bar{c}_{q^{(\text{iv})}} = c_s = c_G = 0$. This arbitrary choice is just for normalization purposes. α_i is a dimensionless coefficient which depends on the DM couplings. As mentioned before, we can expand $\mathcal{F}_{i,a}^{(\nu)}(\mathbf{q}^2)$ order by order in the chiral expansion, but, since we cannot make model-independent statements about the (relative) sizes of the DM couplings $\bar{c}_{q^{(\text{is})}}, \bar{c}_{q^{(\text{iv})}}, c_s, c_G$, we have a separate chiral power counting for each of the fundamental interactions. If it is necessary to consider several DM interactions at the same time then the power counting must be aligned depending on the relative sizes of the couplings under consideration. We discuss this in [section 2.4.4](#) for the case of nonzero $\bar{c}_{q^{(\text{is})}}$ and c_G . Finally, we note that we recover the global counting of Ref. [40] once we assume the various c_i to be of the same size.

We will present our results in terms of response functions $\mathcal{F}_{i,a}^{(\nu)}(\mathbf{q}^2)$ which are classified according to the following

1. $i = \{q^{(\text{is})}, q^{(\text{iv})}, s, G\}$ indicating, respectively, dependence on the various DM couplings we consider $\{\bar{c}_{q^{(\text{is})}}, \bar{c}_{q^{(\text{iv})}}, c_s, c_G\}$,
2. at which chiral order $\nu = 0, 1, \dots$ in the chiral expansion of the currents they appear. The dominant current for each DM interaction, i.e. $\{\bar{c}_{q^{(\text{is})}}, \bar{c}_{q^{(\text{iv})}}, c_s, c_G\}$, starts at order 0.
3. We divide higher order contributions into two-nucleon terms ($a = 2b$) and one-nucleon radius (\mathbf{q}^2) corrections ($a = r$).

We can now expand the structure functions appearing in the cross section as

$$\begin{aligned} \frac{d\sigma}{d\mathbf{q}^2} = \frac{\sigma_N^{(\text{is})} A^2}{4\mu_N^2 v_\chi^2} & \left| \alpha_{q^{(\text{is})}} \left(\mathcal{F}_{q^{(\text{is})}}^{(0)}(\mathbf{q}^2) + \mathcal{F}_{q^{(\text{is}), 2b}}^{(1)}(\mathbf{q}^2) + \mathcal{F}_{q^{(\text{is}), r} }^{(1)}(\mathbf{q}^2) + \dots \right) \right. \\ & + \alpha_{q^{(\text{iv})}} \left(\mathcal{F}_{q^{(\text{iv})}}^{(0)}(\mathbf{q}^2) + \dots \right) + \alpha_s \left(\mathcal{F}_s^{(0)}(\mathbf{q}^2) + \mathcal{F}_{s,r}^{(1)}(\mathbf{q}^2) + \dots \right) \\ & \left. + \alpha_G \left(\mathcal{F}_G^{(0)}(\mathbf{q}^2) + \mathcal{F}_{G, 2b}^{(3)}(\mathbf{q}^2) + \dots \right) \right|^2. \end{aligned} \quad (2.24)$$

Here we expanded the currents up to order (1) and since there appear no new corrections at order (2), the dots indicate missing order (3) corrections. The only order (3) correction

we explicitly consider is the two-nucleon contribution arising from the DM-gluon interactions (see eq. (2.17)). We keep this term as a diagnostic tool to study the contributions of missing higher order corrections. The dimensionless couplings α_i are given by

$$\alpha_{q^{(\text{is})}} = \frac{\bar{c}_{q^{(\text{is})}}}{c_\chi}, \quad \alpha_{q^{(\text{iv})}} = \left(-\frac{\delta m_N}{4\sigma_{\pi N}} \right) \frac{\bar{c}_{q^{(\text{iv})}}}{c_\chi}, \quad \alpha_s = \left(\frac{\sigma_s}{\sigma_{\pi N}} \right) \frac{\bar{c}_s}{c_\chi}, \quad \alpha_G = \left(-\frac{8\pi}{9} \frac{m_N^G}{\sigma_{\pi N}} \right) \frac{c_G}{c_\chi}. \quad (2.25)$$

The factor of c_χ^{-1} is an artifact of the normalization in eqs. (2.22) and (2.23). With these definition, we obtain

$$\begin{aligned} \mathcal{F}_{q^{(\text{is})}}^{(0)}(\mathbf{q}^2) &= \mathcal{F}_s^{(0)}(\mathbf{q}^2) = \mathcal{F}_G^{(0)}(\mathbf{q}^2), \\ \mathcal{F}_{q^{(\text{is})}}^{(0)}(0) &= \mathcal{F}_s^{(0)}(0) = \mathcal{F}_G^{(0)}(0) = 1. \end{aligned} \quad (2.26)$$

The radius corrections $\mathcal{F}_{q^{(\text{is}),r}}^{(1)}(\mathbf{q}^2)$, and $\mathcal{F}_{s,r}^{(1)}(\mathbf{q}^2)$ involve the same nuclear matrix-elements as the order (0) one-nucleon contributions apart from an additional overall dependence on \mathbf{q}^2 . They therefore do not require additional nuclear calculations. The independent structure functions are therefore $\mathcal{F}_{q^{(\text{is})}}^{(0)}(\mathbf{q}^2)$, $\mathcal{F}_{q^{(\text{iv})}}^{(0)}(\mathbf{q}^2)$, $\mathcal{F}_{q^{(\text{is}),2b}}^{(1)}(\mathbf{q}^2)$, and $\mathcal{F}_{G,2b}^{(3)}(\mathbf{q}^2)$, in agreement with the findings of Ref. [40].

Although the ratio of LECs appearing in the definitions of α_i ranges from small values $-\delta m_N/(4\sigma_{\pi N}) \simeq -0.01$ to large values $(-8\pi m_N^G)/(9\sigma_{\pi N}) \simeq -40$, this does not reflect the relative importance of the various terms. The α_i depend on the definition of the DM couplings $c_{u,d,s,G}$ in eq. (2.1). For instance, eq. (2.1) assumes that the scalar couplings between light quarks and DM is proportional to the light-quark mass. While this is a reasonable assumption, it can be easily different in specific UV-complete models. We can only make model-independent statements about the relative sizes of different contributions proportional to the same α_i .

2.3.2 Nuclear wave functions

Our calculations are based on a momentum-space evaluation of matrix-elements that involve the DM interactions as introduced in the previous section and nuclear wave functions. Below, we require wave functions for ${}^2\text{H}$ and ${}^3\text{He}$ (and ${}^3\text{H}$) which we obtain from solutions of the non-relativistic Schrödinger equation in momentum space.

In the case of the deuteron, we directly solve

$$|\psi_d\rangle = \frac{1}{E_d - T} V_{12} |\psi_d\rangle. \quad (2.27)$$

Here, E_d is the deuteron binding energy, T is the two-nucleon (NN) kinetic energy and V_{12} the NN interaction. The deuteron wave function is expanded in momentum eigenstates $|p\alpha\rangle$ where α corresponds to the partial waves contributing to the deuteron

2.3 Generation of nuclear wave functions and scattering matrix-elements

NN interaction	E_d	$\langle T \rangle$	$\langle V \rangle$	r_d	Q_d	P_D	A_S	η
AV18	-2.225	19.81	-22.04	1.967	0.270	5.76	0.884	0.0252
CDB	-2.223	15.60	-17.83	1.966	0.270	4.85	0.884	0.0258
LO (Q^0) Λ_1	-1.989	14.26	-16.25	1.997	0.245	3.27	0.825	0.0219
LO (Q^0) Λ_2	-2.023	13.29	-15.32	1.990	0.230	2.54	0.833	0.0212
LO (Q^0) Λ_3	-2.083	12.47	-14.55	1.979	0.215	1.97	0.849	0.0205
LO (Q^0) Λ_4	-2.167	11.76	-13.92	1.965	0.199	1.53	0.870	0.0198
LO (Q^0) Λ_5	-2.272	11.15	-13.42	1.950	0.183	1.18	0.897	0.0192
NLO (Q^2) Λ_1	-2.191	15.40	-17.59	1.970	0.275	5.23	0.875	0.0256
NLO (Q^2) Λ_2	-2.199	14.25	-16.45	1.968	0.273	4.73	0.877	0.0256
NLO (Q^2) Λ_3	-2.206	13.49	-15.69	1.967	0.271	4.24	0.879	0.0257
NLO (Q^2) Λ_4	-2.211	12.92	-15.14	1.965	0.269	3.77	0.881	0.0258
NLO (Q^2) Λ_5	-2.213	12.48	-14.69	1.965	0.267	3.35	0.881	0.0259
N ² LO (Q^3) Λ_1	-2.228	14.94	-17.16	1.967	0.271	4.87	0.886	0.0254
N ² LO (Q^3) Λ_2	-2.231	13.85	-16.08	1.966	0.270	4.50	0.886	0.0256
N ² LO (Q^3) Λ_3	-2.235	13.17	-15.40	1.964	0.270	4.12	0.888	0.0258
N ² LO (Q^3) Λ_4	-2.237	12.69	-14.93	1.964	0.269	3.75	0.888	0.0260
N ² LO (Q^3) Λ_5	-2.235	12.32	-14.55	1.963	0.269	3.40	0.887	0.0263
N ³ LO (Q^4) Λ_1	-2.223	23.33	-25.55	1.970	0.268	3.78	0.884	0.0255
N ³ LO (Q^4) Λ_2	-2.223	21.58	-23.80	1.972	0.271	4.19	0.884	0.0255
N ³ LO (Q^4) Λ_3	-2.223	19.63	-21.85	1.975	0.275	4.77	0.885	0.0256
N ³ LO (Q^4) Λ_4	-2.223	17.71	-19.94	1.979	0.279	5.21	0.885	0.0256
N ³ LO (Q^4) Λ_5	-2.223	16.13	-18.35	1.982	0.283	5.58	0.885	0.0256
N ⁴ LO (Q^5) Λ_1	-2.223	20.64	-22.86	1.970	0.271	4.28	0.884	0.0256
N ⁴ LO (Q^5) Λ_2	-2.223	18.89	-21.12	1.972	0.271	4.29	0.884	0.0256
N ⁴ LO (Q^5) Λ_3	-2.223	17.48	-19.70	1.974	0.272	4.40	0.884	0.0255
N ⁴ LO (Q^5) Λ_4	-2.223	16.29	-18.51	1.978	0.276	4.74	0.885	0.0256
N ⁴ LO (Q^5) Λ_5	-2.223	15.27	-17.50	1.981	0.280	5.12	0.885	0.0256
Expt.	-2.225 [80]	—	—	1.975 [81]	0.286(2) [82]	—	0.878(4) [83]	0.0256(4) [84]

Table 2.1: Properties of the deuteron wave functions used. The deuteron binding energy E_d , the expectation value of the kinetic energy and of the potential are given in MeV. We also give the point proton rms radius r_d in fm, the quadrupole moment Q_d in fm² and the D-state probability P_D in percent together with the asymptotic normalization A_S in fm⁻¹ and $\eta = \frac{A_D}{A_S}$.

bound state: the orbital angular momentum $l_{12} = 0, 2$, NN spin $s_{12} = 1$ and the total angular momentum $j_{12} = 1$.

We consider both, modern phenomenological NN interactions and interactions based on chiral effective theory to obtain the wave functions. The two standard choices for phenomenological interactions are Argonne v18 (AV18) [78] and CD-Bonn (CDB) [79]. Although both interactions describe the available NN data below the pion production threshold essentially perfectly, their properties are quite different. The CDB interaction is much more non-local than AV18. For the deuteron, the non-observable kinetic energies, potential energies and D-state probabilities differs visibly for both models as can be seen from table 2.1. Therefore, a comparison of results for these models is a good indication of possible model dependences. For the radius and the quadrupole moment, there are slight deviations from the experimental values. These can be traced back to neglected contributions, e.g., meson-exchange currents and relativistic corrections, and uncertainties in the correction of the measured charge radii for the finite radii of the proton and neutron.

For the chiral interactions, we use the ones of Ref. [22]. Following the approach of Weinberg [19, 85], the non-perturbative character of the nuclear interactions is taken

Cutoff	Λ_1	Λ_2	Λ_3	Λ_4	Λ_5
R	0.8 fm	0.9 fm	1.0 fm	1.1fm	1.2 fm
Λ_b	600 MeV	600 MeV	600 MeV	500 MeV	400 MeV

Table 2.2: Cutoff values used to compute wave functions and the uncertainty estimates. Values are taken from Ref. [94].

into account by expanding a nuclear potential perturbatively in the pions mass m_π and the nucleon 3-momentum q over the chiral symmetry breaking or breakdown scale Λ_b . This potential is then used in a Schrödinger equation to obtain observables of nuclear systems.

We note that there has been some discussion of how such a non-perturbative expansion can be made consistently in leading and higher orders [86–93]. The approach used applies all orders of the interaction non-perturbatively. This procedure has been shown to result in a high-quality description of NN observables provided the interactions are regulated using finite values of a cutoff. For the interactions used here, the regularization is defined in configuration space and parameterized by a short-distance scale R . Explicit calculations have shown that R needs to be larger than 0.8 fm. The best description of the NN data is obtained for $R = 0.9$ fm. Based on the description of NN scattering data, the breakdown scale was estimated in [22] and turns out to be dependent on the chosen cutoff. We have summarized the available cutoff values in table 2.2 where we also introduce the shorthand notation Λ_i for the various cutoff values. To finalize our discussion of the NN interactions, we note that AV18 is accompanied by an Electromagnetic (EM) interaction, which we also take into account. Additionally, we have added the same EM interaction to the proton-proton and neutron-neutron interactions in case of CDB and the chiral interactions. In the latter cases, we did not add the EM part to the np interactions, since this would lead to a visible deviation of the deuteron binding energy to experiment. However, at least for CDB, the EM contribution is consistent since the interaction has been fitted to NN data, taking the EM contributions into account. We stress that the EM contribution is small and of minor importance.

In table 2.1, we also summarize the properties of the deuteron wave function for the chiral interactions at different orders of the chiral expansion $Q^i = (q, m_\pi/\Lambda_b)^i$, see section 2.3.3 for more details. It is seen that non-observable quantities like the D -wave probability, the kinetic and the potential energies strongly depend on the cutoff value chosen. Radii, binding energies, quadrupole moments, and asymptotic normalizations show much less variation and, in higher orders, reproduce the experimental values similarly to the phenomenological interactions. We stress, however, that this does not necessarily imply that we can expect results for DM scattering that are independent of the wave function.

In order to obtain the wave functions for ${}^3\text{He}$ (and ${}^3\text{H}$), we rewrite the Schrödinger equation into Faddeev equations

$$|\psi_{12}\rangle = G_0 t_{12} P |\psi_{12}\rangle + G_0 (1 + t_{12}G_0) V_{123}^{(3)} (1 + P) |\psi_{12}\rangle, \quad (2.28)$$

where we have introduced the Faddeev components $|\psi_{12}\rangle$. Due the antisymmetry of the ${}^3\text{He}$ wave function, all Faddeev components can be related to $|\psi_{12}\rangle$ using permutation operators. The combination of transpositions P_{ij} that enters the Faddeev equations is labeled by $P = P_{12}P_{23} + P_{13}P_{23}$. G_0 denotes the $3N$ free propagator. NN interactions enter via the t -matrices t_{12} which are obtained by solving a Lippmann-Schwinger equation for the NN system embedded into a $3N$ system. Finally, for some of the phenomenological calculations, we take TNFs into account. These are first separated in three parts again related by permutation operators $V_{123} = V_{123}^{(1)} + V_{123}^{(2)} + V_{123}^{(3)}$. Only one of these parts is required for the Faddeev equation. The equations are solved using Jacobi relative momenta. Therefore, the basis depends on two momenta, the relative momentum in the subsystem (12) of the first two nucleons p_{12} and the relative momentum p_3 of the third particle with respect to the other two. The angular dependence is expanded in corresponding orbital angular momenta l_{12} and l_3 . As in the NN system above, the orbital angular momentum l_{12} is coupled with the spin of the NN system s_{12} to the total two-body angular momentum j_{12} . The orbital angular momentum l_3 is coupled with the spin of the third nucleon to a spectator angular momentum I_3 . j_{12} and I_3 are finally combined to the total angular momentum $j_3 = 1/2$.

From the isospin t_{12} of the (12) subsystem and the isospin of the third nucleon, we build the total isospin τ_3 of ${}^3\text{He}$. Since we take the charge dependence of the nuclear force and electromagnetic forces into account, both isospins $\tau_3 = 1/2$ and $3/2$ contribute although the $3/2$ component is small [95]. For this work, we do not take the proton/neutron mass difference into account but assume an average nucleon mass of $m_N = 938.9182$ MeV. The number of partial waves states is constrained by the maximal NN angular momentum j_{12}^{max} . We chose $j_{12}^{max} = 6$ for the phenomenological interactions and $j_{12}^{max} = 7$ for the chiral ones. With these constraints on the partial waves and using approximately 60 momentum grids points for p_{12} and p_3 , we were able to obtain binding energies to an accuracy of 1 keV. More details on the calculations can be found in Ref. [96].

The binding energy results together with some basic wave function properties are summarized in table 2.3. The first observation is that the binding energies are generally not in perfect agreement with the experimental value. This discrepancy can be attributed to contributions of TNFs. For the phenomenological interactions, we have added TNFs that have been tuned to describe the mirror nucleus ${}^3\text{H}$ correctly [99]. Thereby, AV18 was augmented by the Urbana IX (URB IX) interaction [100] and CDB with the Tucson-Melbourne (TM) force [101]. Although it is an essential strength of chiral interactions that they are accompanied by TNFs that can be derived within the same framework, we have not added an chiral TNFs to the chiral interactions in this work since their adjustment is a work in progress. We show later that our results here are not significantly affected by URB IX and TM. We, therefore, expect that adding the chiral TNFs is not too important for the results in this work but we stress that this needs to be verified in a future calculation.

The table also gives results for point proton and neutron radii together with the rms distance of two nucleons. The rather strong dependence on the interaction model is due

NN interaction	$E(^3\text{He})$	$\langle T \rangle$	$\langle V \rangle$	r_p	r_n	r_{NN}	P_S	P_P	P_D	$\langle \Psi \Psi \rangle$
AV18	-6.922	45.67	-52.59	1.871	1.677	3.127	91.47	0.065	8.465	0.998752
AV18 + URB IX	-7.754	50.21	-57.97	1.770	1.601	2.966	90.63	0.131	9.241	0.998956
CDB	-7.264	36.77	-44.03	1.819	1.637	3.047	92.95	0.046	7.000	0.999505
CDB + TM	-7.729	38.53	-46.26	1.767	1.598	2.964	92.41	0.090	7.498	0.999589
LO (Q^0) Λ_1	-11.22	54.29	-65.51	1.327	1.258	2.259	95.31	0.031	4.659	0.999959
LO (Q^0) Λ_2	-10.92	48.71	-59.63	1.367	1.289	2.324	96.65	0.015	3.333	0.999969
LO (Q^0) Λ_3	-10.47	43.40	-53.87	1.424	1.334	2.416	97.58	0.008	2.410	0.999972
LO (Q^0) Λ_4	-10.01	38.70	-48.70	1.489	1.388	2.522	98.23	0.004	1.763	0.999976
LO (Q^0) Λ_5	-9.594	34.67	-44.27	1.558	1.444	2.634	98.69	0.002	1.304	0.999979
NLO (Q^2) Λ_1	-7.315	36.61	-43.92	1.805	1.626	3.025	92.19	0.057	7.755	0.999781
NLO (Q^2) Λ_2	-7.481	33.96	-41.44	1.784	1.610	2.992	93.06	0.046	6.890	0.999881
NLO (Q^2) Λ_3	-7.638	32.75	-40.38	1.764	1.595	2.960	93.94	0.037	6.025	0.999924
NLO (Q^2) Λ_4	-7.804	32.21	-40.01	1.744	1.579	2.927	94.76	0.029	5.210	0.999946
NLO (Q^2) Λ_5	-7.969	31.96	-39.93	1.723	1.563	2.895	95.51	0.022	4.466	0.999959
N ² LO (Q^3) Λ_1	-7.305	35.68	-42.99	1.821	1.639	3.050	92.99	0.045	6.966	0.999771
N ² LO (Q^3) Λ_2	-7.409	32.88	-40.29	1.806	1.628	3.027	93.61	0.039	6.357	0.999877
N ² LO (Q^3) Λ_3	-7.540	31.63	-39.17	1.788	1.614	2.999	94.26	0.032	5.713	0.999925
N ² LO (Q^3) Λ_4	-7.680	31.13	-38.81	1.769	1.599	2.969	94.90	0.027	5.078	0.999947
N ² LO (Q^3) Λ_5	-7.824	30.96	-38.79	1.749	1.584	2.937	95.51	0.022	4.470	0.999960
N ³ LO (Q^4) Λ_1	-6.865	51.81	-58.67	1.884	1.691	3.148	94.79	0.027	5.189	0.998593
N ³ LO (Q^4) Λ_2	-6.871	50.74	-57.61	1.890	1.697	3.159	94.07	0.032	5.897	0.998904
N ³ LO (Q^4) Λ_3	-6.832	46.94	-53.77	1.901	1.707	3.180	93.12	0.041	6.842	0.999219
N ³ LO (Q^4) Λ_4	-6.812	42.31	-49.13	1.910	1.716	3.196	92.43	0.048	7.524	0.999481
N ³ LO (Q^4) Λ_5	-6.779	38.21	-44.99	1.921	1.725	3.215	91.89	0.053	8.052	0.999661
N ⁴ LO (Q^5) Λ_1	-6.790	52.31	-59.10	1.898	1.701	3.170	93.96	0.033	6.005	0.998833
N ⁴ LO (Q^5) Λ_2	-6.893	47.33	-54.22	1.886	1.693	3.154	93.92	0.033	6.046	0.999185
N ⁴ LO (Q^5) Λ_3	-6.931	43.30	-50.23	1.885	1.695	3.155	93.71	0.035	6.255	0.999424
N ⁴ LO (Q^5) Λ_4	-6.919	39.84	-46.76	1.893	1.702	3.169	93.17	0.040	6.786	0.999597
N ⁴ LO (Q^5) Λ_5	-6.872	36.75	-43.62	1.906	1.714	3.192	92.60	0.046	7.351	0.999719
Expt.	-7.718 [97, 98]	—	—	1.776	—	—	—	—	—	—

Table 2.3: Properties of the ^3He wave functions used. The ^3He binding energy $E(^3\text{He})$, the expectation value of the kinetic energy and of the potential are given in MeV. We also give the point proton and neutron rms radius and the rms distance of two nucleons, r_p , r_n and r_{NN} , respectively, in fm. The S-, P-, and D-state probabilities P_S , P_P , and P_D are given in %. The deviations of the norm of the wave functions from 1 are a measure of higher partial-wave contributions (see text).

to a high correlation with the binding energy [102] and therefore driven by the long-distance components of the wave function. We compare the point proton radius to an experimental value that is based on the charge radius of ^3He of $r_{ch} = 1.976(15)$ fm [103] and corrected for the finite proton and neutron size along the lines explained in Ref. [94].

We also give the probability to find total orbital angular momentum $L = 0, 1, 2$ in our wave functions. To obtain these numbers, we performed a recoupling of angular momenta to an LS coupling scheme. Besides the dominant S-wave component, we find a sizable D-wave component. The P-wave component is quite small.

The last column of the table gives results for the norm of the wave function. It can be shown using the antisymmetry of the wave function that the scalar product of the wave function $|\Psi\rangle = (1 + P)|\Psi_{12}\rangle$ is

$$\langle \Psi | \Psi \rangle = 3 \langle \psi_{12} | \Psi \rangle. \quad (2.29)$$

Numerically, this relation is not strictly fulfilled since higher partial waves are missing. We use the right-hand side for the normalization of the wave function. This generally leads to larger accuracy since the partial wave convergence of the Faddeev component is faster than that of the wave function. The last column shows the left-hand side of the equation. The deviation from one is small, but still, some higher partial wave contributions are missing. Their contribution to matrix-elements is generally suppressed when finite-range operators are considered as we do in this work.

2.3.3 Chiral expansion and uncertainty estimation

The calculation of the scattering amplitude, or equivalently the response functions, depends on both the nuclear wave function (Ψ) and the DM current (\hat{J}) that is sandwiched between the wave functions. Both quantities can be expanded order by order in the chiral expansion. The LO contribution to the cross section arises from combining LO wave functions with the order (0) one-nucleon current. For isoscalar DM-quark interactions the first corrections arise from applying NLO wave functions and from the order (1) two-nucleon and radius corrections to the currents. For the DM-strange quark interactions, the currents are only altered by the radius corrections, while for the remaining DM interactions only the wave function is affected. Analogously, even higher order wave functions should be combined with higher order corrections to the currents. However, whereas we have access to N³LO and N⁴LO wave functions, we do not control the currents at the same order. That is, a consistent calculation with these wave functions would also require the calculation of missing higher order currents. This can be done with the methods of Refs. [104, 105], but is beyond the scope of this work.

As discussed below, we find that the corrections associated to the inclusion of higher order-currents are smaller than the corrections associated with higher order wave functions. For this reason, we chose to present our uncertainty estimation based on the variation of different orders in the wave functions but fixed current orders: We sandwich the one- and two-nucleon currents derived in section 2.2.1 between wave functions calculated from LO up to N⁴LO nucleon-nucleon potentials. We show that at least N³LO wave functions are required in order to get precise results for two-nucleon currents.

To assign an uncertainty to our calculation at each order in the chiral expansion of the wave function, we follow the scheme of Ref. [94], which we slightly modify in order to account for missing high-order effects of the currents. The objective of this scheme is to make a prediction for the value of the observable X with a well-defined uncertainty estimate. In this work, the observable X corresponds to the magnitude squared of the response functions $X = |\mathcal{F}|^2$, but the procedure can be used for any quantity. As we are only able to approximate X with wave functions at finite chiral order ν , it is desirable to quantify the uncertainty $\delta^{(\nu)}X$ associated with the approximation. The calculation of

$X^{(\nu)}$ is uncertain up to missing corrections proportional to $Q^{\nu+1}$

$$X^{(\nu)} = X + \delta^{(\nu)}X = X + \sum_{i=1}^{\infty} Q^{\nu+i} \Delta X_i^{(\nu)}, \quad (2.30)$$

where X would be the result of a fictitious infinite-order calculation. $\Delta X_i^{(\nu)}$ denotes a set of coefficients parameterizing the uncertainty for a given order in Q – the dimensionless expansion parameter that is given by the generic momentum $p \sim m_\pi \sim q$ divided by the large breakdown scale. For the numerical error estimates we use $Q = \max(q/\Lambda_b, m_\pi/\Lambda_b)$ with Λ_b a regulator scale which depends on the coordinate-space cutoff used in the evaluation of the nuclear wave functions (see [table 2.2](#)). That is, for small momentum transfers, q is determined by m_π/Λ_b .

For a well-behaved expansion, all the coefficients $\Delta X_i^{(\nu)}$ are expected to be of natural order $\Delta X_i^{(\nu)} \sim X$. We approximate the error by assuming that one can find a maximal coefficient $\Delta X_{\max}^{(\nu)} \geq |\Delta X_i^{(\nu)}|$, which allows us to resum the series

$$\delta^{(\nu)}X \leq Q^\nu \left| \Delta X_{\max}^{(\nu)} \right| \sum_{i=1}^{\infty} Q^i = \frac{Q^{\nu+1}}{1-Q} \left| \Delta X_{\max}^{(\nu)} \right|. \quad (2.31)$$

This uncertainty estimate is rather conservative as we have used not only the maximal term but also assumed a coherent summation of uncertainties. To find the size of the coefficient, we analyze the difference of the same observable at two different chiral orders $\nu' > \nu$

$$X^{(\nu)} - X^{(\nu')} = Q^\nu \left(\Delta X_1^{(\nu)} + \mathcal{O}(Q) \right). \quad (2.32)$$

We finally estimate this coefficient by further taking the maximal value over all computed differences at different chiral orders

$$\left| \Delta X_{\max}^{(\nu)} \right| \leq \left| \Delta X_{\max} \right| = \max_{\nu} \left(\left| \Delta X_{\max}^{(\nu)} \right| \right), \quad \Delta X_{\max}^{(\nu)} \simeq \max_{\nu' > \nu} \left(\frac{\left| X^{(\nu)} - X^{(\nu')} \right|}{Q^{\nu+1}} \right). \quad (2.33)$$

The final uncertainty estimate is then given by

$$\delta X^{(\nu)} \leq \frac{Q^{\nu+1}}{1-Q} \left| \Delta X_{\max} \right|. \quad (2.34)$$

While this method provides a conservative estimate of the uncertainty at a given chiral order of the wave functions, we stress again that the estimate does not entirely capture the missing higher order currents. Also, the simple procedure outlined here does not provide a statistical interpretation of the theoretical uncertainty.

2.4 Results and discussion

2.4.1 Convergence and uncertainty estimates

We now turn to the results of our calculation. We mainly discuss the case of the isoscalar quark-DM interactions as they lead to the most interesting higher order currents. The other cases are briefly discussed in [section 2.4.3](#). As discussed above, we calculate the structure functions that appear in [eq. \(2.24\)](#) for different chiral and phenomenological wave functions. When using chiral wave functions, we present results for each order in the chiral expansion and for different values of the cutoff used to regulate the bound-state equations. The theoretical uncertainty of our result at each order in the chiral expansion is obtained by the method described in [section 2.3.3](#). In this work we focus on the nuclear aspects of DM direct detection and we, therefore, do not show the uncertainty associated to hadronic quantities such as the uncertainty on $\sigma_{\pi N}$ and δm_N . We refer to, for example, [Ref. \[58\]](#) for discussions of the latter. We also do not include astrophysical uncertainties related to DM direct detection [\[106\]](#).

We begin with discussing the results for scattering off the deuteron. In the top-panel of [fig. 2.2](#) we show results for $|\mathcal{F}_{q^{(is)}}^{(0)}(\mathbf{q}^2)|^2$ for three different values of the momentum transfer $q = |\mathbf{q}|$. At zero momentum transfer, the results are equal to unity for each applied wave function due to the normalization of the structure functions, see [eq. \(2.26\)](#). For larger values of the momentum transfer, the structure function decreases, which can be described by a Helm form factor as discussed in the next section. We find essentially no dependence on the order of the chiral wave function used nor on the applied cutoff which is reflected by the tiny uncertainty bands on the results.

In the second row, we show the effect of including the higher order currents arising from radius and two-body corrections:

$$|\mathcal{F}_{q^{(is)}}^{(0+1)}(\mathbf{q}^2)|^2 \equiv |\mathcal{F}_{q^{(is)}}^{(0)}(\mathbf{q}^2) + \mathcal{F}_{q^{(is),2b}}^{(1)}(\mathbf{q}^2) + \mathcal{F}_{q^{(is),r}}^{(1)}(\mathbf{q}^2)|^2. \quad (2.35)$$

Compared to the top panel, the results have shifted by only a small amount, indicating that higher order currents only moderately modify the cross section. The uncertainty of the total result, however, has increased significantly in particular for NLO chiral wave functions. As we discuss in more detail below, the increase in uncertainty is caused by a relatively large dependence of the two-body corrections on the applied wave function. Finally, we note that the relative effect of the higher order currents seems to decrease somewhat for larger values of the momentum transfer. This happens because of mutual cancellations between the radius and two-nucleon corrections.

In the last two rows of [fig. 2.2](#), we study the effects of higher order currents in more detail. In the third and fourth row, we show, respectively, the relative contribution of the radius and two-body currents with respect to the full result shown in the second row.

That is,

$$\begin{aligned}\Delta^{(r)} &= \frac{|\mathcal{F}_{q^{(\text{is})}}^{(0+1)}(\mathbf{q}^2)|^2 - |\mathcal{F}_{q^{(\text{is})}}^{(0)}(\mathbf{q}^2) + \mathcal{F}_{q^{(\text{is}),2b}^{(1)}(\mathbf{q}^2)|^2}{|\mathcal{F}_{q^{(\text{is})}}^{(0+1)}(\mathbf{q}^2)|^2}, \\ \Delta^{(2b)} &= \frac{|\mathcal{F}_{q^{(\text{is})}}^{(0+1)}(\mathbf{q}^2)|^2 - |\mathcal{F}_{q^{(\text{is})}}^{(0)}(\mathbf{q}^2) + \mathcal{F}_{q^{(\text{is}),r}^{(1)}(\mathbf{q}^2)|^2}{|\mathcal{F}_{q^{(\text{is})}}^{(0+1)}(\mathbf{q}^2)|^2}.\end{aligned}\tag{2.36}$$

Just like the order (0) structure functions, the radius corrections do not depend on the order of the chiral wave function nor on the applied cutoff. This can be easily understood as the current has the same form as the order (0) one-body current apart from the dependence on $F(|\mathbf{q}|/2m_\pi) \simeq (5/9)|\mathbf{q}^2|/(4m_\pi^2) + \dots$ [see eq. (2.11)]. The nuclear aspects of the calculation are therefore identical. The radius correction vanishes at zero momentum transfer and is only -2% for $q = 100$ MeV.

More interesting are the two-body corrections. In contrast to one-body currents, we obtain a significant dependence on the applied wave function. If we apply NLO wave functions the effects of two-body currents at zero momentum transfer range from $\Delta^{(2b)} = (2 \pm 15)\%$ when using cutoff Λ_1 up to $2 \pm 3\%$ when using cutoff Λ_2 , while the other cutoffs give values in between these extremes. This large uncertainty for all cutoffs indicates that the two-body corrections depend on aspects of the wave function not captured by the observables given in table 2.1. For instance, the NLO wave functions already give good agreement with experiments as far as the binding energy, radius, quadrupole moment, and the asymptotic D/S ratio are concerned. Increasing the order of the chiral wave functions, we observe an order-by-order convergence of the results. Using N²LO wave functions we still observe a significant cutoff dependence of the result ranging from $\Delta^{(2b)} = (3 \pm 4)\%$ for Λ_1 up to $\Delta^{(2b)} = (1.6 \pm 0.8)\%$ for Λ_2 , but for even higher order wave functions almost all cutoff dependence has disappeared and we obtain stable results. This can be seen in more detail from table B.3 given in appendix B.4.

In line with previous observations [67], we find that using the cutoff Λ_2 , gives rise to the fastest convergence pattern. Since all results for different Λ_i are consistent once the most accurate wave functions are applied, in the following sections, we will show results using Λ_2 .

In fig. 2.3 we show the analogous plots for scattering off ${}^3\text{He}$. We do not show the results for ${}^3\text{H}$ as the main features are essentially the same (see table B.3 for numerical results of the two-nucleon matrix-elements.) Regarding one-nucleon currents, the main difference concerning the ${}^2\text{H}$ case is that already the leading structure function has a significant uncertainty at larger momentum transfer even for N²LO wave functions. This uncertainty reflects the more complicated nature of three-nucleon wave functions.

The two-body contributions are smaller than in the deuteron case and significantly more uncertain. The relative two-body correction is roughly a factor 5 smaller than for ${}^2\text{H}$. This smallness is perhaps unexpected as the relative importance of two-body currents is

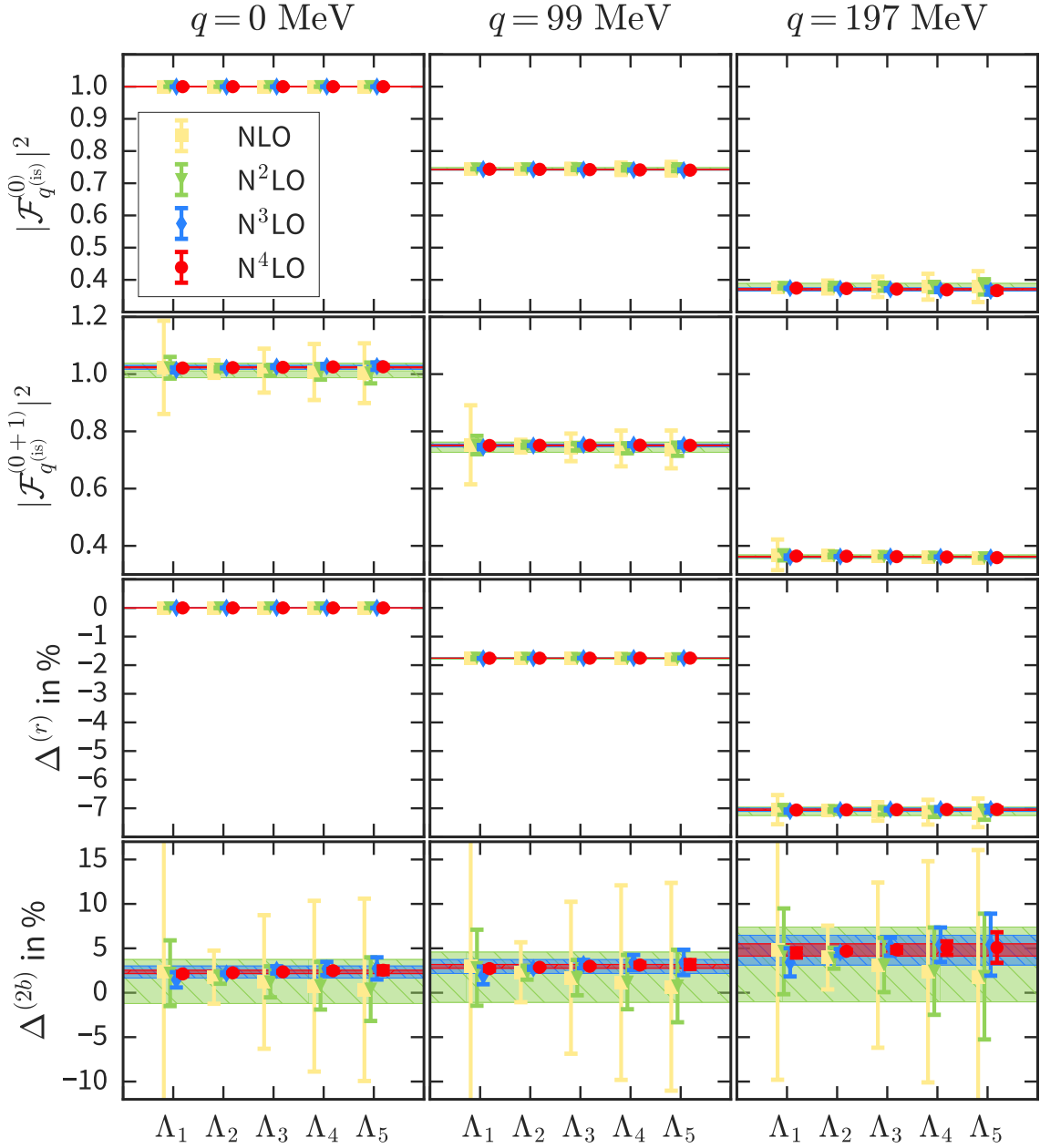


Figure 2.2: The plots show different structure functions for isoscalar quark-DM interaction for the ${}^2\text{H}$ system at three values of the momentum transfer q . From top to bottom the panels indicate, respectively, the leading, order (0), one-nucleon isoscalar structure functions, the full order (0+1) isoscalar structure functions including two-body and radius corrections, the modification in percent due to the radius corrections, and the modification in percent due to two-body corrections. Results are shown for different chiral wave functions (NLO up to $N^4\text{LO}$) and for the five different cutoffs given in table 2.2. The colored bands, from outermost to innermost, correspond to averages over all cutoffs at $N^2\text{LO}$, $N^3\text{LO}$, and $N^4\text{LO}$ in the wave expansion. Results for LO wave functions are not shown because the uncertainty bands are too large.

Target	a (fm)	s (fm)
${}^2\text{H}$	0.47	1.09
${}^3\text{H}$	0.38	0.96
${}^3\text{He}$	0.39	0.98

Table 2.4: Helm form factor coefficients for the order (0) response functions for ${}^2\text{H}$ and ${}^3\text{He}$. The coefficients are fitted to $\mathcal{F}_{q(\text{is})}^{(0)}$ for N²LO wave functions at cutoff Λ_2 .

naively expected to grow with A compared to the one-body results. The smallness for ${}^3\text{He}$ is probably related to the spin-isospin structure of ${}^3\text{He}$ and was also observed in an analysis of pion-nucleus scattering lengths where very similar two-body currents appear [107, 108]. We expect two-body currents to grow in denser nuclei and aim to investigate ${}^4\text{He}$ in a forthcoming study.

Independent of the size, it is interesting to study how accurate we can calculate the two-body corrections. Like for the ${}^2\text{H}$ scenario, we see that using NLO wave functions gives rise to significant uncertainties. The accuracy improves with N²LO wave functions, but unlike the ${}^2\text{H}$ case, even with the fastest-converging cutoff, Λ_2 , the uncertainty on the two-body correction is roughly 100%. At least N³LO wave functions are necessary to obtain results distinguishable from zero.

2.4.2 Discussion

We summarize our results in fig. 2.4 where we show the full isoscalar structure functions, the radius corrections, and the two-body corrections obtained from N²LO-N⁴LO wave functions using the fastest converging cutoff Λ_2 . We also show results using phenomenological wave functions. As is clear from the first panel and the discussions above, the NLO corrections to the isoscalar structure functions for both ${}^2\text{H}$ and ${}^3\text{He}$ are small and the impulse approximation, i.e., neglecting all two-nucleon contributions, is excellent. The q^2 -dependence of the structure functions can be parametrized by a Helm form factor [109, 110] (although this is usually done for heavier nuclei) which we fitted to our results for the leading one-nucleon response functions. We parametrize the form factor as

$$\begin{aligned}
 \mathcal{F}^{(\text{H})}(q) &= 3 \frac{j_1(qr_n)}{qr_n} e^{-(qs)^2/2}, \\
 r_n^2 &= c^2 + \frac{7}{3}\pi^2 a^2 - 5s^2, \\
 c &= (1.23A^{1/3} - 0.60)\text{fm},
 \end{aligned}
 \tag{2.37}$$

and provide fit values for a and s in table 2.4. The fitted form factors describe the full results well over the considered range of momentum transfer. The result is also very stable with respect to different nucleon-nucleon potentials and, essentially, all wave functions

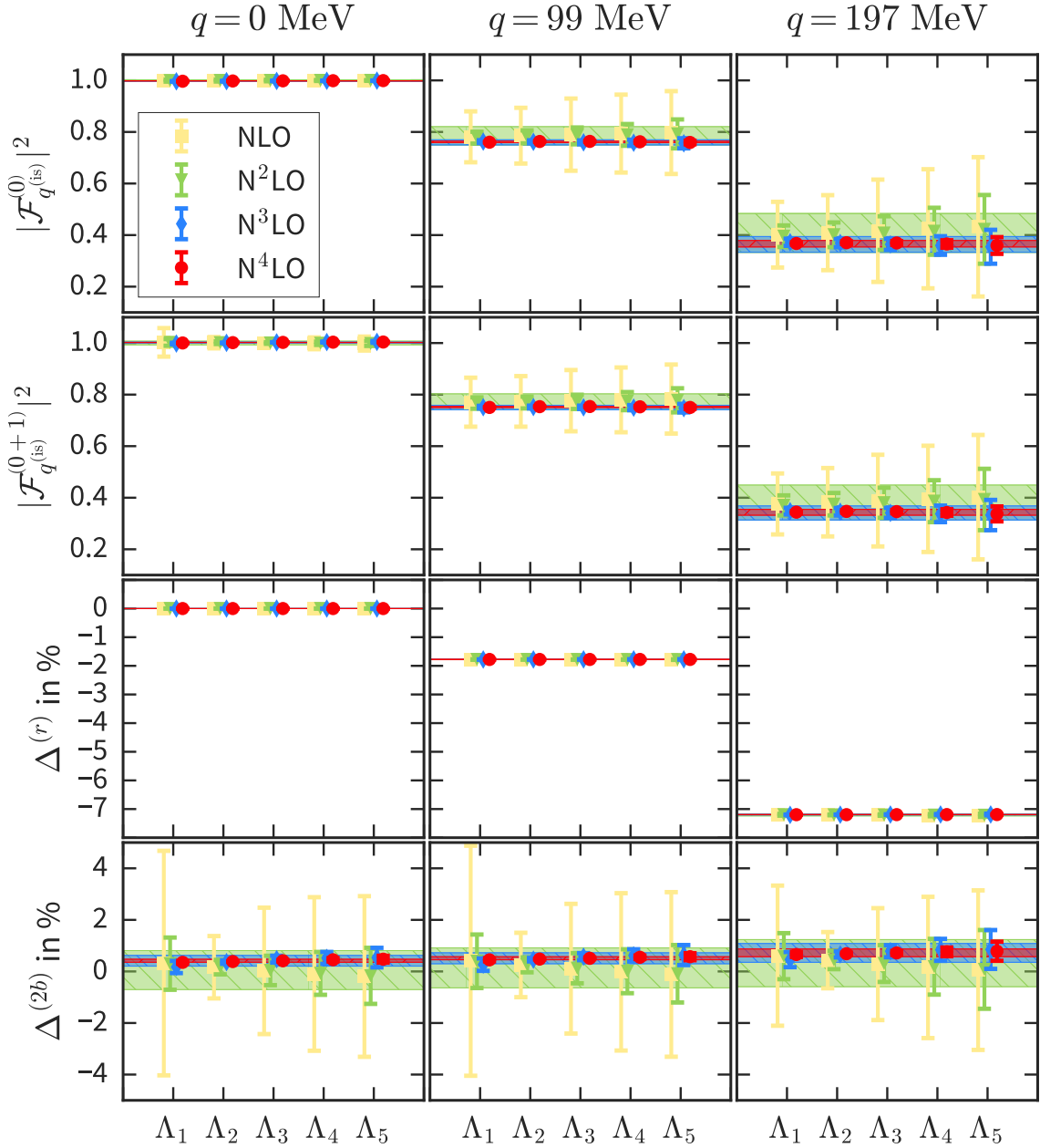


Figure 2.3: The plots show different structure functions for isoscalar quark-DM interaction for the ${}^3\text{He}$ system at three values of the momentum transfer q . From top to bottom the panels indicate, respectively, the leading order (0) one-body isoscalar structure functions, the full order (0+1) isoscalar structure functions including two-body and radius corrections, the modification in percent due to the radius corrections, and the modification in percent due to two-body corrections. Results are shown for different chiral wave functions (NLO up to N⁴LO) and for the five different cutoffs given in table 2.2. The colored bands, from outermost to innermost, correspond to averages over all cutoffs at N²LO, N³LO and N⁴LO in the wave expansion.

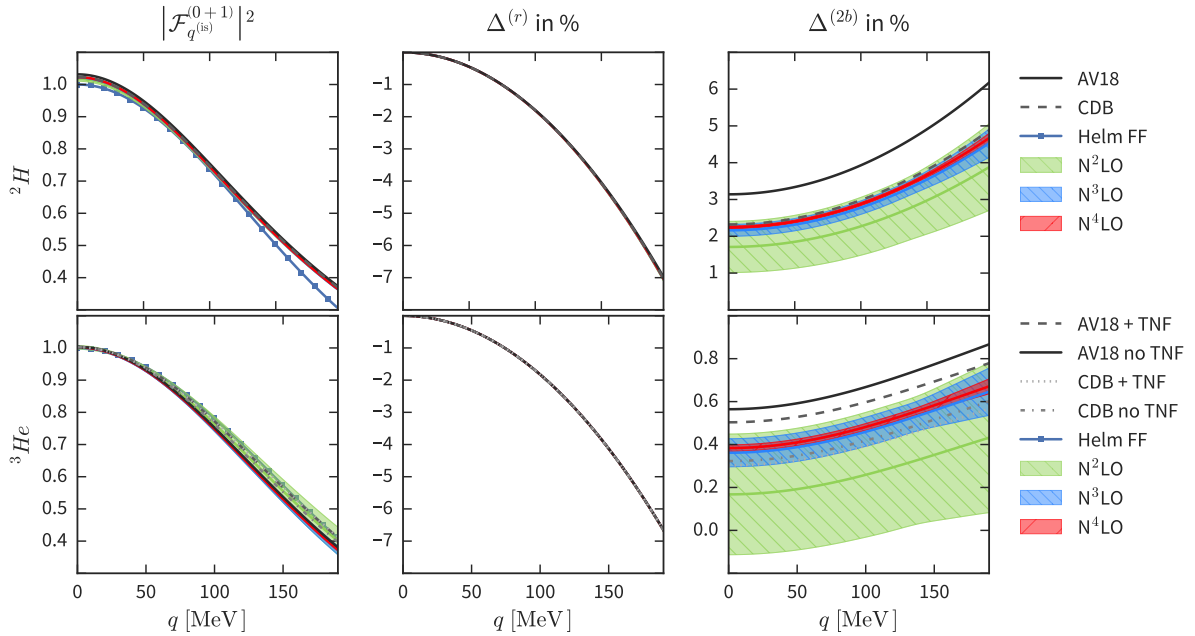


Figure 2.4: The left column shows the full order (0+1) isoscalar-quark DM structure functions for ${}^2\text{H}$ (top) and ${}^3\text{He}$ (bottom). The second and third columns denote, respectively, the radius and two-nucleon corrections as defined in eq. (2.36). The uncertainty bands correspond to chiral wave functions at N^2LO , N^3LO , and N^4LO (from outer- to innermost: green, blue, red). Results from using phenomenological wave functions and for the fitted Helm form factor (left panel only) are also shown. The phenomenological wave functions for ${}^3\text{He}$ are generated with and without TNFs.

give the same results. This is not surprising as the full structure function is dominated by the one-body scalar currents, which were found to be independent of wave-functions. The same holds true for the radius corrections shown in the second column of fig. 2.4.

The effects of two-body currents are summarized in the third panel of fig. 2.4. Their magnitude is very modest in the light nuclei under consideration, and in general cases, it should be safe to neglect them. The fact that they only provide a few-percent correction is not in good agreement with the expected size based on χEFT power counting, which predicts effects of $\mathcal{O}(p/\Lambda_\chi) \sim \mathcal{O}(m_\pi/\Lambda_\chi) \sim (10\text{-}30)\%$. Despite the small size of two-nucleon contributions, it is interesting to study the accuracy with which they can be determined as they can become more relevant in heavier nuclei [40] (as was found in the case of neutrino-nucleus scattering [111]), in cases where one-body contributions are canceled against other contributions [25, 39], or for non-scalar DM interactions that lead to spin-dependent DM-nucleus scattering [26]. Furthermore, the scalar two-nucleon currents at zero momentum transfer provide the dominant two-nucleon contribution to nuclear σ -terms [57], which describe the dependence of the nuclear mass on the quark masses.

Whereas the single-nucleon contributions are very stable, we find much a larger wave-

function dependence for the two-nucleon contributions. Using N²LO chiral wave functions we observe a 50% uncertainty on the ²H two-body matrix-elements and 100% on the ³He matrix-elements. Both uncertainties decrease significantly once N³LO wave functions are applied. At this and higher chiral order, the uncertainty estimates do not include the effects of potential higher order currents. We briefly discuss these in the next section.

Results using high-order chiral wave functions are in good agreement with phenomenological wave functions. Where AV18 predicts somewhat larger two-body corrections, CDB is in very good agreement with the results for N³LO and N⁴LO wave functions. The main advantage of applying chiral wave functions is that they allow for a systematic uncertainty estimate. Finally, our ³He chiral wave functions do not include TNFs which brings in a further uncertainty not quantified by the uncertainty bands. We expect however that TNFs do not affect the results significantly as they only mildly affect the results for phenomenological wave functions. Furthermore, the spread of phenomenological results with and without TNFs is of the same size as the estimated uncertainty of our N³LO results.

It is interesting to study in more detail why the two-body current matrix-elements suffer from large uncertainties even though the NLO and N²LO ²H and ³He wave functions describe several observable quantities quite well (see [tables 2.1](#) and [2.3](#)). While studying the two-body current matrix-elements, we observed a significant correlation between the *D*-wave probability of the wave function and the two-nucleon matrix-element [defined in [eq. \(B.34\)](#)]. This correlation is shown in [fig. 2.5](#). It turns out that the correlation follows an almost linear behavior with different slopes and interceptions for ²H and ³He. The strong dependence of the two-body correction on the *D*-wave probability is also seen in the context of pion-deuteron scattering [[107](#), [108](#)]. The *D*-wave probabilities change significantly from N²LO to N³LO chiral wave functions, see [tables 2.1](#) and [2.3](#), probably due to the appearance of new short-range interactions in the nucleon-nucleon potential. The connection to the *D*-wave probability might also be interesting for LQCD calculations of nuclear σ -terms at non-physical pion masses [[57](#)] as larger pion masses can lead to a suppressed nucleon-nucleon tensor force and thus a reduced *D*-wave probability.

The observation that two-body corrections suffer from large uncertainties when using N²LO chiral wave functions for light nuclei might indicate that the corresponding uncertainties for more complex systems can be even more significant, although further study is required to confirm this. This observation is potentially relevant for two-nucleon corrections in other contexts such as calculations of neutrino scattering off ⁴He and ¹²C nuclei [[111](#)] using N²LO chiral wave functions obtained with Quantum Monte Carlo methods. In any case, it is worthwhile to note that wave functions with very similar properties regarding observables such as binding energies and electromagnetic moments, can still lead to different two-nucleon matrix-elements.

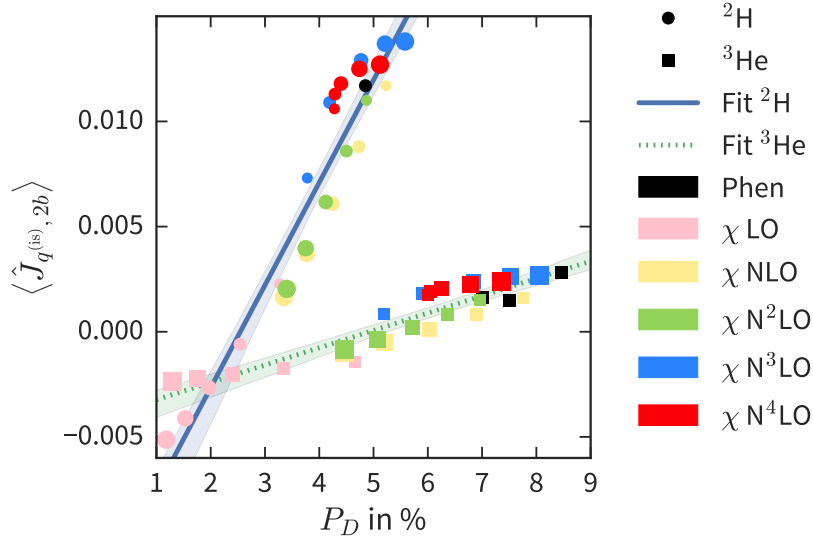


Figure 2.5: Correlation between isoscalar two-nucleon matrix-elements and the D -wave probability. Circles and squares correspond to ${}^2\text{H}$ and ${}^3\text{He}$, respectively. The sizes of the circles and squares correspond to the sizes off the cutoff – the smallest (largest) symbols represent Λ_1 (Λ_5). Different colors correspond to different wave functions. A linear fit results in $\langle J_{q^{(is)}, 2b} \rangle = 4.9 \cdot 10^{-3} P_D - 1.2 \cdot 10^{-2}$ for ${}^2\text{H}$ and $\langle J_{q^{(is)}, 2b} \rangle = 8.2 \cdot 10^{-4} P_D - 4.1 \cdot 10^{-3}$ for ${}^3\text{He}$.

2.4.3 The remaining DM interactions

Having discussed in detail the isoscalar quark-DM interactions, we now briefly turn to the remaining terms in eq. (2.1). As is clear from the parametrization of the differential cross section in eqs. (2.24) to (2.26), the order (0) one-nucleon contributions from strange quark-DM and gluon-DM interactions depend on the same structure function as the isoscalar quark-DM interactions. The order (0) results can therefore be directly read off from the top panels of figs. 2.2 and 2.3. The differential cross sections only differ in their overall size by the dependence on different DM couplings and strong LECs, as indicated in eq. (2.25). Similarly, the order (1) radius corrections for the strange quark-DM interactions can be read off from the third panels of figs. 2.2 and 2.3 after appropriate rescaling of the \mathbf{q}^2 dependence of the strange σ -term with respect to the light-quark σ -term [see eqs. (2.11) and (2.14)]. These radius corrections are not present for isovector quark-DM or gluon-DM interactions until order (3) currents. Furthermore, none of the remaining DM interactions, $\bar{c}_{q^{(iv)}}$, c_s , c_G , lead to two-nucleon corrections until order (3). We discuss one such correction below.

The only nontrivial difference with respect to the isoscalar structure functions then arises from the isospin structure τ_i^3 that appears in eq. (2.11) for the leading one-nucleon current arising from $\bar{c}_{q^{(iv)}}$. At zero momentum transfer, the isoscalar operator counts the number of nucleons giving rise to the factor A^2 in eq. (2.22). Similarly, at $\mathbf{q}^2 = 0$, the isovector interactions count the difference between the number of protons and neutrons. This

implies that these contributions vanish for the DM- ^2H scattering but contribute to DM- ^3He (and ^3H) scattering.

To investigate the typical size of isospin-violating corrections, we choose for the DM couplings in eq. (2.1) the following values $c_u = c_d = c_\chi$ and $c_s = c_G = 0$. This choice implies $\alpha_{q^{(\text{is})}} = 1$ and $\alpha_{q^{(\text{iv})}} = -\delta m_N / (2\sigma_{\pi N}) \simeq -0.02$. Because of the smallness of $\alpha_{q^{(\text{iv})}} / \alpha_{q^{(\text{is})}}$, in this scenario the dominant contribution to the scattering process arises from the one-nucleon isoscalar current² Subleading corrections then arise from the isoscalar radius and two-nucleon corrections and the isovector contributions. The differential cross section is proportional to

$$|\mathcal{F}(\mathbf{q}^2)|^2 = \left| \alpha_{q^{(\text{is})}} \left[\mathcal{F}_{q^{(\text{is})}}^{(0)}(\mathbf{q}^2) + \mathcal{F}_{q^{(\text{is}), 2b}^{(1)}(\mathbf{q}^2) + \mathcal{F}_{q^{(\text{is}), r}^{(1)}(\mathbf{q}^2) \right] + \alpha_{q^{(\text{iv})}} \mathcal{F}_{q^{(\text{iv})}}^{(0)}(\mathbf{q}^2) \right|^2. \quad (2.38)$$

In fig. 2.6, we plot the various contributions to $|\mathcal{F}(\mathbf{q}^2)|^2$ for scattering off ^2H (left panel) and ^3He (right panel) applying N²LO chiral wave functions using the fastest converging cutoff. As mentioned, the main contribution arises from the isoscalar contribution, which is depicted by $\mathcal{F}_{q^{(\text{is})}}^{(0)}$. For scattering of ^2H , there are no isospin-violating corrections and the first correction arises from the interference between the isoscalar one- and two-nucleon contributions depicted by $\mathcal{F}_{q^{(\text{is})}}^{(0)} - \mathcal{F}_{q^{(\text{is}), 2b}^{(1)}}$. As discussed in more detail above, the two-nucleon corrections suffer from significant uncertainties illustrated by the red band. The final corrections come from the order (1) one-nucleon radius corrections and are smaller than the two-nucleon corrections over the considered range of momentum exchange. We do not show contributions from the square of two-nucleon or radius corrections (or their interference) as these are smaller by orders of magnitude.

The pattern is somewhat different for ^3He (and ^3H which is very similar and not shown). In this case, the largest correction arises from the interference between the isoscalar and isovector one-nucleon terms. For the choice $c_u = c_d$ this correction amounts to only (1-2)% roughly because of the smallness of $\alpha_{q^{(\text{iv})}} / \alpha_{q^{(\text{is})}}$, but this can change for different parameter choices. As discussed in the previous section, the two-nucleon contributions are rather small and suffer from $\mathcal{O}(100\%)$ uncertainties for ^3He in the case of N²LO chiral wave functions. Despite the large uncertainty, the two-nucleon corrections are smaller than isospin-breaking terms. This finding is different from scattering off Xe isotopes where two-nucleon corrections were found to be larger than isospin-breaking corrections by roughly an order of magnitude [40] for the same choices of c_u and c_d . It is not unexpected as the two-nucleon corrections are expected to grow with increasing A . Finally, radius corrections are typically smaller than isospin-violating terms.

² Clearly other choices for c_u and c_d can lead to drastically different relative contributions. For instance, the choice $c_u = -c_d = c_\chi$ would enhance the ratio of $\alpha_{q^{(\text{iv})}} / \alpha_{q^{(\text{is})}}$ by a factor $\varepsilon^{-2} \simeq \mathcal{O}(10)$.

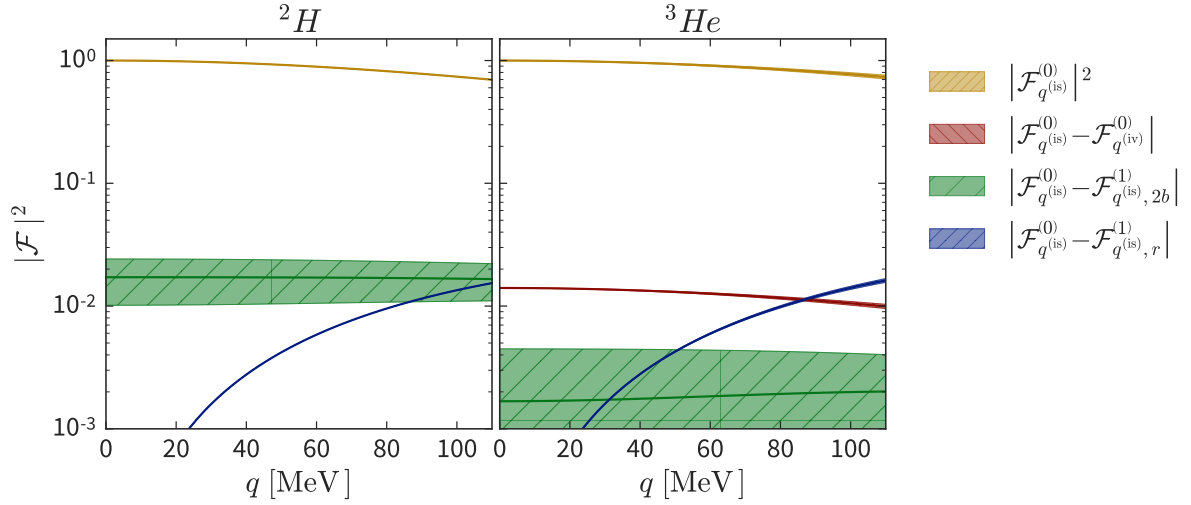


Figure 2.6: Hierarchy of contributions to $|\mathcal{F}(\mathbf{q}^2)|^2$ for the choice $c_u = c_d$ and $c_s = c_G = 0$ using N²LO chiral wave functions with cutoff Λ_2 . The diagram displays the absolute values of the various terms. For more explanation we refer to the main text.

2.4.4 Suppressing the leading order contributions

In specific scenarios of DM, it might occur that specific values of the DM coefficients in eq. (2.1) lead to cancellations in the leading one-nucleon contributions to the cross sections. In such scenarios, for instance in the framework of isospin-violating DM [112], subleading contributions to the scattering process become relatively enhanced and crucial to include as was argued in Refs. [25, 39, 58]. In this section, we consider such a scenario assuming nonzero isoscalar quark-DM and gluon-DM interactions at the same time. We set $c_s = 0$ in this section as the strange contributions are almost degenerate with respect to the gluon contributions.

Focusing on isoscalar and gluonic interactions, we see that the differential cross section is proportional to

$$\mathcal{F}(\mathbf{q}^2) = \left(\alpha_{q^{(\text{is})}} + \alpha_G \right) \mathcal{F}_{q^{(\text{is})}}^{(0)}(\mathbf{q}^2) + \alpha_{q^{(\text{is})}} \left(\mathcal{F}_{q^{(\text{is}), r}^{(1)}}(\mathbf{q}^2) + \mathcal{F}_{q^{(\text{is}), 2b}^{(1)}}(\mathbf{q}^2) \right) + \alpha_G \mathcal{F}_{G, 2b}^{(3)} + \dots \quad (2.39)$$

where we used $\mathcal{F}_{q^{(\text{is})}}^{(0)}(\mathbf{q}^2) = \mathcal{F}_G^{(0)}(\mathbf{q}^2)$, see eq. (2.26). We also included the order (1) isoscalar corrections and the order (3) two-nucleon correction arising from the DM-gluon interactions, see eq. (2.17). We stress that the order (3) currents are not complete and that additional contributions appear at this order.

The sizes of $\alpha_{q^{(\text{is})}}$ and α_G are unknown such that we cannot determine the relative sizes of their contributions in a model-independent way. In this section, we investigate the case where $\alpha_G/\alpha_{q^{(\text{is})}} = r$ and set $\alpha_{q^{(\text{is})}} = 1$ for simplicity. For values of $|r| \simeq 1$, the order (0) isoscalar and gluon contributions are of similar size. The power counting then predicts that the dominant corrections arise from the order (1) isoscalar corrections,

while the (incomplete) order (3) gluon corrections are expected to be small. As discussed in detail above, for most values of r the leading one-nucleon contributions dominate the scattering process and the subleading terms only provide percent-level corrections. However, around $r = -1$ the leading contributions are suppressed and the subleading terms become relatively enhanced. Clearly, such a scenario corresponds to a tuning of the fundamental couplings c_u , c_d , and c_G , which, admittedly, is rather *ad hoc*. Nevertheless, similar scenarios have been invoked to reduce the tension between positive DM and negative DM signals in different DM direct detection experiments. Furthermore, the tuned scenarios make higher order corrections more relevant allowing for a test of the chiral power counting to higher orders.

We investigate a scenario where a value of r is chosen such that the order (1) currents corrections provide a 50% correction to the differential cross section at $\mathbf{q}^2 = 0$. For the deuteron, this turns out to require $r = r_0 \simeq -0.96$. Clearly, the choice for 50% is arbitrary and for values of $-2 - r_0 < r < r_0$ the corrections become larger. In the top panels of [fig. 2.7](#) we plot $|\mathcal{F}(\mathbf{q}^2)|^2$ for different orders of the current for scattering off ${}^2\text{H}$ using N²LO (top-left panel) and N³LO (top-right panel) chiral wave functions. The green line just includes the order (0) one-nucleon contribution. Because of the cancellation between $\alpha_{q(\text{is})}$ and α_G , $\mathcal{F}(\mathbf{q}^2)$ is suppressed by $(1 + r_0)^2$ with respect to [fig. 2.6](#). The blue line and band also include the order (1) two-nucleon and radius corrections. The uncertainty for N²LO wave functions is significant, but much reduced once we apply N³LO wave functions. By construction, the inclusion of the order (1) currents enhances the differential cross section by 50% at zero momentum transfer, but due to the radius corrections this enhancement becomes smaller for larger momentum transfer.

We repeat this analysis for scattering off ${}^3\text{He}$. Because the order (1) corrections are smaller in this case, we need to further tune $r = r_0 \simeq -0.99$ in order to obtain a 50% correction. In this case, the uncertainties for N²LO wave functions are large enough to cover the order (0) one-nucleon contributions (the green line), but the results improve significantly once N³LO wave functions are applied. Radius corrections are relatively more important such that $\mathcal{F}(\mathbf{q}^2)$ vanishes for $|\mathbf{q}| \simeq 90$ MeV.

As discussed in [section 2.3.3](#), the uncertainty bands do not cover the effects of missing higher order currents. To investigate this, we also included the contributions from the order (3) two-nucleon correction $\mathcal{F}_{G,2b}^{(3)}$. The result is depicted by the red line and bands in [fig. 2.7](#). Although the power counting indicates that these contributions should be suppressed by $Q^2 \sim m_\pi^2/\Lambda_b^2 \sim 0.05$ concerning the order (1) currents, they are actually of similar size. Also, for N²LO wave functions the uncertainties are large enough to get a result consistent with zero for both ${}^2\text{H}$ and ${}^3\text{He}$. The uncertainty improves once we use N³LO wave functions, but we still find that adding formally higher order corrections suppresses $\mathcal{F}(\mathbf{q}^2)$, and thus the differential cross section, by roughly a factor 2.5 (7) for ${}^2\text{H}$ (${}^3\text{He}$).

The significant impact of formally higher order contributions might seem to indicate that the power counting is not working satisfactorily. It must be stressed, however,

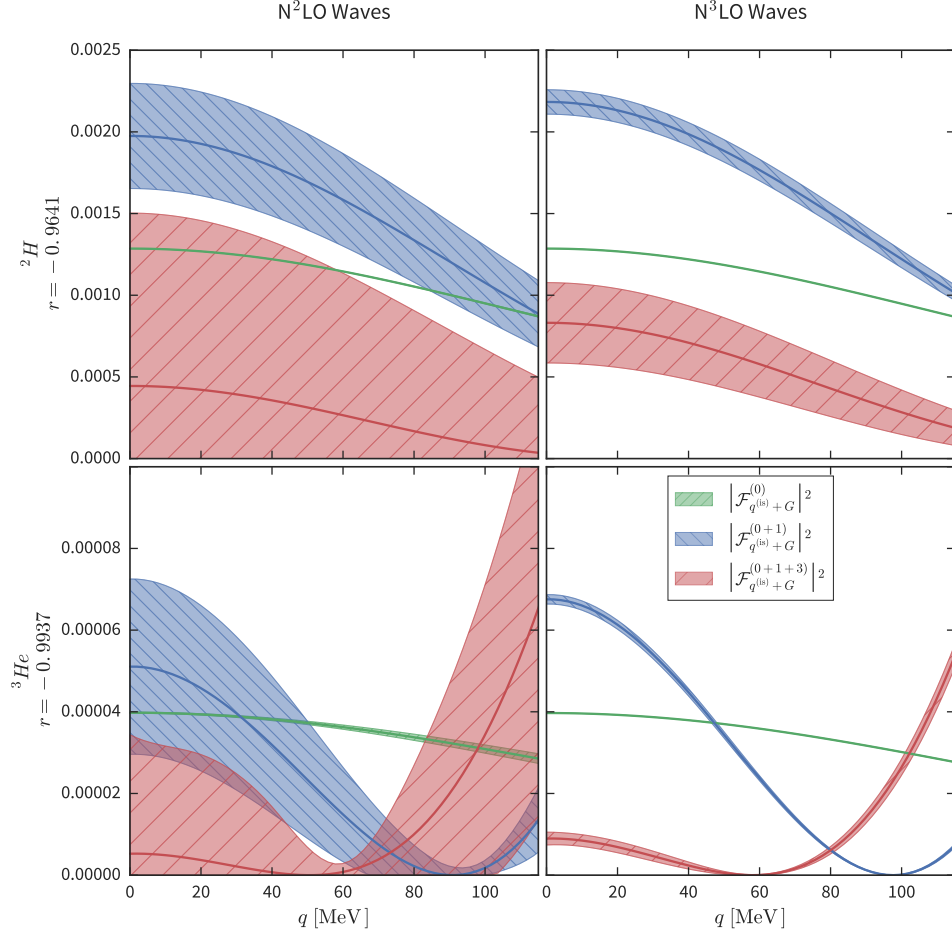


Figure 2.7: Plots corresponding to the scenario with nonzero isoscalar and gluonic DM interactions discussed in [section 2.4.4](#). The coefficient r has been chosen such that the order (1) currents provide a 50% correction to the leading order results. We plot the square of the response functions $|\mathcal{F}|^2(q^2)$. The upper (lower) row represents ${}^2\text{H}$ (${}^3\text{He}$) results, while the left (right) panel corresponds to N²LO (N³LO) chiral wave functions using cutoff Λ_2 . The green bands correspond to the leading contribution, while the blue and red bands include the order (1) and order (3) currents, respectively.

that we have not included the full order (3) currents, which would consist of many additional terms. In particular, as discussed below eq. (2.17), the order (3) two-nucleon current requires a structure function that appears at the same order for renormalization purposes. Furthermore, it might be that for denser nuclei the chiral series shows better convergence because the order (1) two-nucleon currents could be less suppressed than in light nuclei. Nevertheless, the calculated order (3) contributions can be taken as an order-of-magnitude estimate of the uncertainty due to higher order corrections to the currents, indicating that scenarios, where one-nucleon contributions are suppressed, might suffer from sizable additional uncertainties.

2.5 Summary and outlook

In this work, we have performed calculations of DM scattering off light nuclei within the framework of chiral perturbation theory. A major aspect is that both ingredients of the calculations, i.e., the nuclear wave functions and the DM-nucleus interactions, are derived from chiral EFT. In this way, we can test the convergence of the chiral series and provide a systematic uncertainty estimate that goes beyond simple cutoff variations. We have focused for now on the lightest bound nuclei, ^2H , ^3H , and ^3He , as these systems are simple enough such that the bound-state and scattering equations can be solved with direct methods to very high accuracy and precision. These nuclei are therefore great theoretical tools to study the framework and provide the first step towards calculations on heavier systems with other many-body methods. Furthermore, there has been a recent interest in using helium isotopes as DM direct detection targets as light targets are more sensitive to relatively light DM and ^3He can potentially be used for directional DM detection.

We have focused on one particular class of DM interactions at the quark-gluon level, namely scalar interactions that can be parametrized by four parameters describing interactions between light quarks, gluons, and DM particles. At leading order in the chiral expansion, each scalar interaction gives rise to an interaction between DM and a single nucleon, while at higher orders also two-nucleon interactions appear. Our framework allows for the systematic inclusion of these and other higher order effects. Two-nucleon interactions are particularly interesting as they can give rise to a different dependence of the DM-nucleus cross section on the atomic number. In fact, we observed that two-nucleon interactions are much larger for ^2H -DM than for ^3He -DM or ^3H -DM scattering, although in both cases the effects are modest.

We find that the impulse approximation, where it is assumed that the DM-nucleus interactions arise from a sum of DM-nucleon interactions, works well for the scalar DM interactions under investigation. We have provided expressions in terms of Helm form factors fitted to our results that can be used in future studies of DM direct detection using light-nuclear targets. The smallness of two-nucleon contributions for light nuclei,

at the few-percent level, justifies the approach of Ref. [61] at least for scalar DM interactions. The smallness of two-nucleon corrections is somewhat unexpected as they appear at next-to-leading order in the chiral expansion indicating a relative contribution at the (10-30)% level. The specific spin-isospin properties and/or the diluteness of light nuclei might be the cause for this suppression, and we aim to investigate this soon with studies of the deeper-bound ${}^4\text{He}$.

Because two-nucleon corrections are expected to grow for heavier nuclei, as explicitly found in Ref. [40], we studied how accurate these contributions can be calculated. We found a significant dependence on the applied nuclear wave function due to a strong correlation between the D -wave probability of the considered nucleus and the two-nucleon matrix-element. As such, at least N^3LO chiral nuclear wave functions are required to accurately calculate two-nucleon corrections. Whether this is unique to the scalar interactions we investigated here or generalizes to other interactions such as vector or axial-vector currents remains to be seen. We plan to perform such calculations in future work. This analysis is also relevant beyond the topic of DM direct detection as two-nucleon currents are found to be essential for, for example, neutrino-nucleus scattering [111].

Finally, we studied a specific scenario where one-nucleon contributions are suppressed due to a cancellation mechanism such that two-nucleon corrections become crucial to include [25, 58]. While the systematic nature of our framework allows for controlled calculations of such scenarios, we found that the missing higher order currents can become relevant. However, as the currents at higher orders have not been fully developed, a more careful analysis has to be postponed.

As becomes clear from the above discussion, much work still remains to be done. Our calculations need to be generalized to other DM interactions along the lines of Ref. [28]. Furthermore, we need to extend the calculations to heavier nuclei. As the four-nucleon system can be solved with methods analogous to those applied here, our first target is the ${}^4\text{He}$ nucleus. This system is interesting as it is a candidate for a direct-detection target [13] and is much denser than nuclei considered in this work. More specifically, we want to study the correlation between the D -wave probability and isoscalar two-nucleon matrix-elements. In recent years, major progress has been made in first-principle calculations of light- to medium-heavy nuclei. It would be extremely interesting to use methods such as nuclear lattice EFT [38], the Jacobi no-core shell model [113], and quantum Monte Carlo methods [62] to perform systematic calculations on heavier systems for the fascinating problem of DM direct detection.

Acknowledgements

JdV acknowledges support by the Dutch Organization for Scientific Research (NWO) through a VENI grant. We are very grateful to Martin Hoferichter, Evgeny Epelbaum,

Hermann Krebs, Ulf Meißner, and Thomas Luu for valuable discussions and comments on the manuscript. The numerical calculations have been performed on JUQUEEN and JURECA of the Jülich Supercomputing Centre, Jülich, Germany.

Nuclear Lattice Effective Field Theory

3.1 Introduction

Most low-energy high-precision experiments which probe fundamental symmetries Beyond the Standard Model (BSM) use heavy nuclear targets. Theoretical studies of such complex A -nucleon systems, with the number of nucleons well beyond the few-body regime ($A \gtrsim 3$), must capture the collective quantum behavior of the individual constituents. The range of nuclear targets includes Silicon ($A \sim 28$), Argon ($A \sim 40$), Germanium ($A \sim 70$) and Xenon ($A \sim 132$) in the case of Dark Matter (DM) experiments. It is especially valuable to have a variety of different nuclear test systems because only a collection of distinctive scattering responses will be able to disentangle the more fundamental behavior of possible DM particles. If one wants to understand fundamental symmetries and possible extensions to the Standard Model (SM) theoretically, then one must be able to describe a variety of nuclear systems by the fundamental degrees of freedom. One must first bridge the scale from the SM-BSM intersection to the level of individual nucleons **and** secondly one must utilize nuclear many-body methods to describe experimental systems.

The bridge between SM and individual nucleons is mostly built by exploiting an Effective Field Theory (EFT), such as Chiral Effective Field Theory (χ EFT)—which was used in the previous [chapter 2](#)—and through numerical simulations of the SM degrees of freedom in terms of Lattice Quantum Chromodynamics (LQCD). Most importantly, it is possible to systematically construct an EFT at the level of individual nucleons which can be used to compute the Nuclear Matrix-Elements (NMEs) on the many-nucleon level. While χ EFT and LQCD will improve the knowledge about the relevance of individual nuclear-BSM interactions, at the same time many-body computations must provide complementary information about collective few-nucleon effects.

The available toolkit for computing nuclear observables can be split in three different regimes

1. *traditional* few-body methods like techniques for solving the Schrödinger, Faddeev[114] and Faddeev-Yakubowsky[115] equations,

2. ‘*ab initio*’ many-body methods for example like Coupled Cluster[116] computations, the No-Core Shell Model[117], Greens Function Monte Carlo[62], In-Medium Similarity Renormalization Group[118] and Nuclear Lattice Effective Field Theory (NLEFT)[32],
3. many-body models¹ such as the Shell Model[119] and Density Functional Theory[120].

To drastically simplify the idea behind many-body methods in nuclear physics: *one has to trade off the accuracy of computations by making simplifying assumptions to gain access to larger systems.* As an example, if one considers the description of individual nucleon interactions just as an *input* to computations—neglecting the corresponding uncertainties—then traditional few-body methods will produce numerically exact results for the given input. The ‘*ab initio*’ many-body methods usually truncate the domain of the computation. For instance, lattice methods discretize the *a priori* continuous space which enables the numerical treatment of a problem. It is essential for ‘*ab initio*’ many-body methods to recover the non-truncated results of computations in the limit of removing the truncation. Concerning lattice methods, this corresponds to shrinking the lattice spacing to zero: the so-called continuum limit. Last but not least, many-body models make uncontrolled approximations which cannot be easily quantified. As an illustration in Shell Model computations, the individual nucleons of the outermost shell are assumed to interact with a core representing the remaining nucleons. Though predictions of many-body models can qualitatively reproduce results with high precision, it is in principle not possible to guarantee accuracy by solely relying on a single many-body model computation only.

In addition to the tradeoff between system accessibility and accuracy of the computational method of choice, unfortunately, one cannot take the individual interactions of nucleons as exact input without uncertainty (in case one truly wants to make predictions for experimental observables). However, by using Chiral Perturbation Theory (χ PT) to describe nuclear forces, it is possible to estimate and to quantify uncertainties in the description of individual nucleons. To fully understand the collective uncertainty of the nuclear description in many-nucleon systems, one must propagate the individual nucleon uncertainties to the observable of choice. Thus, one must execute several many-body computations for slightly different nuclear inputs to obtain a complete estimation of all uncertainties. This requirement constrains the range of many-body methods of choice. If one wants to make accurate predictions for many-body observables, then it is crucial that the many-body method can propagate the uncertainties of individual nucleon

¹ I have to emphasize the inconsistent usage of the word ‘model’ and ‘theory’ in physics. In my definition, which formed through the accumulation of several expert opinions, the difference between a model and a theory is that a theory provides an intrinsic framework to systematically increase its accuracy. The *enhancing* of the description must be possible prior to the computation of observables. Example candidates for theories are EFTs because of their power counting scheme. On the other hand, to improve a model, one uses an iterative improvement scheme which enhances the description post the computation of observables: first one computes a known observable, and secondly one adjusts the description to match the outcome.

interactions to the level of many-nucleon observations **and** the size of the many-body method approximations can be estimated and quantified.

As mentioned above, there is a vast range of available many-body methods. However, the choice for the remaining part of this work is the NLEFT framework for the following reasons

1. NLEFT is a lattice theory. Thus its basis is defined by the discretization of space and time within a finite volume. For this reason, the extraction of *physical* results manifests in continuum limits² and infinite volume extrapolations. As will be presented in [chapter 5](#), the functional dependence is known and, in principal, can be improved to arbitrary precision.
2. One computes the path integral for the chiral Lagrangian with nucleons as fundamental degrees of freedom. Thus NLEFT has the most direct link to the fundamental theory. One must not make any further simplifications to obtain the interactions which build the basis of nuclear computations. *A priori* there are no constraints on the allowed form of interactions and any few-nucleon forces can be incorporated. [Chapter 4](#) presents a specific example how to incorporate such few-nucleon forces.
3. Nuclear interactions must be regularized and renormalized to make it possible to make physical predictions. In traditional frameworks, this is mostly done by introducing a cutoff. One must ask if there is a consistent way to regularize for example two- and three-nucleon interactions. In lattice methods, the lattice spacing acts as an ultra-violet cutoff. The lattice theory is renormalized by matching the Low-Energy Constants (LECs) of the theory to experimental observables. On the one hand, this correlates the lattice spacing with the nuclear description—making it more challenging to obtain continuum results. On the other hand, this is one of the few existing prescriptions which is able to regularize nuclear forces in an entirely consistent way. There are notions on how to improve lattice actions in a way which makes it possible to analyze the continuum limit while not affecting the regularizations. These notions will be briefly addressed in [chapter 5](#).
4. The introduction of Hubbard-Stratonovitch (HS) transformation on the level of the Lagrangian enables to linearize the action in the density operator, effectively rendering the many-nucleon problem as many uncorrelated single-nucleon computations. Thus, the exponential scaling in terms of nucleon degrees of freedom becomes polynomial³ and much larger systems can be accessed. More will be discussed in this and the following chapter.

² Here, one must be more precise with the definition of continuum limits. Because it is not possible to remove the cutoff in non-perturbative nuclear computations which make use of chiral forces, it is even theoretically not possible to make NLEFT computation at zero spatial lattice spacing. In this context, the continuum limit does not mean the removal of the cutoff but the removal of discretization effects. Ideas on how to possibly disentangle these two effects will be discussed in [chapter 5](#).

³ Note that the reduced nuclear scaling gets accompanied by a stochastic lattice integration with potential sign problem.

5. Additional to the reduced scaling in terms of involved nucleons, also the number of quantum channels scales polynomially because one expresses the nuclear wave function as a Slater determinant of single-nucleon wave functions—without any approximations. The scaling is briefly mentioned in the next section.
6. Because one works with a lattice basis, it is straightforward to have massive computational parallelization. For this, also see [appendix C](#).
7. The direct link of NLEFT to other lattice methods; specifically to LQCD. The direct connections can be used two-fold, on the one hand one can use existing LQCD-techniques to improve NLEFT computations. On the other hand, because both NLEFT and LQCD make use of the lattice basis, it is in principle possible to directly match NLEFT energy levels to LQCD energy levels, circumventing the uncertainties of the intermediate continuum⁴ and infinite volume extrapolations.

3.2 The NLEFT formalism

The starting point for NLEFT (see also [32]) is the lattice partition function for nuclear observables

$$\mathcal{Z}_\chi^{(\nu)} \propto \int D\psi D\psi^* D\pi \exp \left\{ -S_\chi^{(\nu)} [\psi^*, \psi, \pi] \right\}. \quad (3.1)$$

Hereby, ψ and ψ^* are Grassmann numbers which represent the nucleon fields and the real number π represents the pion field. Besides the dependence on spacetime, the nucleon fields have two spin- (spin up and down) and two isospin-components (proton and neutron) while the pion has three isospin-components (π^+ , π^0 and π^-). The path integral in NLEFT is discrete in spacetime and placed inside a finite volume L^4 . Thus, the path integrations can be factorized with the following definitions

$$D\psi D\psi^* \equiv \prod_{\mathbf{n} \in L^4} \prod_{s,t \in \{\uparrow, \downarrow\}} d\psi_{s,t}(\mathbf{n}) d\psi_{s,t}^*(\mathbf{n}), \quad D\pi \equiv \prod_{\mathbf{n} \in L^4} \prod_{t \in \{\pm, 0\}} d\pi_t(\mathbf{n}). \quad (3.2)$$

The action $S_\chi^{(\nu)}$ is constructed from a chiral Lagrange density and infinite volume at chiral order ν . For example, the leading order action in terms of operators in the infinite volume

⁴ Even if it is not possible to do NLEFT computations for the same exact lattice spacing and Finite Volume as LQCD, the extrapolation range and thus the propagated uncertainties are smaller compared to the continuum and infinite volume limits.

continuum limit must be equal to

$$\begin{aligned}
 S_X^{(\text{LO})} [\hat{\psi}^*, \hat{\psi}, \hat{\pi}] &= \int d^4x \mathcal{L}_X^{(\text{LO})} [\hat{\psi}^*, \hat{\psi}, \hat{\pi}] \\
 &= \int d^4x \left[-\frac{1}{2} \nabla \hat{\pi} \cdot \nabla \hat{\pi} - \frac{1}{2} m_\pi^2 \hat{\pi} \cdot \hat{\pi} \right. \\
 &\quad \left. + \hat{\psi}^\dagger \cdot i \partial_0 \hat{\psi} + \hat{\psi}^\dagger \cdot \frac{\Delta}{2m_N} \hat{\psi} - \frac{g_A}{2f_\pi} \hat{\psi}^\dagger \cdot \boldsymbol{\tau} \boldsymbol{\sigma} \cdot \nabla \hat{\pi} \cdot \hat{\psi} \right. \\
 &\quad \left. - \frac{1}{2} c_{SU(4)} (\hat{\psi}^\dagger \cdot \hat{\psi}) (\hat{\psi}^\dagger \cdot \hat{\psi}) - \frac{1}{2} c_I (\hat{\psi}^\dagger \cdot \boldsymbol{\tau} \cdot \hat{\psi}) \cdot (\hat{\psi}^\dagger \cdot \boldsymbol{\tau} \cdot \hat{\psi}) \right].
 \end{aligned} \tag{3.3}$$

In the above equation, the hat denotes fields (operators) which act on the Fock space, vectors denote spatial, spin- and isospin-components of the operators and a dot denotes the scalar product in isospin and/or spin space. The definition of the scalar product goes as follows: neighboring objects in the same dimension have the same indices and one sums over all open numbers, e.g.,

$$\hat{\psi}^\dagger \cdot \boldsymbol{\tau} \boldsymbol{\sigma} \cdot \nabla \hat{\pi} \cdot \hat{\psi} = \sum_{b,s,s'} \sum_{a,t,t'} \hat{\psi}_{s',t'}^*(\mathbf{n}) \tau_{t't}^a \sigma_{s's}^b [\nabla^b \hat{\pi}^a(\mathbf{n})] \hat{\psi}_{s,t}(\mathbf{n}). \tag{3.4}$$

The remaining quantities are defined as follows:

- m_π — the pion mass ($m_\pi = 138.04$ MeV),
- m_N — the nucleon mass ($m_N = 938.92$ MeV),
- f_π — the pion decay constant ($f_\pi = 92.4$ MeV),
- g_A — the nucleon axial charge ($g_A = 1.27$),
- $\boldsymbol{\sigma}$ — the Pauli spin matrix vector and
- $\boldsymbol{\tau}$ — the Pauli isospin matrix vector.

Note that the above Lagrangian has no time derivatives for pions. Thus, nucleons instantaneously exchange pions, and one cannot compute matrix-elements for external pion sources.

This chapter focuses on the effects of discretizing time. The effects of discretizing (spatial) space within a finite volume will be discussed in [chapter 5](#). Furthermore, this chapter focuses on another, similar but equivalent derivation of NLEFT, compared to the standard derivation of [\[32\]](#).

Instead of deriving NLEFT from the path integral formalism, in a non-relativistic framework one can equivalently express the idea of NLEFT by utilizing a Hamiltonian operator. One constructs an effective potential utilizing the interactions present in the Lagrangian, and instead of computing correlators in the path integral formalism, one can equivalently solve the Schrödinger equation and compute observables using the eigenvectors of the A -body Hamiltonian

$$\hat{H} |\psi_i\rangle = E_i |\psi_i\rangle. \tag{3.5}$$

The major problem with this method is the scaling in terms of involved nucleons: the dimension of the Hamiltonian scales with the spatial volume V squared, or equivalently size

of the basis B squared. But because the potential operator correlates each nucleon with another nucleon, the total space must correspond to an operator product of individual spaces and therefore the total scaling S is non-polynomial in A . This is the reason why traditional methods are not able to solve problems with sufficient accuracy for $A > 4$

$$S = \left(\prod_{a=1}^A \|B\| \right)^2 = \|B\|^{2A}. \quad (3.6)$$

Similarly to solving the Schrödinger equation, one can look at the large time projection properties of the Hamiltonian

$$\mathcal{Z}(T) := \langle \psi | \exp\{-\hat{H}T\} | \psi \rangle = \langle \psi_0 | \psi_0 \rangle e^{-E_0 T} + \langle \psi_1 | \psi_1 \rangle e^{-E_1 T} + \dots. \quad (3.7)$$

For sufficiently large times⁵ T , the temporal decay of the matrix-element is dominated by the smallest energy of the system E_0 . One can extract information about the wave function or excited energy levels $E_i > E_0$ by inserting additional operators in the matrix-element or by explicitly manipulating the input wave function (e.g., by using Gram-Schmidt like procedures within the temporal propagation). For the purpose of this section, the Hamiltonian of choice is normal ordered $\hat{H} = : \hat{H} :$ —that is all annihilation operators are promoted to the right side of an operator product. It does not make sense to work with a non-normal ordered Hamiltonian in a non-relativistic framework. In this context, one can exactly reproduce the starting point by discretizing time

$$\mathcal{Z}(a_T N_T) = \left\langle \psi \left| \left(\exp\{-a_T : \hat{H} : \} \right)^{N_T} \right| \psi \right\rangle. \quad (3.8)$$

Next, one expresses the exponential of the normal ordered Hamiltonian by the normal ordered exponential of the Hamiltonian. Expanding both expressions, it is straightforward to show that this is equivalent up to additional corrections coming at order a_T^2

$$\mathcal{Z}(a_T N_T) = \left\langle \psi \left| \hat{T}(a_T)^{N_T} \right| \psi \right\rangle + \mathcal{O}(a_T^2), \quad \hat{T}(a_T) := : \exp\{-a_T \hat{H}\} :. \quad (3.9)$$

NLEFT calculations compute the matrix-elements for a given input wave function $|\psi\rangle$ of the so-called transfer matrix $\hat{T}(a_T)$ for a finite temporal spacing a_T . Indeed, one can directly prove that nuclear path integral is equal to the trace of products of transfer matrices for different time steps [121]. The controlled approximation NLEFT makes is that the corrections at order a_T^2 are assumed to be small and can be removed by an extrapolation procedure⁶ with $a_T \rightarrow 0$ for $N_T \rightarrow \infty$. In case of the ground state energy

⁵ The scale for ‘largeness’ is defined by the energy separation $(E_1 - E_0)T \gg 1$.

⁶ Up to this date, NLEFT computations have only demonstrated a temporal continuum analysis for two-nucleon systems [32]. It remains to be tested how much further many-body correlations affect the temporal continuum limit.

this corresponds to

$$E_0 = \lim_{a_T \rightarrow 0} \lim_{N_T \rightarrow \infty} \left[\frac{1}{a_T} \log \left(\frac{\langle \psi | \hat{T}(a_T)^{N_T} | \psi \rangle}{\langle \psi | \hat{T}(a_T)^{N_T+1} | \psi \rangle} \right) \right]. \quad (3.10)$$

At this point, one has not made any statements about the basis of choice, and therefore, *a priori* there are no further benefits in computing the large-time projected matrix-elements of the transfer matrix compared to computing eigenvalues of the Hamiltonian from a scaling point of view. However, this reformulation of the problem allows employing powerful tools with a better scaling in terms of ‘*ab initio*’ degrees of freedom.

The tool of choice is the so-called Hubbard-Stratonovitch transformation⁷, which can be best explained in terms of second quantization. If the Hamiltonian of the system is composed of purely non-interacting operators—one-body operators—the system is exactly described by a Slater determinant⁸ of individual nucleon wave functions. Thus the total scaling would be polynomial in terms of the involved nucleons. Moreover, this is the basic idea of the HS transformation: rewrite two-body operators in terms of one-body operators.

Suppose the interacting part of the system can be rewritten as

$$\hat{V} = -\frac{1}{2} \sum_{i,j \in I} v_{ij} \hat{\rho}_i \hat{\rho}_j, \quad (3.11)$$

where the density operators correspond to an arbitrary pair of creation and annihilation operators with the only constraint that any product of density operators commute under normal ordering. In the case of nucleons the indices represent the spin, isospin and discretized coordinates of the nucleons

$$i, j \in I \equiv \left\{ (s, t, \mathbf{n}) \mid s \in \{\uparrow, \downarrow\}, t \in \{p, n\}, \mathbf{n} \in L^3 \right\}. \quad (3.12)$$

Because the transfer matrix is a normal ordered operator, one can permute individual terms and thus factorize transfer the matrix in terms of pairs of density operators for each possible pair of indices. At this point one can complete the squares to obtain

$$\begin{aligned} \hat{T}(a_T) &= : e^{-\hat{H}_0 a_T} \prod_{i,j \in I} \left(\exp \left\{ \frac{v_{ij}}{2} \hat{\rho}_i \hat{\rho}_j a_T \right\} \right) : \\ &= : e^{-\hat{H}_0 a_T} \sqrt{(2\pi)^{\|I\|} \det(v)} \int d\phi \exp \left\{ -\frac{1}{2} \sum_{i,j \in I} \phi_i (v^{-1})_{ij} \phi_j + \sqrt{a_T} \sum_{i \in I} \phi_i \hat{\rho}_i \right\} :, \end{aligned} \quad (3.13)$$

$$(3.14)$$

⁷ Historically more correct, the transformation should be called Gaussian Quadrature, but for some reason, the literature has fixated its terminology to HS transformation.

⁸ Or permanent in case of bosons.

where each component of the vector ϕ is real and $\|I\|$ denotes the number of elements in I . This integral is well defined if all the eigenvalues of v are greater than zero⁹. Thus, this transformation has effectively rendered the transfer matrix as a one-body operator dependent on the auxiliary field

$$\hat{T}(a_T) = \int d\phi P(\phi) \hat{T}^{(1)}(a_T, \phi), \quad \hat{T}^{(1)}(a_T, \phi) \equiv : \exp \left\{ -\hat{H}_0 a_T + \sqrt{a_T} \sum_i \phi_i \hat{\rho}_i \right\} : , \quad (3.15)$$

where the quadratic ϕ dependence and the determinant was absorbed in a probability distribution $P(\phi)$. Expectation values of this operator can be expressed by Slater determinants of individual one-body wave functions¹⁰ corresponding to a polynomial scaling in A

$$\begin{aligned} |\Psi\rangle &= |\psi_1\rangle \otimes |\psi_2\rangle \otimes \cdots \otimes |\psi_A\rangle \\ \Rightarrow \langle \Psi | \hat{T}(a_T) | \Psi \rangle &= \int d\phi P(\phi) \det \left(\langle \psi_i | \hat{T}^{(1)}(a_T, \phi) | \psi_j \rangle_{i,j \leq A} \right) . \end{aligned} \quad (3.16)$$

The action of multiple iterations of the transfer matrix for different time slices is given by the action of the product of all one-body transfer matrices on the one-body wave functions. For each time slice, one introduces and integrates over another auxiliary field vector. Here one should also mention that while other methods must construct final state quantum numbers by contracting each individual nucleon spin and angular momenta index, NLEFT takes this into account by the definition of the Slater determinant. One only must make sure that the trial state overlaps with the state of choice and its quantum numbers.

At this point one has to emphasize the above derivation relied on three assumptions only:

- the temporal continuum extrapolation is well behaved (which is guaranteed for nuclear spectra and an appropriate choice for lattice parameters),
- the potential of the system is described by a two-body interaction and
- the (spatial) basis for the computation is discrete.

While the last point holds true for any numerical computation by definition, this also means that one does not necessarily have to work in a traditional lattice basis (spatial cubic volume with equal distanced lattice spacings in each direction). One could also

⁹ If all the eigenvalues of v are smaller than zero, one can substitute $v = -v$ and thus the linear term in the density in eq. (3.14) becomes imaginary.

¹⁰ One has to stress that the size of the Hilbert space is not reduced in this case. The HS transformation just allows selecting a subspace which is sufficient to completely describe the action of one-body operators. Nevertheless, the action of the operator within the subspace is equivalent to the action of the operator in the whole space.

picture scenarios where one describes the operators in proper eigenfunctions of the systems like Kohn-Sham orbitals for molecular systems or also Harmonic Oscillator states for Shell Model applications.

The second point is more critical in terms of the proposed analysis of DM NMEs because, as described in the previous section, it is essential to include chiral high-order wave functions systematically. For wave functions at Next-to-Next-to-Leading Order (N²LO), one already has to include Three-Nucleon Forces (TNFs). In the next chapter, an idea on how to generalize the HS transformation to include general N -body forces is presented.

Sampling general N-body interactions with auxiliary fields

The following chapter is accepted for publication in Europhysics Letters [3].

Sampling General N-Body Interactions with Auxiliary Fields

C. Körber^a, E. Berkowitz^a and T. Luu^a

^a *Institute für Kernphysik and Institute for Advanced Simulations,
Forschungszentrum Jülich,
D-52425 Jülich, Germany*

We present a general auxiliary field transformation which generates effective interactions containing all possible N-body contact terms. The strength of the induced terms can analytically be described in terms of general coefficients associated with the transformation and thus are controllable. This transformation provides a novel way for sampling 3- and 4-body (and higher) contact interactions non-perturbatively in lattice quantum Monte Carlo simulations. As a proof of principle, we show that our method reproduces the exact solution for a two-site quantum mechanical problem.

4.1 Introduction

The introduction of auxiliary fields, e.g., via the Hubbard-Stratonovitch (HS) transformation [122, 123], as a means of linearizing the interaction term of the Hamiltonian in terms of its density operator is common practice in many areas of theoretical physics, and is particularly prevalent in condensed matter and nuclear physics [124, 125]. Upon linearization of the theory, the problem becomes that of many particles undergoing one-body interactions with the fluctuating background auxiliary field. In occupation number formalism, the problem becomes very similar to that of *non-interacting* (amongst themselves) particles, which in some cases can be evaluated via steepest-descent methods (e.g. 1-D Ising model). At the very least, the transformation greatly facilitates numerical treatment of the many-body problem [33, 62, 126, 127]. In path integral formalisms that involve Grassmann fields, the transformation is essential as it reduces the Lagrangian to terms bilinear in fermionic fields, which can subsequently be integrated out exactly via Grassmann gaussian integration (e.g. bosonization of fermionic theories [128]). The HS transformation is ideal for theories that initially have 2-body interactions (i.e., terms quadratic in the density operator). In principle, many-body interactions can be linearized through recursive application of the HS transformation, but at the cost of introducing numerous auxiliary fields. Also, in the framework of time-dependent mean-field theory, Ref. [129] worked out how the HS transformation can be utilized to describe many-body interactions through a non-linear effective interaction. In contrast, in this Letter, we present a way to linearize the effective interaction and provide explicit derivations for this transformation. A transformation that naturally includes 3-body interactions, for example, would be beneficial for studying ultra-cold gases of polar molecules, where 3-body (and higher) interactions can be tuned to become dominant [130, 131].

In this Letter, we detail a generalization of the HS transformation that includes two-body and all possible *higher* contact interactions that involves only one auxiliary field. The standard HS transformation can be viewed as a particular limit of this general transformation. Our transformation, in principle, induces all possible n -body interactions $\lambda^{(n)} \hat{\rho}^n$ where $\hat{\rho}$ is the density operator. The coefficients $\lambda^{(n)}$, which are known as low energy coefficients (LECs) in an Effective Field Theory framework, are analytically determined and controllable through a set of accompanying coefficients c_j . These coefficients c_j control the coupling of the density operator with the j^{th} power of the auxiliary field in the linearized theory. The numerical implementation of this transformation is trivial as the sampling of the fields can be obtained from known distributions. For 2-flavor fermionic systems (e.g., nucleons), this transformation allows for complete control of contact interactions up to 4-body in nature.

4.2 Formalism

Consider the following integral which is intended to correspond to the interacting part of a partition function at a single space-time point

$$\mathcal{Z}_{c,N} \equiv \int_{-\infty}^{\infty} d\phi P_N(\phi) \exp \left\{ - \sum_{j=1}^{2N-1} c_j \phi^j \hat{\rho} \right\}, \quad (4.1)$$

where $P_N(\phi)$ is the normalized probability distribution

$$P_N(\phi) = \frac{N}{\Gamma\left(\frac{1}{2N}\right)} e^{-\phi^{2N}}. \quad (4.2)$$

Here, ϕ is an auxiliary field which couples to the fermionic density operator¹ $\hat{\rho} = \sum_f \bar{\psi}_f \psi_f$, where $f = 1, \dots, F$ runs over the different fermion species at a given site, $N \geq 1$ and the coefficients c_j can be complex in general. Also, for the integral to converge, the leading exponent is not allowed to be odd in ϕ . Because the density operators at different spacetime points commute, we present only the derivation for a single point.

The argument of the exponential in eq. (4.1) describes interaction vertices with an incoming and outgoing fermionic field (the density operator) and from one to $2N - 1$ auxiliary fields associated with interaction strength c_j . The integral is normalized such that $\mathcal{Z}_{c,N} \rightarrow 1$ for $c_j \rightarrow 0$. The result of the integration over the largest exponent of ϕ times another polynomial in ϕ is given by

$$\int_{-\infty}^{\infty} d\phi e^{-\phi^{2N}} \phi^{2k} = \frac{\Gamma\left(\frac{1+2k}{2N}\right)}{N} \xrightarrow{N \rightarrow \infty} \frac{2}{1+2k}, \quad \forall k \in \mathbb{N}_0, N \in \mathbb{N}. \quad (4.3)$$

It is sufficient to only consider polynomials in even powers of ϕ because of the symmetry of the integration – odd powers vanish.

In this work we identify the integral $\mathcal{Z}_{c,N}$ with an effective action consisting of general $2k$ -fermionic field vertices

$$\mathcal{Z}_\lambda \equiv \exp \left\{ - \sum_{k=1}^{\infty} \lambda^{(k)} \hat{\rho}^k \right\}. \quad (4.4)$$

To emphasize different notations in the following context: an object with upper index without parenthesis denotes the power of an object (e.g. $\hat{\rho}^k$), while an object with upper

¹ In this work we concentrate on central interactions. It would be an interesting exercise to extend the framework to more general interactions corresponding to quantum number dependent densities like $\hat{\rho}_i \equiv \bar{\psi} \Gamma_i \psi$ by introducing an auxiliary field ϕ_i for each matrix component i . Eventually, the coupling coefficients c_j must be replaced by tensors structures to form scalar quantities. As an example, Γ_i could represent a Pauli spin matrix for nucleon degrees of freedom. However, this task is beyond the scope of this work.

index within parenthesis corresponds to a label for the object within a given set (e.g. $\lambda^{(k)}$). We expand $\mathcal{Z}_{c,N}$ and \mathcal{Z}_λ in powers of the density operator $\hat{\rho}$ and systematically match order-by-order, relating the auxiliary field interactions to the induced many-body forces. Using Faà di Bruno's formula [132] we find that

$$\mathcal{Z}_{c,N} = \sum_{M=0}^{\infty} \mathcal{Z}_{c,N}^{(M)} \hat{\rho}^M, \quad (4.5)$$

$$\mathcal{Z}_{c,N}^{(M)} = \sum_{k=\lceil M/2 \rceil}^{\lfloor (2N-1)M/2 \rfloor} \frac{\Gamma\left(\frac{1+2k}{2N}\right)}{\Gamma\left(\frac{1}{2N}\right)} \sum_{\mathbf{m} \in \mathcal{M}_{NM}^{(2k)}} \prod_{j=1}^{2k} \left[\frac{(-c_j)^{m_j}}{m_j!} \right] \quad (4.6)$$

where the sum runs over the set

$$\mathcal{M}_{NM}^{(2k)} = \left\{ \mathbf{m} \in \mathbb{N}_0^{2k} \left| \left(\sum_{j=1}^{2k} j m_j = 2k \right) \wedge \left(\sum_{j=1}^{2k} m_j = M \right) \wedge (j \geq 2N \Rightarrow m_j = 0) \right. \right\}, \quad (4.7)$$

and

$$\mathcal{Z}_\lambda = \sum_{M=0}^{\infty} \mathcal{Z}_\lambda^{(M)} \hat{\rho}^M, \quad \mathcal{Z}_\lambda^{(M)} = \sum_{\mathbf{m} \in \mathcal{M}^{(M)}} \prod_{k=1}^M \left[\frac{(-\lambda^{(k)})^{m_k}}{m_k!} \right] \quad (4.8)$$

where the sum in $\mathcal{Z}_\lambda^{(M)}$ is over the set

$$\mathcal{M}^{(M)} = \left\{ \mathbf{m} \in \mathbb{N}_0^M \left| \sum_{k=1}^M k m_k = M \right. \right\}. \quad (4.9)$$

As the highest coefficient $\lambda^{(k)}$ (in terms of k) in eq. (4.8) is given by $\lambda^{(M)}$ and is also linear in exactly this coefficient (because if $m_M = 1$ then $m_{j \neq M} = 0$), one can recursively determine all coefficients $\lambda^{(M)}$ for $M > 0$ by

$$\mathcal{Z}_\lambda^{(M)} = -\lambda^{(M)} + \mathcal{Z}_\lambda^{(M)}|_{\lambda^{(M)} \rightarrow 0} = \mathcal{Z}_{c,N}^{(M)}, \quad \mathcal{Z}_\lambda^{(1)}|_{\lambda^{(1)} \rightarrow 0} = 0. \quad (4.10)$$

Note that one can prove by induction that each coefficient $\lambda^{(M)}$ is proportional to a sum where each term is a products of M fermion auxiliary-field coefficients²: $\lambda^{(M)} \propto c_{j_1} \cdots c_{j_M}$. Furthermore, when matching both expansions in eq. (4.10), in general, it is not possible to guarantee that terms at higher orders M , with M larger than the number available coefficients $M > (2N-1)$, agree. Thus, one can only guarantee that forces are correctly induced up to order $(2N-1)$, and therefore one must pick N large enough to reproduce all relevant forces; e.g., $(2N-1) \geq F$. If this is the case, than any normal ordered matrix-elements with expansion coefficients in eqs. (4.6) and (4.8) with $M > (2N-1)$ must result in zero, and thus matrix-elements of the expansions agree to all orders.

² Because each fermion-auxiliary field interaction has exactly one incoming and outgoing fermion line, a diagram with M incoming and outgoing fermion lines (and without fermion loops) must be proportional to exactly M vertices and thus M different c_j coefficients.

	$N = 1$	$N = 2$	$N = \infty, c_{j>3} = 0$
$\lambda^{(1)}$	0	$\gamma_{3,1}c_2$	$\frac{1}{3}c_2$
$\lambda^{(2)}$	$-\frac{1}{4}c_1^2$	$-\left(\frac{1}{8} - \frac{\gamma_{3,1}^2}{2}\right)c_2^2 - \frac{1}{4}c_1c_3 - \frac{1}{2}\gamma_{3,1}c_1^2 - \frac{3}{8}\gamma_{3,1}c_3^2$	$-\frac{1}{6}c_1^2 - \frac{2}{45}c_2^2 - \frac{1}{5}c_1c_3 - \frac{1}{14}c_3^2$
$\lambda^{(3)}$	0	$\left(\frac{1}{8} - \frac{\gamma_{3,1}^2}{2}\right)c_1^2c_2 + \left(\frac{5}{32} - \frac{3\gamma_{3,1}^2}{8}\right)c_2c_3^2$ $+ \frac{1}{2}\gamma_{3,1}c_1c_2c_3 + \frac{1}{3}\gamma_{3,1}^3c_2^3$	$\frac{2}{45}c_1^2c_2 + \frac{8}{2835}c_2^3 + \frac{8}{105}c_1c_2c_3 + \frac{2}{63}c_2c_3^2$
$\lambda^{(4)}$	0	$\left(\frac{\gamma_{3,1}^2}{8} - \frac{1}{96}\right)c_1^4 - \frac{\gamma_{3,1}}{2}c_1^2c_2^2 - \left(\frac{3}{64} - \frac{3\gamma_{3,1}^2}{16}\right)c_1^2c_3^2$ $-\frac{\gamma_{3,1}}{8}c_1c_3^3 - \left(\frac{1}{8} - \frac{\gamma_{3,1}^2}{2}\right)c_1c_2^2c_3 - \frac{\gamma_{3,1}+3\gamma_{3,1}^3}{8}c_2^2c_3^2$ $-\left(\frac{1}{192} - \frac{\gamma_{3,1}^4}{4}\right)c_2^4 - \left(\frac{15}{512} - \frac{9\gamma_{3,1}^2}{128}\right)c_3^4$	$\frac{1}{180}c_1^4 + \frac{4}{14175}c_2^4 + \frac{1}{105}c_1^3c_3 - \frac{52}{10395}c_2^2c_3^2 - \frac{1}{7644}c_3^4$ $-\frac{4}{945}c_1^2c_2^2 + \frac{13}{3150}c_1^2c_3^2 - \frac{16}{1575}c_1c_2^2c_3 - \frac{1}{1155}c_1c_3^3$

Table 4.1: We show the results of the matching for $N = 1$, $N = 2$, and $N = \infty$ with all $c_{j>3} = 0$. The first column is the Hubbard-Stratonovich case, which produces only a two-body interaction. We repeatedly used $\Gamma(x) = (x-1)\Gamma(x-1)$ to simplify many $N = 2$ coefficients, and use the shorthand $\gamma_{3,1} = \Gamma(3/4)/\Gamma(1/4)$. We provide a *Mathematica* notebook useful for generating the $\lambda^{(M)}$ for a given N in the Supplementary Material [3].

In table 4.1 we show the coefficients of the induced forces up to the order of four-body forces ($M = 4$) for three different choices of N .

To avoid numerical sign problems, one hopes to find a set of c_j that are all real for a given set of $\lambda^{(1)} \dots \lambda^{(M)}$. Identifying when this is possible is known as the truncated Hamburger moments problem[133, 134], and the solution is to consider the square matrices

$$\Lambda_{ij}^{(k)} = (i+j)! \times \mathcal{Z}_\lambda^{(i+j)}, \quad (4.11)$$

where i and j start at 0 and each go to k . When the determinants of all the $\Lambda^{(k)}$ are positive for k from 1 to $\lceil M/2 \rceil$, one can find a set of entirely real c_j . When M is odd, one may include $\lambda^{(M+1)}$ and adjust it to help satisfy the positivity conditions. The determinants of the first $\Lambda^{(k)}$ for the first two k are

$$\begin{aligned} \det \Lambda^{(1)} &= -2\lambda^{(2)} \\ \det \Lambda^{(2)} &= -4 \left(4 [\lambda^{(2)}]^3 + 9 [\lambda^{(3)}]^2 - 12\lambda^{(2)}\lambda^{(4)} \right), \end{aligned} \quad (4.12)$$

and we see that requiring the determinant of $\Lambda^{(1)}$ to be positive means requiring an attractive two-body force, a familiar result from the Hubbard-Stratonovich case.

4.3 Numerical results

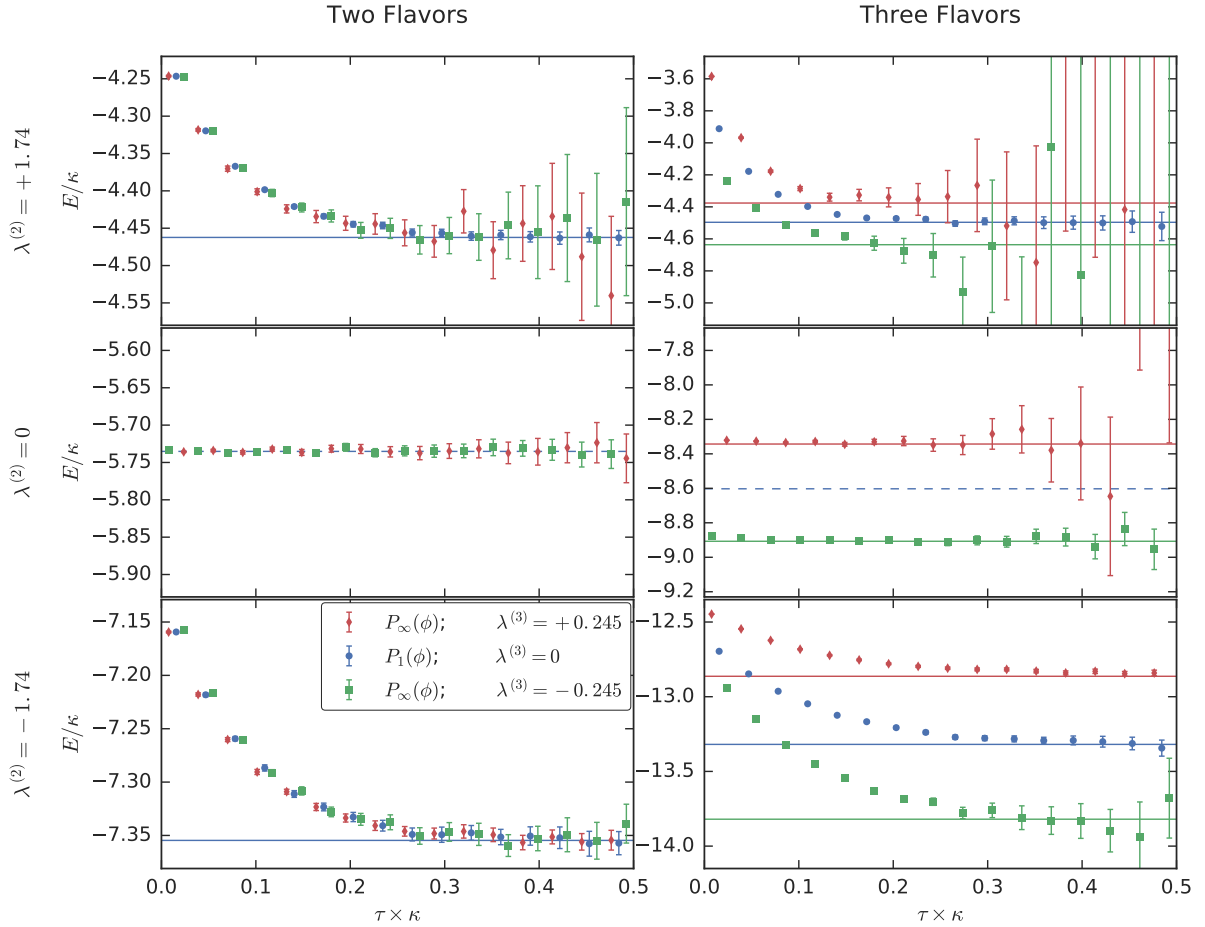


Figure 4.1: $E(\tau)/\kappa$ for different systems. All systems were studied with 2×10^8 measurements. Some systems show a Signal-To-Noise problem and others yield an easy extraction of a constant plateau in the long-time limit. The left panels all show two-fermion systems and the corresponding right panels show the three-fermion systems with the same parameters. In the top (middle) [bottom] two panels we show a system with repulsive (absent) [attractive] two-body forces. Red (blue) [green] points correspond to repulsive (absent) [attractive] three-body forces. The blue points were sampled according to the HS distribution P_1 and the other points according to P_∞ . The data in the middle two panels were generated with P_∞ and coefficients $c_j = 0$ for $j > 3$ tuned to exactly cancel the two-body force, and we show dashed lines for the corresponding non-interacting energies.

To demonstrate the efficacy of our transformation, we consider a system of 3 different fermion species f interacting on a two-site model (with sites $\{0, 1\}$) with the following Hamiltonian,

$$\hat{H} = \kappa \left(-3 \sum_{f=1}^3 \sum_{\langle i,j \rangle} \hat{a}_{f,i} \hat{a}_{f,j}^\dagger + \lambda^{(2)} \sum_{i \in \{0,1\}} \hat{\rho}_i^2 + \lambda^{(3)} \sum_{i \in \{0,1\}} \hat{\rho}_i^3 \right), \quad (4.13)$$

where $\hat{a}_{f,i}^\dagger$ ($\hat{a}_{f,i}$) is a creation (annihilation) operator for a fermion of species f at site i and $\hat{\rho}_i = \sum_f \hat{a}_{f,i}^\dagger \hat{a}_{f,i}$ is the number operator at site i . Here the sum over $\langle i, j \rangle \in \{(0, 1), (1, 0)\}$ represents nearest neighbor hoppings between the two sites, and κ is a dimensionful parameter that sets the dynamical scale of our problem. As is evident in eq. (4.13), $\lambda^{(2)}$ and $\lambda^{(3)}$ represent the size of two- and three-body interactions (relative to κ), respectively, and are dimensionless. A positive (negative) value of $\lambda^{(i)}$ indicates a repulsive (attractive) interaction. We quote results in units of κ . The two-site model can be diagonalized and its spectrum directly determined from its eigenvalues. We use the transfer matrix formalism [33] to obtain this spectrum³. With the spectrum in hand, we compare these results with those obtained from a stochastic lattice projection calculation [33] where the introduction of auxiliary fields via our transformation is needed. A detailed description of these calculations is in preparation [135]. In what follows, we give a succinct description.

The projection method extracts the lowest energy level E in the spectrum of the system via

$$E = - \lim_{\tau \rightarrow \infty} \partial_\tau \log Z[\tau, \Psi_T], \quad (4.14)$$

where Z is given by

$$Z[\tau, \Psi_T] \equiv \langle \Psi_T | e^{-\tau \cdot \hat{H}} | \Psi_T \rangle = \int \left(\prod_x d\phi_x P_N(\phi_x) \right) \mathcal{K}[\tau, \phi, c_j, \Psi_T], \quad (4.15)$$

Ψ_T is an initial trial wavefunction, and ϕ indicates the collection of all ϕ over x , all space (both sites) and time from 0 to τ .

After discretizing time $\tau \rightarrow a_\tau N_\tau$, the exponential of the normal ordered Hamiltonian gets replaced by the normal ordered exponential of the Hamiltonian—the so-called transfer matrix[33]. This introduces a quadratic error in the time discretization

$$e^{-a_\tau \cdot \hat{H}} = : e^{-a_\tau \hat{H}} : + \mathcal{O}(a_\tau^2). \quad (4.16)$$

In the last step of the eq. (4.15) we have applied our transformation with its associated probability distribution $P_N(\phi)$ at each spacetime point and introduced \mathcal{K} which is a functional of ϕ and depends explicitly on the coefficients c_j , the trial wavefunction Ψ_T , and the time separation τ . The form of $P_N(\phi)$ depends on the order N of the transformation that is applied. For the work presented here, we consider the two extreme cases

$$N = 1 \quad P_1(\phi) = \frac{1}{\sqrt{\pi}} \exp(-\phi^2) \quad (4.17)$$

$$N = \infty \quad P_\infty(\phi) = \begin{cases} 1/2 & |\phi| < 1 \\ 0 & \text{otherwise} \end{cases} \quad (4.18)$$

³ We compare the spectrum obtained from the transfer matrix (instead of direct diagonalization of the Hamiltonian) since it incorporates lattice discretization effects. This enables a direct comparison with our lattice projection calculations.

The case $N = 1$ corresponds to the gaussian distribution of the original Hubbard-Stratonovich transformation (and thus only $\lambda^{(2)}$ is nonzero), whereas for $N = \infty$ we have uniform sampling and in principle all allowed many-body contact interactions. In the $N = \infty$ case, there are in principle an infinite number of c_j —we set them all to zero for $j > 3$.

As our trial wavefunction for multifermion systems $|\Psi_T\rangle$ we pick a direct product state of single-particle ground state wavefunctions, $|\psi_f\rangle = \frac{1}{\sqrt{2}}[a_{f,0}^\dagger - a_{f,1}^\dagger]|0\rangle$ for each flavor f . The direct product structure allows us to write the functional \mathcal{K} in eq. (4.15) as

$$\mathcal{K}[\tau, \phi, c_j, \Psi_T] = \left(K^{-1}[\tau; \phi, c_j] \right)^\alpha \quad (4.19)$$

where α is the number of fermion types and

$$K^{-1}[\tau; \phi, c_j] = \frac{1}{2} \left(K^{-1}[0, \tau; 0, 0; \phi, c_j] - K^{-1}[0, \tau; 1, 0; \phi, c_j] - K^{-1}[1, \tau; 0, 0; \phi, c_j] + K^{-1}[1, \tau; 1, 0; \phi, c_j] \right), \quad (4.20)$$

After introducing a time discretization $\tau = a_\tau t$, the K matrix is given by

$$K[i, t; i', t'; \phi, c_j] \equiv \delta_{i,i'} \delta_{t,t'} + a_\tau \delta_{\langle i,i' \rangle} \delta_{t,t'+1} + \delta_{i,i'} \delta_{t,t'+1} \left(c_1 \phi_{i,t} + c_2 \phi_{i,t}^2 + c_3 \phi_{i,t}^3 - 1 \right). \quad (4.21)$$

Here we have used the fact that we let $c_j = 0$ for $j > 3$. We attach the indices i and t on the auxiliary field to indicate that there exists auxiliary fields for each spatial and temporal point.

Because we work with discretized time, we analyze the discretized version of eq. (4.14),

$$E(\tau) \equiv -\frac{1}{a_\tau} \log \left(\frac{Z[\tau + a_\tau, \Psi_T]}{Z[\tau, \Psi_T]} \right) \quad (4.22)$$

and search for constant plateaus at long times to numerically determine the $\tau \rightarrow \infty$ limit.

In fig. 4.1 we show the numerical results of $E(\tau)/\kappa$ for combinations of $\lambda^{(M)}$ where $\lambda^{(2)} \in \{\pm 1.74, 0.0\}$ and $\lambda^{(3)} \in \{\pm 0.245, 0.0\}$ for two and three-fermion systems. For calculations with $\lambda^{(3)} = 0.0$, ϕ was sampled according to the HS distribution P_1 and all other calculations sampled according to P_∞ . The solid lines correspond to the exact answers from diagonalization of the transfer matrix, and the dashed lines correspond to non-interacting energies. We note that for all two-fermion calculations, both $N = 1$ and $N = \infty$ calculations agree with each other, regardless of the value of $\lambda^{(3)}$, since the 3-body interaction plays no role. Furthermore, with $\lambda^{(2)} = 0.0$ but nonzero $\lambda^{(3)}$, the two-fermion system reproduces the non-interacting result. In the three-fermion system, the effects of $\lambda^{(3)}$ are apparent and agree well with exact diagonalization.

Note that the coefficients c_j can be complex in general. The bottom row of [fig. 4.1](#) (with negative $\lambda^{(2)}$, corresponding to an attractive two-body force) satisfies the determinant conditions and has the cleanest statistical results since we have chosen a set of only real c coefficients. The other rows have statistical fluctuations that are harder to tame, which is unsurprising as they violate the determinant conditions and have complex c coefficients. A quantitative analysis will be given in [\[135\]](#), as well as an analysis of signal-to-noise behavior for the different systems.

4.4 Summary and discussion

The HS transformation has been a useful tool for making analytic and numerical progress in problems of physical interest and is a special case of the transformation described in this work. Our transformation, which uses a self-interacting auxiliary field, allows for the direct inclusion of controllable many-body forces into numerical calculations.

Choosing a degree of auxiliary field self-interaction fixes the sampling distribution and limits the types of fermion/auxiliary-field interaction vertices. These interactions, in turn, generate a slew of n -body forces. Sampling a normal distribution for the auxiliary field recovers the original HS transformation, while uniform sampling in principle allows for the independent control of all possible n -body forces, while intermediate distributions yield correlated forces.

We have demonstrated that on a two-site model, different sampling techniques reproduce the exact results in a variety of cases, correctly handling all combinations of attractive, repulsive, and absent two-body forces with attractive and repulsive three-body forces. While even the agreement of the one-body energies found with the different methods is nontrivial, the agreement of the two-body systems between methods and agreement of three-body systems with exact results indicate a solid understanding and definite control over many-fermion interactions.

Similar to the situation of the original HS transformation with repulsive two-body interactions, there exist certain combinations of many-body forces which are only achievable with complex c_j . Such cases are in general susceptible to numerical sign problems for any auxiliary field distribution [\[134\]](#), though this is not guaranteed and in some systems can be avoided [\[136, 137\]](#). Because the c coefficients appear nonlinearly in the higher-body λ coefficients, there is not a unique set of c s that yield a particular set of λ s. However, one may still use the determinant conditions [\[eqs. \(4.11\) and \(4.12\)\]](#) to check whether a set of forces described by a set of λ s suffers from a sign problem arising from complex c_j .

It would be interesting to consider sampling by more generic functions such as $P_N(\phi) = \exp(-\sum_n \alpha^{(n)} \phi^n)$ with multiple tuneable ϕ self-interactions, or cases where ϕ is restricted to only a finite set of values, such as ± 1 . For field-theoretic applications, it may prove fruitful to understand how the renormalization of different $\lambda^{(M)}$ control renormalization of the parameters c_j .

We expect our transformation to be useful in a variety of physical systems where many-body interactions are relevant. Numerical applications may include density functional theory approaches to nuclear physics [138], the nonperturbative inclusion of multinucleon forces into Nuclear Lattice Effective Field Theory (NLEFT) which might unlock precision characterizations of halo nuclei, the study of systems near the Efimov threshold such as cold atoms (see Refs. [139, 140] and references therein), systems at high density, and any other system where contact interactions need stochastic implementation.

Acknowledgements

We thank A. Rokash, D. Lee and A. Cherman for insightful discussions. This work was done in part through financial support from the Deutsche Forschungsgemeinschaft (Sino-German CRC 110).

Currents within a box

5.1 Introduction

As it was demonstrated in [chapter 2](#), Dark Matter (DM)-nuclei scattering observables can be parameterized as Nuclear Matrix-Elements (NMEs) of external DM-current operators \hat{J}_χ and nuclear states ψ_N

$$\langle \hat{J}_\chi(\mathbf{q}) \rangle = \langle \psi_N | \hat{J}_\chi(\mathbf{q}) | \psi_N \rangle . \quad (5.1)$$

The external DM current operator \hat{J}_χ in general depends on the external momentum exchange \mathbf{q} . The most simple exchange current, the isoscalar light quark exchange current at leading order $\hat{J}_{q(\text{is})}^{(\text{LO})}$, is simply given by an one-nucleon contact interaction (see [fig. 2.1\(a\)](#)), which shifts the momentum of one of the nucleons. For a two-nucleon bound state this results in

$$\begin{aligned} \langle \hat{J}_{q(\text{is})}^{(\text{LO})}(\mathbf{q}) \rangle &= \int \frac{d^3\mathbf{p}}{(2\pi)^3} \int \frac{d^3\mathbf{p}'}{(2\pi)^3} \delta^{(3)}\left(\mathbf{p}' - \mathbf{p} - \frac{\mathbf{q}}{2}\right) \psi^*(\mathbf{p}') \psi(\mathbf{p}) \\ &= \int \frac{d^3\mathbf{p}}{(2\pi)^3} \psi^*\left(\mathbf{p} + \frac{\mathbf{q}}{2}\right) \psi(\mathbf{p}) = \int d^3\mathbf{x} \exp\left\{\frac{i\mathbf{x} \cdot \mathbf{q}}{2}\right\} |\psi(\mathbf{x})|^2 , \end{aligned} \quad (5.2)$$

where the current coupling constant has been set to one in respective units. The vectors \mathbf{p} and \mathbf{x} represent the relative particle coordinates, e.g. the relative momentum in terms of its single nucleon momenta is given by $\mathbf{p} = (\mathbf{p}_1 - \mathbf{p}_2)/2$. Moreover, because this NME corresponds to an one-nucleon operator, the exchange-momentum \mathbf{q} is divided by two.

Even though this current operator is relatively easy to implement, it is the most dominant operator for scalar DM scattering observables. Compared to the corresponding two-nucleon currents, it makes up more than 97% of the differential cross section for light nuclear targets [[chapter 2](#)] and at the order of 80% for a Xenon target [[40](#)]. This supposed to remain true for other potential DM-quark or gluon interactions, e.g., spin-dependent interactions, because two-nucleon operators are predicted to appear at higher chiral orders as in the case of scalar DM interactions.

The objective of this chapter is to understand how to compute such current matrix-elements for nuclear bound-states on a lattice within a Finite-Volume (FV)—in the following I will denote this by **box**. An example of a nuclear box analysis of matrix-elements was carried out by [141] in the case of radiative capture reactions. As discussed in chapter 3, the advantage of box computations, compared to traditional methods, is the improved scaling of resources in terms of involved degrees of freedom. In principle, it is possible to express all theory-space truncations by the finite (spatial) volume L^3 and lattice spacing a_L , which enables the reduction or removal of the effects of all unphysical simplifications/approximations. To express it more directly: the box prescriptions are defined by their limits—FV and lattice discretization procedures are formulated such that in the infinite volume and continuum limit, one recovers the physical results

$$\langle \hat{J}_{\text{phys}} \rangle = \lim_{a_L \rightarrow 0} \lim_{L \rightarrow \infty} \langle \hat{J}_{a_L, L} \rangle . \quad (5.3)$$

Note that the spatial continuum limit is generally not obtainable in Nuclear Lattice Effective Field Theory (NLEFT) because nuclear forces must be regularized—which is *a priori* done by the spatial lattice spacing. If one wants to take the continuum limit, one must disentangle the discretization effects from the cutoff effects. The most common ideas are the introduction of an additional cutoff which is independent of the lattice spacing, or the improvement of the implemented operators such that one reduces discretization effects. These two procedures are described in this chapter. Even if one does not execute a continuum limit in actual computations, the analysis presented in this chapter can be useful to estimate the magnitude of uncertainty coming from the discretization.

An additional idea for executing the continuum limit in NLEFT computations without introducing another cutoff involves estimating the uncertainty due to the chiral truncations. As a starting point for this idea, one can picture the following scenario: suppose one finds a range of spatial lattice spacings where observables are independent of the cutoff. The variation of the lattice spacing just changes discretization effects. If one can find such a range, then one could make a continuum extrapolation which does not remove the cutoff. It only accounts for discretization effects. In praxis, it is generally not possible to find such a range in which no cutoff effects are observable. However, one knows that the cutoff dependence should decrease if one increases the chiral order of the nuclear interactions. Thus, similar to the uncertainty estimation in section 2.3.3, one could take raw lattice data at a finite lattice spacing but at different chiral orders to estimate the chiral truncation uncertainty. This uncertainty estimation includes the uncertainties coming from the cutoff (or the chiral breakdown scale to be more precise). If this chiral truncation uncertainty estimation is accurate, then these raw data points are—within their uncertainty—-independent of the cutoff. Thus one can propagate these uncertainties and execute the continuum limit. It remains to be tested if one can successfully implement such an uncertainty estimation scheme to compute observables in the continuum limit in NLEFT.

This procedure is illustrated in fig. 5.1 for synthetic lattice data which was generated

according to

$$X^{(\nu)}(a_L, Q) = X_{\text{exp}} \left[1 + \sum_{n=1}^{N_a} \Delta X_{a_L}^{(2n)} (\gamma a_L)^{2n} + \sum_{m=\nu}^{N_\nu} \Delta X_\nu^{(m)}(a_L) Q^m \right], \quad (5.4)$$

where: $X^{(\nu)}(a_L, Q)$ — is the chiral observable at order ν (for the LO one has $\nu = 2$ and increments by one afterwards),

- Q — is the chiral expansion parameter ($Q \sim m_\pi/\Lambda_b \approx 130/500$),
- γ — is a problem relevant energy scale (e.g., $\gamma \sim \sqrt{m_N E_D} \approx 50\text{MeV}$),
- $\Delta X_{a_L}^{(2n)}$ — are the discretization errors without cutoff dependence (which are removable by a continuum extrapolation). These uncertainties follow an uniform distribution $\Delta X_{a_L}^{(2n)} \sim U(0.2, 0.6)$,
- $\Delta X_\nu^{(m)}(a_L)$ — are the *a priori* cutoff dependent chiral truncation uncertainties (which are not defined at $a_L = 0$). Different uncertainties are generated for each of the lattice spacings and follow an uniform distribution: $\Delta X_\nu^{(m)}(a_L) \sim U(-0.7, 0.7)$.

The boundaries of the uniform distributions as well as the series truncations ($N_a = 3$ and $N_\nu = 5$) are arbitrarily chosen in problem relevant dimensions.

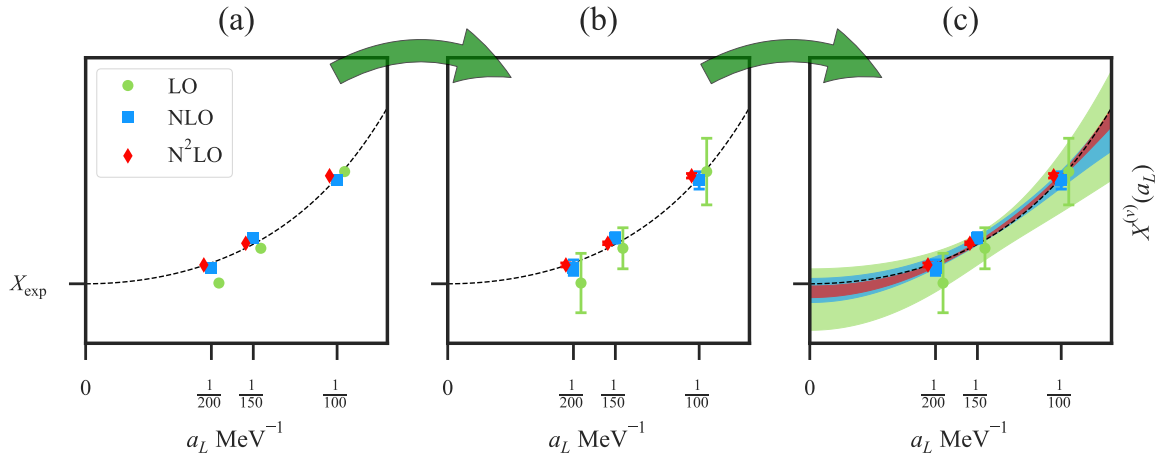


Figure 5.1: Schematic illustration for the idea on how to do a continuum limit extrapolation— with the objective to eliminate discretization effects—in NLEFT. At first one must compute the observable $X^{(\nu)}(a_L)$ at different chiral orders $\nu = \{\text{LO, NLO, N}^2\text{LO, } \dots\}$ and at different lattice spacings a_L [diagram (a)]. Next, one must estimate the chiral truncation uncertainty [diagram (b)] in a similar spirit as was presented in [section 2.3.3](#). From this, one can propagate the chiral uncertainty, which incorporates the effects of the theory cutoff, by extrapolating to the continuum [diagram (c)]. The dashed line corresponds to the (in this case known) effects of discretization without cutoff dependence and the deviations from this line are effects of the chiral truncation errors. This plot was created using synthetic data generated according [eq. \(5.4\)](#). It remains to be shown if it is possible to repeat this analysis in a meaningful way for actual nuclear lattice data [more specifically, if [eq. \(5.4\)](#) indeed describes nuclear lattice data].

Ideally, one would like to analytically describe the FV and continuum limit convergence pattern and thus either estimate the size of uncertainties or even use different information to extrapolate to the physical limit. In the best case scenario, one can find a functional dependence of the convergence pattern which scales independently of the exact shape of the current and wave functions. This desired scaling independence does not mean that the NMEs of the currents are independent of the current or wave function; just that the **scaling** of the result in a_L or L behaves similarly for different currents and wave functions. Indeed, this convergence pattern will depend on how one discretizes space, e.g., on the specific implementation of the derivative, or how one limits the spatial extent, for instance by choosing the boundary conditions of the volume. But, if the NMEs of the currents of interest are regular, e.g., that the kernel of the integral in eq. (5.2) is smooth, and the wave function is finite in extent (which is the case when $\psi(x)$ goes exponentially fast to zero for $x > L/2$), then it is the hope that the a_L - and L -scaling of the convergence pattern is relatively independent on the explicit form of nuclear wave function and currents.

This chapter presents a feasibility study for nuclear currents within a box with the goal to estimate uncertainties coming from the box prescription, to find the parameter space needed for accurate computations and to identify possible bottlenecks or showstoppers for large-scale stochastic many-nucleon computations.

5.2 Analytical solutions to separable potentials

In this section an analytically soluble separable potential

$$\langle \mathbf{p}' | \hat{V} | \mathbf{p} \rangle = V(\mathbf{p}', \mathbf{p}) = -g^*(\mathbf{p}')g(\mathbf{p}), \quad (5.5)$$

which mimics short-ranged nucleon-nucleon interactions, is chosen to determine a nuclear bound-state wave function and to compare analytical solutions to the corresponding numerical FV lattice counterparts.

5.2.1 Two-body solutions to separable potentials

As the start pointing one solves the Schrödinger equation in the infinite volume and continuum

$$\frac{\mathbf{p}^2}{2\mu}\psi(\mathbf{p}) - \int \frac{d^3\mathbf{p}'}{(2\pi)^3} g^*(\mathbf{p})g(\mathbf{p}')\psi(\mathbf{p}') = E_B \psi(\mathbf{p}), \quad E_B < 0, \quad (5.6)$$

where $\mu = m_N/2$ is the reduced two-nucleon mass and E_B is the binding energy of the state, e.g. fixed to the binding energy to the Deuteron $E_B \stackrel{!}{=} E_D = -2.225\text{MeV}$. From

the previous equation one can infer that the integral over the potential is a constant

$$G \equiv \int \frac{d^3 \mathbf{p}'}{(2\pi)^3} g(\mathbf{p}') \psi(\mathbf{p}'), \quad (5.7)$$

times the separable part of the potential $g^*(\mathbf{p})$. Thus, one can factorize the solution for the wave function and solve the problem recursively

$$\psi(\mathbf{p}) = \frac{G g^*(\mathbf{p})}{p^2/2\mu - E_B} \Rightarrow G = \int \frac{d^3 \mathbf{p}}{(2\pi)^3} g(\mathbf{p}) \frac{G g^*(\mathbf{p})}{p^2/2\mu - E_B} \Rightarrow 2\mu \int \frac{d^3 \mathbf{p}}{(2\pi)^3} \frac{|g(\mathbf{p})|^2}{p^2 + \gamma^2} = 1, \quad (5.8)$$

where $\gamma^2 = -2\mu E_B$ is the binding momentum. Since the denominator of eq. (5.8) is independent of the direction of \mathbf{p} , it is useful to first compute the angular integration before solving the integral equation for the binding momentum

$$\int_0^\infty \frac{dp}{2\pi} p^2 \frac{\Gamma(p)}{p^2 + \gamma^2} \stackrel{!}{=} 1, \quad \Gamma(p) \equiv \frac{2\mu}{(2\pi)^2} \int d\Omega |g(\mathbf{p})|^2 \geq 0. \quad (5.9)$$

5.2.2 Specific choice of potential

The chosen potential for the comparisons between the physical and the box results is defined by its separable part

$$g(\mathbf{p}) = \bar{g} \sqrt{8\pi} \frac{M^4}{(p^2 + M^2)^2}, \quad M, \bar{g} \in \mathbb{R}. \quad (5.10)$$

In principle the choice is arbitrary, but to guarantee that the potential behaves smoothly in the ultra-violet limit, e.g., under discretization, one must avoid singularities. In coordinate space, the potential will have the form

$$\langle \mathbf{r}' | \hat{V} | \mathbf{r} \rangle = |\bar{g}|^2 f(M, \gamma) \exp\{-M(r + r')\}, \quad (5.11)$$

which is always finite for finite M (no $r \rightarrow 0$ divergency). The usual *Yukawa* like denominator would result in a $1/r$ scaling in coordinate space. The M^4 numerator is chosen to mimic contact interactions. If one takes $M \rightarrow \infty$, the potential would be constant in \mathbf{p} and \mathbf{p}' and thus correspond to a delta function in coordinate space. However, to reproduce the Deuteron binding energy, one must solve eq. (5.9) and match \bar{g}

$$\Gamma(p) = |\bar{g}|^2 \frac{16M^8\mu}{(p^2 + M^2)^4} \Rightarrow \bar{g} \stackrel{!}{=} \frac{2(\gamma + M)^2}{\sqrt{\mu M^3 (\gamma^2 + 5M^2 + 4\gamma M)}}. \quad (5.12)$$

The correlation of \bar{g} with M can be interpreted as a renormalizing procedure for the potential, if one views M as a regulator. However, for finite M , the problem is well defined and *a priori* one has not introduced any *external* regulators like cutoffs. This choice for the potential allows to make continuum limit extrapolations in the discretized form of this problem. Nevertheless, as will be pointed out later on, M needs to be sufficiently large compared to the box parameters in order to ensure infinite volume convergence, but sufficiently small to ensure continuum convergence.

Since the potential is now fixed, one can compute the proper normalized wave function in momentum and coordinate space

$$\begin{aligned}\psi_M(\mathbf{p}) &= \sqrt{\frac{8M^5(\gamma + M)^5}{8M^2 + 5\gamma M + \gamma^2}} \frac{1}{(M^2 + p^2)^2} \frac{\sqrt{8\pi\gamma}}{(\gamma^2 + p^2)} \quad \xrightarrow{M \rightarrow \infty} \frac{\sqrt{8\pi\gamma}}{(\gamma^2 + p^2)}, \\ \psi_M(\mathbf{r}) &= \int \frac{d^3\mathbf{p}}{(2\pi)^3} e^{i\mathbf{p}\cdot\mathbf{r}} \psi_M(|\mathbf{p}|) = \frac{4\pi}{(2\pi)^3} \int dp p^2 \frac{\sin(pr)}{pr} \psi_M(p) \quad \xrightarrow{M \rightarrow \infty} \sqrt{\frac{\gamma}{2\pi}} \frac{e^{-\gamma r}}{r}.\end{aligned}\tag{5.13}$$

Note that the asymptotic expressions have the correct $M \rightarrow \infty$ behavior which matches the result of delta function potentials. The densities of the wave functions for different values of M (colors) are visualized in the two left diagrams in [fig. 5.2](#) (regular plot and log-plot). As is evident from the long-range part of the wave function plot, for sufficiently large r , the density decays exponentially to zero (with slope γ). Only for values with $M \approx \gamma$, the asymptotic behavior of the potential affects the wave function itself, and thus one sees a mixed convergence pattern. Furthermore, [fig. 5.2](#) demonstrates that the short-range aspect of the potential (the size of M) dictates the extension of the wave function—for large values of M , the density is sharply peaked, while small values of M broaden the structure.

Finally, inserting the results of [eq. \(5.13\)](#) in [eq. \(5.2\)](#), one can compute the expected current matrix-element results

$$\langle \hat{J}_{q(\text{is})}^{(\text{LO})}(\mathbf{q}) \rangle = 8\pi \int_0^\infty dr r^2 \frac{\sin\left(\frac{qr}{2}\right)}{qr} |\psi_M(r)|^2 \quad \xrightarrow{M \rightarrow \infty} \frac{4\gamma}{q} \operatorname{arccot}\left(\frac{4\gamma}{q}\right).\tag{5.14}$$

Results for the currents for different values of M are visualized in the right diagram of [fig. 5.2](#). The current expectation values seem to have a drastic dependence on the short-range aspect of the potential. One can understand this dependence by analyzing the kernel of [eq. \(5.14\)](#). Expanding for small q values, one has

$$\frac{\sin\left(\frac{qr}{2}\right)}{qr} \approx 1 - \frac{1}{2 \cdot 3!} \left(\frac{qr}{2}\right)^2,\tag{5.15}$$

and thus, the more area the wave function density contains for small r , the less is subtracted off from the current density result. This discretization dependence has potentially

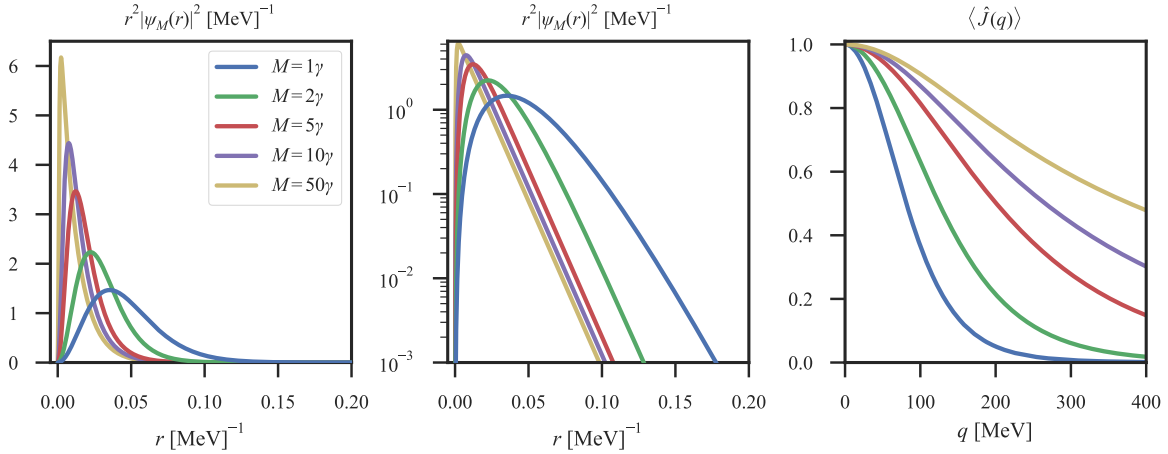


Figure 5.2: Analytic results for the wave function densities [wave function defined in eq. (5.13)] and current NMEs [eq. (5.14)] for different values of M in units of the binding momentum γ . Note that the left diagram and the middle diagram are the same but on different scales (regular vs. log scale).

high relevance for lattice results, where the lattice spacing plays the role of the regulator and would make a continuum analysis essential to the computation of current matrix-elements.

5.3 Currents within the box

5.3.1 Living within a box

For the definition used in this work, a box has two basic properties: space is finite with some form of periodicity (usually periodic boundary conditions), and space is discrete. Combining both effects, the infinite space of \mathbb{R}^N becomes the finite space N_L^N with $L = a_L N_L$, where a_L is the lattice spacing and L^N the volume of the space. One usually introduces the box in coordinate space, but it is not essential to do so. For example, one could introduce a finite discrete and periodic volume in momentum space and obtain the same results. One only has to require a proper definition of the Fourier Transformation (FT) (and normalization of delta functions). Also, in principal one can also work in a just discretized but infinite space or a finite but continuous space.

If one discretizes coordinate space, derivatives correspond to finite step differences and

Coordinate Space	Momentum Space
Finite and periodic	Discrete
Discrete	Finite and periodic

Table 5.1: Effects of discretization and FV on different spaces.

the integral measure becomes a sum. In the most simple cases this becomes

$$\mathbb{R}^N \mapsto a_L \mathbb{Z}^N \equiv \{a_L \mathbf{n} | \mathbf{n} \in \mathbb{Z}^N\}, \quad (5.16)$$

$$\int_{\mathbf{r} \in \mathbb{R}^N} d^N \mathbf{r} f(\mathbf{r}) \mapsto a_L^N \sum_{\mathbf{n} \in \mathbb{Z}^N} f(a_L \mathbf{n}), \quad (5.17)$$

$$\hat{\Delta} f(\mathbf{r} = a_L \mathbf{n}) \mapsto \sum_{i=1}^N \frac{f(a_L[\mathbf{n} + \hat{\mathbf{e}}_i]) - 2f(a_L \mathbf{n}) + f(a_L[\mathbf{n} - \hat{\mathbf{e}}_i])}{a^2}. \quad (5.18)$$

Because the exponential of the kernel of a FT to momentum space has the argument $a_L \mathbf{n} \cdot \mathbf{p}$, any function in momentum space is periodic in \mathbf{p}

$$\begin{aligned} \tilde{f}(\mathbf{p}) &= a_L^N \sum_{\mathbf{n} \in \mathbb{Z}^N} f(a_L \mathbf{n}) \exp\{i a_L \mathbf{p} \cdot \mathbf{n}\}, \\ \Rightarrow \tilde{f}(\mathbf{p}) &= \tilde{f}\left(\mathbf{p} + \frac{2\pi}{a_L} \mathbf{n}\right) \quad \forall \mathbf{p} \in \mathbb{R}^N, \forall \tilde{f} \in C(\mathbb{R}), \forall \mathbf{n} \in \mathbb{Z}. \end{aligned} \quad (5.19)$$

Furthermore, because the momentum operator is defined as the FT of the derivative, the allowed momenta depend on the realization of the derivative

$$\hat{p}^2 \tilde{f}(\mathbf{p}) = \text{FT}(\hat{\Delta} f(\mathbf{x})) = \frac{2}{a_L^2} \sum_{i=1}^N [1 - \cos(p_i a_L)] \tilde{f}(\mathbf{p}). \quad (5.20)$$

Here, the so-called ‘one-step derivative’ or ‘order a^2 improved derivative’ has been presented. The naming scheme is related to the range of the differences: $f(a_L[\mathbf{n} + 1\hat{\mathbf{e}}_i])$ or the order at which corrections appear $(p^2 - \hat{p}^2)\tilde{f}(\mathbf{p}) = \tilde{f}(\mathbf{p})\mathcal{O}(a^2)$. This can be further generalized by defining

$$\begin{aligned} \hat{\Delta}^{(N_S)} f(\mathbf{r} = a_L \mathbf{n}) &\mapsto \frac{1}{a^2} \sum_{n_s=0}^{N_S} \sum_{d=\pm 1} \sum_{i=1}^N \omega_{n_s}^{(N_S)} f(a_L[\mathbf{n} + d n_s \hat{\mathbf{e}}_i]) \\ &\text{with } \left[p^2 - (\hat{p}^{(N_S)})^2 \right] \tilde{f}(\mathbf{p}) = \tilde{f}(\mathbf{p}) \mathcal{O}(a^{2N_S}), \end{aligned} \quad (5.21)$$

where N_S is the number of derivative steps and the $\omega_{n_s}^{(N_S)}$ coefficients have been matched to fulfill the second part of the equation. In the same manner, one can define derivatives corresponding to odd powers of \mathbf{p} . This improvement of derivatives can be used to make a continuum analysis without affecting the actual size of the lattice spacing—if unitless

combinations of a and other problem relevant parameters are small, then one does not see much improvement when improving the derivative order.

Similarly, if one limits coordinate space to a FV and requires that all functions are periodic at the boundaries $f(\mathbf{r}) = f(\mathbf{r} + \hat{\mathbf{e}}_i L)$ for all $i = 1, \dots, N$ and for all $f \in C(\mathbb{R})$, then one can simply reuse the previous result and revert the procedure. Hence

$$\mathbf{p} \in \frac{2\pi}{L} \mathbb{Z}^N. \quad (5.22)$$

In order to fulfill all of the previous conditions, one introduces functions within the box by choosing one of the following replacements (and uses FTs to get the same function in respective Fourier transformed space)

$$f(\mathbf{r} = a_L \mathbf{n}) \mapsto \sum_{\mathbf{m} \in \mathbb{Z}^N} f(a_L \mathbf{n} + L \mathbf{m}), \quad (5.23)$$

$$\tilde{f}\left(\mathbf{p}^2 = \frac{4\pi^2}{L^2} \mathbf{n}^2\right) \mapsto \tilde{f}\left(\frac{2}{a_L^2} \sum_{n_s=0}^{N_s} \sum_{d=\pm 1} \sum_{i=1}^N \omega_{n_s}^{(N_s)} \cos\left(\frac{2\pi a_L n_i d n_s}{L}\right)\right). \quad (5.24)$$

Of the two, eq. (5.24) is more practical because it corresponds to a finite sum of terms.

In the next section, first estimates of corrections associated with the box computation are analytically computed.

5.3.2 Estimation of discretization errors

The discretization errors can be estimated by the corrections coming from the implementation of the derivatives. For example, the kinetic Hamiltonian for a simple one step derivative becomes

$$\hat{H}_0 \mapsto \hat{H}_{0,a_L} = \frac{1}{2\mu} \frac{2}{a_L^2} \sum_{i=1}^3 [1 - \cos(\hat{p}_i a_L)], \quad (5.25)$$

$$\Delta_{a_L}(\hat{H}_0) \equiv \hat{H}_{0,a_L} - \hat{H}_0 = -\frac{a_L^2}{4!\mu} \sum_{i=1}^3 \hat{p}_i^4 + \mathcal{O}(a_L^4 \hat{p}_i^6). \quad (5.26)$$

If one views the discretization as a perturbation to the continuum result, than the difference of the discretized result to the continuum result can be computed in perturbation theory. The leading correction is the matrix-element of the continuum wave function with this continuous correction operator $\langle \psi_M | \Delta_{a_L}(\hat{H}_0) | \psi_M \rangle$.

To simplify the computation of the expectation value, for this specific separable potential case one can use the spherical symmetry of the wave function (S-wave): each matrix-element for different \hat{p}_i will have the same result. Hence the total result is equal to three

times the result of one direction. In case of the z direction, $p_z = p \cos \theta$, this results in

$$\langle \psi_M | \Delta_{a_L}(\hat{H}_0) | \psi_M \rangle = -\frac{3a_L^2}{24\mu} \int \frac{d^3\mathbf{p}}{(2\pi)^3} |\psi_M(p)|^2 p^4 \cos^4 \theta \quad (5.27)$$

$$= -\frac{a_L^2}{80\pi^2\mu} \int dp p^2 p^4 |\psi_M(p)|^2 \quad (5.28)$$

$$= -\frac{a_L^2 \gamma M^4 (5\gamma + M)}{40\mu (\gamma^2 + 8M^2 + 5\gamma M)}. \quad (5.29)$$

Note that for $M \rightarrow \infty$, this expression diverges. However, since M is viewed as a constant parameter, the goal of this task is just the estimation of uncertainties. The result is that the discretization errors of kinetic terms profit from small values of M . One can understand this by analyzing the shape of the wave function (fig. 5.2): the smaller the slopes of the wave function, the smaller the needed lattice spacing for an accurate approximation of the derivative.

5.3.3 Estimation of Finite-Volume errors

The same perturbative analysis can be done for FV effects[142–145]. The leading contribution is given by

$$\langle \psi | \Delta_L(\hat{H}) | \psi \rangle = \sum_{|\mathbf{n}|=1} \int_{\mathbb{R}^3} d^3\mathbf{r}' d^3\mathbf{r} \psi_M(r') V(r, r') \psi_M(|\mathbf{r} + \mathbf{n}L|), \quad (5.30)$$

which expresses the corrections coming from the overlap of shifted-by-one-box-copies of the wave function. Higher order contributions are given by $|\mathbf{n}| > 1$. Expanding the result of the integration in $\alpha = \gamma/M$, one has

$$\begin{aligned} \langle \Delta_L(\hat{H}) \rangle = & -\frac{6\gamma}{\mu L} e^{-\gamma L} \left[1 + \frac{35\alpha}{8} + \mathcal{O}(\alpha^2) \right] \\ & + \frac{\gamma^4 L^2}{8\mu\alpha^3} e^{-ML} \left[1 + \alpha \frac{35\gamma L + 72}{8\gamma L} + \mathcal{O}(\alpha^2) \right]. \end{aligned} \quad (5.31)$$

Note that one recovers the well known (short-range dynamics independent) two-body bound state FV dependence for $M \rightarrow \infty$

$$\langle \Delta_L(\hat{H}) \rangle \xrightarrow{M \rightarrow \infty} -\frac{6\gamma}{\mu L} \exp\{-\gamma L\}. \quad (5.32)$$

This expression is less problematic in M (compared to the discretization effects) because the only assumptions which has been made was the asymptotic behavior of the wave in the regions with $r > L/2$. This is true if $M > \gamma$ and thus the further corrections result in terms proportional to $\exp\{-ML\}$ and γ/M .

In contrast to the discretization analysis, the FV dependence profits from rather large values in M . This study views M as a parameter, this means one can find an optimal value for M in order to minimize the total error coming from discretization and FV effects. Computation time scales with the number of lattice points $N_L = L/a_L$, and therefore one would like to keep N_L as small as possible. Requiring both corrections to be equal to a fixed value, e.g., $\langle \Delta_L(\hat{H}) \rangle (M_0) \stackrel{!}{=} 10\% \stackrel{!}{=} \langle \Delta_{a_L}(\hat{H}) \rangle (M_0)$, one can solve for an optimal M_0 which minimizes N_L . This monotonously growing $N_L(M)$ dependence is shown in fig. 5.3, which suggests to take minimal values for M .

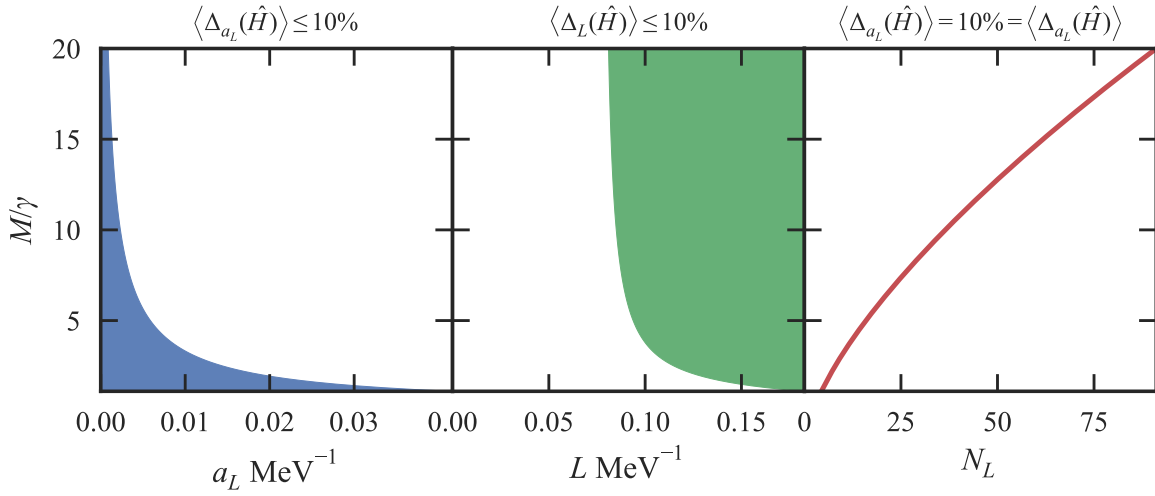


Figure 5.3: Convergence pattern of box parameters depending on parameter M . In the first [second] column, the shaded area displays the allowed values for a_L [L], for a given M , such that the discretization [FV] effects of the energy are smaller than 10%. The third column displays the minimal values for N_L which correspond to a 10% correction of the binding energy for both discretization and FV effects individually.

5.4 Results

In this section, the results of the box computations are compared to the analytical results. The results in the box are implemented on a spatial lattice of size N_L^3 through the use of eq. (5.24) for three different derivative step sizes $N_S = 1, 2$ and 3 . The wave function and energy levels are obtained by diagonalizing the corresponding box Hamiltonian where the potential parameter M was fixed to $M = 2$. Furthermore, the coupling \bar{g} was fixed to the infinite volume continuum result (the analytical result). Thus, in the limit of $L \rightarrow \infty$ and $a_L \rightarrow 0$, results must converge against their analytical counterpart. Current NMEs are computed by sandwiching the box current operator matrices with obtained box wave functions. The following diagrams show absolute values for the box computations as well

as relative errors

$$\Delta O_{a_L,L} \equiv \frac{O_{a_L,L} - O_{0,\infty}}{O_{0,\infty}}. \quad (5.33)$$

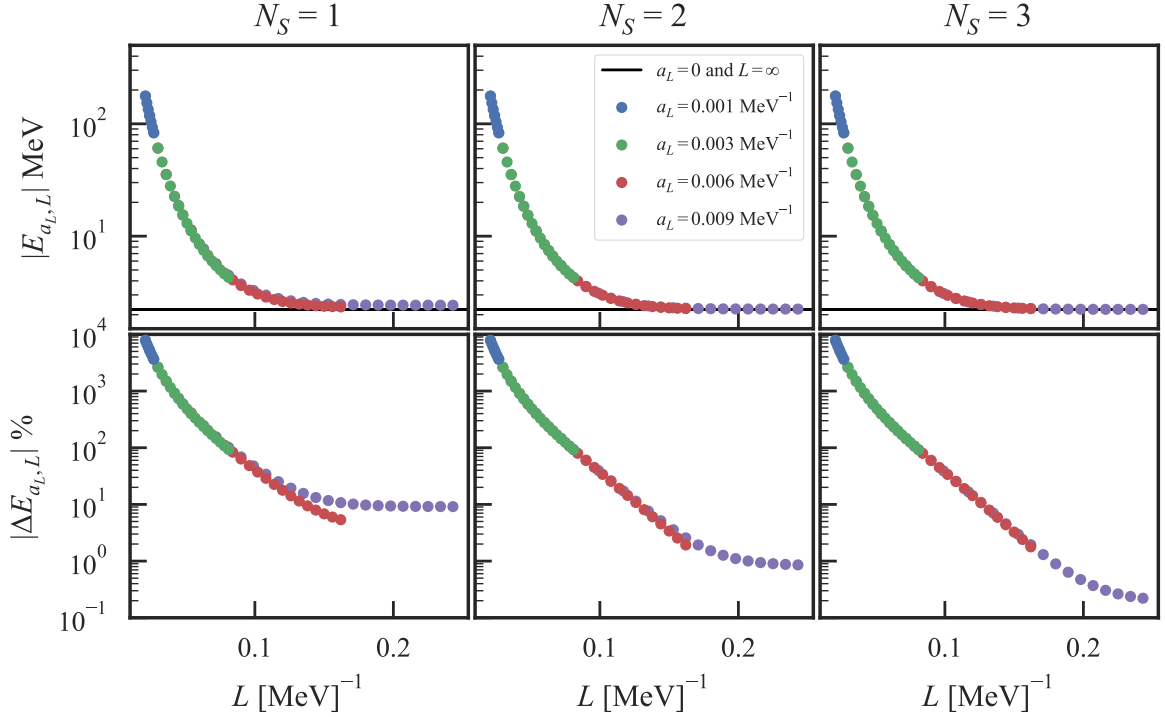


Figure 5.4: Box results of the binding energy for different lattice spacings a_L depending on the box extend L . Results are presented for different implementations of the derivative with step range N_S [see eq. (5.24)].

Figure 5.4 displays the volume dependence of the binding energy for different lattice spacings and different implementations of the derivative. The maximal number of lattice points is fixed to $\max(N_L) = 25$ because of memory limitations. Therefore, computations for smaller lattice spacings correspond to computation for smaller volumes. For all implementations of different derivatives, one observes an exponential decay of the binding energy in the spatial extent. However, the linear slope of the density in the relative error plot is limited to a sub-interval. Next-to-Leading Order (NLO) FV corrections are expected to influence the lower non-linear L part and discretization effects dominate the large L energy corrections. One can recognize that the energy corrections for large L are consequences of the discretization prescription for two reasons: one can observe that the computations with $N_S = 1, 2$ seem to be independent on L for $L \gtrsim 0.2 \text{ MeV}^{-1}$, and the improvement of the derivative shrinks the size of the correction for similar L and a_L .

The absolute values for the box results of the current matrix-elements are displayed in fig. 5.5 and the difference to the analytic counterparts in fig. 5.6. Because of the periodicity in the momentum structure, the matrix-elements are only displayed until

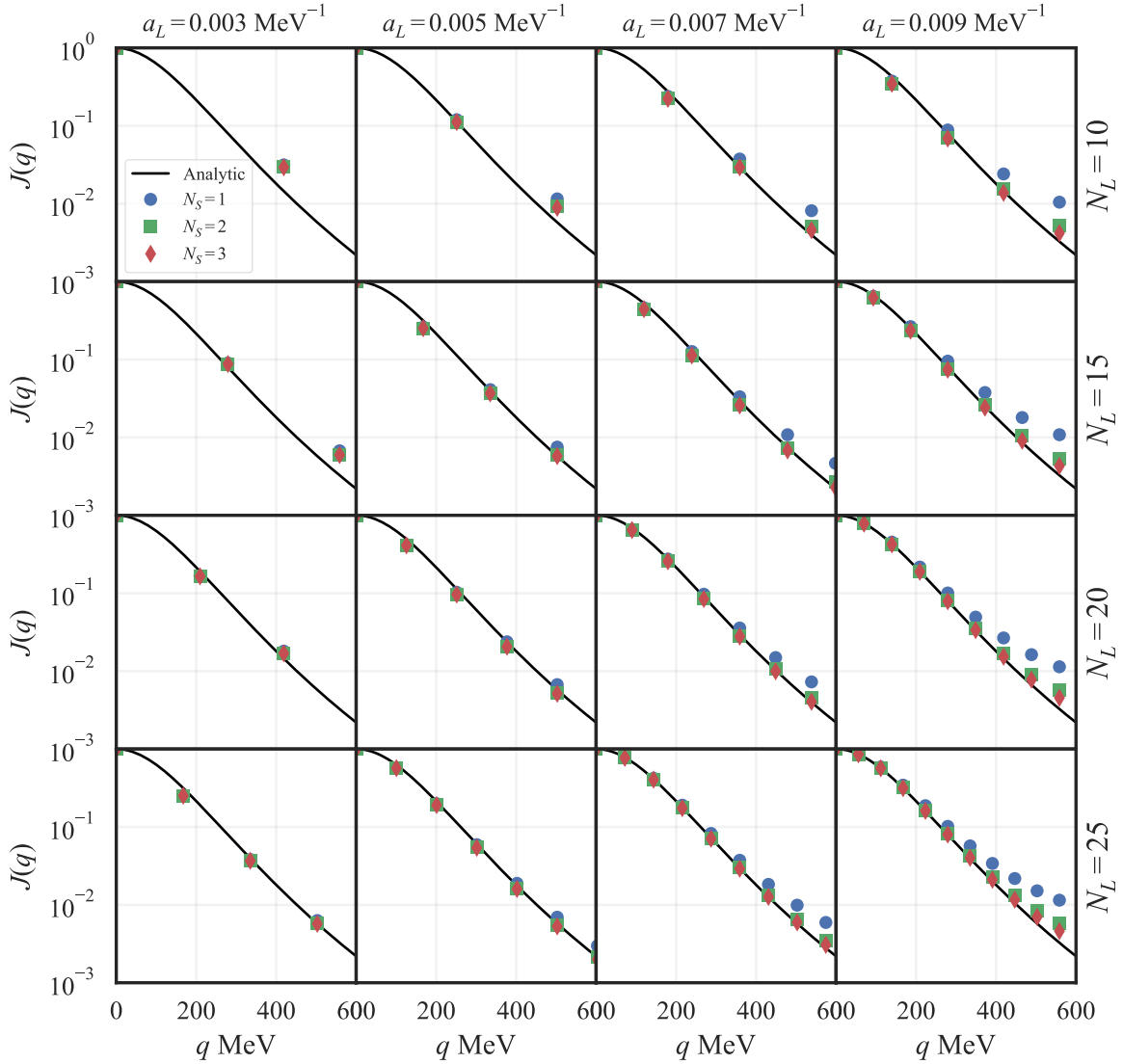


Figure 5.5: Absolute values of box current results for different values of L and a_L depending on the momentum exchange q . Results are presented for different implementations of the derivative with step range N_S [see eq. (5.24)].

$q_{\max} = 4\pi/a_L/2$. Note that the lattice spacing defines the range of allowed momenta and therefore different columns have a different q -range and values within this range. As is evident from the diagrams, the agreement between box results and analytical counterparts is better for smaller values of q —a consequence of the coordinate space discretization which induces periodicity for functions of momenta. The dips in the functional form of the current matrix-elements in fig. 5.6 correspond to a relative switch of the sign (note that the absolute value is plotted). For large lattice spacings, increasing the number of lattice points—corresponding to increasing the volume—has a positive effect on the size of the correction. However, for $a_L \sim 0.008\text{MeV}^{-1}$, the effect is seemingly less rele-

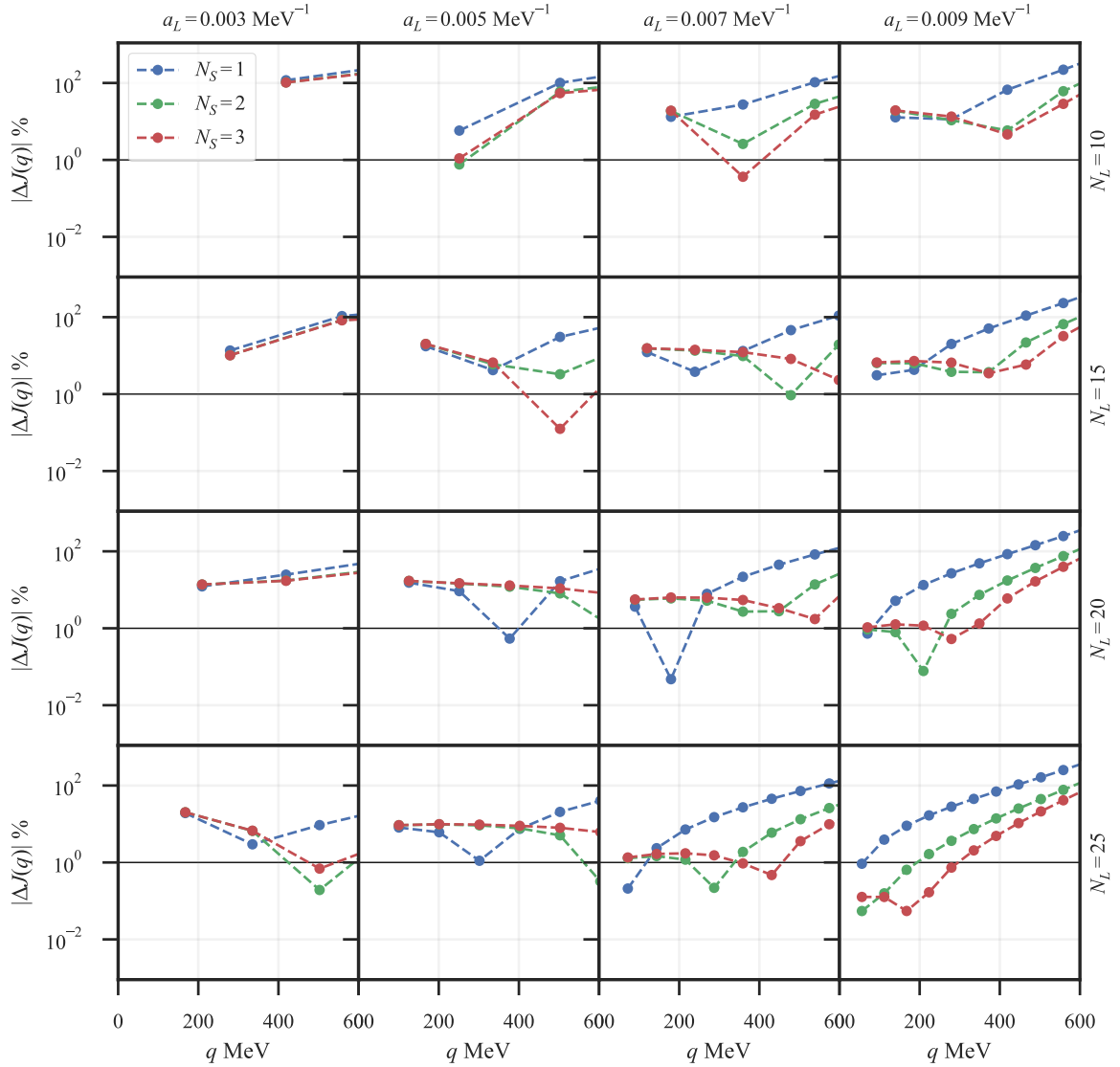


Figure 5.6: Relative difference of box current results compared to analytical results for different values of L and a_L depending on the momentum exchange q . Results are presented for different implementations of the derivative with step range N_S [see eq. (5.24)]. The central black line indicates the sub-percent threshold.

vant. On the other hand, the larger the lattice spacing, the more significant the effect of improving the implementation of the derivative. An important note is that the results within an exchange-momentum range $q \in [0, 100] \text{MeV}$ are of physical interest. Using this implementation of box observables, this essentially requires lattice spacings at the order of $a_L \sim 0.01 \text{MeV}^{-1}$ or box volumes above $L \sim 0.2 \text{MeV}^{-1}$. Otherwise, the momentum lattice is too coarse in the region of interest. Fortunately, it seems possible to obtain results within in the sub-percent precision regime as long as the lattice volume is large enough $L \sim 0.2 \text{MeV}^{-1}$.

5.5 Summary and conclusion

In this chapter, it was explained how one converts continuum and infinite volume observables to discretized FV observables. Analytical estimations based on exact computations for a separable potential have been made to approximate FV and discretization effects. Finally, numerical computations in the box were compared to the analytical infinite volume continuum results. The analysis has shown that it is possible to compute *simple* external current matrix-element within a box formalism. However, there are several constraints which make the procedure, in general, more difficult.

From a general field theory point of view, it seems that cutoff effects, induced by the potential, could drastically influence the results of current matrix-elements. As it was shown, this seems not to be the case for the one-nucleon currents and potentials considered in [chapter 2](#). However, it may be that the cutoff dependence might become more problematic for two-nucleon currents, which have a nontrivial spin-angular momentum structure. To answer this question definitely, one must repeat the analysis of this chapter for chiral interactions.

Additionally, from the box point of view, discretization errors seem to be somewhat sensitive to hard potentials, while FV effects are more sensitive to soft potentials. Here one does not have a free parameter M to minimize the associated uncertainties and it remains an open question, which effect is more dominant. As mentioned in the introduction of this chapter, if one wants to remove discretization effects, one must try disentangle the regularization from the discretization effects. For example, one could try to improve the implementation of the operators (e.g., derivatives) to prove that results are converged. It is not possible to make a straightforward continuum limit extrapolation on the lattice because the lattice spacing is the required ultra-violet cutoff of the theory. However, it might be possible to absorb the effect of the cutoff within a chiral uncertainty estimation and extrapolate these results to the continuum. Similarly to the previous paragraph, the next step for a successful implementation is the repetition of this analysis for chiral interactions with the additional quantification of nuclear uncertainties.

Another difficulty might be the volume dependence of different current NMEs. While wave functions seem to converge exponentially against their infinite volume counterpart, it is *a priori* not apparent that a similar convergence can be expected from external current matrix-elements. Expanding such matrix-elements in unitless quantities, one must in principle include a term given by $qL \sim 4\pi L/L$, which is independent of the volume size. Fortunately, for test problem considered here, the results converge against their analytical counterpart in the infinite volume limit. Unless one does not find a general description for such matrix-elements, this convergence pattern must be analyzed for different current operator matrix-elements case by case.

In conclusion, it seems to be possible to compute one-nucleon current NME on the lattice and, as the next step, one should extend the analysis to chiral potentials before analyzing different current NMEs. Because chiral potentials are local and thus diagonal

in coordinate space, diagonalization computations can be extended to larger values of N_L and thus allow a more careful analysis of the convergence pattern for fixed exchange momentum values.

Last but not least, it is the long-term goal to evaluate NMEs of currents in Hybrid Monte Carlo (HMC) computations. Currently, NLEFT computations make use of actions renormalized to lattice spacings $a_L \in \{0.010, 0.008, 0.007, 0.005\}$ MeV⁻¹ [36]—matching the range of presented benchmarks. Because of time constraints, the range of spatial lattice points in most recent Monte Carlo simulations is at the order of $N_L \sim 8$ [146]. As presented in this section: in order to reach a relative uncertainty in the few percent regime for the NME presented in this chapter, one must at least double this number. In addition, to probe momentum values of physical interest, this constraint must be fulfilled as well—independent of the current operator. If one is not able to overcome this obstacle, then there is no need to continue the box analysis and should use already existing methods.

The strategy for realizing computations of external current NME within the framework of NLEFT is two-fold. On the one hand, the implementation of the NLEFT algorithm on Graphics Processing Units (GPUs) could drastically reduce the computational costs and allow the access to larger box volumes for same lattice spacings. For first steps in this direction see [appendix C](#). On the other hand, it is known from Lattice Quantum Chromodynamics (LQCD) that it is possible to reduce FV effects by adjusting the boundary conditions of the box[147]. This adjustment of boundary conditions also affects the range of allowed lattice momenta with the potential to probe smaller momentum values at fixed box volumes. The implementation of such Twisted Boundary Conditions (TBCs) is presented in the next chapter.

Applying Twisted Boundary Conditions for few-body nuclear systems

The following chapter is published in Physical Review C [1].

Applying Twisted Boundary Conditions for Few-body Nuclear Systems

Christopher Körber^a and Thomas Luu^a

^a *Institute for Advanced Simulations 4, Institute für Kernphysik 3, Jülich
Center for Hadron Physics, and JARA - High Performance Computing,
Forschungszentrum Jülich, D-52425 Jülich, Germany*

We describe and implement Twisted Boundary Conditions for the deuteron and triton systems within Finite-Volumes using the Nuclear Lattice Effective Field Theory formalism. We investigate the Finite-Volume dependence of these systems with different twist angles. We demonstrate how various Finite-Volume information can be used to improve calculations of binding energies in such a framework. Our results suggest that with an appropriate twisting of boundaries, infinite-volume binding energies can be reliably extracted from calculations using modest volume sizes with cubic length $L \approx 8 - 14$ fm. Of particular importance are our derivation and numerical verification of three-body analogs of ‘i-periodic’ twist angles that eliminate the Leading Order Finite-Volume effects to the three-body binding energy.

6.1 Introduction

Numerical simulations of nuclear observables often utilize Finite-Volume (FV) to perform calculations. Lattice Quantum Chromodynamics (LQCD) calculations of quarks and gluons, for example, utilize cubic volumes with spatial length L typically of size $\sim 4 - 6$ fm. Nuclear Lattice Effective Field Theory (NLEFT) calculations using nucleon degrees of freedom, on the other hand, employ volumes that are an order of magnitude larger. Despite being intrinsically stochastic, both methods have calculated nuclear binding energies of light hadronic systems with impressive, quantitative uncertainties. Recent LQCD calculations, albeit at unphysical pion masses, have calculated the binding energies of S -shell nuclei and light hyper nuclei [148–155]. NLEFT calculations have readily performed binding-energy calculations of P -shell nuclei [34, 37, 126, 156, 157] and some medium mass nuclei [38]. With ever increasing computer resources, calculations of such systems will become even more precise.

All of these calculations, however, suffer from a systematic error that cannot be reduced from increased computer resources: The calculated energies in a FV differ from their infinite-volume counterparts. In principle, this FV error can be removed by performing calculations of energies in multiple volumes followed by an extrapolation to infinite-volume. In practice, this is very difficult due to the enormous computational costs of performing calculations in multiple volumes. However, the number of different volume calculations needed to perform a reliable extrapolation may not be exceedingly large if the functional dependence of the FV correction is known. For the two-body system with periodic boundary conditions, for example, the FV correction to the binding energy is well known and the Leading Order (LO) contribution scales as $\exp(-\kappa L)/L$, where κ is the binding momentum [143, 158]. In [159] the functional dependence for three identical bosons in a FV (with periodic boundary conditions) and at the unitary limit was derived, and was also determined to fall off exponentially with volume size. For higher A-body systems, the dependence is also expected to be exponential, but a general formula is yet to be determined.

Periodic Boundary Conditions (PBCs) are a specific case of Twisted Boundary Conditions (TBCs) [160] at the faces of the cubic volume. These ‘twist’ conditions can be parametrized by a vector of angles θ_i at each boundary, with range $0 \leq \theta_i < 2\pi$, such that

$$\psi(\mathbf{x} + \mathbf{n}L) = e^{i\theta \cdot \mathbf{n}} \psi(\mathbf{x}). \quad (6.1)$$

Equation (6.1) shows that $\theta_i = 0$ corresponds to PBCs, while $\theta_i = \pi$ gives anti-Periodic Boundary Conditions (aPBCs). In LQCD, TBCs are equivalent to introducing a background $U(1)$ gauge field imposed on the quarks, subsequently endowing them with an arbitrary momentum dependent on the twist angle [161, 162]. With TBCs momentum states are no longer restricted to the discrete modes within a box with PBCs, and therefore calculations with different twist boundary conditions will give rise to different FV corrections. As initially found within condensed matter calculations, averaging results with different twist angles significantly cancels FV effects [163]. This has motivated the

use of ‘twist averaging’ in LQCD calculations to reduce the FV dependence in hadronic masses [164] and more recently to calculations of phases of nuclear matter in dense astrophysical environments [165].

Because of the non-linear nature of interactions in the non-perturbative regime between quarks and gluons and also between nucleons, twist averaging does not entirely eliminate FV effects. To what extent it does eliminate FV effects is an open question, and most certainly depends on the nature of interactions. In [147] the behavior of FV corrections for the two-body system was investigated for specific sets of twist angles. It was found that certain linear combinations of twist angles indeed reduce significantly FV effects. Just as important, it was shown that a particular set of twist angles ($\theta_i = \pi/2$), dubbed ‘i-periodic’, also significantly reduced the LO exponential dependence of the FV.

In this paper we extend the work done in [147] to three-body systems. Except for particular three-body limits (see, e.g., [159]), analytic calculations in this regime are not possible, and we utilize the NLEFT formalism to perform our calculations. In this case, nucleons are the relevant degrees of freedom, not quarks, and therefore twist angles are applied to nucleon state functions directly. We perform a detailed statistical analysis of our calculations, accounting for and propagating all relevant systematic errors in our extrapolations. From our analysis, we find the analogs of ‘i-periodic’ angles for the three-body system, which not only reduce FV effects, but cancels exactly the LO FV contribution.

Our paper is organized as follows: In section 6.2 we discuss the formalism for the implementation of twisted boundaries on general terms. We then derive in section 6.3 the LO non-relativistic FV corrections (with twists), focusing on the two- and three-body systems. We describe in detail in section 6.4 the application of twists within NLEFT algorithms, which we coded specifically for this work. Included in this same section is an enumeration of sources of systematic errors due to lattice artifacts and the FV, and a detailed discussion of our error analysis used to propagate errors. We present results of the two-body (deuteron) system and the three-body (triton) system in sections 6.5 and 6.6, respectively. We reserve section 6.7 for a discussion of discretization effects and the potential impact they have on extensive twist calculations. Finally, we recapitulate our findings and discuss possible future applications in section 6.8.

6.2 Implementation of Twisted Boundary Conditions for N -body systems

Assuming a non-relativistic N -body system, this system’s state can be written as a linear combination of tensor products of the individual particle states which include their internal quantum numbers,

$$|\mathcal{N}_1(I_1, S_1)\rangle \otimes \cdots \otimes |\mathcal{N}_N(I_N, S_N)\rangle ,$$

where I_i and S_i refer to the isospin and spin of the i^{th} nucleon, respectively. To realize such states computationally, an appropriate bra basis, either in configuration or momentum space, must be used. For example, momentum space calculations using a finite cube with PBCs would utilize a discrete momentum basis $\mathbf{p}_n = 2\pi\mathbf{n}/L$, where \mathbf{n} represents a triplet of integers. With an eye towards our lattice simulations presented in later sections, we adopt a discretized coordinate basis: $\mathbf{r} \mapsto a\mathbf{n}$, where a is the lattice spacing between lattice nodes. We denote this discretized basis as $|\mathbf{n}\rangle$. We stress that the results of this section do not depend on the choice of basis, however.

A spatial cutoff L is introduced by limiting the basis to a cubic box of volume L^3 with application of particular boundary conditions at the faces of the cube. This introduces FV effects (errors) that can only be removed by extrapolating to infinite-volume, $L \rightarrow \infty$. In this paper, we focus our analysis mainly on these FV effects for the lattice. Objects defined inside the box, such as matrix-elements of operators using the discretized basis $|\mathbf{n}\rangle$, will be denoted with a subscript L to differentiate them from their infinite-volume counterparts.

The most commonly used boundary conditions are PBCs, where the wave function is periodically continued outside of the box¹, which in turn produces images of the wave function outside of the original cubic volume. Periodic boundary conditions are just a subset of the more general TBCs defined as follows:

$${}_i\langle \mathbf{x}_i + L\mathbf{n} | \Psi_L \rangle_N = {}_i\langle \mathbf{x}_i | \Psi_L \rangle_N e^{i\phi_i \cdot \mathbf{n}}, \quad \forall \mathbf{x}_i \in L^3, \forall \mathbf{n} \in \mathbb{Z}^3. \quad (6.2)$$

The variable $\phi_i \in \mathbb{R}^3$ represents the twisted boundary angle of the i^{th} particle with components for each spatial direction. Suppressing the spin and isospin components, one can now define a basis for the discretized box (with N_L nodes in each spatial direction where $L = aN_L$) which satisfies TBCs and is useful for computing matrix-elements,

$$\begin{aligned} |\mathcal{N}_{i,L}\rangle &= \sum_{\mathbf{n} \in \mathbb{Z}^3} \mathcal{N}_{i,L}(\mathbf{n}) |\mathbf{n}\rangle_i = \frac{1}{\sqrt{M^3}} \sum_{\substack{\mathbf{m} \in \mathbb{Z}^3 \\ \mathbf{n} \in N_L^3}} \mathcal{N}_{i,L}(\mathbf{n} + N_L\mathbf{m}) \cdot |\mathbf{n} + N_L\mathbf{m}\rangle_i \\ &= \frac{1}{\sqrt{M^3}} \sum_{\substack{\mathbf{m} \in \mathbb{Z}^3 \\ \mathbf{n} \in N_L^3}} \mathcal{N}_{i,L}(\mathbf{n}) e^{i\phi_i \cdot \mathbf{m}} e^{-i\phi_i \cdot \mathbf{n}/N_L} e^{i\phi_i \cdot \mathbf{n}/N_L} |\mathbf{n} + L\mathbf{m}\rangle_i \\ &=: \sum_{\mathbf{n} \in N_L^3} \tilde{\mathcal{N}}_{i,L}(\mathbf{n}) |\mathbf{n}\rangle_i^{\phi_i}, \end{aligned} \quad (6.3)$$

where we have used the following definitions,

$$M^3 := \sum_{\mathbf{m} \in \mathbb{Z}^3} 1, \quad \tilde{\mathcal{N}}_{i,L}(\mathbf{n}) := \mathcal{N}_{i,L}(\mathbf{n}) \cdot e^{-i\phi_i \cdot \mathbf{n}/N_L}.$$

All phases can be absorbed by the newly defined basis states $|\mathbf{n}\rangle_i^{\phi_i}$ and the wave function

¹ This kind of behavior can also be defined for a finite continuous space.

$\tilde{\mathcal{N}}_{i,L}(\mathbf{n})$. This new ‘twisted basis’, which we denote collectively by $\{|\mathbf{n}\rangle_i^{\phi_i}\}$, can be understood as a grid of vectors multiplied by a phase associated with the different images of the original cube:

$$|\mathbf{n}^{\phi_i}\rangle_i := \frac{1}{\sqrt{M^3}} \sum_{\mathbf{m} \in \mathbb{Z}^3} e^{i\phi_i \cdot (\mathbf{n} + N_L \mathbf{m}) / N_L} \cdot |\mathbf{n} + N_L \mathbf{m}\rangle_i \quad (6.4)$$

Note that this description of twisted boundary states is in general different from the twisting convention used in LQCD. In LQCD one directly applies twists to the quarks and, in principle, there are different associated twist angles for each quark flavor. In our case, the twists are directly applied to the configuration space coordinates of the nucleons. Thus the number of twists is directly related to the number of nucleons – for N -nucleons one could choose N different twist angles.

We note that for numerical simulations, there is some freedom in how one implements TBCs. Typically TBCs are applied at the boundaries of the box where the application of the phase ϕ_i only occurs when a particle passes the boundary. We have instead chosen to apply twists incrementally $\propto \phi_i / N_L$ each time a particle changes its coordinates within the volume. In this manner, the accumulation of the entire phase ϕ_i also occurs when a particle passes a boundary. In [fig. 6.1](#) we provide a schematic comparison of our twist basis to the case where twists are applied at the boundaries only. In the demonstrated case of anti-periodic boundaries, one has that the wave function flips its sign after a shift in L , $\psi(\mathbf{x} + \mathbf{e}L) = -\psi(\mathbf{x})$, $|\mathbf{e}| = 1$. The upper two diagrams ([figs. 6.1\(a\)](#) and [6.1\(b\)](#)) use a basis where the boundary conditions are just applied at the edges of the spatial box. For this basis, the wave function only changes its phase when the particle ‘hops’ outside of the box [fig. 6.1\(b\)](#) but stays the same if moving within the box [fig. 6.1\(a\)](#). The lower diagrams ([figs. 6.1\(c\)](#) and [6.1\(d\)](#)) use the previously defined twisted boundary basis where a partial phase is applied each time a particle changes its spatial direction. After N_L steps in the same spatial direction, the accumulated phase becomes π , and thus the wave function changes its sign. This behavior also holds true at the boundaries. However, it depends on the direction of the ‘hops’.

The main reason for including the twisted boundary phases at each particle ‘hop’ is that this procedure ensures translational invariance at each point on the lattice, including the boundaries, and is thus more amenable to the NLEFT formalism. As a consequence of the translational invariance, the momentum modes in the lattice are well defined,

$$\langle \mathbf{p} | \mathbf{x} \rangle_i^{\phi_i} = \exp\left(\frac{2\pi i}{L} \mathbf{x} \cdot \mathbf{n}_p\right) \delta^{(3)}(L\mathbf{p} - 2\pi\mathbf{n}_p - \phi_i). \quad (6.5)$$

The delta function in [eq. \(6.5\)](#) shows that the allowed momenta inside the box are shifted by the twists for each particle,

$$\mathbf{p} = \frac{2\pi\mathbf{n}_p + \phi_i}{L}. \quad (6.6)$$

It is therefore possible to induce a non-zero Center of Mass (CM) energy for the zero

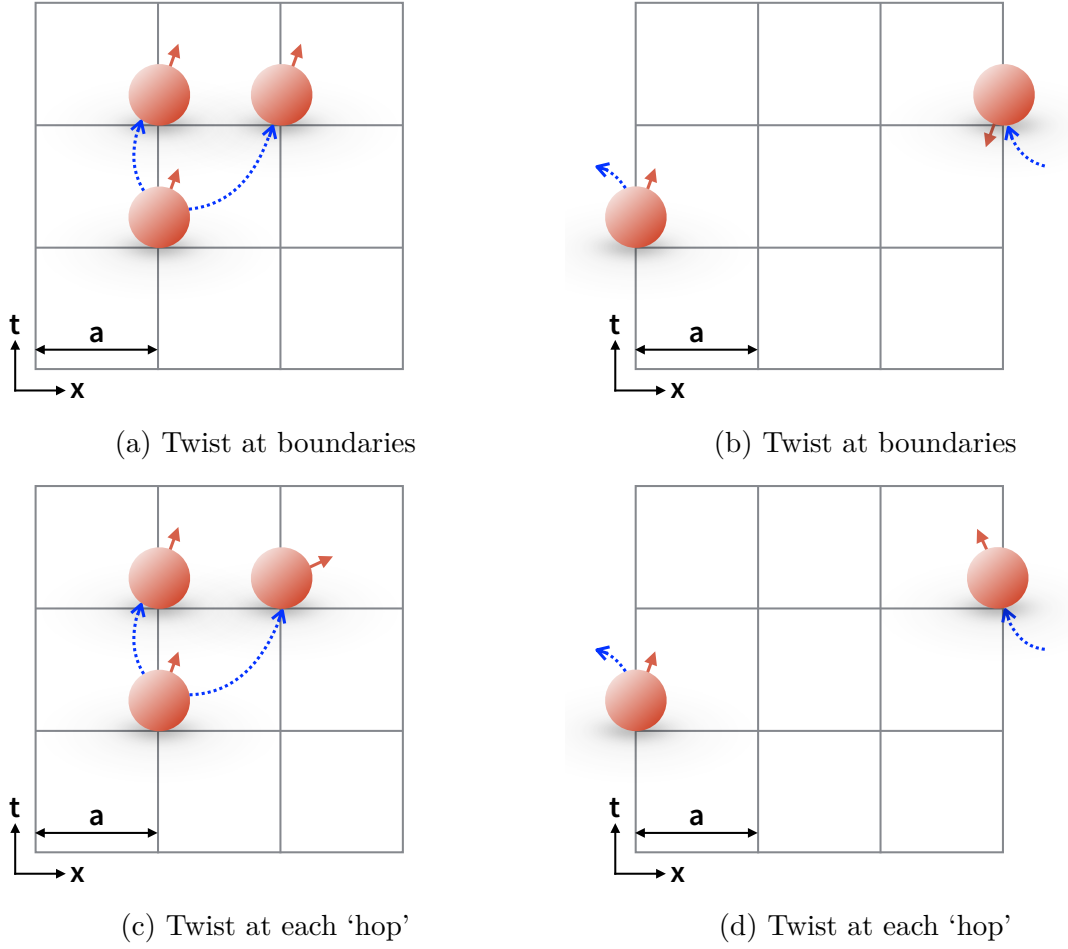


Figure 6.1: A demonstration of the different choices of twisted boundary basis for a simple 2-dimensional lattice with anti-periodic boundary conditions in spatial direction ($\phi = \pi$). The phase of the particles is represented by the direction of the red arrow.

momentum modes, which is proportional to the twist angles,

$$E_0^{(CM)} = \frac{\mathbf{P}_0^2}{2M_{CM}} = \frac{1}{2M_{CM}} \left(\sum_{i=1}^N \phi_i \right)^2. \quad (6.7)$$

This CM motion must be accounted for when comparing calculations of the relative binding energies of N -body systems. We note that twist angles subject to the constraint that $\phi_1 + \dots + \phi_N = 0$ will induce no CM motion.

To conclude this section, we consider the matrix-element of some arbitrary operator O using the basis in eq. (6.4),

$$\langle \mathbf{m}_1^{\phi_1}, \dots; \mathbf{m}_N^{\phi_N} | O | \mathbf{n}_1^{\phi_1}, \dots; \mathbf{n}_N^{\phi_N} \rangle. \quad (6.8)$$

As the operator O can be written in terms of products over creation and annihilation operators, it suffices to consider the following term,

$$\begin{aligned} \sum_{\mathbf{n}' \in \mathbb{Z}^3} a_i^\dagger(\mathbf{n}' + \mathbf{l}) a_i(\mathbf{n}') |\mathbf{n}^{\phi_i}\rangle_i &= \frac{1}{\sqrt{M^3}} \sum_{\mathbf{m} \in \mathbb{Z}^3} e^{i\phi_i \cdot (\mathbf{n} + N_L \mathbf{m}) / N_L} |\mathbf{n} + \mathbf{l} + N_L \mathbf{m}\rangle_i \\ &= |(\mathbf{n} + \mathbf{l})^{\phi_i}\rangle_i e^{-i\phi_i \cdot \mathbf{l} / N_L}. \end{aligned} \quad (6.9)$$

This term is off-diagonal in the basis of creation and annihilation operators, and represents a ‘hopping term’ from site \mathbf{n} to site $\mathbf{n} + \mathbf{l}$. Equation (6.9) explicitly shows how a particle picks up an incremental phase through such a translation between sites. More generally, any operator O with non zero off-diagonal matrix-elements in creation and annihilation operators will be modified by a phase within the ‘twisted basis’,

$$\begin{aligned} \langle \mathbf{m}_1^{\phi_1}, \dots; \mathbf{m}_N^{\phi_N} | O | \mathbf{n}_1^{\phi_1}, \dots; \mathbf{n}_N^{\phi_N} \rangle \\ = \langle \mathbf{m}_1^0, \dots; \mathbf{m}_N^0 | O | \mathbf{n}_1^0, \dots; \mathbf{n}_N^0 \rangle \exp \left(i \sum_{i=1}^N \phi_i / N_L \cdot (\mathbf{n}_i - \mathbf{m}_i) \right). \end{aligned} \quad (6.10)$$

Therefore the off-diagonal N -body matrix-element with TBCs are equal to the N -body matrix-element with PBCs multiplied by a phase that depends on the twist angles. It is important to stress that these matrix-elements still represent a hermitian matrix if the evaluated operator is hermitian as well. In other words, twisted boundaries do not induce (extra) sign oscillations.

6.3 Non-relativistic Finite-Volume effects

As already mentioned, the FV corrections as a function of twist angles have been previously determined in [147] in the form of quantization conditions. If one assumes the interaction is S -wave dominated and therefore ignores the mixing angle, and D -wave contributions (and higher), the FV corrections can be expanded in a series of exponentials with amplitudes that depend on the twist angles. We provide the three lowest orders in this expansion, with their accompanying twist angle dependence, in table 6.1. We will use these functional forms to perform our fits of our deuteron twist calculations in later sections.

An analogous expansion of the general three-body system is unfortunately not known. To motivate our functional form that we use for fitting our triton results, we present a non-relativistic derivation of FV corrections. This derivation follows that of [144, 145, 166–168] and provides the LO FV dependence of the binding energy. The exponential dependence of higher-order terms can, in principle, be determined using this method, but the exact form of the amplitude at each order is only known if the complete form of the asymptotic many-body wave function can be determined, which is not the case

here. As such, these unknown amplitudes are folded into our systematic uncertainties as described in later sections.

To arrive at our final expression of the LO FV twist-dependent correction for the three-body system, we first present the derivation for the two-body case as originally shown in [145]. For non-relativistic systems within a FV of spatial size L^3 with periodic boundary conditions, the physical quantities inside the box overlap with copies of themselves. As an example the potential represented in L^3 is given by

$$V_L(\mathbf{r}) = \sum_{\mathbf{n} \in \mathbb{Z}^3} V(\mathbf{r} + \mathbf{n}L), \quad \forall \mathbf{r} \in L^3, \quad (6.11)$$

where V is the infinite-volume representation of the potential. Accordingly a bound solution to the Schrödinger equation will also have a similar form of periodicity

$$\left(\hat{H}_0 + \hat{V}_L\right) |\psi_L\rangle = E_L(L) |\psi_L\rangle, \quad \langle \mathbf{r} + \mathbf{n}L | \psi_L \rangle = \langle \mathbf{r} | \psi_L \rangle. \quad (6.12)$$

As the FV solution should converge against the infinite-volume solution for increasing L , one can define the FV energy shift by its deviation from the infinite-volume solution,

$$\Delta E_L(L) := E_L(L) - E_\infty, \quad (6.13)$$

which should converge to zero for large L . When rewriting the FV wave function as periodic copies of the infinite-volume wave function plus corrections

$$|\psi_L\rangle = |\psi_0\rangle + \lambda |\epsilon\rangle, \quad \langle \mathbf{r} | \psi_0 \rangle := \sum_{\mathbf{n} \in \mathbb{Z}^3} \langle \mathbf{r} + \mathbf{n}L | \psi_\infty \rangle, \quad \forall \mathbf{r} \in L^3, \quad (6.14)$$

the FV energy shift can be rewritten with infinite-volume quantities only²

$$\Delta E_L(L) = \frac{\langle \psi_0 | \eta \rangle}{\langle \psi_0 | \psi_0 \rangle} + \lambda^* \frac{\langle \epsilon | \eta \rangle}{\langle \psi_0 | \psi_0 \rangle}. \quad (6.15)$$

The state $|\eta\rangle$ is the result of the difference operator $\hat{H}_L - E_\infty$ acting on the state $|\psi_0\rangle$. Note that this result is completely general in terms of the number of nucleons. For the two-body case gives one has

$$\begin{aligned} \langle \psi_0 | \eta \rangle &= \langle \psi_0 | \hat{H}_L - E_\infty | \psi_0 \rangle \\ &= \int_{L^3} d\mathbf{x}_1 \int_{L^3} d\mathbf{x}_2 \psi_0^*(\mathbf{x}_1, \mathbf{x}_2) [H_L(\mathbf{x}_1, \mathbf{x}_2) - E_\infty] \psi_0(\mathbf{x}_1, \mathbf{x}_2), \end{aligned} \quad (6.16)$$

where it is assumed that the Hamiltonian is local. As the next step, the infinite-volume

² It still depends on the FV Hamiltonian \hat{H}_L , which can be rewritten as copies of the infinite-volume Hamiltonian.

information are implemented according to eq. (6.14)

$$\begin{aligned} \langle \psi_0 | \eta \rangle &= \int d\mathbf{x}_1 d\mathbf{x}_2 \sum_{n_{i,j} \in \mathbb{Z}^3} \psi_\infty^*(\mathbf{x}_1 + n_{1,1}L, \mathbf{x}_2 + \mathbf{n}_{1,2}L) \\ &\quad [H_0 + V(\mathbf{x}_1 + n_{2,1}L, \mathbf{x}_2 + \mathbf{n}_{2,2}L) - E_\infty] \psi_\infty(\mathbf{x}_1 + n_{3,1}L, \mathbf{x}_2 + \mathbf{n}_{3,2}L). \end{aligned} \quad (6.17)$$

In the following, it is useful to transform to a relative Jacobi coordinate system $\mathbf{r} = \mathbf{x}_2 - \mathbf{x}_1$, $\mathbf{R} = (\mathbf{x}_1 + \mathbf{x}_2)/2$. Assuming that the center of mass motion is zero, which will be the case in all our calculations that follow, one has

$$\langle \psi_0 | \eta \rangle = \int_{L_r^3} d\mathbf{r} \sum_{n_i \in \mathbb{Z}_r^3} \psi_\infty^*(\mathbf{r} + \mathbf{n}_1L) [H_0 + V(\mathbf{r} + \mathbf{n}_2L) - E_\infty] \psi_\infty(\mathbf{r} + \mathbf{n}_3L). \quad (6.18)$$

The vectors \mathbf{n}_i are obtained by the individual two body coordinates, $\mathbf{n}_i = \mathbf{n}_{i,2} - \mathbf{n}_{i,1}$, and the subscript r denotes quantities that depend on these relative vectors. For $\mathbf{n}_2 = \mathbf{n}_3$ one has the infinite-volume Schrödinger operator acting on its infinite-volume solution, which provides the eigenvalue E_∞ . Thus only terms with unequal $\mathbf{n}_2, \mathbf{n}_3$ remain

$$\langle \psi_0 | \eta \rangle = \sum_{n_1, n_2 \in \mathbb{Z}} \sum_{n_3 \neq n_2} \int d\mathbf{r} \psi_\infty^*(\mathbf{r} + \mathbf{n}_1L) V(\mathbf{r} + \mathbf{n}_2L) \psi_\infty(\mathbf{r} + \mathbf{n}_3L). \quad (6.19)$$

As $\psi_\infty(r) \propto e^{-\kappa r}/\mu r$ (and $\kappa^2 = -2\mu E_\infty$ being the binding momentum with the relative mass μ) in asymptotic regions r outside of the finite range of the potential, i.e. $V(r) \approx 0$, the LO contributions of eq. (6.19) are given by $\mathbf{n}_1 = \mathbf{0} = \mathbf{n}_2$ and \mathbf{n}_3 being a unit vector (six different choices for three spacial dimensions and two directions each). Furthermore, the second term in eq. (6.15) containing the state $|\epsilon\rangle$ scales as $e^{-2\kappa r}$ and thus only appears at higher orders [166]. For the deuteron one finds

$$\Delta E_L^{(LO)}(L) = \sum_{|\mathbf{n}|=1} \int d\mathbf{r} \psi_\infty^*(\mathbf{r}) V(\mathbf{r}) \psi_\infty(\mathbf{r} + \mathbf{n}L). \quad (6.20)$$

The inclusion of arbitrary TBCs is realized by including a phase³ according to eq. (6.2)

$$\langle \mathbf{x}_1 + \mathbf{n}_1L, \mathbf{x}_2 + \mathbf{n}_2L | \psi_\infty \rangle \mapsto \langle \mathbf{x}_1, \mathbf{x}_2 | \psi_\infty \rangle e^{-i\phi_1 \cdot \mathbf{n}_1 - i\phi_2 \cdot \mathbf{n}_2}. \quad (6.21)$$

When executing the coordinate transformation, the relevant term dotted into the relative box vector $\mathbf{n} = \mathbf{n}_2 - \mathbf{n}_1$ is now given by $\boldsymbol{\theta} = (\boldsymbol{\phi}_2 - \boldsymbol{\phi}_1)/2$ and thus the relative wave function transforms as

$$\langle \mathbf{r} + \mathbf{n}L | \psi_\infty \rangle \mapsto \langle \mathbf{r} | \psi_\infty \rangle e^{-i\boldsymbol{\theta} \cdot \mathbf{n}}. \quad (6.22)$$

Thus, to obtain the LO FV energy shift for general TBCs, the previous result for periodic

³ Note the relative minus sign of the phase. This sign for the infinite-volume wave function phase ensures that the wave function on the lattice transforms as in eq. (6.2).

boundary conditions simply gets multiplied by this phase

$$\Delta E_L^{(LO)}(L, \boldsymbol{\theta}) = \sum_{|\mathbf{n}|=1} \int d\mathbf{r} \psi_\infty^*(\mathbf{r}) V(r) \psi_\infty(\mathbf{r} + \mathbf{n}L) e^{-i\boldsymbol{\theta} \cdot \mathbf{n}}. \quad (6.23)$$

The expression above only depends on the relative twist angle $\boldsymbol{\theta}$ since we choose twist angles that ensure zero CM motion, i.e. $\boldsymbol{\phi}_1 + \boldsymbol{\phi}_2 = 0$.

The exponential dependence of the FV corrections shown in [table 6.1](#) can be reproduced from this derivation, which in turn comes from the asymptotic behavior of the infinite-volume wave function. For example, in the case of the S-wave, one finds [\[145\]](#)

$$\Delta E_L^{(LO)}(L, \boldsymbol{\theta}) = -\frac{\sqrt{\pi} A_\kappa}{\mu} \sum_{|\mathbf{n}|=1} \psi_\infty^*(\mathbf{n}L) = -3 |A_\kappa|^2 \frac{e^{-\kappa L}}{\mu L}, \quad (6.24)$$

where the information of the wave function in the asymptotic region was used. Furthermore A_κ is the amplitude of the wave function which depends on properties of the interaction, such as the scattering length or the binding momentum $\kappa = \sqrt{-2\mu E_\infty}$.

Next-to-Leading Order (NLO) terms can be obtained by systematically allowing the displacement vector \mathbf{n} to be larger, e.g. the NLO corresponds to $|\mathbf{n}| = \sqrt{2}$ and so on. Though the box size scaling as well as the twist dependence of the FV corrections can be computed using this method, to obtain the size of the amplitudes A_κ of the exponential decay for FV energy shifts, the exact form of the asymptotic wave function needs to be known, which in turn depends on the specific form of the interaction.

Table 6.1: Twist dependence of different orders for the S-wave deuteron FV effects.

Order	Scaling in L	Twist dependence
LO	$\exp(-\kappa L)/L$	$2(\cos(\theta_x) + \cos(\theta_y) + \cos(\theta_z))$
NLO	$\exp(-\sqrt{2}\kappa L)/(\sqrt{2}L)$	$4(\cos(\theta_x)\cos(\theta_y) + \cos(\theta_x)\cos(\theta_z) + \cos(\theta_y)\cos(\theta_z))$
N ² LO	$\exp(-\sqrt{3}\kappa L)/(\sqrt{3}L)$	$8\cos(\theta_x)\cos(\theta_y)\cos(\theta_z)$

We now turn to the three-body system. Here the only difference is that the full potential now contains three pair interactions (neglecting the three-body interaction which, when included, gives rise to the same FV dependence). Thus the state $|\eta\rangle$ now produces the LO term [\[159\]](#)

$$\Delta E_L^{(LO)}(L, \{\boldsymbol{\phi}_i = \mathbf{0}\}) = \sum_{i=1}^3 \sum_{(\mathbf{n}_i, \mathbf{n}_j, \mathbf{n}_k) \in M_i} v(\mathbf{n}_i, \mathbf{n}_j, \mathbf{n}_k), \quad (6.25)$$

where $v(\mathbf{n}_i, \mathbf{n}_j, \mathbf{n}_k)$ is the three-body analog of eq. (6.19),

$$v(\mathbf{n}_i, \mathbf{n}_j, \mathbf{n}_k) := \int d^3\mathbf{x}_i \int d^3\mathbf{y}_i \psi_\infty^*(\mathbf{x}_i, \mathbf{y}_i) V_i(x_i) \psi_\infty(\mathbf{x}_i - (\mathbf{n}_j + \mathbf{n}_k)L, \mathbf{y}_i + \frac{1}{\sqrt{3}}(\mathbf{n}_j + \mathbf{n}_k - 2\mathbf{n}_i)L). \quad (6.26)$$

Here $\mathbf{x}_i = r_j - r_k$ and $\mathbf{x}_2 = (r_j + r_k - 2r_i)/\sqrt{3}$ are a particular choice of Jacobi coordinates which describe the three body system. The set M_i is chosen such that eq. (6.25) reassemble the LO difference of the FV Hamiltonian and the infinite-volume energy – e.g. the vectors are chosen such that the hyper radius $\rho^2 = \sum_i (\mathbf{r}_i + \mathbf{n}_i L)^2$ is minimal while $\mathbf{n}_j \neq \mathbf{n}_k$,

$$M_i := \min_\rho \left(\left\{ (\mathbf{n}_i, \mathbf{n}_j, \mathbf{n}_k) \in \mathbb{Z}^9 \mid \{i, j, k\} = \{1, 2, 3\} \text{ and } \mathbf{n}_j - \mathbf{n}_k \neq 0 \right\} \right). \quad (6.27)$$

Similar to the two-body case, an extension of this result to twisted boundaries is given by multiplying this expression with a phase containing a sum over all twist angles:

$$\Delta E_L^{(LO)}(\{\phi_i\}) = \sum_{i=1}^3 \sum_{(\mathbf{n}_i, \mathbf{n}_j, \mathbf{n}_k) \in M_i} v(\mathbf{n}_i, \mathbf{n}_j, \mathbf{n}_k) e^{-i \sum_{l=1}^3 \phi_l \cdot \mathbf{n}_l}, \quad (6.28)$$

where in this case we express the twist angles in the single-particle basis. Equation (6.28) gives the LO twist-dependent FV dependence of the three-body system. As we will numerically verify later, appropriate choices of twist angles can eliminate this LO dependence.

6.4 Applying twists within the NLEFT formalism

To study the effects of the FV on two- and three-body systems, we perform calculations on a discretized space-time lattice within a cubic volume. Our implementation follows closely that of the Nuclear Lattice Effective Field Theory (NLEFT) formalism. Though the NLEFT algorithm is well documented (for a review of NLEFT, see [33]), we provide a cursory description of our algorithm mainly to point out differences with past NLEFT calculations and to describe our implementation of TBCs within the NLEFT formalism.

6.4.1 Twists on the transfer matrix

To obtain results of nuclear observables on a lattice, one computes the trace of products of the transfer matrix, \mathcal{M} , which in our case is identified with the chiral interaction of nucleons. Formally, the transfer matrix in Euclidean time is given by the normal-ordered

exponential of the corresponding effective Hamiltonian,

$$\mathcal{M} := : \exp(-Ha_t) : . \quad (6.29)$$

The spectrum of H can be ascertained from eigenvalues of the transfer matrix \mathcal{M} ,

$$\mathcal{M} |\psi_n\rangle = \epsilon_n |\psi_n\rangle \quad , \quad \epsilon_0 > \epsilon_i, \forall i > 0. \quad (6.30)$$

In particular, the ground state energy E_0 of the system is related to the largest eigenvalue of \mathcal{M} , which we denote as ϵ_0 , and can be obtained through the following logarithmic derivative

$$E_0 = -\frac{\log(\epsilon_0)}{a_t}. \quad (6.31)$$

The Lagrangian which generates the transfer matrix contains the LO chiral contact interactions given in, for example, [127]. Effectively one obtains a two-body force as well as the one-pion exchange at LO,

$$V_X^{(LO)}(q) = V_{NN}^{(LO)}(q) + V_{\pi N}^{(LO)}(q), \quad (6.32)$$

where

$$V_{\pi N}^{(LO)}(q) = -\left(\frac{g_A}{2f_\pi}\right)^2 \frac{(\boldsymbol{\sigma}_1 \cdot \mathbf{q})(\boldsymbol{\sigma}_2 \cdot \mathbf{q})}{q^2 + m_\pi^2} (\tau_1 \cdot \tau_2). \quad (6.33)$$

Here the nucleon mass and the pion mass are set their physical value $m_N = 938.92$ MeV and $m_\pi = 134.98$ MeV. The pion decay constant is $f_\pi = 92.2$ MeV and the axial coupling has a strength of $g_A = 1.29$ respecting the Goldberger-Treiman discrepancy for representing the strong πNN -coupling. Furthermore the momentum $\mathbf{q} = \mathbf{p}' - \mathbf{p}$ is the nucleon momentum transfer. In this work, the contact potential was implemented using a gaussian-like smearing in momentum space similar to the one used in [32],

$$V_{NN}^{(LO)}(q) = (c_{SU4} + c_I \tau_1 \cdot \tau_2 + c_S \boldsymbol{\sigma}_1 \cdot \boldsymbol{\sigma}_2 + c_{SI} \tau_1 \cdot \tau_2 \boldsymbol{\sigma}_1 \cdot \boldsymbol{\sigma}_2) e^{-b_4 q^4}. \quad (6.34)$$

Furthermore, the coefficients $(c_{SU4}, c_S, c_I, c_{SI})$ were related to each other through the LO singlet and triplet coefficients C_S and C_T when evaluating nucleonic matrix-elements,

$$\begin{aligned} c_{SU4} &= \frac{1}{16} (3c_S + 3c_T) & c_S &= \frac{1}{16} (-3c_S + c_T) \\ c_I &= \frac{1}{16} (3c_S - c_T) & c_{SI} &= \frac{1}{16} (-c_S - c_T). \end{aligned} \quad (6.35)$$

The contact interactions were fitted to reproduce the deuteron binding energy as well as the 3S_1 scattering length. We tabulate their values, as well as other parameters relevant to our simulations, in table 6.2. To reduce the dimensionality of the problem, the spin breaking part of the pion exchange was assumed to be small and computations with this part were done for one specified spin channel only. This induced a small error when

Table 6.2: Numerical values of parameters used in our simulations.

$1/a_L$	$1/a_T$	c_S	c_T	$\Delta^{(n)}$	b_4
MeV	MeV	10^{-5} MeV^{-2}	10^{-5} MeV^{-2}	$\mathcal{O}(a^{2n})$	MeV^4
100	150	-4.2000	-6.0513	$\mathcal{O}(a^{2.4})$	0.07

comparing to the ‘experimental result’ at the order of 0.05 MeV for the deuteron.

Because of our ‘low-order’ interaction, we do not expect to have a perfect agreement for the three-body energy levels when compared to experiment. However, since the goal of this paper is to emphasize the dependence of the binding energy of few-body systems on FV corrections, this level of simplicity for the nucleon interactions is sufficient. As such, one should compare calculated energy levels in a fixed volume to their converged results for large (infinite) volumes instead of to the experimental results themselves.

Furthermore, at this order, our potential does not contain any derivatives acting on the nucleon coordinates and therefore does not induce translations on the nucleon states. The inclusion of TBCs is therefore realized by implementing eq. (6.10) for the kinetic Hamiltonian operators only.

As a final comment, we point out that the normal ordering of the transfer matrix for two nucleons $\mathcal{M}^{(2)}$ is exact at order a_t^2 ,

$$\mathcal{M}^{(2)} = \mathbb{1} - a_t \left(H_0^{(1)} + H_0^{(2)} + V^{(1,2)} \right) + a_t^2 H_0^{(1)} H_0^{(2)}. \quad (6.36)$$

To identify the CM motion of such a system, one can rewrite the absolute momenta of the individual particles as combinations of the CM momentum \mathbf{P} and the relative momentum \mathbf{q} ,

$$\mathcal{M}^{(2)} = \mathbb{1} - a_t \left(H_0^{(rel)} + H_0^{(CM)} + V^{(rel)} \right) + a_t^2 \left(\frac{1}{4} \left(H_0^{(rel)} + H_0^{(CM)} \right)^2 - \left(\frac{\mathbf{P} \cdot \mathbf{q}}{M_{CM}} \right)^2 \right). \quad (6.37)$$

Equation (6.37) shows that the term of second order in a_t couples CM motion to relative motion for non-zero CM momenta. Thus the procedure of subtracting the CM motion from the computed spectrum is more complicated. If one computes the spectrum of a two-nucleon system using general twisted boundaries, the energy eigenvalues of the transfer matrix are shifted by the non-zero CM contributions generated by these twists. This also holds true for more general N -body systems as well. For this current work we avoid the extra complication of non-zero CM coupling by utilizing twists that induce zero CM motion, which is determined by the following constraint,

$$\sum_{n=1}^N \phi_n = 0. \quad (6.38)$$

6.4.2 Identification of systematic errors and description of error analysis

NLEFT calculations employ Monte Carlo methods to estimate the ground state energy of N -body systems. Because such methods are intrinsically stochastic, the extracted energies have an associated statistical uncertainty. Because the dimensions of our systems are small compared to the stochastic computations, we can extract our energies via direct diagonalization of the transfer matrix. Our energies therefore have no statistical uncertainty.

Nevertheless, our results are not completely free of ‘errors’, as there still exists sources of theoretical and systematic uncertainties which can induce an effect on the final result. We enumerate these sources here and discuss each in turn below:

- FV effects
- Discretization errors
- Numerical/rounding errors
- Uncertainties associated with the fitting of lattice parameters (LECs on the lattice for NLEFT)

Since the aim of our study is the analysis of the FV dependence of the ground state binding energy, the uncertainties associated with the fitting procedure of LECs are neglected. We also neglect the errors associated with discretization, which are connected to the implementation of the derivatives and the fitting of the LECs. In LQCD, when one wants to rigorously compute physical observables, one also has to take the $a \rightarrow 0$ continuum limit. Here a careful accounting of the discretization errors is needed to perform a robust extrapolation. In NLEFT this procedure is more complicated since the interactions themselves are cutoff dependent at a given order in the effective expansion. In our case, we do not perform a continuum analysis since, again, we only focus on comparing the computed energies in a FV to their infinite-volume counterparts. As such, all our calculations use the same lattice spacing. However, even though we do not include any systematics due to finite lattice spacing in our error propagation, we do observe discretization errors, particularly for large twist angles. We defer this point to [section 6.7](#) where we discuss these observations in detail.

Our numerical errors are associated with the solving procedure only, which involves a Lanczos-like iteration for diagonalizing the transfer matrix and obtaining eigenvalues. This method of solving does not introduce any statistical errors. These numerical errors are of the order $\epsilon = e^{-Ea_t} \leq 10^{-5}$, which corresponds to an energy error budget of⁴

$$\delta E_\epsilon \leq \frac{\delta\epsilon}{a_T\epsilon} \simeq 0.002 \text{ MeV} . \quad (6.39)$$

⁴ For convenience in presentation, we will always denote FV effects using the symbol Δ , while errors and uncertainties used for the error estimation and propagation are labeled with the symbol δ .

In contrast to the previous errors, which are volume independent, we note that the FV energy corrections are only asymptotically diminishing if the potential vanishes within the cubic volume. Formally the FV needs to be of size $L/2 \gtrsim R$, where $V(R) \simeq 0$. Furthermore, for small boxes, NLO FV corrections become more relevant. As an example, the functional form of the LO FV expression of the energy shift for two-body states does not perfectly describe our numerical results. This discrepancy holds particularly true at small volumes since the complete energy shift includes higher order corrections described by several exponential functions of different exponents and amplitudes (see [table 6.1](#) for the deuteron case). Since one of our objectives of this study is to use calculations within small volumes to extract infinite-volume observables, we must explicitly take into account the errors from neglecting NLO (and higher) FV effects. We do this by estimating the size of the NLO FV systematic error, $\Delta E_L^{(NLO)}(L)$, and inflating our binding energy uncertainties by this amount when performing our fitting and error analysis

$$\Delta E_L^{(NLO)}(L, \phi) \mapsto \delta(\Delta E_L^{(LO)}(L, \phi)). \quad (6.40)$$

We stress that ΔE_L denotes the analytic form of the FV corrections, while quantities labeled with a small delta, δ , are treated as uncertainties of the computation and fitting procedure.

In principle, this NLO FV term should be interpreted as a weight for the fitting procedure which increases the relevance of data points at larger box sizes (where NLO FV effects become less important).

With the sources of errors described above, we parametrize the total *uncertainty* for the binding energy, $\delta(E_L - E_\infty)$, by the following terms,

$$\delta(E_L - E_\infty) \simeq \delta(\Delta E_L^{(LO)}(L, \phi)) + \delta E_\epsilon =: \delta E_L(L, \phi) + \delta E_\epsilon \quad (6.41)$$

Note that one can assume that the errors associated with this effect might be correlated, e.g., that each data point for a given twist is shifted in the same direction by the NLO FV corrections. To emphasize this, in the case of the deuteron, the known twist dependence of the NLO effects have also been computed.

Our final objective is to extract the infinite-volume binding energy E_∞ as well as the coefficients obtained by fitting the LO FV behavior $\Delta E_L^{(LO)}(L, \phi)$. To estimate the uncertainties of the fitted parameters, we employed a bootstrap-like procedure in our fitting process. We first performed calculations of binding energies at different values of L and twist angles ϕ (for the entire set of computations see [table 6.3](#)). We designate the collection of such results as D_0 . From D_0 we generated N_s new distributions D_i by sampling data points within D_0 assuming the data points were randomly distributed⁵ within the interval $\delta E(L)$. Finally, the spread in our fits of the new distributions D_i provided the variations in our fit parameters. Thus, the error as well as the mean value of the fitting

⁵ Quantitatively similar results have been obtained for a gaussian distribution and a uniform distribution. The propagated errors of the uniform distribution have slightly more spread.

parameters F were obtained by sampling the new distributions $P(F)$ of fitted parameters (which contain N_s data points),

$$\mu_F = \int dF F P(F), \quad \Delta F^{(\pm\alpha)} \leftrightarrow \int_{\mu_F}^{\mu_F \pm \Delta F^{(\pm\alpha)}} dF P(F) = \pm\alpha. \quad (6.42)$$

In our analysis, $\alpha = 0.341$ was chosen to give 1- σ confidence intervals. The overall χ^2 per degrees of freedom χ_{avg}^2 is given by an average over all individual fit χ^2 for each fit of distributions D_i .

$$\chi_{avg}^2 := \frac{1}{N_s} \sum_{i=1}^{N_s} \chi_{d.o.f.}^2(D_i) \quad (6.43)$$

6.5 Two-body system: the deuteron

As shown in [section 6.3](#) it is possible to analytically compute the FV corrections of the binding energy for a two-body system. In general this correction depends on the associated boundary angles $\boldsymbol{\theta}$ in relative coordinates, the box size L as well as infinite-volume quantities,

$$E_L - E_\infty \simeq \Delta E_L^{(LO)}(L, \boldsymbol{\theta}) = -\mathcal{N}^{(LO)} \frac{e^{-\kappa L}}{\kappa L} \sum_{i=1}^3 \cos(\theta_i). \quad (6.44)$$

Here κ is the binding momentum $\kappa^2 = -m_N E_\infty > 0$ and $\mathcal{N}^{(LO)}$ is a numerical amplitude which in general depends on the binding energy and the nucleon mass as well as the angular momentum quantum numbers. The boundary angle $\boldsymbol{\theta}$ is defined for the relative system and can be associated with the shift of the relative momentum. Thus the individual nucleon twists ϕ_i can be related to $\boldsymbol{\theta}$ by

$$\boldsymbol{\theta} = \frac{\phi_2 - \phi_1}{2}.$$

The NLO FV effect are parametrized as follows

$$\Delta E_L^{(NLO)}(L) = \frac{e^{-\kappa L}}{\kappa L} \left(A_1^{(NLO)}(\theta) e^{-(\sqrt{2}-1)\kappa L} + A_2^{(NLO)}(\theta) \frac{1}{\kappa L} \right). \quad (6.45)$$

Because the deuteron is mostly S -wave, the factor containing higher partial wave contributions is set to zero, $A_2^{(NLO)}(\theta) = 0$. Since the main goal of the paper is to analyze the three-body FV effects, where this dependence is not as trivial as in the deuteron case (and analytic forms are not in general known), we initially choose twist independent NLO errors. Such a choice is conservative and one in which we apply to the triton case as well. Furthermore, for error estimation, the error amplitude $A_1^{(NLO)}(\theta)$ is assumed to

Table 6.3: Parameters for the computation: number of twist angle combination, maximal box size, number of sampled distributions for the error analysis and the lattice spatial spacing.

System	N_Φ	$N_{L,max}$	N_s	a/fm
Deuteron	41	20	1000	1.97
Triton	121	7	1000	1.97

be of the order of the fitted amplitudes $\mathcal{N}^{(LO)}$, and we therefore set $A_1^{(NLO)}(0) = \mathcal{N}^{(LO)}$. We also choose twists that are anti-parallel to ensure zero CMS motion. Lastly each spatial direction is boosted equally by $\phi_2 = \phi = -\phi_1$ resulting in $\boldsymbol{\theta} = \boldsymbol{\phi}$. Therefore the FV energy correction amplitude is proportional to a single cosine factor depending on the twist angle ϕ ,

$$\Delta E_L^{LO}(L, \phi) = -3\mathcal{N}^{LO} \frac{e^{-\kappa L}}{\kappa L} \cos(\phi) =: A^{LO}(\phi) \frac{e^{-\kappa L}}{\kappa L}. \quad (6.46)$$

We have performed calculations using 41 different twist boundary conditions, each at multiple volumes $L = aN_L$ with N_L from 3 to 20 and a spatial lattice spacing $a = 1.97$ fm. In [fig. 6.2](#) we show a small subset of our twist calculations with their corresponding fits. The infinite-volume binding energy of the deuteron E_∞ as well as the coefficients in front of the exponential $A^{LO}(\phi)$, shown in [fig. 6.3](#), have been extracted from the computed data points using both a constrained fitting procedure where we enforce the same infinite-volume E_∞ but different amplitude coefficient for all distributions, and from individual fitting procedures where we make no constraint on E_∞ . The cumulative average of $N_s = 1000$ distributions within the data errors results in $\chi_{avg}^2 = 0.36$. The normalized amplitudes $\mathcal{A}(\phi) := A^{LO}(\phi)/A_{max}^{LO} = -\cos(\phi)$ with $A_{max}^{LO} = \max(|A(\phi)^{LO}|)$ have been fitted to $f(\phi) = c_1 \mathcal{A}(\phi) + c_2$ ([fig. 6.3](#)).

To emphasize the convergence of the twist averaging, we show in [fig. 6.4](#) the relative deviation of the extracted binding energies and the infinite-volume binding energy using various fit ranges (from $N_{L,start} = 4$ to $N_{L,end} = N_L$) for periodic boundary fits, periodic and anti-periodic constrained fits, and fits with ‘i-periodic’ twists. In [fig. 6.4](#), one can see results obtained without making use of the fitting error propagation – results which would have been obtained without making explicit use of the NLO FV corrections.

We find that aPBC + PBC average results improve and particularly i-Periodic Boundary Condition (iPBC) greatly improve the precision of FV results compared to PBC results. These findings are in complete agreement with those of [\[147\]](#) and gives us confidence that our implementation of twists is correctly done. Since the computational costs grow exponentially with the size of the box, studies computing ground state binding energies can greatly profit using such twists, particularly if similar conditions hold for more complicated N -body systems.

Examination of [fig. 6.3](#) shows that, for the two-body case with zero induced CM twists,

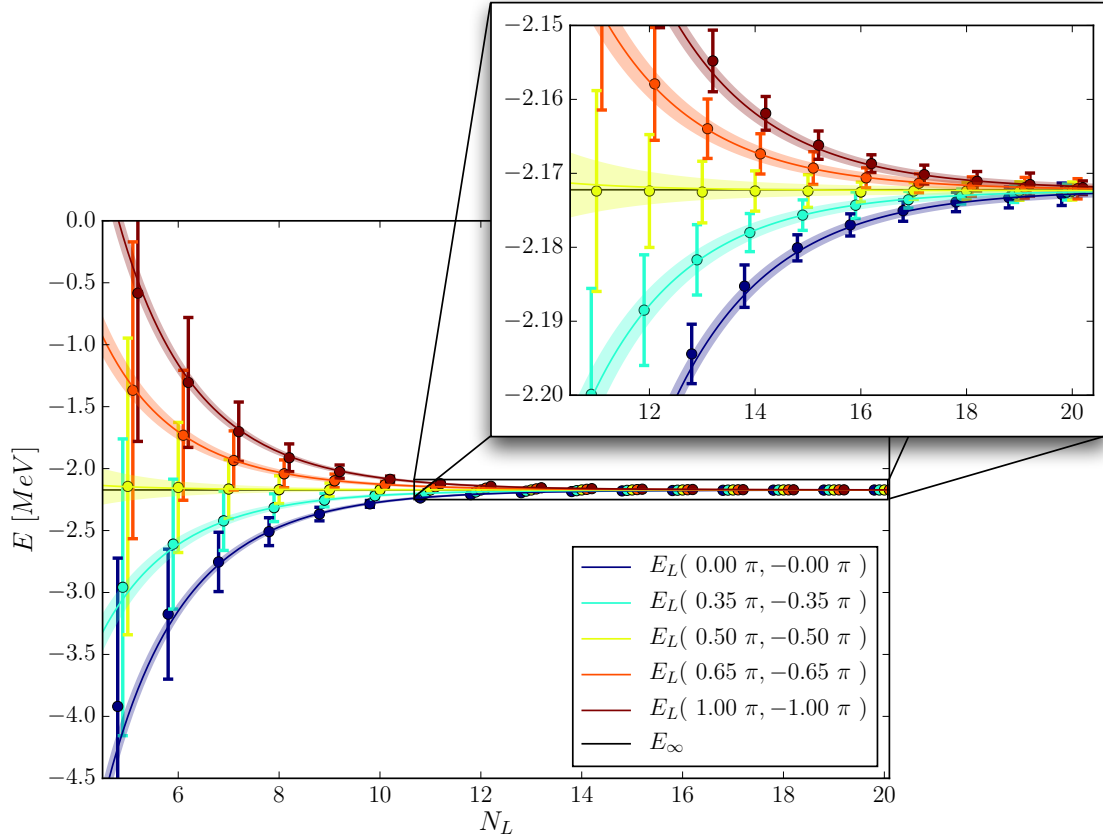


Figure 6.2: Selected individual fits of two-body binding energy depending on FV for $L = aN_L$ with N_L from 4 to 20 and $a = 1.97$ fm. $E_B = \left(-2.172^{+0.000}_{-0.001}\right)$ MeV and $\chi^2_{avg} = 0.36$ have been similar for each twist configuration according to error propagation. The error bars and error bands correspond to $1\text{-}\sigma$. Data points and bands are slightly shifted in N_L direction for visualization purposes.

the iPBCs are superior to an average over several twists. We notice an apparent offset in our calculations, particularly around $\phi = \pi$, which can be seen by comparing the data points to the analytic red line in fig. 6.3. Indeed, an integration over all twists points in fig. 6.3 results in an offset at the order $\delta E_\infty = -0.04 \times \delta \Delta E_L^{LO}(L, 0)$. This offset leads to a larger uncertainty in our extracted energies, compared with iPBCs, even when averaging over small sets of twists, as shown in fig. 6.4. As we show in the next section, similar offsets are also seen in our three-body calculations. We return to the subject of this offset in section 6.7.

Since the NLO FV twist dependence for the deuteron is analytically known, we have also performed fits using this dependence for several fitting ranges. This analysis is based on

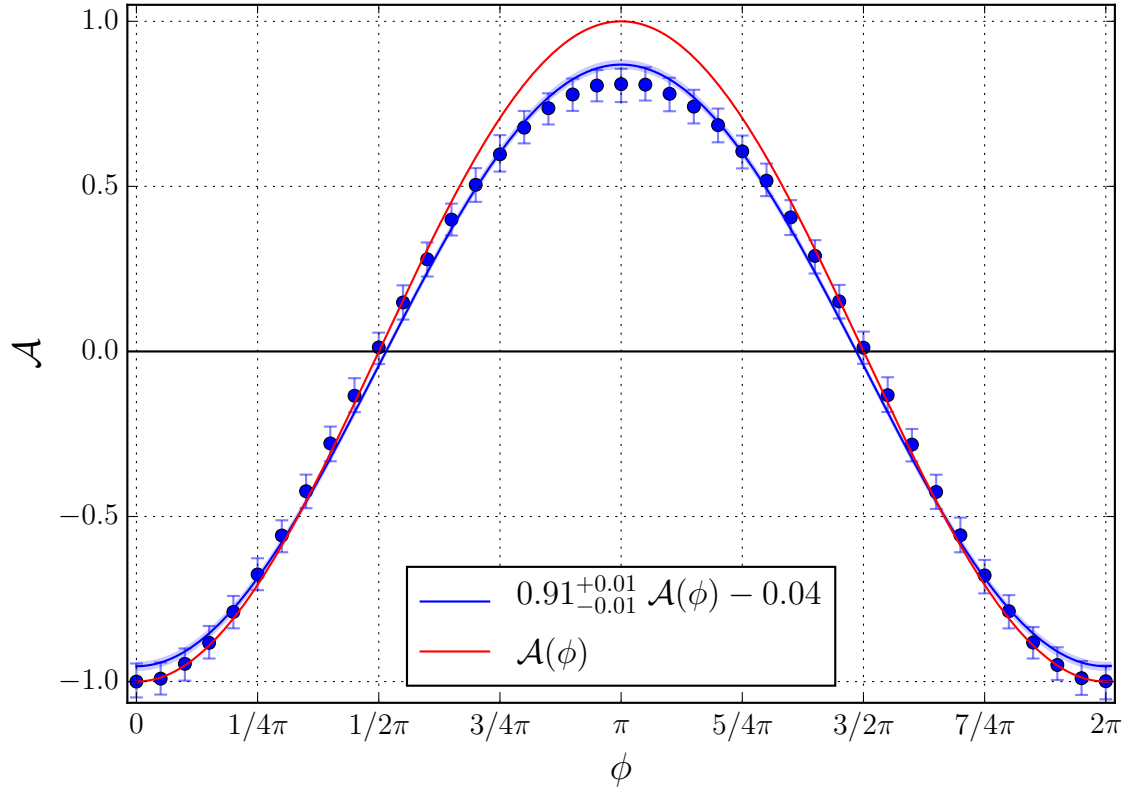


Figure 6.3: Fit of two-body coefficient $\mathcal{A}(\phi)$ depending on relative twist angle $(\phi_1, \phi_2) = (\phi, -\phi)$ with $\chi_{avg}^2 = 0.92$. The blue line correspond to a fit of the form $f(\phi) = c_1 \mathcal{A}(\phi) + c_2$, while the red line is the theoretical prediction $\mathcal{A}(\phi) = -\cos(\phi)$. The error bars and error bands correspond to $1\text{-}\sigma$.

the error propagation explained in [section 6.4.2](#), where the NLO twist dependence and scaling of the FV effects are extracted from [table 6.1](#). Again the deuteron is assumed to be purely S -wave and in this case the Next-to-Next-to-Leading Order (N²LO) is assumed to be twist independent. We provide the fit results in [fig. 6.5](#) and the corresponding fitting errors in [fig. 6.6](#). We find that the obtained data interval is consistent with the infinite-volume result for each fitting range (though the errors, especially for small ranges, are exceptionally large). Nevertheless the size of the uncertainties for an aPBC plus PBC average are just slightly smaller than the uncertainties for just PBCs. This is the case since for both twists the error amplitude $A^{NLO_1}(\phi)$ are maximal in ϕ . For the combined fit one nevertheless has relatively more data points than parameters and thus the total error of the fitted parameters reduced. For the iPBCs, on the other hand, the NLO errors are entirely removed, and thus accuracy is better compared to the previous twists.

Although our individual fits of E_∞ at different volumes are consistent within uncertainties, as shown in [fig. 6.6](#), we find that our χ_{avg}^2 per degree of freedom are typically below one ($\chi_{avg}^2 \approx 1/3$). As expected, this indicates that our results are correlated and/or our errors have been overestimated. Indeed, one source of overestimation comes from the fact

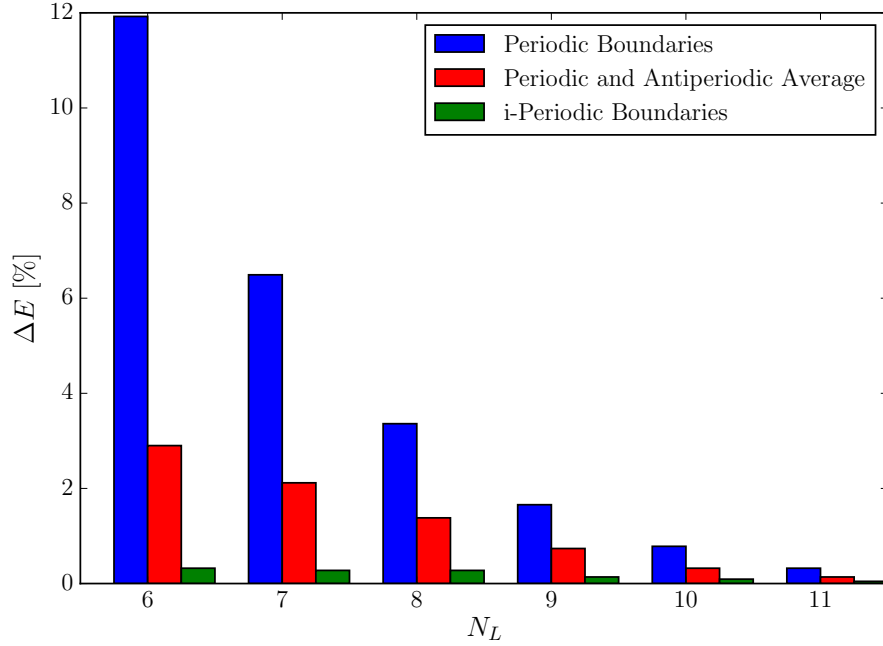


Figure 6.4: Relative error of the extracted binding energy for a given fit range compared to the infinite-volume result. This fit ignores the NLO FV errors.

that we have conservatively assigned the magnitudes of the error to be roughly of the same size as the fitted amplitude: $A_1^{(NLO)}(0) \approx \mathcal{N}^{LO}$. Nevertheless, these results allow a quantitative comparison since the overestimation is multiplicative and thus the relative size of the errors stay the same. For $N_L \geq 15$, as a result of the analysis, the FV errors are of the size of the numerical precision and therefore twist independent.

6.6 Three-body case: the triton

The exact form of FV corrections for the general three-body case has not been determined to date. In [159], however, the three-body LO FV corrections for three identical particles with PBCs ($\phi_i = 0$ for $i = 1, 2, 3$) in the unitary limit was derived,

$$\Delta E_L^{LO}(L, \{\phi_i = \mathbf{0}\}) = \mathcal{N}_{PB}^{LO} \frac{\exp\left(-\frac{2}{\sqrt{3}}\kappa L\right)}{(\kappa L)^{3/2}}. \quad (6.47)$$

Though this form is not rigorously applicable for our system (our system is not at the unitary limit), it is sufficient for our analysis we describe below. We stress that our main conclusions of this section do not depend on the specific FV functional dependence shown in eq. (6.47).

As was done in the two-body case, we assume that the NLO FV corrections come from

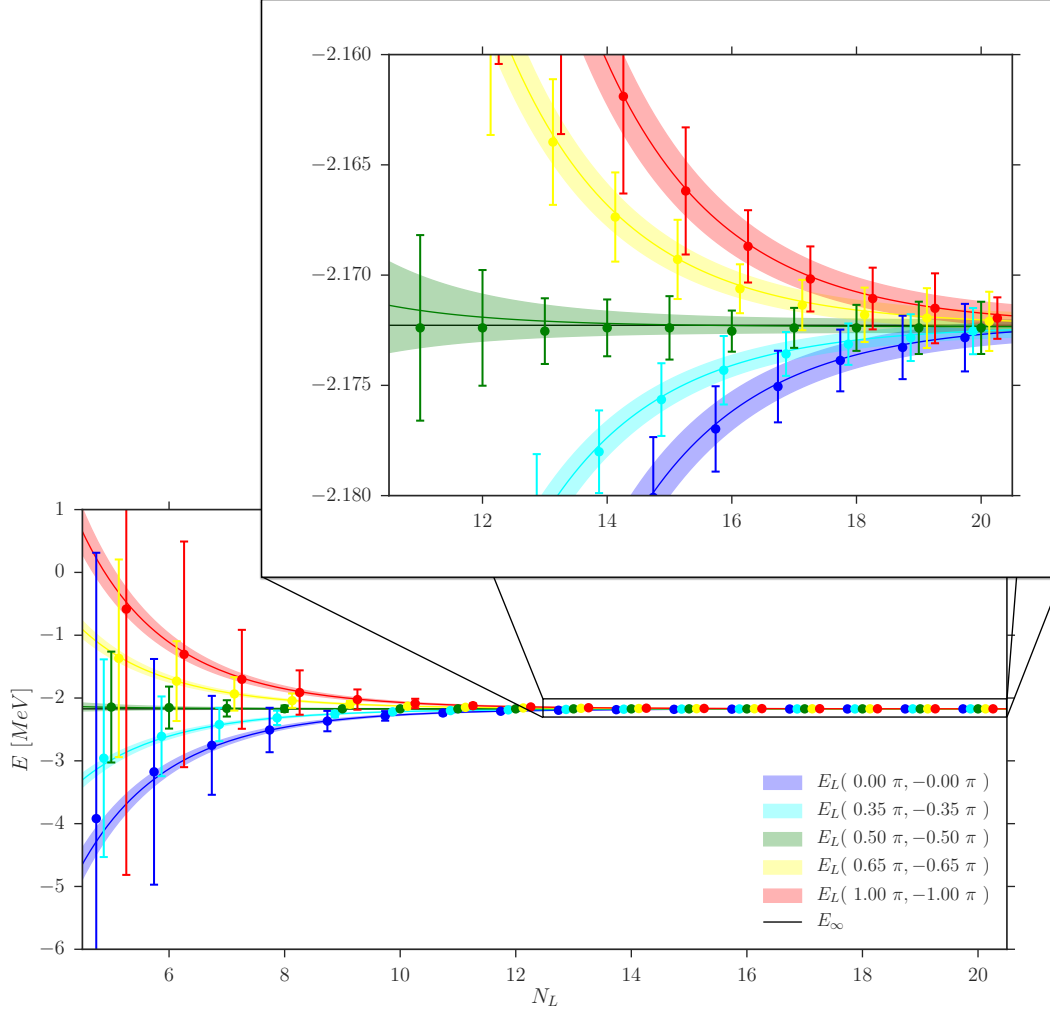


Figure 6.5: Example fits for a fit range from $N_L \in [4, 20]$ with $\chi_{avg}^2 = 0.33$. Fit errors include twist dependent NLO FV correction information. The error bars correspond to $1\text{-}\sigma$.

additional powers of $(\kappa L)^{-1}$ for different partial-wave channels as well as suppressed terms coming from the overlap of diagonally shifted images of the wave functions⁶ with the original wave function,

$$\Delta E_L^{(NLO)}(L, \{\phi_i = \mathbf{0}\}) = \mathcal{N}_{1,PB}^{(NLO)} \frac{\exp\left(-\sqrt{\frac{8}{3}}\kappa L\right)}{(\kappa L)^{3/2}} + \mathcal{N}_{2,PB}^{(NLO)} \frac{\exp\left(-\sqrt{\frac{2}{3}}\kappa L\right)}{(\kappa L)^{5/2}}. \quad (6.48)$$

We also assume the amplitude to the NLO corrections to be of the size of the LO amplitude and again set $\mathcal{N}_{PB}^{(LO)} = \mathcal{N}_{i,PB}^{(NLO)}$ in the expressions above.

As discussed in [section 6.3](#), the effects of general TBCs in an N -body system is obtained

⁶ The argument of the wave function gets shifted by one box size in two different directions:
 $\psi(\mathbf{n}) \mapsto \psi(\mathbf{n} + (\mathbf{e}_1 + \mathbf{e}_2)L)$

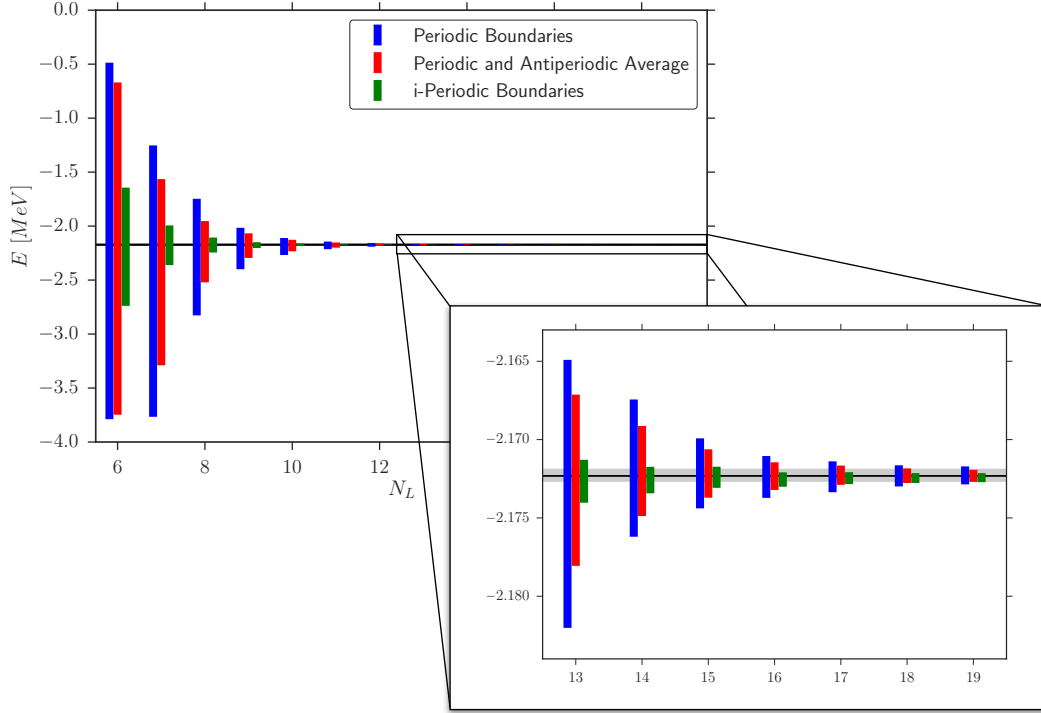


Figure 6.6: Fit range dependence of deuteron binding energy. Fit errors include twist dependent NLO FV correction information. For each individual fit, the χ^2_{avg} has been around $\chi^2_{avg} = 0.33 \pm 0.01$. The error bars correspond to $1\text{-}\sigma$.

by multiplying the wave function in a box by a phase related to the twists whenever one leaves the box (eq. (6.28))

$$\Delta E_L^{(LO)}(\{\phi_i\}) = \sum_{i=1}^3 \sum_{(\mathbf{n}_i, \mathbf{n}_j, \mathbf{n}_k) \in M_i} v(\mathbf{n}_i, \mathbf{n}_j, \mathbf{n}_k) e^{i \sum_{l=1}^3 \phi_l \cdot \mathbf{n}_l}.$$

Instead of a factor of $3 \times 2 \times 2 \times 3$ (spatial dimensions \times sign of vector \times permutations of (j, k) for fixed i \times permutations of i) when executing the sum over all neighboring lattice vectors, the restriction $(\mathbf{n}_i, \mathbf{n}_j, \mathbf{n}_k) \in M_i$ [eq. (6.27)] reduces the sum to factors involving cosines that depend on the twist angles ⁷,

⁷ It is interesting to study this scenario in the N -body case as well. Since one expects no directional dependence of the LO FV energy shift in the unitary limit of N -identical bosons, one can assume that the general twist dependence of this shift can be expressed by eq. (6.50) when changing 3 to N . We are currently studying the twist dependence in the N -body fermionic case [169].

$$\Delta E_L^{(LO)}(L, \{\phi_i\}) = A^{(LO)}(\{\phi_i\}) \frac{\exp\left(-\frac{2}{\sqrt{3}}\kappa L\right)}{(\kappa L)^{3/2}} \quad (6.49)$$

$$A^{(LO)}(\{\phi_i\}) = \frac{\mathcal{N}_{PB}^{(LO)}}{9} \sum_{i,j=1}^3 \cos(\mathbf{e}_j \cdot \phi_i). \quad (6.50)$$

Again, as in the two-body case, we restrict ourselves to equal boosts in each spatial direction $\mathbf{e}_j \cdot \phi_i = \phi_i \in [0, 2\pi]$ and the sum of all twist angles is constrained to zero to ensure zero CM motion. To analyze the twist-angle dependence of the LO FV corrections, calculations were performed using three different angle orientations,

$$(\phi_1, \phi_2, \phi_3) = (\phi, -\phi, 0), (\phi, \phi, -2\phi), (\phi, 2\phi, -3\phi) \quad (6.51)$$

The number of different computed configurations can be found in [table 6.3](#), selected energy fits from our calculated distributions are displayed in [fig. 6.7](#) and the corresponding amplitudes coming from all our fits as well as their predictions can be found in [fig. 6.8](#).

In contrast to the two-body case, the extrapolated infinite-volume energy, as well as their average χ_{avg}^2 of individual fits, depend on the twists, as can be seen by comparing the top and bottom panels of [fig. 6.8](#). This is to be expected since we have used in our fits a FV functional form ([eq. \(6.47\)](#)) that does not represent our system exactly. Errors in the fitted amplitudes and energies can, and most certainly are, correlated in this case (compare top and center panels of [fig. 6.8](#)). We can explicitly see how such correlations come about by considering the following example. Let us assume that the exact LO FV expression is parametrized by

$$\Delta E_{L,exact}^{(LO)}(L, \phi) = A^{(LO)}(\phi) \left[\Delta E_{L,used}^{(LO)}(L, 0) + \Delta E_{L,corr}^{(LO)}(L) \right],$$

where $\Delta E_{L,used}^{(LO)}(L, 0)$ is given by [eq. \(6.47\)](#) and $\Delta E_{L,corr}^{(LO)}(L)$ its correction. The extracted infinite-volume energy will have an explicit dependence on the twist angles since

$$\begin{aligned} E(L, \phi) &= E_\infty + \Delta E_{L,exact}^{(LO)}(L, \phi) + \delta E(L) \\ &= E_\infty + A^{(LO)}(\phi) \left[\Delta E_{L,used}^{(LO)}(L, 0) + \Delta E_{L,corr}^{(LO)}(L) \right] + \delta E(L) \end{aligned} \quad (6.52)$$

$$= E_\infty + \delta E_\infty(L, \phi) + \Delta E_{L,used}^{(LO)}(L, \phi) + \delta E(L). \quad (6.53)$$

The expression above shows how errors in the form of the fitting function $\Delta E_{L,used}^{(LO)}$ can induce twist angle dependence and correlations $\delta E_\infty(L, \phi)$ on our extrapolated energies E_∞ . Comparing [eqs. \(6.52\)](#) and [\(6.53\)](#), we note that as $A^{(LO)}(\phi) \rightarrow 0$, one has $\delta E_\infty(L, \phi) \rightarrow 0$. Thus the fitting expression, regardless of form, becomes exact in this limit.

Returning to [fig. 6.7](#), we find that the shape of the LO FV corrections is similar to that of the two-body deuteron system. In particular, one finds energies converging from

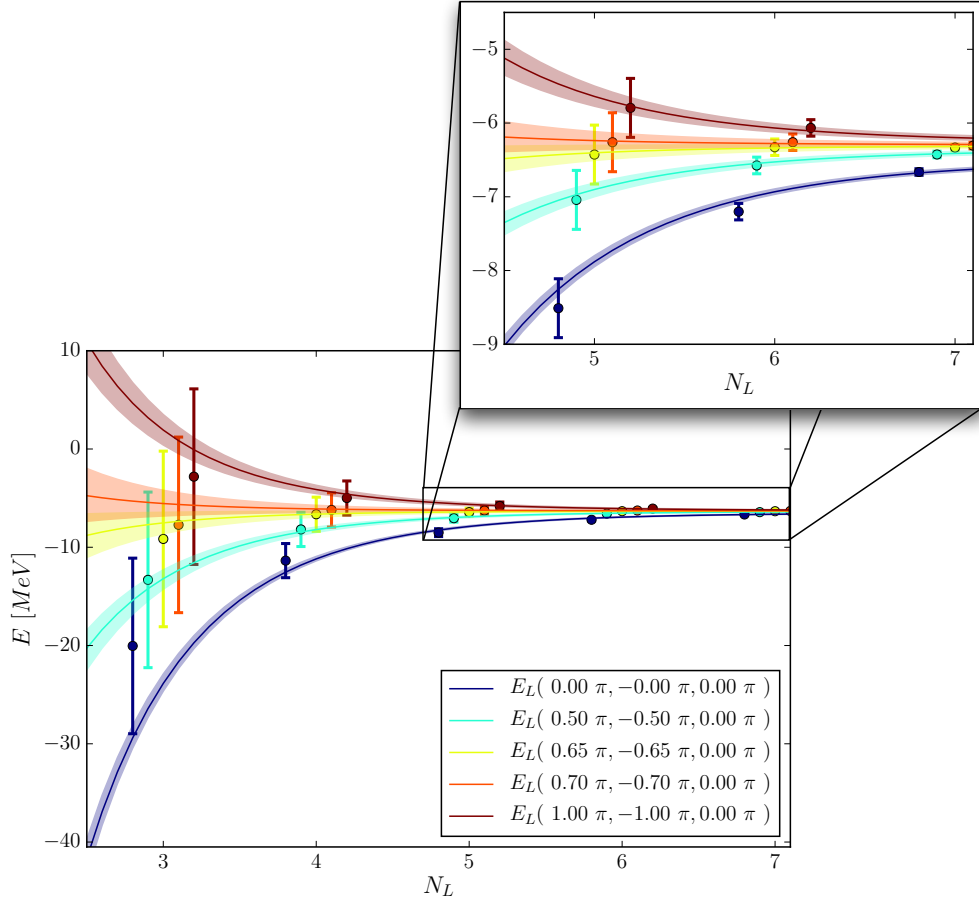


Figure 6.7: Individually selected three-body fits for a fit range from $N_L \in [3, 7]$ which corresponds to $L = aN_L$ with $a = 1.97$ fm. Extracted infinite-volume energies, amplitudes and average χ^2 can be extracted from fig. 6.8. The error bars and error bands correspond to 1- σ . Data points and bands are slightly shifted in N_L direction for visualization purposes.

below and above the infinite-volume energy. However, because of the dimensionality of the problem, the accessible box sizes were not sufficiently large to enter the asymptotic region where the error bands overlap.

The amplitude fits in the center panel of fig. 6.8 suggests that certain twist angle combinations have significantly reduced FV corrections (i.e. when $\mathcal{A}(\phi) := -A(\phi)/A(0) = 0$), similar to the iPBC case in the two-body system⁸. Indeed, from the predicted shape of the amplitude twist dependence in eqs. (6.49) and (6.50), the three-body analogue to

⁸ The term ‘i-periodic’ in the two-body case refers to angles that produce a purely imaginary phase (i.e. $\theta = \pi/2$), and that also significantly reduce LO FV effects. For the three-body case, we designate the term ‘i-periodic analogues’ to refer to twist angles that eliminate the LO FV effects, but are not in general purely imaginary.

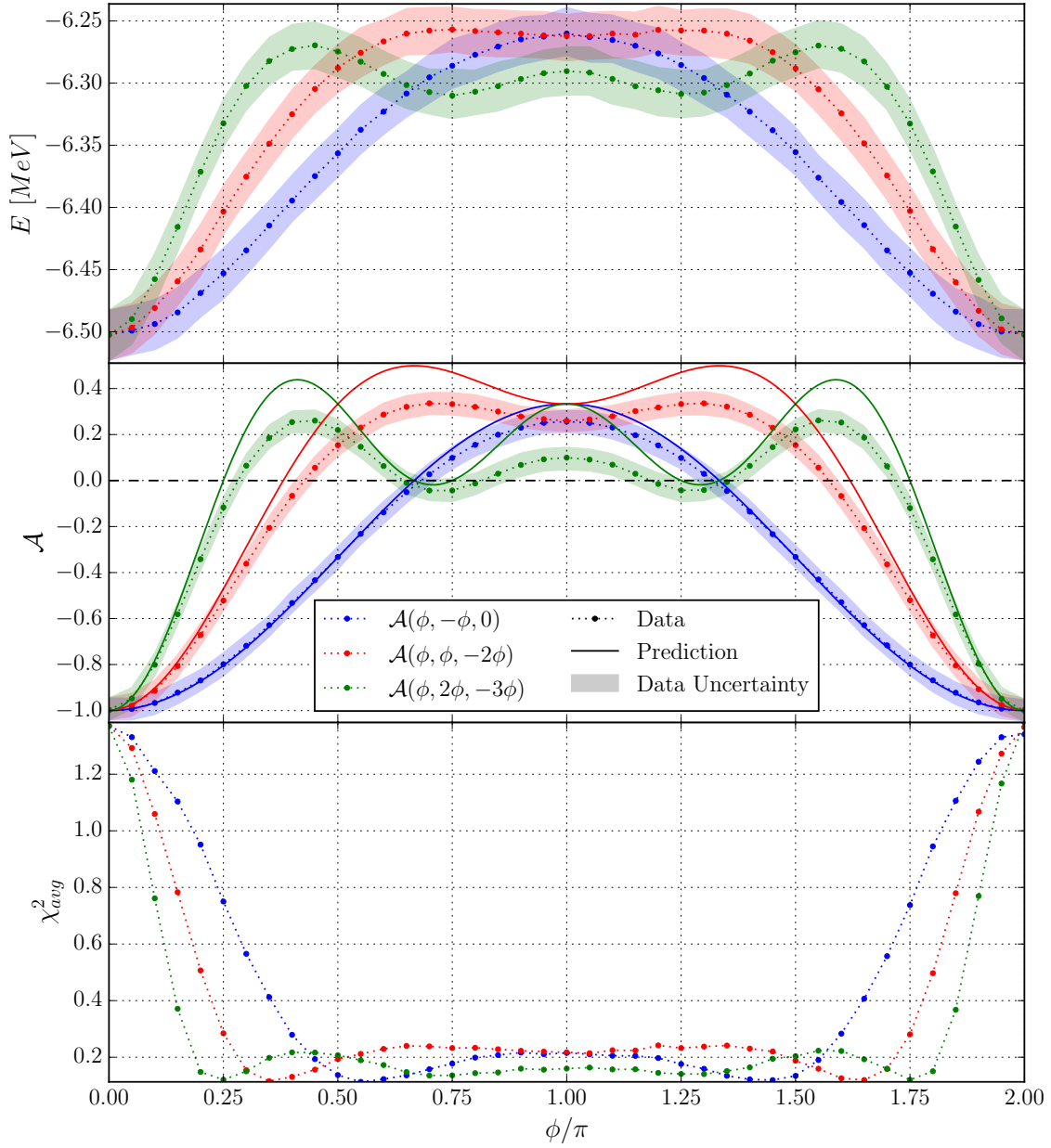


Figure 6.8: Triton results for individual twist fitting procedure. The figure contains the individually extracted infinite-volume energy results (top), the amplitudes of the LO FV behavior (center) as well as the average χ_{avg}^2 (bottom) for each fit in a fitting range from $N_L \in [3, 7]$. The data points are obtained for three different angle configurations (red, blue, green). Data points correspond to dots (and are connected via dotted lines), the uncertainties of the data points correspond to the bands, and the solid lines are the predictions for the behavior of the amplitude. The error bands correspond to an 1- σ confidence interval of the propagated errors.

iPBCs occurs for twist angles that solve the following equation,

$$\sum_{j=1}^3 \cos(\boldsymbol{\phi}_1 \cdot \mathbf{e}_j) + \cos(\boldsymbol{\phi}_2 \cdot \mathbf{e}_j) + \cos((\boldsymbol{\phi}_1 + \boldsymbol{\phi}_2) \cdot \mathbf{e}_j) = 0. \quad (6.54)$$

If one twists each spatial direction equivalently, this reduces to

$$\cos(\phi_1) + \cos(\phi_2) + \cos(\phi_1 + \phi_2) = 0. \quad (6.55)$$

Note that the analogue to iPBC twists are not unique in the three-body system, as opposed to the deuteron case. In particular, there is a one-dimensional set of values for ϕ which eliminate the LO FV effect. In [fig. 6.8](#), for example, the iPBC analogue twist angles correspond to the values of ϕ where the solid curves of $\mathcal{A}(\phi) = 0$ (center panel).

As found in the deuteron case, we point out here that our numerical results deviate from their predictions in the regions of higher twist momenta, e.g. for the blue $\phi_1 = -\phi_2$, $\phi_3 = 0$ line, this data is inconsistent within errors with the prediction at twist angles around $p_{\phi_1} = 0.8 \pi/L$. For the red $\phi_1 = \phi_2$, $\phi_3 = 2\phi_1$ and the green $\phi_2 = 2\phi_1$, $\phi_3 = 3\phi_1$ line, the discrepancies are prominent once $p_{\phi_3} = 0.6 \pi/L$ and $p_{\phi_3} = 0.6 \pi/L$ respectively. We return to this topic in [section 6.7](#).

In [fig. 6.9](#) we give a contour plot which shows all the allowed iPBC analog twist values for the three-body system investigated in this paper. The contour itself represents the left-hand-side of [eq. \(6.55\)](#) and thus the predicted relative amplitude of the LO FV corrections. The maximal values correspond to the dark blue regions (periodic and other boundaries) and the minima to the white regions ('i-periodic' boundaries). The solid line corresponds to the exact solutions of [eq. \(6.55\)](#) and the points are the locations of pairs of (ϕ_1, ϕ_2) which were used for in our numerical investigations. The larger points give the numerically extracted twist angles that are consistent (within errors) with $\mathcal{A}(\phi) = 0$, results which are valid to all orders of the FV corrections. The data points of [fig. 6.9](#) use the same color designations as in [fig. 6.8](#). The results in the middle panel of [fig. 6.8](#) represent cross-sections of [fig. 6.9](#) along the dotted lines and thus the data points share a 2π periodicity.

Similar to the two-body case, we find that a complete averaging of twists does not entirely remove FV effects in the three-body system.

6.7 Comment on discretization effects

As already pointed out, we find systematic differences between our numerical results and their predictions in regions of large twist angles $\phi \gtrsim 0.6 \pi$, as can be seen from [figs. 6.3](#) and [6.8](#). Also for the three-body case, due to the periodicity of the twist angles, one would expect all our numerical results to be equivalent at $\phi = \pi$, in addition to having an agreement with their analytic predictions. We now present arguments that show that these discrepancies originate most likely from discretization errors. Because the dispersion relation for free particles in a discrete space follows cosine and sine functions instead of the analytic $p^2/2m$, depending on the implementation of the derivatives, derivations

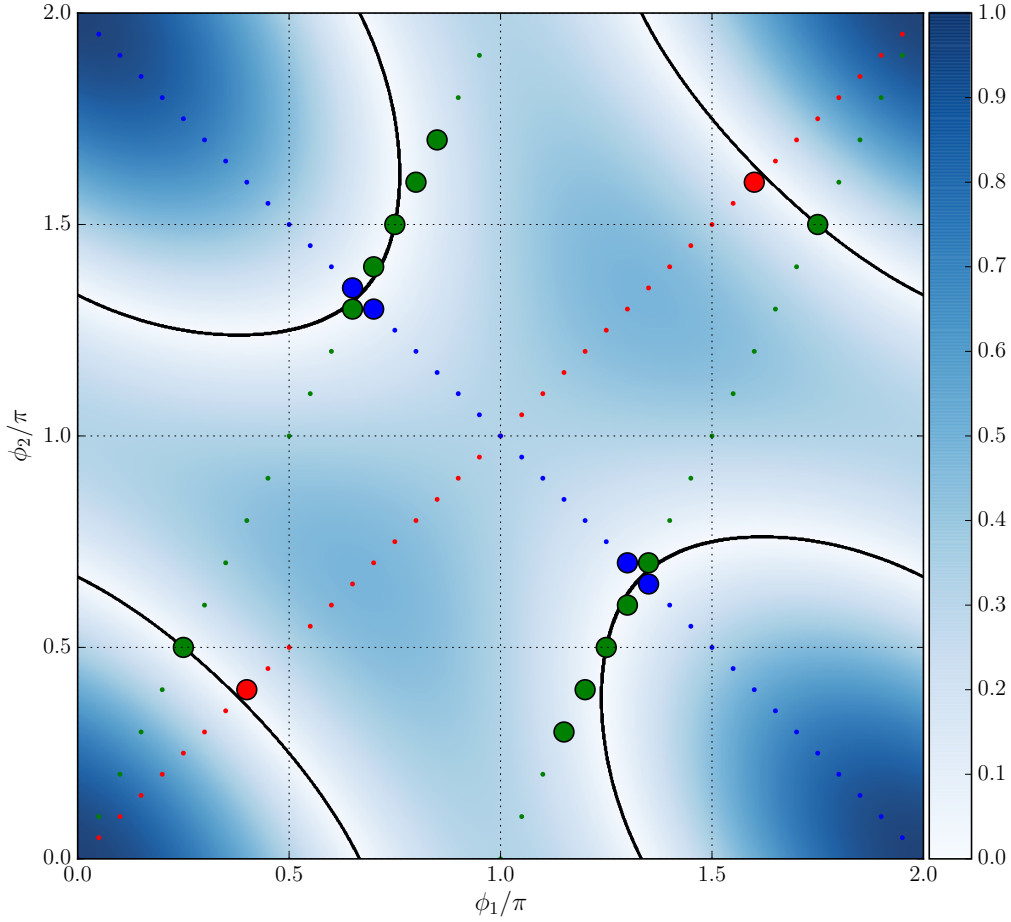


Figure 6.9: Contour plot for three-body iPBC analogues. The contour expresses the relative amplitude of the predicted analytic LO FV corrections depending on the twists: $\mathcal{A}^{(LO)}(\phi_1, \phi_2, -\phi_1 - \phi_2)$ (eq. (6.50)). The black line correspond to the solutions for the three-body iPBC analogues: $\mathcal{A}^{(LO)} = 0$ (eq. (6.55)) and the points (both large and small) represent the twist angles we have used in our study. The larger points have been identified with the numerically found iPBC analogues extracted from fig. 6.8 (see text). As in fig. 6.8 the color code represents data for a fixed ratio of ϕ_2/ϕ_1 : (blue, red, green) = $(-1, 1, 2)$.

are expected to appear at higher orders. Consider the following picture of a simple discrete ‘one-step’ derivative in the context of TBCs

$$\partial_{x,a}^2 f(\mathbf{r}) := \frac{1}{a^2} \left(e^{i\phi_x a/L} f(\mathbf{r} + a\mathbf{e}_x) - 2f(\mathbf{r}) + e^{-i\phi_x a/L} f(\mathbf{r} - a\mathbf{e}_x) \right). \quad (6.56)$$

If one now computes the expectation value of the momentum operator squared $\langle p_{x,a}^2 \rangle$ for a given wave function ψ and twist angle ϕ , then expands this wave function and rewrites this with the continuum expectation values of the momentum operator for periodic boundaries

$$\langle p_x^n \rangle := \int dx \psi^*(\mathbf{x}) (-i\partial_x^n) \psi(x), \quad (6.57)$$

one finds that

$$\langle p_{x,a}^{\phi^2} \rangle = \langle (p_x + \phi_x/L)^2 \rangle - \frac{a^2}{12} \langle (p_x + \phi_x/L)^4 \rangle + \mathcal{O}(a^4). \quad (6.58)$$

As the first term in eq. (6.58) can be identified with the continuum limit twist momentum, the expectation value of the momentum operator squared obtains a negative shift for a non-zero lattice spacing. Such a shift scales as $a^2(\phi/L)^2$ plus higher terms for a ‘single-step’ derivative. These results are entirely consistent with our findings of a reduced offset in our numerical results for large shift angles since in our computations the potential was purely local and the only structure affected by twists was the kinetic energy operator. Therefore the total energy of all the computed states experience a shift to more negative values compared to the continuum limit – the larger the twist momentum (modulo periodicity), the bigger the shift. As this effect is most dominant for small boxes and the FV shift exponentially decays as well, the magnitude of the exponential decay is eventually smaller compared to the result in a continuous space. Definitive proof that our offsets are indeed due to discretization effects would require calculations performed at smaller lattice spacings, as well as the use of higher order improved differencing schemes. We are actively investigating this.

6.8 Conclusion

In this paper, we investigated the effects of TBCs on two- and three-body nuclear systems. We performed investigations using the NLEFT formalism, with appropriate modifications to affect twisted boundaries and utilized a simplified NN interaction. We benchmarked our two-body results to known analytic results from [147], and extended the analysis in the two-body sector to additional twist angles. We performed the same analysis to the three-body (triton) sector, where we derived the three-body iPBC analog quantization condition and numerically verified their corresponding FV cancellations. As opposed to the deuteron case, we found multiple iPBC analog twist possibilities in the three-body sector.

We have attempted a detailed analysis of our fitting and extraction routines, where we enumerate all (known) sources of systematic errors. Where possible, we assign realistic errors or very conservative errors in our error budget. We find that, in both two-body and three-body systems, results obtained with iPBC analogs were superior to twist averaging, under the constraint that the allowed twists preserved zero CM motion. In our three-body calculations, we found correlations and twist-angle dependence in our extrapolated binding energies. As we demonstrated, this finding is to be expected since the LO FV functional form we used to extract our results was derived for three particles at the unitary limit [159], which does not describe our system exactly.

Our analysis suggests that discretization effects also influence FV effects for non-zero twists. We have provided formal arguments to support this finding, and we intend to do a more detailed analysis of this effect using several lattice spacings as well as more complex A -body systems to confirm this.

Our work also shows that the implementation of twisted boundaries for N -body systems within the NLEFT formalism is, in principle, relatively simple. One merely has to multiply off-diagonal matrix-elements of the transfer matrix by a phase associated with the twists. One might fear that this procedure increases sign oscillations during stochastic computations. However, the corresponding operators remain hermitian, and the eigenvectors and corresponding eigenvalues remain real. Furthermore, though in this case only two-body interactions were considered, this can be readily generalized to N -body interactions.

In this study, we applied twists to nucleon degrees of freedom within a non-relativistic formulation. We found that the iPBC analogue twists exactly cancelled the LO FV effects. This is a contrast to LQCD calculations that employ twists (or partial twists) since here the twists are applied directly to quarks. The interactions, in this case, can also depend on the twist angles due to a propagation of pions around the torus. As such, we do not expect exact cancellation of LO FV effects, but rather a suppression. It would be interesting to quantify this level of suppression from LQCD studies that utilizes our iPBC analogue twist-angle condition in eqs. (6.54) and (6.55).

The most intriguing aspect of this work is the demonstration of iPBC analog twists for the three-body sector, which have vastly reduced FV corrections compared to PBCs. This raises the question of whether or not there exists more general iPBC analog twists for N -body systems. The possibility of iPBC analog twist angles for higher N -body systems would be an outstanding finding for FV numerical simulations since this would allow for calculations in smaller volumes accompanied by their significant reduction in computational costs. Our findings in the three-body sector, coupled with our current investigations of more general N -body systems [169], provides credence that analogs of iPBC angles exist for non-relativistic N -body systems in general.

6.9 Acknowledgments

We acknowledge financial support from the Magnus Ehrnrooth Foundation of the Finnish Society of Sciences and Letters, which enabled some of our numerical simulations. We are indebted to S. König, T. Lähde and A. Shindler for insightful discussions. We thank D. Lee for initial discussions related to applying TBCs within the NLEFT formalism.

Conclusion

Summary and conclusion

Low-energy high precision experiments are a powerful tool for analyzing extensions of the Standard Model (SM) of particle physics—complementing and sometimes even surpassing ongoing efforts at higher energies in their discovery potential. This work discussed a procedure which takes possible interactions of Beyond the Standard Model (BSM) candidates with SM particles, propagates them to the nuclear level and computes scattering observables through external current low-energy Nuclear Matrix-Elements (NMEs). The specific example for this analysis were hypothetical scalar Dark Matter (DM) interactions with quarks and gluons. A chiral power counting expansion in the DM-nucleon current structure has been presented and few-nucleon matrix-elements, which characterize the scattering of DM and light nuclear targets (^2H , ^3H and ^3He), have been computed and analyzed. The feasibility of computing such matrix-elements within nuclear lattice computations has been demonstrated, but it was shown that the nuclear lattice method has to overcome several obstacles in order to achieve similar accuracy as traditional methods. Two extensions of the nuclear lattice method which help to overcome those obstacles, a prescription for including few-body forces and a prescription for accessing lattice matrix-elements at arbitrary momenta, have been presented.

The second chapter of this thesis focussed on the derivation of Leading Order (LO) and Next-to-Leading Order (NLO) DM-nucleon current structures for scalar DM quark and gluon interactions. This effective ansatz allows to connect BSM theories to the level of individual nucleons by matching the *a priori* unknown effective coefficients at the quark-gluon level. The DM interactions with nucleons were derived using Chiral Perturbation Theory (χPT) and can be characterized into three categories related to the dependence of operators on the effective BSM coefficients: isospin scalar light quark interactions with DM, isospin vector light quark interactions with DM and strange quarks and gluon interactions with DM. Since the effective BSM coefficients are *a priori* unknown, without making any model assumptions one can just compare operators within one category with each other. The analysis presented in this work incorporated all for this comparison relevant uncertainties—including the uncertainties coming from the nuclear

sector. Traditional methods (the Schrödinger and Faddeev equations in this case) have been used to compute DM- ^2H , ^3H and ^3He scattering responses. As a result, the work concludes that one-nucleon interactions are under control and can be well described by the impulse approximation (coherent behavior of individual nucleons) for the analyzed systems. Two-body currents are smaller than expected by the chiral power counting and come with more considerable relative uncertainties. Even though the total magnitude is smaller than predicted by power counting, the relevance of these two-nucleon currents is expected to grow for larger systems. These two-nucleon DM interaction uncertainties seem to be strongly correlated with the accuracy of the nuclear description but can be controlled by increasing the accuracy [e.g., the N^3LO chiral order or higher in the description of nuclear forces for the bound states]. The control of two-nucleon DM scattering uncertainties is essential because, in the case of scalar DM, this is one of the only ways to disentangle the fundamental behavior of DM with quarks and gluons. It is an ongoing project to extend this work to ^4He , a target for proposed experiments, and spin-dependent DM interactions with quarks and gluons.

Because many DM experiments utilize much bigger nuclear systems ($A \gtrsim 28$), with individual nucleon numbers well beyond the range of traditional few-body methods, one must utilize many-body methods in order to make theoretical predictions. These many-body methods make simplifications and approximations in order to access larger systems. As it was demonstrated in [chapter 2](#), it is essential to control all relevant uncertainties if one wants to disentangle different theories for DM. For this reason, the many-body method of choice must be able to not only quantify all the uncertainties coming from the nuclear description but, additionally, must be able to quantify the simplifications made by the method itself. The third chapter briefly motivates the basic idea behind Nuclear Lattice Effective Field Theory (NLEFT)—the stochastic many-body method used in this work. It is presented how this lattice method with individual nucleons as degrees of freedom makes it possible to access larger systems and how it is related to Chiral Effective Field Theory (χEFT).

As one of the essential prerequisites for accurate many-body methods, NLEFT must be able to include Three-Nucleon Forces (TNFs). The fourth chapter derives a formalism, which makes it possible to extend any stochastic lattice method in such a way that one can include any local N -body contact interaction. The basic idea is the generalization of the Hubbard-Stratonovitch (HS) transformation. A background field, which interacts with the fundamental degrees of freedom of the theory (nucleons in the case of NLEFT), is introduced in such a way that the new theory can be computed more efficiently. By the introduction of this general background or auxiliary field, one induces an arbitrary amount of freely tunable coefficients which must be matched to reproduce the original theory. Once one has stochastically integrated out the auxiliary fields, the original theory is exactly obtained. It was found that different choices of freely tunable parameters come with different stabilities in the stochastic integration. This stability is related to a more fundamental problem: the sign problem—specific nuclear interactions increase the standard deviations of stochastic computations. It remains to be tested if or how much the non-perturbative inclusion of few-body forces will affect the stochastic uncertainties

of nuclear lattice computations. Also, it is an interesting task to further generalize this technique such that one can include quantum number dependent interactions and long range interactions.

The fifth chapter presents a feasibility study for box computations—defined by a discrete basis within a finite but periodic space—for the most dominant scalar DM NME. A simple separable potential model, which mimics the short-range part of nuclear interactions, is used in analytical and numerical box computations. The numerical box results are compared to the analytical result to identify the infinite volume and continuum limit convergence behavior as well as the desired parameter space for accurate computations. Results do converge with reasonable precision for direct diagonalization methods and within the investigated parameter space range. In general, NME box computations seem feasible. It remains an ongoing investigation how extrapolation procedures, specifically the continuum limit can be realized for realistic interactions. Different notions of such an analysis, which do not affect the required cutoff of the theory, are presented in the fifth chapter. It is intended that a similar analysis will be executed for chiral interactions. However, lattice stochastic computations must be extended to, (a), meet the accuracy demands in terms of Finite-Volume (FV) effects and, (b), guarantee sufficient overlap between the set of allowed box momentum values and the physically relevant range of the DM momentum transfer values. While demand (a) generally depends on the nuclear wave function and operator used in the computation, demand (b) is true for any momentum dependent NME. One possible extension to meet these two demands is given by increasing the spatial lattice notes by a factor of $\sim 2^3$ or larger in order to have sufficient predictability. First steps into implementing the stochastic NLEFT algorithm on Graphics Processing Units (GPUs) are promising, with the potential to drastically increase the size of accessible volumes by a factor of more than 4^3 .

Complementary to *brute forcing* algorithms to larger systems, in Lattice Quantum Chromodynamics (LQCD) exists a notion which makes it possible to access desired predictions and simultaneously increase the accuracy of small volume computations by tuning the boundary conditions within the box. The implementation of such Twisted Boundary Conditions (TBCs) in the NLEFT algorithm is presented in [chapter 6](#). It is presented that one can extract similarly precise results for binding energies for systems of $1/2^3$ this size but carefully chosen boundary conditions. Furthermore, the *a priori* discrete range of box momenta can be scanned continuously by choosing different twist angles—making it possible to compute physically interesting current NME for any box size. It is still an open task to implement TBCs in the stochastic lattice algorithm and analyze their potential effect on sign oscillations—which most probably are unaffected because of the Hermitian implementation of the TBCs.

In conclusion, uncertainty estimates using a traditional framework emphasize that single-nucleon interactions are well under control for the light nuclei systems considered in this thesis. For these systems, the two-nucleon matrix-elements, which are primarily relevant to identify the nature of BSM structures, are smaller than expected but also heavily dependent on the accuracy in the description of the nuclear interactions. To make reliable

estimates for experiments, one must execute several computations to understand the propagated uncertainty coming from the nuclear description. It is possible to compute such NMEs of BSM current operators on the lattice. While further investigations have to be made for realistic descriptions of nuclear interactions at larger system sizes, no potential showstopper¹ was identified in this thesis. However, in order to make reliably accurate estimates of such NMEs, one has to execute several computations for the same observable:

$$N_{\text{runs}} = N_{\nu} \times N_{\text{mb}} = N_{\nu} \times (N_L \times N_{a_L} \times N_{a_T}) , \quad (7.1)$$

where N_{ν} is the number of different chiral interactions and N_{mb} the number of computations for a reliable many-body estimate. In the case of NLEFT, the number of estimates is a product of the number of runs for different lattice volumes (L^3) and different spatial and temporal discretization spacings (a_L and a_T). A minimal set for NLEFT current NMEs computations² is at the order of $N_{\text{runs}} = 81$, where each coefficient was chosen to be equal to three (in order to see a slope for extrapolation procedures). This is challenging because computations without or with incomplete uncertainty estimations require a fraction of the computational effort compared to full computations. Moreover, this does not even include the additional time spent on the analysis of uncertainties. Even though the scientific community emphasizes the need for such complete uncertainty estimations, studies without these estimates still dominate the literature—independent of the utilized many-body method.

Last but not least, the specific candidate for representing the BSM theory considered in this thesis was DM. However, because this work considered an effective approach for describing the extensions to the standard model, it is quite general in its predictive capabilities. For example, the theoretical description of the Neutrinoless Double β Decay ($0\nu\beta\beta$ -decay), which might help to resolve the nature of neutrinos and therefore helps to resolve the matter asymmetry puzzle, is very similar to the theoretical description associated with scalar DM. Thus, once such a framework is established, it can be used to address multiple problems at once.

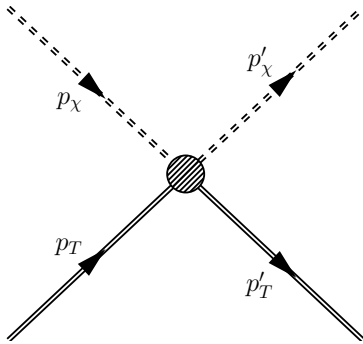
¹ The only remaining showstopper I can think of is unexpected additional sign oscillations in stochastic many-body computations. This was not investigated in this thesis.

² It is possible to insert a set of different NMEs in one run of a NLEFT computations at close to no additional cost.

Scattering currents and recoil rates

This chapter demonstrates how one can obtain differential cross sections as well as the differential recoil ratios for the elastic scattering process of a Dark Matter (DM) particle χ hitting a target nucleus T

$$\chi(p_\chi) + T(p_T) \mapsto \chi(p'_\chi) + T(p'_T). \quad (\text{A.1})$$



$$=: -i (2\pi)^4 \delta^{(4)}(p_\chi + p_T - p'_\chi - p'_T) \mathcal{M}(p_\chi, p_T, p'_\chi, p'_T)$$

Figure A.1: Definition of the elastic scattering amplitude for the DM particle χ hitting a target T . The amplitude is related to the cross section for an elastic two-to-two particle scattering process [see eq. (A.2)].

The starting point is for cross sections taken from [170, page 200], which relates any two-to-two relativistic scattering matrix-element to a differential cross section

$$d\sigma = \frac{S}{4\sqrt{(p_\chi \cdot p_T)^2 - m_\chi^2 m_T^2}} \left[\frac{d^3 \mathbf{p}'_\chi}{(2\pi)^3} \frac{1}{2E_{\mathbf{p}'_\chi}} \frac{d^3 \mathbf{p}'_T}{(2\pi)^3} \frac{1}{2E_{\mathbf{p}'_T}} \right] \times (2\pi)^4 \delta^{(4)}(p_\chi + p_T - p'_\chi - p'_T) \left| \mathcal{M}(p_\chi, p_T, p'_\chi, p'_T) \right|^2. \quad (\text{A.2})$$

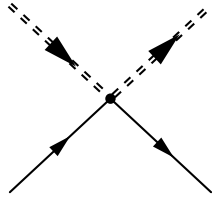
Herby $E_{\mathbf{p}_a} := \sqrt{m_a^2 + \mathbf{p}_a^2}$ is the relativistic energy of the particle a , S is a constant containing the symmetry factors of the amplitude [the number of permutations; $S = 1$ in the scenario of [chapter 2](#)] and the amplitude is defined according to [fig. A.1](#).

In the case of this work, the the target is a composite object, more generally an N -nucleon bound state. The computation of amplitudes or equivalently matrix-elements for bound states is discussed in the next section.

A.1 Bound state matrix-elements

This section follows the normalization convention of [\[171\]](#).

As a first step, one can analyze the action of operators acting on one nucleon line only



$$= -ig \sum_A \int dx^4 [\bar{\chi}(x) \Gamma_\chi^A \chi(x)] [N^\dagger(x) \Gamma_N^A N(x)] . \quad (\text{A.3})$$

For now, the exact form of the DM field χ regarding spin or other symmetries is not relevant. Thus, one expresses the *external* matrix-element of this field by

$$\langle \chi(\mathbf{p}'_\chi) | \bar{\chi}(x) \Gamma_\chi^A \chi(x) | \chi(\mathbf{p}_\chi) \rangle = \langle \Gamma_\chi^A \rangle e^{-i(p_\chi - p'_\chi) \cdot x} . \quad (\text{A.4})$$

The non-relativistic nucleon field is expressed by [\[172\]](#)

$$\hat{N}(x) := \sum_{i,s=\uparrow,\downarrow} \int \frac{d^3\mathbf{p}}{(2\pi)^3} \frac{1}{\sqrt{2m_N}} u_s v_i e^{-ip \cdot x} \hat{b}_{is}(\mathbf{p}) , \quad (\text{A.5})$$

where u and v are Pauli spinors for the spin and isospin component of the nucleon and the nucleon states are defined by the action of the creation operator $\hat{b}_{i,s}^\dagger(\mathbf{p})$ on the vacuum state

$$\sqrt{2m_N} \hat{b}_{i,s}^\dagger(\mathbf{p}) |0\rangle := |N_{is}(\mathbf{p})\rangle . \quad (\text{A.6})$$

These Fock-space operators must fulfill the anti-commutation relations

$$\begin{aligned} \{ \hat{b}_{i's'}^\dagger(\mathbf{p}'), \hat{b}_{is}(\mathbf{p}) \} &= (2\pi)^3 \delta^{(3)}(\mathbf{p}' - \mathbf{p}) \delta_{i'i} \delta_{s's} , \\ \{ \hat{b}_{i's'}(\mathbf{p}'), \hat{b}_{is}(\mathbf{p}) \} &= 0 = \{ \hat{b}_{i's'}^\dagger(\mathbf{p}'), \hat{b}_{is}^\dagger(\mathbf{p}) \} . \end{aligned} \quad (\text{A.7})$$

To describe bound states within the framework of a field theory in the non-relativistic limit, one must make a similar state definition for precisely these bound states. Since bound states are compound objects, one now also has to deal with more than just two

spin ($s = \uparrow, \downarrow$) and isospin ($i = p, n$) polarizations. Furthermore, the total internal spin S couples with the bound state angular momentum L resulting in the total spin quantum number J . Thus, to use the bound state in eq. (A.2), one needs the normalization of the form

$$\langle N_{i's'}(\mathbf{p}') | N_{is}(\mathbf{p}) \rangle = 2m_N (2\pi)^3 \delta^{(3)}(\mathbf{p}' - \mathbf{p}) \delta_{i'i} \delta_{s's} \quad (\text{A.8})$$

$$\langle B_{\alpha'}(\mathbf{P}') | B_{\alpha}(\mathbf{P}) \rangle \stackrel{!}{=} 2m_B (2\pi)^3 \delta^{(3)}(\mathbf{P}' - \mathbf{P}) \delta_{\alpha'\alpha}, \quad (\text{A.9})$$

where α' and α are a collective set of channel quantum numbers which uniquely determine the nuclear state (e.g., the isospin polarization and total spin J).

A.1.1 Two body bound states

Because the DM interactions are acting on individual nucleon lines, one has to compute the action of the action of single nucleon operators on this bound state. A desirable description of the bound state in terms of single nucleon operators is given by

$$\begin{aligned} |B_{\alpha}(\mathbf{P})\rangle &:= \mathcal{C} \sum_{i_1, i_2} \sum_{s_1, s_2} \int \frac{d^3 \mathbf{p}_1}{(2\pi)^3} \int \frac{d^3 \mathbf{p}_2}{(2\pi)^3} \\ &\times \psi_{\alpha; (i_1 i_2)_{s_1 s_2}}(\mathbf{p}_1, \mathbf{p}_2) |N_{i_1 s_1}(\mathbf{p}_1); N_{i_2 s_2}(\mathbf{p}_2)\rangle (2\pi)^3 \delta^{(3)}(\mathbf{p}_1 + \mathbf{p}_2 - \mathbf{P}). \end{aligned} \quad (\text{A.10})$$

The constant \mathcal{C} is the normalization of the state, \mathbf{P} the center of mass momentum and ψ the bound state wave function—a negative energy solution to the two-nucleon Schrödinger equation. For example, one can express the wave function by its partial wave components L, S, I and J with the fixed quantum numbers $\alpha = (J, M_J; M_I)$. In this case, the wave function corresponds to sums of Clebsch-Gordan coefficients times the partial wave components

$$\begin{aligned} \psi_{(J, M_J; M_I); (i_1 i_2)_{s_1 s_2}}(\mathbf{p}_1, \mathbf{p}_2) &= \sum_{LS} \sum_{M_L M_S} \left\langle \frac{1}{2} i_1, \frac{1}{2} i_2 \middle| IM_I \right\rangle \left\langle \frac{1}{2} s_1, \frac{1}{2} s_2 \middle| SM_S \right\rangle \\ &\times \langle LM_L, SM_S | JM_J \rangle Y_{LM_L}^* (\widehat{\mathbf{p}_1 - \mathbf{p}_2}) \psi_{(LS)J; I} \left(\left| \frac{\mathbf{p}_1 - \mathbf{p}_2}{2} \right| \right). \end{aligned}$$

Here, it was used that the wave momentum-space dependent component in a partial wave basis does not depend on polarization components and the angular dependence is described by spherical harmonics.

To simplify the notation in the following context, the individual nucleon spin and isospin quantum numbers will be indicated by one combined subscript only, e.g., for the previous

case

$$|B_\alpha(\mathbf{P})\rangle = \mathcal{C} \sum_{a,b} \int \frac{d^3\mathbf{p}_1}{(2\pi)^3} \int \frac{d^3\mathbf{p}_2}{(2\pi)^3} \psi_{\alpha;ab}(\mathbf{p}_1, \mathbf{p}_2) |N_a(\mathbf{p}_1); N_b(\mathbf{p}_2)\rangle (2\pi)^3 \delta^{(3)}(\mathbf{p}_1 + \mathbf{p}_2 - \mathbf{P}). \quad (\text{A.11})$$

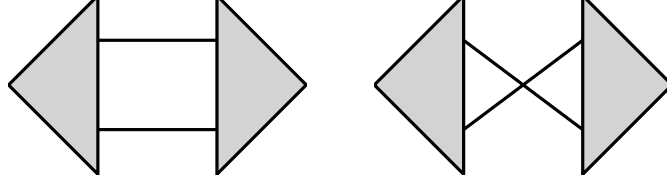


Figure A.2: Possible choices for contracting the nucleon lines for the bound state wave functions. The triangle represents the two-nucleon bound state and the lines correspond to individual nucleon lines. The order of lines symbolizes how nucleon operators are contracted.

Next, one would like to determine the normalization of the bound state. When evaluating the matrix-element for two-nucleon states, one has to contract the nucleon operators in all possible ways (see fig. A.2)

$$\langle N_{a'}; N_{b'} | N_a; N_b \rangle = \langle 0 | \overbrace{\hat{N}_{a'} \hat{N}_{b'} \hat{N}_b \hat{N}_a} | 0 \rangle + \langle 0 | \overbrace{\hat{N}_{a'} \hat{N}_{b'} \hat{N}_b \hat{N}_a} | 0 \rangle = \delta_{a'a} \delta_{b'b} - \delta_{b'a} \delta_{a'b}. \quad (\text{A.12})$$

Thus the normalization is given by

$$\begin{aligned} \langle B_{\alpha'}(\mathbf{P}') | B_\alpha(\mathbf{P}) \rangle &= |\mathcal{C}|^2 (2\pi)^3 \delta^{(3)}(\mathbf{P}' - \mathbf{P}) \sqrt{2m_N}^4 \sum_{a,b} \int \frac{d^3\mathbf{p}_1}{(2\pi)^3} \\ &\times \left[\psi_{\alpha';ab}^*(\mathbf{p}_1, \mathbf{P} - \mathbf{p}_1) \psi_{\alpha;ab}(\mathbf{p}_1, \mathbf{P} - \mathbf{p}_1) - \psi_{\alpha';ba}^*(\mathbf{P} - \mathbf{p}_1, \mathbf{p}_1) \psi_{\alpha;ab}(\mathbf{p}_1, \mathbf{P} - \mathbf{p}_1) \right]. \quad (\text{A.13}) \end{aligned}$$

Since the wave function is completely antisymmetric in the exchange of nucleons, the terms in parenthesis are actually the same modulo a minus sign. Also, when shifting the momentum by $\mathbf{p}_1 \mapsto \mathbf{p} + \mathbf{P}/2$ one can use the fact that the wave function just depends on the relative momentum and thus apply the orthonormality of the wave function

$$\begin{aligned} \sum_{a,b} \int \frac{d^3\mathbf{p}}{(2\pi)^3} \psi_{\alpha';ab}^*(\mathbf{p}) \psi_{\alpha;ab}(\mathbf{p}) &= \delta_{\alpha\alpha'} \\ \Rightarrow \langle B_{\alpha'}(\mathbf{P}') | B_\alpha(\mathbf{P}) \rangle &= |\mathcal{C}|^2 (2\pi)^3 \delta^{(3)}(\mathbf{P}' - \mathbf{P}) \sqrt{2m_N}^4 \times 2 \delta_{\alpha\alpha'}. \quad (\text{A.14}) \end{aligned}$$

Thus, to agree with the single-nucleon state convention, the normalization must be chosen as follows

$$\mathcal{C} = \frac{1}{\sqrt{2}} \times \sqrt{2M_B} \frac{1}{\sqrt{2m_N}^2}. \quad (\text{A.15})$$

The first factor of $1/\sqrt{2}$ comes from the fact that the individual nucleon quantum numbers are not fixed—the nucleons can completely interchange their position and *flip* the wave

function. This is similar when going from the relative momentum basis to an also anti-symmetric second quantization basis of nucleon fields: one has to include a factor of $1/\sqrt{N!}$,

$$|\mathbf{k}_1, \mathbf{k}_2\rangle_{reg. mom.} = \frac{1}{\sqrt{2!}} |\mathbf{k}_1, \mathbf{k}_2\rangle_{sec. quant.} . \quad (\text{A.16})$$

Next, one has to compute the matrix-element of an one-nucleon operator $\hat{N}(x)\Gamma\hat{N}(x)$, where Γ is in general matrix in spin and isospin space. The matrix-element is, as before, given by the sum over all possible contractions (see fig. A.3)

$$\begin{aligned} \langle B_{\alpha'}(\mathbf{P}') | \hat{N}(x)\Gamma\hat{N}(x) | B_{\alpha}(\mathbf{P}) \rangle &= \frac{2M_B}{2(2m_N)^2} \sum_{a,a',b,b'} \prod_{n=1,2} \left(\int \frac{d^3\mathbf{p}_n}{(2\pi)^3} \int \frac{d^3\mathbf{p}'_n}{(2\pi)^3} \right) \\ &\times (2\pi)^3 \delta^{(3)}(\mathbf{p}'_1 + \mathbf{p}'_2 - \mathbf{P}') (2\pi)^3 \delta^{(3)}(\mathbf{p}_1 + \mathbf{p}_2 - \mathbf{P}) \\ &\times \psi_{\alpha';a'b'}^*(\mathbf{p}'_1, \mathbf{p}'_2) \psi_{\alpha;ab}(\mathbf{p}_1, \mathbf{p}_2) \langle N_{a'}; N_{b'} | \hat{N}^\dagger(x)\Gamma\hat{N}(x) | N_a; N_b \rangle . \quad (\text{A.17}) \end{aligned}$$

For simplifying purposes it was assumed that $M_{B'_\alpha} = M_B = M_{B_\alpha}$.

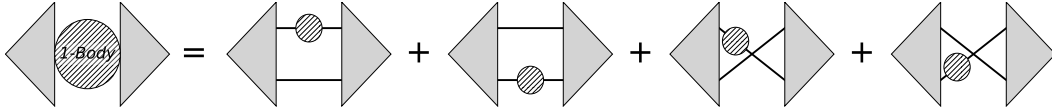


Figure A.3: Diagrammatic interpretation of an one-nucleon operator matrix-elements for a two-nucleon bound state.

When summing over all possible contractions one finds anti-symmetric patterns similar to the normalization part [fig. A.3]. Hereby one can show that the results of such anti-symmetric structures are actually the same. As an example: for the result where the the operator is inserted on the upper (first) nucleon line one finds

$$\begin{aligned} \langle N_{a'}; N_{b'} | \hat{N}^\dagger(x)\Gamma\hat{N}(x) | N_a; N_b \rangle &= \frac{2M_B}{2(2m_N)^2} \sum_{a,a',b,b'} \prod_{n=1,2} \left(\int \frac{d^3\mathbf{p}_n}{(2\pi)^3} \int \frac{d^3\mathbf{p}'_n}{(2\pi)^3} \right) \\ &\times (2\pi)^3 \delta^{(3)}(\mathbf{p}'_1 + \mathbf{p}'_2 - \mathbf{P}') (2\pi)^3 \delta^{(3)}(\mathbf{p}_1 + \mathbf{p}_2 - \mathbf{P}) \\ &\times \psi_{\alpha';a'b'}^*(\mathbf{p}'_1, \mathbf{p}'_2) \langle \overbrace{N_{a'}; N_{b'}} | \hat{N}^\dagger(x)\Gamma\hat{N}(x) | \overbrace{N_a; N_b} \rangle \psi_{\alpha;ab}(\mathbf{p}_1, \mathbf{p}_2) . \quad (\text{A.18}) \end{aligned}$$

with the result of the contraction

$$\langle \overbrace{N_{a'}; N_{b'}} | \hat{N}^\dagger(x)\Gamma\hat{N}(x) | \overbrace{N_a; N_b} \rangle = \sqrt{2m_N}^4 \times \left[\left(u_{a'}^\dagger v_{a'}^\dagger \Gamma v_a u_a \right) \frac{e^{-i(p_1-p'_1)\cdot x}}{\sqrt{2m_N}^2} \right] \times (2\pi)^3 \delta^{(3)}(\mathbf{p}'_2 - \mathbf{p}_2) \delta_{bb'} . \quad (\text{A.19})$$

The square root of the masses to the power of 4 is coming from the normalization of the states, the matrix-element from the operator field contractions and the delta function

from the blank nucleon line contraction. On the other hand, when contracting the first incoming nucleon with the second outgoing nucleon, one finds

$$\langle \overbrace{N_{a'}; N_{b'}}^{\overbrace{\hat{N}^\dagger(x)\Gamma\hat{N}(x)}^{\overbrace{N_a; N_b}}} \rangle = -\sqrt{2m_N^4} \times \left[(u_b^\dagger v_b^\dagger \Gamma v_a u_a) \frac{e^{-i(p_1-p_2)\cdot x}}{\sqrt{2m_N^2}} \right] \times (2\pi)^3 \delta^{(3)}(\mathbf{p}'_1 - \mathbf{p}_2) \delta_{a'b}. \quad (\text{A.20})$$

Last but not least, one can relabel the integrations and sums according to $(\mathbf{p}'_1, a', b' \leftrightarrow \mathbf{p}'_2, b', a')$ and the part of eq. (A.17) containing eq. (A.20) is equal to the part of eq. (A.17) containing eq. (A.19). And, again, when simultaneously interchanging the components of the wave function $(\mathbf{p}'_1, a', b' \leftrightarrow \mathbf{p}'_2, b', a')$, one obtains an additional minus sign

$$\psi_{\alpha'; a'b'}^*(\mathbf{p}'_1, \mathbf{p}'_2) = -\psi_{\alpha'; b'a'}^*(\mathbf{p}'_2, \mathbf{p}'_1). \quad (\text{A.21})$$

Most interestingly, this is also true the other way around—relabeling the non primed indices and momenta. Because of this, one can simply interchange for example the indices where the operator is inserted on the first nucleon line such that one obtains the same structure where the operator is inserted on the second nucleon line (times $(-1)^2$ for interchanging the primed and non-primed wave function). Accordingly, the sum over all four possible contractions is equal to four times one of the diagrams. Note that the factor of four appears because of the normalization choice of the wave function which includes another factor of one half (symmetry factor). Thus, the result of an one-nucleon operator matrix-element is equal to four times the matrix-element, where the operator is inserted on one nucleon line (see fig. A.4).

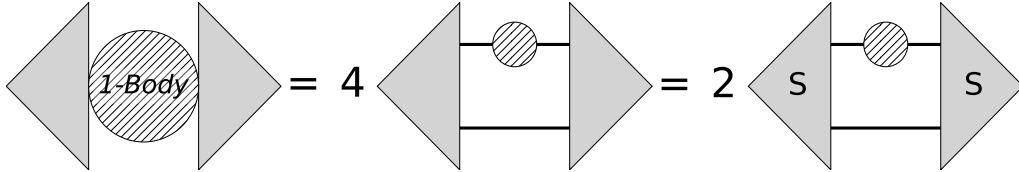


Figure A.4: Matrix-element of one-nucleon operator for a two-nucleon bound state is equal two four times the result for a specific contraction in terms of a regular momentum basis. In case one chooses the second quantization basis (counting of twisted line contractions within states), this makes two times the insertion on one nucleon line.

Combing all this one finds

$$\begin{aligned} & \langle B_{\alpha'}(\mathbf{P}') \mid \hat{N}(x)\Gamma\hat{N}(x) \mid B_{\alpha}(\mathbf{P}) \rangle \\ &= 2 \frac{M_B}{m_N} e^{-i(P-P')\cdot x} \sum_{a,b,a'} \int \frac{d^3\mathbf{p}}{(2\pi)^3} \psi_{\alpha'; a'b}^* \left(\left| \mathbf{p} - \frac{\mathbf{q}}{2} \right| \right) \langle \Gamma \rangle_{a'a} \psi_{\alpha; ab}(\mathbf{p}) \\ &=: 2 \frac{2M_B}{2m_N} e^{-i(P-P')\cdot x} \mathcal{F}_{\Gamma}(\mathbf{q}), \quad (\text{A.22}) \end{aligned}$$

where it was used that the wave function only depends on the relative momenta and with $\mathbf{q} \equiv \mathbf{P} - \mathbf{P}'$. Finally combining this with the DM only matrix-element eq. (A.4) to obtain the full scattering amplitude eq. (A.3) one finds

$$i\mathcal{M}(p_\chi, p_T, p'_\chi, p'_T) = 2 \frac{M_B}{m_N} \times \sum_A \mathcal{F}_{\Gamma^A}(\mathbf{q}) \langle \Gamma_\chi^A \rangle. \quad (\text{A.23})$$

This can be repeated for two-nucleon operators $\hat{\mathcal{O}} = (\hat{N}^\dagger \Gamma_1 \hat{N})(\hat{N}^\dagger \Gamma_2 \hat{N})$. The things which will be different can be identified in a straightforward manner: On the one hand, the symmetry factor will not change. Because one just has two-nucleon lines at proposal, once one has contracted the first single nucleon operator, the next one is fixed. Note that symmetry factors for one- and two-nucleon operators will be different once one computes matrix-elements of N -nucleon bound states with $N > 2$. On the other hand, since the operator consists out of four nucleon fields, one will obtain an additional factor of $1/\sqrt{2m_N^2}$ from the state normalization. The overall exponential of the momenta is not affected by the shape of the operator, one will always obtain $-i(p_{\text{in}} - p_{\text{out}}) \cdot x$. Thus, the result is of the form

$$\begin{aligned} \langle B_{\alpha'}(\mathbf{P}') \mid [\hat{N}^\dagger(x)\Gamma_1\hat{N}(x)] [\hat{N}^\dagger(x)\Gamma_2\hat{N}(x)] \mid B_\alpha(\mathbf{P}) \rangle &= 2 \frac{2M_B}{(2m_N)^2} e^{-i(P-P') \cdot x} \\ &\times \sum_{a,a'} \sum_{b,b'} \int \frac{d^3\mathbf{p}'_1}{(2\pi)^3} \int \frac{d^3\mathbf{p}_1}{(2\pi)^3} \psi_{\alpha';a'b'}^*(\mathbf{p}'_1, \mathbf{P}' - \mathbf{p}'_1) \langle \Gamma_1 \rangle_{a'a} \langle \Gamma_2 \rangle_{b'b} \psi_{\alpha;ab}(\mathbf{p}_1, \mathbf{P} - \mathbf{p}_1). \end{aligned} \quad (\text{A.24})$$

The whole procedure can be generalized in a straight forward manner to any N -nucleon bound state and M -nucleon operator. Besides the mass factors coming from the normalization of the Fock-space states, one only has to consider the possible permutations of nucleon lines.

A.2 Recoil rates

This section presents how one obtains the differential cross section per recoil energy in the lab frame of the target

$$\frac{d\sigma}{dE_R}, \quad E_R := \frac{\mathbf{q}^2}{2m_T},$$

where \mathbf{q} is the recoil momentum of the target with mass m_T . Again one starts with the equation for the differential cross section

$$\begin{aligned} d\sigma &= \frac{S}{4\sqrt{(p_\chi \cdot p_T)^2 - m_\chi^2 m_T^2}} \left[\frac{d^3\mathbf{p}'_\chi}{(2\pi)^3} \frac{1}{2E_{\mathbf{p}'_\chi}} \frac{d^3\mathbf{p}'_T}{(2\pi)^3} \frac{1}{2E_{\mathbf{p}'_T}} \right] \\ &\times (2\pi)^4 \delta^{(4)}(p_\chi + p_T - p'_\chi - p'_T) \left| \mathcal{M}(p_\chi, p_T, p'_\chi, p'_T) \right|^2. \end{aligned} \quad (\text{eq. (A.2)})$$

In the Lab frame of the target, one finds for the three-vectors

$$\mathbf{p}_\chi = \gamma m_\chi \mathbf{v}_\chi, \quad \mathbf{p}_T = \mathbf{0}, \quad \mathbf{p}'_T = \mathbf{q}, \quad \mathbf{p}'_\chi = \mathbf{p}_\chi - \mathbf{q}, \quad (\text{A.25})$$

where γ is the relativistic Lorentz factor. Also, in the case of this work, the scattering amplitude \mathcal{M} depends on the momentum transfer \mathbf{q} , or more precisely \mathbf{q}^2 . One can simplify the denominator once one substitutes these expressions in the denominator of eq. (A.2)

$$\sqrt{(p_\chi \cdot p_T)^2 - m_\chi^2 m_T^2} = m_T |\mathbf{p}_\chi|. \quad (\text{A.26})$$

It is preferable to execute the \mathbf{p}'_χ integration since one wants to work with $E(\mathbf{q})$ later on. Last but not least, for this work, $S = 1$, since one can distinguish between DM and any other nuclear target

$$d\sigma = \frac{1}{4 \cdot 2 \cdot 2 m_T |\mathbf{p}_\chi|} \left[\frac{d^3 \mathbf{q}}{(2\pi)^3} \frac{1}{E'_\chi E'_T} \right] (2\pi) \delta^{(1)}(E_\chi + E_T - E'_\chi - E'_T) |\mathcal{M}(\mathbf{q}^2)|^2. \quad (\text{A.27})$$

Note that the energies still depend on the three momenta, e.g., E'_χ depends on $\mathbf{p}_\chi \cdot \mathbf{q}$. In the next step, one has to split up the \mathbf{q} integration in its angular and radial parts. Afterwards one can relate the radial part to the relativistic target energy

$$dE'_T = d\left(\sqrt{m_T^2 + \mathbf{q}^2}\right) = \frac{|\mathbf{q}|}{E'_T} d\mathbf{q} \quad \Rightarrow \quad \frac{d^3 \mathbf{q}}{(2\pi)^3} = d\phi dx dE'_T |\mathbf{q}|. \quad (\text{A.28})$$

Plugging this back into eq. (A.2), executing the angular integration and using the fact that one can choose the orientation of the coordinate system to simplify the azimuthal ϕ integration, one obtains

$$d\sigma = \frac{(2\pi) \cdot (2\pi)}{16 \cdot (2\pi)^3 m_T |\mathbf{p}_\chi|} dE'_T |\mathbf{q}| |\mathcal{M}(\mathbf{q}^2)|^2 \int_{-1}^1 dx \frac{1}{E'_\chi(x)} \delta^{(1)}(E_\chi + E_T - E'_\chi(x) - E'_T). \quad (\text{A.29})$$

The solution of the integration over the delta function is given by

$$\int_{-1}^1 dx \frac{1}{E'_\chi(x)} \delta^{(1)}(E_\chi + E_T - E'_\chi(x) - E'_T) = \sum_i \frac{1}{E'_\chi(x_i)} \frac{1}{|\partial_x E'_\chi(x_i)|}, \quad (\text{A.30})$$

where x_i are the zeros of the argument of the delta function within the range $|x_i| \leq 1$. The derivative of the energy $E'_\chi(x)$ with respect to x can fortunately be expressed with $E'_\chi(x)$ itself

$$\partial_x E'_\chi(x) = \partial_x \left(\sqrt{m_\chi^2 + \mathbf{p}_\chi^2 + \mathbf{q}^2 - 2|\mathbf{q}||\mathbf{p}_\chi|x} \right) = \frac{-|\mathbf{q}||\mathbf{p}_\chi|}{E'_\chi(x)}. \quad (\text{A.31})$$

The only remaining task is the computation of the zeros of the delta function

$$E_\chi + E_T - E'_T - \sqrt{m_\chi^2 + \mathbf{p}_\chi^2 + \mathbf{q}^2 - 2|\mathbf{q}||\mathbf{p}_\chi|x} = 0, \quad (\text{A.32})$$

or

$$2|\mathbf{q}||\mathbf{p}_\chi| \geq 2|\mathbf{q}||\mathbf{p}_\chi|x = m_\chi^2 + \mathbf{p}_\chi^2 + \mathbf{q}^2 - (E_\chi + E_T - E'_T)^2 \geq -2|\mathbf{q}||\mathbf{p}_\chi|. \quad (\text{A.33})$$

Further simplifying this equation one has

$$m_\chi^2 + \mathbf{p}_\chi^2 + \mathbf{q}^2 - (E_\chi + E_T - E'_T)^2 = \mathbf{q}^2 + (2E_\chi + E_T - E'_T)(E'_T - E_T). \quad (\text{A.34})$$

In the non-relativistic limit the energy difference of the target will be given by the change in the kinetic energy $E'_T - E_T = \mathbf{q}^2/2m_T + \mathcal{O}(\mathbf{q}^4)$ and, additionally one can use that the relativistic energy of the DM particle ($m_\chi \gtrsim 10^3\text{MeV}$) is larger than the target recoil energy $E_\chi \gg E_T - E'_T = \mathbf{q}^2/m_T \lesssim 1\text{MeV}$, one has

$$2|\mathbf{q}||\mathbf{p}_\chi| \geq \mathbf{q}^2(1 + E_\chi/m_T) \quad \Rightarrow \quad |\mathbf{q}| \leq \frac{2|\mathbf{p}_\chi|}{1 + E_\chi/m_T} \simeq 2\mu_T|\mathbf{v}_\chi|, \quad (\text{A.35})$$

where μ_T is the reduced mass of the DM and target particle. The approximation in eq. (A.35) is for non-relativistic DM with $\mathbf{v}_\chi \ll 1$ and $E_\chi = m_\chi$.

To conclude this for elastic DM scattering with a target T , the differential cross section is given by

$$d\sigma = \frac{1}{32\pi} \frac{|\mathcal{M}(\mathbf{q}^2)|^2}{m_T|\mathbf{p}_\chi|^2} dE'_T, \quad |\mathbf{q}| \leq \frac{2|\mathbf{p}_\chi|}{1 + E_\chi/m_T}, \quad (\text{A.36})$$

which becomes in the limit for non-relativistic DM particles

$$dE'_T = d\left(\sqrt{m_T^2 + 2m_TE_R}\right) = \frac{m_T}{E'_T} dE_R \simeq dE_R \quad (\text{A.37})$$

and

$$\frac{d\sigma}{dE_R} = \frac{1}{32\pi} \frac{|\mathcal{M}(\mathbf{q}^2)|^2}{m_T m_\chi^2 v_\chi^2}, \quad |\mathbf{q}| \leq 2\mu_T v_\chi. \quad (\text{A.38})$$

And finally, one obtains the differential recoil rate by averaging the differential cross section over the DM velocity distribution (see also [76])

$$\frac{dR}{dE_R} = \frac{\xi_T}{m_T} \frac{\rho_\chi^0}{m_\chi} \int_{v_{min}} d^3\mathbf{v} v f_E(\mathbf{v}) \frac{d\sigma}{dE_R}. \quad (\text{A.39})$$

Here, the parameters are

- $\rho_\chi^0 \simeq 0.3\text{GeV}/\text{cm}^3$, the DM energy density at the Earths location

- $f_E(\mathbf{v})$, the DM velocity distribution in the Earth's frame. Ref. [76] uses a truncated Maxwell-Boltzmann distribution corresponding to an isothermal sphere density profile for the DM. One can relate the distribution on Earth to the distribution in the galaxy by $f_E(\mathbf{v}) = f_G(\mathbf{v} + \mathbf{v}_E)$ with

$$f_G(\mathbf{v}) = \frac{\exp(-v^2/v_0^2)}{(v_0\sqrt{\pi})^3 \operatorname{erf}(v_{esc}/v_0) - 2v_0^3\pi(v_{esc}/v_0)\exp(-v_{esc}^2/v_0^2)} \quad (\text{A.40})$$

normalized to

$$\int_{v \leq v_{esc}} d^3\mathbf{v} \frac{f_G(\mathbf{v})}{v} = 1 \quad (\text{A.41})$$

with $v_0 = 220\text{km/s}$ and $v_{esc} = 544\text{km/s}$.

- v_{min} is the minimal velocity for the DM to hit a target at rest such that it has momentum \mathbf{q} after the scattering process. It is given by $2\mu_T v_{min} \simeq q = \sqrt{2m_T E_R}$ as shown above. This is the reason why heavy target detectors find it easier to measure heavy DM: since the smallest detected recoil energy is limited by the detector resolution, one desires relatively large recoil energies. In case of light DM, this ratio improves if m_T is light as well.
- ξ_T is the target 'mass fraction' taking into account numeric abundances (see [112]).

Operator partial wave decomposition

The primary objective of this work is the computation of Nuclear Matrix-Elements (NMEs) with a complete estimation of all relevant uncertainties. For this reason, one has to compute multiple matrix-elements for the same observable but different parameter sets. An important part of these uncertainty estimations involves the variation of chiral orders: one has to sandwich the same operator with several wave functions at different chiral orders. Therefore, from a computational point of view, it is desirable to have the operators in a *portable* basis which is adjustable the input basis of the nuclear wave functions. In the case of this work, the nuclear states are expressed in a partial wave decomposed basis in momentum space (see also [96, Appendix A-E]). This section describes the newly developed framework which was used to numerically cast operators in a partial wave basis.

B.1 The idea

The basic idea behind the reusability of operators is the Wigner-Eckart theorem: the matrix-element of an operator can be expressed by a Clebsch-Gordan coefficient times a reduced matrix-element (following the convention of [173])

$$\langle j' m'_j | \hat{\mathcal{O}}_{\xi m_\xi} | j m_j \rangle = \langle j m_j, \xi m_\xi | j' m'_j \rangle \langle j' || \hat{\mathcal{O}}_\xi || j \rangle . \quad (\text{B.1})$$

If it is possible to extract the so called reduced matrix-element, which is independent on polarization quantum numbers m , then one can reduce the total number of sums and integrations. As will be presented later, this also allows to make further use conservation laws.

To numerically implement this theorem in an efficient way, we project the matrix-elements on their associated operator rank ξ and m_ξ

$$\mathcal{O}_{(j'j)\xi m_\xi} := \sum_{\substack{\hat{\xi} \\ \hat{j}'}} \sum_{m_j m'_j} \langle j m_j, \xi m_\xi | j' m'_j \rangle \langle j' m'_j | \hat{\mathcal{O}} | j m_j \rangle , \quad (\text{B.2})$$

where $\hat{a} := 2a + 1$. Note that for scalar operators $\xi = 0 = m_\xi$, this becomes an average over all diagonal elements

$$\mathcal{O}_{(j'j)00} = \delta_{jj'} \frac{1}{\hat{j}} \sum_m \langle jm \mid \hat{\mathcal{O}} \mid jm \rangle . \quad (\text{B.3})$$

Furthermore, one can reobtain the original matrix-element by summing over the operator channels

$$\langle j'm' \mid \hat{\mathcal{O}} \mid jm \rangle = \sum_{\xi=0}^{\infty} \sum_{|m_\xi| \leq \xi} \langle j m_j, \xi m_\xi \mid j' m'_j \rangle \mathcal{O}_{(j'j)\xi m_\xi} . \quad (\text{B.4})$$

The two m_j, m'_j sums are effectively replaced by the ξ and m_ξ sums. This is, for the operators evaluated in this work, more practical because for spin independent operators, $m_\xi = 0$ and the expansion converged with correction in the sub-precent regime after $\xi = 2$.

Eventually, one is interested in computing cross section and thus one needs the spin averaged amplitude squared

$$|\overline{\mathcal{M}^{(j)}}|^2 := \frac{1}{\hat{j}} \sum_{m_j m'_j} \left| \mathcal{M}_{m'_j m_j}^{(j)} \right|^2 . \quad (\text{B.5})$$

Using the previous projection on the operator ranks, one can rewrite the amplitude by its partial wave decomposition

$$\mathcal{M}_{m'_j m_j}^{(j)} = \sum_{\xi m_\xi} \langle j m_j, \xi m_\xi \mid j m'_j \rangle \mathcal{M}_{(jj)\xi m_\xi} , \quad (\text{B.6})$$

and therefore the spin averaged amplitude squared becomes

$$|\overline{\mathcal{M}^{(j)}}|^2 = \frac{1}{\hat{j}} \sum_{m_j m'_j} \mathcal{M}_{m'_j m_j}^{(j)} \left(\mathcal{M}_{m'_j m_j}^{(j)} \right)^* = \sum_{\xi m_\xi} \frac{1}{\hat{\xi}} \left| \mathcal{M}_{(jj)\xi m_\xi} \right|^2 . \quad (\text{B.7})$$

B.2 Partial wave basis of nuclear states

B.2.1 Two-nucleon states

In terms of a partial wave basis for the nuclear states in a $(ls)j$ coupling scheme, defined by the representation of spin states

$$|\alpha, m_j\rangle = |(ls)jm_j\rangle = \sum_{m_l m_s} \langle l m_l, s m_s \mid j m_j \rangle |j m_j\rangle , \quad (\text{B.8})$$

the result for the operator decomposition is given by

$$\mathcal{O}_{(\alpha'\alpha)\xi m_\xi}(\mathbf{p}', \mathbf{p}, \mathbf{q}) = \frac{\hat{\xi}}{\hat{j}'} \sum_{m'_j m_j} \langle j m_j, \xi m_\xi | j' m'_j \rangle \langle (l' s') j' m'_j | \hat{\mathcal{O}}(\mathbf{p}', \mathbf{p}, \mathbf{q}) | (l s) j m_j \rangle \quad (\text{B.9})$$

$$= (-)^{2\xi} \sqrt{\hat{j} \hat{l}' \hat{s}' \hat{\xi}} \sum_{\lambda \sigma} \begin{Bmatrix} j & \xi & j' \\ l & \lambda & l' \\ s & \sigma & s' \end{Bmatrix} \mathcal{O}_{\left(\begin{smallmatrix} (l'l)\lambda \\ (s's)\sigma \end{smallmatrix}\right)\xi m_\xi}(\mathbf{p}', \mathbf{p}, \mathbf{q}) \quad (\text{B.10})$$

where the total spin decomposed operator can be factorized in an angular momentum- and spin-dependent part

$$\mathcal{O}_{\left(\begin{smallmatrix} (l'l)\lambda \\ (s's)\sigma \end{smallmatrix}\right)\xi m_\xi}(\mathbf{p}', \mathbf{p}, \mathbf{q}) := \sum_{m_\lambda m_\sigma} \langle \lambda m_\lambda, \sigma m_\sigma | \xi m_\xi \rangle \times \int d\hat{\mathbf{p}}' \int d\hat{\mathbf{p}} \mathcal{O}_{(l'l)\lambda m_\lambda}^{(L)}(\hat{\mathbf{p}}', \hat{\mathbf{p}}) \mathcal{O}_{(s's)\sigma m_\sigma}^{(S)}(\mathbf{p}', \mathbf{p}, \mathbf{q}) \quad (\text{B.11})$$

the angular momentum-dependent part is a function of spherical harmonics while the spin-dependent part evaluates the remaining matrix-element

$$\mathcal{O}_{(l'l)\lambda m_\lambda}^{(L)}(\hat{\mathbf{p}}', \hat{\mathbf{p}}) := \frac{\hat{\lambda}}{\hat{l}'} \sum_{m'_l m_l} \langle l m_l, \lambda m_\lambda | l' m'_l \rangle Y_{l' m'_l}^*(\hat{\mathbf{p}}') Y_{l m_l}(\hat{\mathbf{p}}) \quad (\text{B.12})$$

$$\mathcal{O}_{(s's)\sigma m_\sigma}^{(S)}(\mathbf{p}', \mathbf{p}, \mathbf{q}) := \frac{\hat{\sigma}}{\hat{s}'} \sum_{m'_s m_s} \langle s m_s, \sigma m_\sigma | s' m'_s \rangle \langle s' m'_s | \hat{\mathcal{O}}(\mathbf{p}', \mathbf{p}, \mathbf{q}) | s m_s \rangle. \quad (\text{B.13})$$

Conservation laws which simplify the angular-integration in eq. (B.11) can be applied depending on the spin matrix-elements of the operator $\mathcal{O}_{(s's)\sigma m_\sigma}^{(S)}$. Note that this matrix-element does not depend on isospin. This is the case because the isospin can be factored out is thus computed individually in the same manner. Following this procedure, the matrix-element for two-nucleon systems can be expressed by

$$\mathcal{M}_{(jj)\xi m_\xi} = \sum_{\alpha, \alpha'} \int dp_{12} p_{12}^2 \int \frac{dp'_{12} p_{12}^2}{(2\pi)^3} \psi_{\alpha'}^*(p'_{12}) \mathcal{O}_{(\alpha'\alpha)\xi m_\xi}(p'_{12}, p_{12}, \mathbf{q}) \psi_\alpha(p_{12}), \quad (\text{B.14})$$

for wave functions normalized to

$$\sum_\alpha \int dp_{12} p_{12}^2 |\psi_\alpha(p_{12})|^2 = 1. \quad (\text{B.15})$$

B.2.2 Three-nucleon states

In case of the three-nucleon states of a fixed total momentum j_3 , the following coupling scheme was employed. One first considers the (12)-subsystem and couples the spin $s_{12} \in \{0, 1\}$ to the angular momentum l_{12} forming a subsystem total spin j_{12} . Next one

couples the third nucleon spin s_3 to the remaining angular momentum l_3 forming the total subsystem spin I_3 . Finally the subsystem spins are coupled to a total spin j_3 with polarization m_{j_3}

$$|\alpha, m_{j_3}\rangle := \left| \left((l_{12}, s_{12}) j_{12}, (l_3, s_3) I_3 \right) j_3 m_{j_3} \right\rangle. \quad (\text{B.16})$$

For three-nucleon states, the matrix-element is given by

$$\begin{aligned} \mathcal{M}_{(j'_3 j_3) \xi m_\xi} &= \sum_{\alpha, \alpha'} \int dp_{12} p_{12}^2 \int dp_3 p_3^2 \int \frac{dp'_{12} p_{12}'^2}{(2\pi)^3} \int \frac{dp'_3 p_3'^2}{(2\pi)^3} \\ &\quad \times \psi_{\alpha'}^*(p'_{12}, p'_3) \mathcal{O}_{(\alpha' \alpha) \xi m_\xi}^{(123)}(p'_{12}, p'_3, p_{12}, p_3, q) \psi_\alpha(p_{12}, p_3) \end{aligned} \quad (\text{B.17})$$

with the partial wave decomposed operator

$$\begin{aligned} \mathcal{O}_{(\alpha' \alpha) \xi m_\xi}^{(123)} &= \sum_{m'_3 m_{j_3}} \sum_{\xi_{12} m_{\xi_{12}}} \sum_{\xi_3 m_{\xi_3}} \langle j_3 m_{j_3}, \xi m_\xi | j'_3 m_{j'_3} \rangle \langle \xi_{12} m_{\xi_{12}}, \xi_3 m_{\xi_3} | \xi m_\xi \rangle \\ &\quad \times (-)^{-j_{12}+j'_{12}+I_3-I'_3-j_3+j'_3+\xi_{12}-\xi_3+\xi} \sqrt{\hat{j}'_{12} \hat{I}'_3 \hat{\xi} \hat{j}_3} \begin{Bmatrix} \xi_3 & \xi & \xi_{12} \\ I_3 & j_3 & j_{12} \\ I'_3 & j'_3 & j'_{12} \end{Bmatrix} \mathcal{O}_{(\alpha' \alpha) \xi_{12} m_{\xi_{12}}}^{(12)} \mathcal{O}_{(\alpha' \alpha) \xi_3 m_{\xi_3}}^{(3)}, \end{aligned} \quad (\text{B.18})$$

which can be rewritten by individual decomposed operators of each sub system. Note that $\mathcal{O}^{(S)}$ just depends on the quantum numbers of the subsystem (S) and one only has to compute sums over the operator dimensions.

In the derivation of this decomposition, the following identity¹ was used

$$\begin{aligned} &\frac{\hat{\xi}}{\hat{j}'_3} \sum_{m_{j_{12}} m_{I_3}} \sum_{m'_{j'_{12}} m'_{I'_3}} \sum_{m_{j_3} m_{j'_3}} \langle j_{12} m_{j_{12}}, \xi_{12} m_{\xi_{12}} | j'_{12} m_{j'_{12}} \rangle \langle I_3 m_{I_3}, \xi_3 m_{\xi_3} | I'_3 m_{I'_3} \rangle \\ &\quad \times \langle j_{12} m_{j_{12}}, I_3 m_{I_3} | j_3 m_{j_3} \rangle \langle j'_{12} m_{j'_{12}}, I'_3 m_{I'_3} | j'_3 m_{j'_3} \rangle \langle j_3 m_{j_3}, \xi m_\xi | j'_3 m_{j'_3} \rangle \\ &= (-)^{-j_{12}+j'_{12}+I_3-I'_3-j_3+j'_3+\xi_{12}-\xi_3+\xi} \sqrt{\hat{j}'_{12} \hat{I}'_3 \hat{\xi} \hat{j}_3} \langle \xi_{12} m_{\xi_{12}}, \xi_3 m_{\xi_3} | \xi m_\xi \rangle \begin{Bmatrix} \xi_3 & \xi & \xi_{12} \\ I_3 & j_3 & j_{12} \\ I'_3 & j'_3 & j'_{12} \end{Bmatrix}. \end{aligned} \quad (\text{B.19})$$

B.3 Advantage of operator decomposition

Because spin-independent DM scattering has been invested one finds that $m_\xi = 0$. Also, operators usually converge relatively fast in terms of their ranks: $\sigma \leq 2$. These facts

¹ This identity was analytically derived and test with Fortran for $j_i, \xi_i \in \{0, \frac{1}{2}, \dots, 3\}$.

drastically reduces the number of sums compared to the case where one has to sum over all m_l, m_s, m_j, \dots polarizations. Also, besides the reduction of sums in terms of the polarization quantum numbers, one can use a further trick to analytically execute one of the angular integrations. The spin matrix-element [see eq. (B.13)] is in the most cases proportional to structures $|\mathbf{k}| := |\mathbf{p} + \alpha\mathbf{p}' + \beta\mathbf{q}|$. Because the absolute of the vector \mathbf{k} just depends on the difference of azimuthal angles $\phi_p - \phi'_p$ (using $\mathbf{q} = q\hat{e}_z$), it is useful to split up the angular integrations and introduce new angles

$$\int d\phi_p \int d\phi'_p \mapsto \int d\phi \int d\Phi \quad (\text{B.20})$$

with

$$\phi := \phi_p - \phi'_p \quad \Phi := \frac{\phi_p + \phi'_p}{2} \quad \Rightarrow \quad \phi_p = \Phi + \frac{\phi}{2} \quad \phi'_p = \Phi - \frac{\phi}{2}. \quad (\text{B.21})$$

Using this transformation one obtains

$$\mathcal{O}_{(l'l)\lambda m_\lambda}^{(L)}(\hat{\mathbf{p}}', \hat{\mathbf{p}}) := \frac{\hat{\lambda}}{\hat{l}'} \sum_{m'_l m_l} \langle l m_l, \lambda m_\lambda | l' m'_l \rangle Y_{l' m'_l}(x', 0) Y_{l m_l}(x, 0) e^{i\phi m_l} \times e^{im_\lambda(\frac{\phi}{2} - \Phi)}, \quad (\text{B.22})$$

where it was used that $m_l + m_\lambda = m'_l$, and thus

$$-m'_l \phi'_p + m_l \phi_p = \frac{m_l + m'_l}{2} \phi + (m_l - m'_l) \Phi = (m_l + \frac{m_\lambda}{2}) \phi - m_\lambda \Phi. \quad (\text{B.23})$$

In the special case where $m_\xi = 0$, one knows that $m_\lambda = -m_\sigma$ and thus one can redefine eq. (B.11) to absorb one integration in the spin matrix-element

$$\begin{aligned} \mathcal{O}_{(s's)\sigma}^{(L)\lambda}(\xi m_\xi)(p', p, q) &= \sum_{m_\lambda m_\sigma} \langle \lambda m_\lambda, \sigma m_\sigma | \xi 0 \rangle \\ &\times \int dx' \int dx \int d\phi \tilde{\mathcal{O}}_{(l'l)\lambda m_\lambda}^{(L)}(x', x, \phi) \tilde{\mathcal{O}}_{(s's)\sigma m_\sigma}^{(S)}(p', p, q, x', x, \phi) \end{aligned} \quad (\text{B.24})$$

with

$$\tilde{\mathcal{O}}_{(l'l)\lambda m_\lambda}^{(L)}(x', x, \phi) := \frac{\hat{\lambda}}{\hat{l}'} \sum_{m'_l m_l} \langle l m_l, \lambda m_\lambda | l' m'_l \rangle Y_{l' m'_l}(x', 0) Y_{l m_l}(x, 0) e^{i\phi m_l} \quad (\text{B.25})$$

$$\tilde{\mathcal{O}}_{(s's)\sigma m_\sigma}^{(S)}(p', p, q, x', x, \phi) := \frac{\hat{\sigma}}{\hat{s}'} \sum_{m'_s m_s} \langle s m_s, \sigma m_\sigma | s' m'_s \rangle \int d\Phi \langle s' m'_s | \hat{\mathcal{O}}(\mathbf{p}', \mathbf{p}, \mathbf{q}) | s m_s \rangle \times e^{im_\sigma(\Phi - \frac{\phi}{2})} \quad (\text{B.26})$$

In most of the cases, the last expression is actually either Φ independent or easy to integrate. This drastically reduces the numerical scaling and is eventually used for computation.

B.4 Example: Dark Matter two-nucleon operator

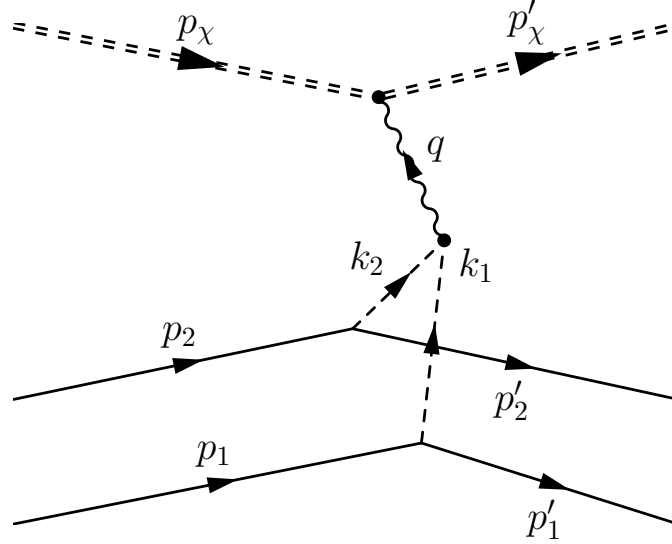


Figure B.1: DM-nucleon interaction through two-body pion exchange. DM corresponds to double dashed lines, pions to dashed lines and nucleons to solid lines. The wiggly line just visualizes the momentum transfer and is in principle absent. The arrows indicate the direction of the momentum three-vectors.

At the Next-to-Leading Order (NLO) for the isoscalar scattering currents one finds a two-nucleon operator where the DM particle interacts with the nucleons via a two-pion exchange [see fig. B.1]. The matrix-element in a single nucleon momentum basis is given by

$$\langle \mathbf{p}'_1, \mathbf{p}'_2 | \hat{J}_{q^{(is)}, 2b} | \mathbf{p}_1, \mathbf{p}_2 \rangle = -2c_\chi \left(\frac{g_A}{2f_\pi} \right)^2 \left(\frac{\boldsymbol{\sigma}_1 \cdot \mathbf{k}_1}{\mathbf{k}_1^2 + m_\pi^2} \right) \left(\frac{\boldsymbol{\sigma}_2 \cdot \mathbf{k}_2}{\mathbf{k}_2^2 + m_\pi^2} \right) \tau_1 \cdot \tau_2, \quad (\text{B.27})$$

with the axial coupling $g_A = 1.27$, the pion constant $f_\pi = 92.4 \text{ MeV}$, the average pion mass $m_\pi = 138.04 \text{ MeV}$. The unknown coupling of this operator c_χ (between the pions and DM) corresponds to the strength of the interaction and the additional factor of two comes from the number of nucleon line contractions. The single nucleon momenta are expressed in terms of relative and total momenta

$$\mathbf{p} := \frac{\mathbf{p}_1 - \mathbf{p}_2}{2}, \quad \mathbf{p}' := \frac{\mathbf{p}'_1 - \mathbf{p}'_2}{2}, \quad \mathbf{P} := \mathbf{p}_1 + \mathbf{p}_2, \quad \mathbf{P}' := \mathbf{p}'_1 + \mathbf{p}'_2, \quad (\text{B.28})$$

$$\mathbf{k}_1 = \frac{\mathbf{q}}{2} + \mathbf{p} - \mathbf{p}', \quad \mathbf{k}_2 = \frac{\mathbf{q}}{2} - \mathbf{p} + \mathbf{p}'. \quad (\text{B.29})$$

The partial wave decomposed isospin structure can be found in [table B.1](#).

t'	t	ξ_t	m_{ξ_t}	$\mathcal{O}_{(t't)\xi_t m_{\xi_t}}$
0	0	0	0	-3
1	1	0	0	1

Table B.1: Operator partial wave decompositions for $\mathcal{O} = \tau_1 \cdot \tau_2$ according to eq. (B.2). Elements have been evaluated for two-nucleon states. All other matrix-elements for different ξ_t , m_{ξ_t} are zero.

The spin-momentum decomposition structure of the operator

$$\tilde{\mathcal{O}}_{(s's)\sigma m_\sigma}^{(S,q)} := -\frac{\hat{\sigma}}{\hat{s}'} \sum_{m_s m'_s} \langle s m_s, \sigma m_\sigma | s' m'_s \rangle \times \int d\Phi \langle s' m'_s | \boldsymbol{\sigma}_1 \cdot \mathbf{k}_1 \boldsymbol{\sigma}_2 \cdot \mathbf{k}_2 | s m_s \rangle e^{im_\sigma(\Phi - \phi/2)}, \quad (\text{B.30})$$

for the angles of the relative momenta $\phi := \phi_p - \phi'_p$ and $\Phi := \frac{\phi_p + \phi'_p}{2}$ is given by eleven channels presented in table B.2 for $c_\chi = 1$ in respective units.

s'	s	σ	m_σ	$\tilde{\mathcal{O}}_{(s's)\sigma m_\sigma}^{(S,q)}$
0	0	0	0	$-2\pi(\alpha - 2\gamma)$
0	1	1	-1	$\sqrt{6}\pi\beta q$
0	1	1	1	$\sqrt{6}\pi\beta^* q$
1	0	1	-1	$\sqrt{2}\pi\beta q$
1	0	1	1	$\sqrt{2}\pi\beta^* q$
1	1	0	0	$\frac{2}{3}\pi(\alpha - 2\gamma)$
1	1	2	-2	$2\sqrt{\frac{5}{3}}\pi\beta^2$
1	1	2	-1	$4\sqrt{\frac{5}{3}}\pi\beta\delta$
1	1	2	0	$\frac{1}{3}\sqrt{10}\pi(\alpha + 3\delta^2 - 3 \beta ^2 - 2\gamma - \frac{3}{4}q^2)$
1	1	2	1	$-4\sqrt{\frac{5}{3}}\pi\beta^*\delta$
1	1	2	2	$2\sqrt{\frac{5}{3}}\pi(-\beta^*)^2$

Table B.2: Partial wave decomposition of the spin operator in eq. (B.30) for all non-zero spin channels. The coefficients α , β and γ are defined in eq. (B.31).

The coefficients used table B.2 are given by

$$\begin{aligned} \alpha &:= p^2 + p'^2 - \left(\frac{q}{2}\right)^2 & \beta &:= e^{i\phi} p \sin(\theta_p) - p' \sin(\theta'_p) \\ \gamma &:= pp' \left(\cos(\theta_p) \cos(\theta'_p) + \cos(\phi) \sin(\theta_p) \sin(\theta'_p) \right) & \delta &:= p \cos(\theta_p) - p' \cos(\theta'_p). \end{aligned} \quad (\text{B.31})$$

Furthermore, the momenta $\mathbf{k}_{1,2}$ and denominator itself are given by

$$\mathbf{k}_{1,2}^2 = \alpha - 2\gamma \pm \delta q + \frac{1}{2}q^2 \quad \Rightarrow \quad (\mathbf{k}_1^2 + m_\pi^2)(\mathbf{k}_2^2 + m_\pi^2) = \left(\alpha - 2\gamma + \frac{1}{2}q^2 + m_\pi^2 \right)^2 - \delta^2 q^2 . \quad (\text{B.32})$$

This structure is spin independent. All these terms are combined and numerically integrated to obtain the total partial wave decomposed operator.

B.5 Current normalization

We have normalized our currents such that the scattering amplitude is given as

$$\left| \mathcal{M}_T(\mathbf{q}^2) \right|^2 = (2m_T)^2 (2m_\chi)^2 \sum_{\xi=0}^{\infty} \left| \langle \Psi_{T,j} \mid \hat{J}(\mathbf{q}^2, \xi) \mid \Psi_{T,j} \rangle \right|^2 . \quad (\text{B.33})$$

In the limit of $q \rightarrow 0$, one can show that for spin-conserving structures, only contributions with $\xi = 0$ survive. Following eq. (2.24), we further define

$$\langle \hat{J}_a \rangle_T := \frac{\langle \Psi_{T,j} \mid \hat{J}_a(\mathbf{q}^2, \xi) \mid \Psi_{T,j} \rangle}{A \mid \sigma_{\pi N} c_\chi \mid} \Bigg|_{\xi=0} . \quad (\text{B.34})$$

For benchmarking purposes, we present the expectation values for the isoscalar quark-DM two-nucleon contributions at $\mathbf{q} = 0$ in table B.3. We estimate the numerical uncertainty to be below the 1%-level with respect to the value of each matrix-element.

NN interaction	$\langle \hat{J}_{q^{(is)},2b} \rangle_{2\text{H}}$	$\langle \hat{J}_{q^{(is)},2b} \rangle_{3\text{H}}$	$\langle \hat{J}_{q^{(is)},2b} \rangle_{3\text{He}}$
AV18 + URB IXF	/	$2.62 \cdot 10^{-3}$	$2.52 \cdot 10^{-3}$
AV18	$1.58 \cdot 10^{-4}$	$2.62 \cdot 10^{-3}$	$2.83 \cdot 10^{-3}$
CDB + TM	/	$1.38 \cdot 10^{-3}$	$1.51 \cdot 10^{-3}$
CDB	$1.17 \cdot 10^{-4}$	$1.47 \cdot 10^{-3}$	$1.62 \cdot 10^{-3}$
NIJM	$1.57 \cdot 10^{-4}$	/	/
LO (Q^0) Λ_1	$2.28 \cdot 10^{-3}$	$-1.46 \cdot 10^{-3}$	$-1.45 \cdot 10^{-3}$
LO (Q^0) Λ_2	$-5.95 \cdot 10^{-4}$	$-1.77 \cdot 10^{-3}$	$-1.77 \cdot 10^{-3}$
LO (Q^0) Λ_3	$-2.66 \cdot 10^{-3}$	$-2.01 \cdot 10^{-3}$	$-2.02 \cdot 10^{-3}$
LO (Q^0) Λ_4	$-4.12 \cdot 10^{-3}$	$-2.20 \cdot 10^{-3}$	$-2.22 \cdot 10^{-3}$
LO (Q^0) Λ_5	$-5.13 \cdot 10^{-3}$	$-2.36 \cdot 10^{-3}$	$-2.38 \cdot 10^{-3}$
NLO (Q^2) Λ_1	$1.17 \cdot 10^{-4}$	$1.48 \cdot 10^{-3}$	$1.62 \cdot 10^{-3}$
NLO (Q^2) Λ_2	$8.80 \cdot 10^{-3}$	$7.08 \cdot 10^{-4}$	$8.18 \cdot 10^{-4}$
NLO (Q^2) Λ_3	$6.09 \cdot 10^{-3}$	$2.72 \cdot 10^{-5}$	$1.08 \cdot 10^{-4}$
NLO (Q^2) Λ_4	$3.70 \cdot 10^{-3}$	$-5.47 \cdot 10^{-4}$	$-4.91 \cdot 10^{-4}$
NLO (Q^2) Λ_5	$1.65 \cdot 10^{-3}$	$-1.01 \cdot 10^{-3}$	$-9.78 \cdot 10^{-4}$
N ² LO (Q^3) Λ_1	$1.10 \cdot 10^{-4}$	$1.37 \cdot 10^{-3}$	$1.51 \cdot 10^{-3}$
N ² LO (Q^3) Λ_2	$8.59 \cdot 10^{-3}$	$7.25 \cdot 10^{-4}$	$8.39 \cdot 10^{-4}$
N ² LO (Q^3) Λ_3	$6.17 \cdot 10^{-3}$	$1.06 \cdot 10^{-4}$	$1.93 \cdot 10^{-4}$
N ² LO (Q^3) Λ_4	$3.97 \cdot 10^{-3}$	$-4.39 \cdot 10^{-4}$	$-3.75 \cdot 10^{-4}$
N ² LO (Q^3) Λ_5	$2.04 \cdot 10^{-3}$	$-8.98 \cdot 10^{-4}$	$-8.55 \cdot 10^{-4}$
N ³ LO (Q^4) Λ_1	$7.31 \cdot 10^{-3}$	$7.54 \cdot 10^{-4}$	$8.61 \cdot 10^{-4}$
N ³ LO (Q^4) Λ_2	$1.09 \cdot 10^{-4}$	$1.66 \cdot 10^{-3}$	$1.81 \cdot 10^{-3}$
N ³ LO (Q^4) Λ_3	$1.29 \cdot 10^{-4}$	$2.21 \cdot 10^{-3}$	$2.38 \cdot 10^{-3}$
N ³ LO (Q^4) Λ_4	$1.37 \cdot 10^{-4}$	$2.44 \cdot 10^{-3}$	$2.62 \cdot 10^{-3}$
N ³ LO (Q^4) Λ_5	$1.38 \cdot 10^{-4}$	$2.50 \cdot 10^{-3}$	$2.69 \cdot 10^{-3}$
N ⁴ LO (Q^5) Λ_1	$1.06 \cdot 10^{-4}$	$1.62 \cdot 10^{-3}$	$1.77 \cdot 10^{-3}$
N ⁴ LO (Q^5) Λ_2	$1.13 \cdot 10^{-4}$	$1.77 \cdot 10^{-3}$	$1.92 \cdot 10^{-3}$
N ⁴ LO (Q^5) Λ_3	$1.18 \cdot 10^{-4}$	$1.91 \cdot 10^{-3}$	$2.07 \cdot 10^{-3}$
N ⁴ LO (Q^5) Λ_4	$1.25 \cdot 10^{-4}$	$2.10 \cdot 10^{-3}$	$2.27 \cdot 10^{-3}$
N ⁴ LO (Q^5) Λ_5	$1.27 \cdot 10^{-4}$	$2.20 \cdot 10^{-3}$	$2.38 \cdot 10^{-3}$

Table B.3: Central values for spin-independent isoscalar-quark two-pion-exchange operators $\hat{J}_{q^{(is)},2b}$ for all applied wave functions at zero momentum transfer $\mathbf{q} = 0$. For more details, we refer to [appendix B.4](#).

NLEFT on GPUs

This chapter presents the ongoing effort to implement a new generation Nuclear Lattice Effective Field Theory (NLEFT) algorithm in a massively parallel and scalable manner and to make use of modern High Performance Computing (HPC) structures.

As it was presented in [chapter 3](#), the nuclear path integral is reformulated through the application of the transfer matrix on multi-nucleon states. The Hubbard-Stratonovitch (HS) transformation is then used to linearize the transfer matrix which recasts the exponential scaling in the number of nucleons to a polynomial scaling at the cost of an additional multi-dimensional integration. This multi-dimensional integration is numerically implemented through a stochastic Hybrid Monte Carlo (HMC) integration. Current NLEFT algorithms are parallelized in the number of stochastic samples (HMC trajectories), which effectively farm a massive integration over many independent cores. Even though this implementation is scalable, it is yet not possible to extend the scaling in terms of number of nucleons and the lattice sizes. This requires a more sophisticated implementation which must communicate intermediate results between individual computing units.

In order to minimize power consumption while allowing highly parallel computations, many core architectures like Graphics Processing Units (GPUs) have become increasingly popular. As it will be presented in this section, NLEFT is a perfect candidate for an implementation on GPUs because of its memory demands—whole HMC iterations can be executed on a single GPU.

The work presented in this chapter is the product of the collaboration¹ with the JSC² and especially Paul F. Baumeister—without whom the implementation on GPUs would not have been possible.

¹ I would like to *emphasize* that this collaboration exists because of the IAS colloquium 2016. It is not possible to evolve interdisciplinary synergies without reducing barriers, e.g., by providing a proper infrastructure.

² Jülich Supercomputing Centre, Forschungszentrum Jülich, 52425 Jülich, Germany.

C.1 Hybrid Monte Carlo integration

As it was presented in [chapter 3](#), the nuclear path integral is cast into a matrix-element of the *so-called* transfer matrix and the application of the transfer matrix on nuclear states can be written as the integration over a probability-density times a determinant

$$\mathcal{Z}(N_T) = \langle \Psi | \hat{T}^{N_T} | \Psi \rangle = \prod_{n_t=1}^{N_T} \left(\int d\phi P_N(\phi_{n_t} | 0, 1) \right) \det_{n'_a, n_a} \left| \langle \psi_{n'_a} | \hat{T}^{(1)}(\phi_1) \cdots \hat{T}^{(1)}(\phi_{N_t}) | \psi_{n_a} \rangle \right|, \quad (\text{C.1})$$

where: $n_t \in \{1, \dots, N_T\}$ — the index for time slice,
 $n_a \in \{1, \dots, A\}$ — the index for the nucleon,
 $P_N(x | \mu, \sigma^2)$ — the probability density for variable $x \sim N(\mu, \sigma^2)$ following a normal distribution with mean μ and variance σ^2 .

Furthermore, in the most simple case of a single contact interaction, the transfer matrix is given by

$$\hat{T}^{(1)}(a_T, \phi) \equiv : \exp \left\{ -\hat{H}_0 a_T + \sqrt{a_T c} \phi \hat{\rho} \right\} : . \quad (\text{C.2})$$

Here, \hat{H}_0 is the kinetic Hamiltonian, a_T the temporal lattice spacing and $\hat{\rho}$ a nucleon-number operator. The original action contains a contact term $\hat{V} = -c/2 \hat{\rho} \hat{\rho}$ with $c > 0$. In general the transfer matrix acts on coordinate, spin and isospin space. This will become relevant later on. For the sake of brevity, one can rewrite this as

$$\mathcal{Z}(N_T) = \int D[\phi] \bar{P}_N(\phi) \det |F(\phi, N_T)|, \quad (\text{C.3})$$

with: ϕ — the collective vector of auxiliary fields for all time slices
 $D[\phi]$ — the measure as a product of all individual ϕ_{n_t} intergations
 $\bar{P}_N(\phi)$ — the collective product of normal distributions for all ϕ_{n_t}
 $F(\phi, N_T)$ — the fermion matrix defined by the action of the transfer matrix and eventual matrix-element. The square matrix has A^2 entries.

Clearly, for sufficiently large N_T and considering that one has additional field components for each lattice site N_L^3 , the $N_T \times N_L^3$ dimensional integral cannot be computed directly. One must apply statistical Monte Carlo integration techniques like importance sampling to approximate the integral

$$\frac{1}{N_H} \sum_{n_H=1}^{N_H} \mathcal{O}(\phi^{(n_H)}) \xrightarrow{N_H \rightarrow \infty} \int D[\phi] P_D(\phi) \mathcal{O}(\phi) \equiv \langle \mathcal{O} \rangle . \quad (\text{C.4})$$

Here, the auxiliary fields follow the distribution $\phi^{(n_H)} \sim D$ and P_D is the associated probability density. In the context of nuclear physics, one usually calls the collection of fields which follow the distribution D an *ensemble of configurations*.

As the first guess, one could identify the product of densities $\bar{P}_N(\boldsymbol{\phi})$ in eq. (C.3) as the Markov Chain (MC) probability distribution $P_D(\boldsymbol{\phi})$ and the Slater determinant of the fermion matrix $F[\boldsymbol{\phi}]$ as the observable $\mathcal{O}(\boldsymbol{\phi})$. Because the collective probability distribution of the auxiliary fields at different time slices is a product of normal distributions with mean $\mu = 0$ and variance $\sigma^2 = 1$, the generation of the ensemble is easy and inexpensive. However, the sum converges relatively slowly. This is the case because certain regions of the integration correspond to minimal values for the observable. For example, the determinant is zero if two nucleons with the same quantum numbers accidentally hop on the same site.

In order to optimize the rate of convergence for the summation, the next idea is to include the fermion determinant $\det |F(\boldsymbol{\phi})|$ into the probability distribution $P_D(\boldsymbol{\phi})$. Thus the MC knows which values cause minimal integration results and weights them accordingly. Note that one has to take more care in this case. Defining $N_T^- \equiv N_T - 1$, explicitly writing the temporal dimensions in the exponents and multiplying by unity in terms of a normal distribution, one has

$$\frac{\mathcal{Z}(N_T^-)}{\mathcal{Z}(N_T)} = \frac{\int \mathcal{D}^{N_T^-}[\boldsymbol{\phi}] \bar{P}_N^{N_T^-}(\boldsymbol{\phi}) \det |F(\boldsymbol{\phi}, N_T^-)|}{\int \mathcal{D}^{N_T}[\boldsymbol{\phi}] \bar{P}_N^{N_T}(\boldsymbol{\phi}) \det |F(\boldsymbol{\phi}, N_T)|} \times \int d\phi_{N_T} P(\phi_{N_T}|0, 1) \xrightarrow{N_T \rightarrow \infty} \exp\{a_T E_0\}. \quad (\text{C.5})$$

If one slightly reorders terms and introduces an one in terms of the fermion determinant at N_T steps, one finally finds

$$\frac{\mathcal{Z}(N_T^-)}{\mathcal{Z}(N_T)} = \int \mathcal{D}^{N_T}[\boldsymbol{\phi}] \underbrace{\frac{\bar{P}_N^{N_T}(\boldsymbol{\phi}) \det |F(\boldsymbol{\phi}, N_T)|}{\int \mathcal{D}^{N_T}[\boldsymbol{\phi}] \bar{P}_N^{N_T}(\boldsymbol{\phi}) \det |F(\boldsymbol{\phi}, N_T)|}}_{\stackrel{!}{=} P_D(\boldsymbol{\phi})} \underbrace{\frac{\det |F(\boldsymbol{\phi}, N_T^-)|}{\det |F(\boldsymbol{\phi}, N_T)|}}_{\stackrel{!}{=} \mathcal{O}(\boldsymbol{\phi})}. \quad (\text{C.6})$$

Thus the fermion determinant is incorporated in the probability distribution P_D which is used to generate new configurations and the observable effectively becomes the ratio of the fermion determinants at two different time slices. Note that one has a determinant in the denominator of the observable, however, since a zero determinant also corresponds to zero probability, one is relatively safe.

The preferred choice for generating an ensemble or MC of fields is based on the Metropolis-Hastings algorithm [174, 175]. Given a configuration $\boldsymbol{\phi}$ one wants to generate a new configuration $\boldsymbol{\phi}'$ with transition probability $P_T(\boldsymbol{\phi}'|\boldsymbol{\phi})$. The Markov process asymptotically generates configurations $\boldsymbol{\phi} \sim D$ if D is ergodic and it is a stationary distribution. A sufficient but not necessary requirement is that detailed balance is fulfilled, e.g., it is equally likely to find inverse transitions

$$P_D(\boldsymbol{\phi})P_T(\boldsymbol{\phi}'|\boldsymbol{\phi}) = P_D(\boldsymbol{\phi}')P_T(\boldsymbol{\phi}|\boldsymbol{\phi}'). \quad (\text{C.7})$$

Practically, the transition probability $P_T(\boldsymbol{\phi}'|\boldsymbol{\phi})$ is a product of the *proposal probability* $P_P(\boldsymbol{\phi}'|\boldsymbol{\phi})$ of choosing a new configuration $\boldsymbol{\phi}'$ given $\boldsymbol{\phi}$ and the *acceptance probability*

$P_A(\phi'|\phi)$, which describes how likely it is to keep ϕ' given ϕ

$$P_T(\phi'|\phi) = P_A(\phi'|\phi)P_P(\phi'|\phi). \quad (\text{C.8})$$

A proper choice for acceptance distribution which fulfills detailed balance is given in the Metropolis algorithm by

$$P_A(\phi'|\phi) = \min \left(1, \frac{P_D(\phi') P_P(\phi|\phi')}{P_D(\phi) P_P(\phi'|\phi)} \right). \quad (\text{C.9})$$

The ‘so-called’ Hybrid Monte Carlo algorithm [176] is used to update the fields by introducing a specific proposal probability $P_P(\phi'|\phi)$. Thus, once one has defined the proposal probability, one has to verify that this choice enables detailed balance [eq. (C.7)].

The probability density in eq. (C.6) can be adjusted by the introduction of another auxiliary field $\boldsymbol{\pi}$

$$P_D(\phi) = \int D[\boldsymbol{\pi}] \tilde{P}_D[\boldsymbol{\pi}, \phi] \propto \int D[\boldsymbol{\pi}] \int D[\phi] \exp \{-H(\boldsymbol{\pi}, \phi)\},$$

$$H(\boldsymbol{\pi}, \phi) = \frac{\boldsymbol{\pi}^2}{2} + \frac{\phi^2}{2} - \log(\det |F(\phi)|), \quad (\text{C.10})$$

where the normalization factors have been left out. As the notation in eq. (C.10) already suggests, the argument of the exponential looks like a Hamiltonian where $\boldsymbol{\pi}$ is the conjugate momentum to ϕ . Thus one can make use of the Hamiltonian equations of motions to evolve the fields without changing the value of $H(\boldsymbol{\pi}, \phi)$

$$\dot{\boldsymbol{\pi}} = -\frac{\partial}{\partial \phi} H(\boldsymbol{\pi}, \phi), \quad \dot{\phi} = \frac{\partial}{\partial \boldsymbol{\pi}} H(\boldsymbol{\pi}, \phi). \quad (\text{C.11})$$

The specific (improper) proposal density suggested by the HMC algorithm is an unique and deterministic mapping from $\{\boldsymbol{\pi}, \phi\} \rightarrow \{\boldsymbol{\pi}', \phi'\}$, depending on an additional external parameter τ , namely a delta function for the configuration pair

$$P_P(\{\boldsymbol{\pi}', \phi'\}|\{\boldsymbol{\pi}, \phi\}, \tau) = \delta(\{\boldsymbol{\pi}', \phi'\} - \{\boldsymbol{\pi}(\tau), \phi(\tau)\}). \quad (\text{C.12})$$

The quantities $\{\boldsymbol{\pi}(\tau), \phi(\tau)\}$ in eq. (C.12) are the Molecular Dynamics (MD) evolved fields, e.g., they are the solutions to the Hamiltonian equations of motions at MD flow time τ with initial conditions $\{\boldsymbol{\pi}(0), \phi(0)\} = \{\boldsymbol{\pi}, \phi\}$. In other words, for a pair of input fields $\{\boldsymbol{\pi}, \phi\}$ one proposes the evolved fields $\{\boldsymbol{\pi}(\tau), \phi(\tau)\}$.

The acceptance probability for new configurations given the old configurations depends on the energy difference for old and new values of the Hamiltonian

$$P_A(\{\boldsymbol{\pi}', \phi'\}|\{\boldsymbol{\pi}, \phi\}) = \min(1, \exp\{H(\boldsymbol{\pi}', \phi') - H(\boldsymbol{\pi}, \phi)\}). \quad (\text{C.13})$$

Note that if it is possible to use an exact MD integration, the Hamiltonian will be constant

and independent of the flow time. Thus the acceptance rate would be one. Once one implements a numerical derivative, this will not be the case. Here, the MD flow time parameter τ provides a control on how much the fields are changing and eventually determines the acceptance rate. It is usually tuned to $P_A(\phi'|\phi, \tau) \approx 2/3$ to generate sufficiently decorrelated configurations in an acceptable amount of time.

Finally, the marginalized transition probability is given by

$$P_T(\phi'|\phi, \tau) = \int D[\boldsymbol{\pi}] \bar{P}_N(\boldsymbol{\pi}) \int D[\boldsymbol{\pi}'] P_P(\{\boldsymbol{\pi}', \phi'\}|\{\boldsymbol{\pi}, \phi\}, \tau) P_A(\{\boldsymbol{\pi}', \phi'\}|\{\boldsymbol{\pi}, \phi\}) , \quad (\text{C.14})$$

and one can indeed show that it fulfills detailed balance. The only important quantity is that the MD integration remains reversible

$$P_P(\{\boldsymbol{\pi}', \phi'\}|\{\boldsymbol{\pi}, \phi\}, \tau) = P_P(\{-\boldsymbol{\pi}, \phi\}|\{-\boldsymbol{\pi}', \phi'\}, \tau) . \quad (\text{C.15})$$

One is not able to guarantee detailed balance if this is not the case. Typically, one employs a leap frog [see [fig. C.1](#)] integrator to ensure reversibility.

Finally, the computation of the observable is given by the sum over $n_H = 1, \dots, N_H$ pairs $\{\boldsymbol{\pi}^{(n_H)}, \phi^{(n_H)}\}$, but since the observable does not depend on $\boldsymbol{\pi}$, one does not need to store the $\boldsymbol{\pi}$ fields. They exist just for the purpose of evolving ϕ .

From a practical point of view, the ensemble of ϕ fields is generated in the following manner. Initially, one computes a normal distributed $\phi^{(0,0)}$ field. This does in principal not follow the correct distribution, but suffices as a starting point. Next, one generates a normal distributed $\boldsymbol{\pi}^{(0,0)}$ field and computes the initial $H(\boldsymbol{\pi}^{(0,0)}, \phi^{(0,0)})$. Because the $\boldsymbol{\pi}$ fields indeed follow a normal distribution, one can trust these values from the beginning. As the next step, one numerically integrates the equation of motion to obtain $\phi^{(0, N_M)}$ and $\boldsymbol{\pi}^{(0, N_M)}$, where n_M is the number of molecular dynamic integration steps. At this point one tests the acceptance of the new configurations at $(0, N_M)$ against the initial configurations $(0, 0)$ and if positive $\{\boldsymbol{\pi}^{(0,0)}, \phi^{(0,0)}\} \leftarrow \{\boldsymbol{\pi}^{(0, n_M)}, \phi^{(0, n_M)}\}$, otherwise the initial configurations stay the same. Following this, one repeats the same procedure with $n_H \rightarrow n_H + 1$ but chooses $\phi(n_H + 1, 0)$ to be the last accepted field. The same procedure for the NLEFT algorithm is presented in [fig. C.2](#). In the next section, this will be worked out in detail for NLEFT.

C.2 Hybrid Monte Carlo implementation for NLEFT

C.2.1 Computational details

In the update procedure for the auxiliary fields, one has to compute the derivatives of the Hamiltonian with respect to the HS auxiliary field ϕ and its conjugated momentum field π . While the derivative of the Hamiltonian with respect to π is straight forward

$$\dot{\phi} = \frac{\partial}{\partial \pi} H(\pi, \phi) = \pi, \quad (\text{C.16})$$

the derivative of the Hamiltonian with respect to ϕ —the computation of the ‘so-called’ *force term*—is the bottle neck of the computation because it involves both, the inverse and the derivative of the fermion determinant with respect to ϕ

$$\dot{\pi} = -\frac{\partial}{\partial \phi} H(\pi, \phi) = -\phi + \frac{\partial}{\partial \phi} \log(\det |F(\phi)|) = -\phi + \text{Tr} \left[F^{-1}(\phi) \frac{\partial}{\partial \phi} F(\phi) \right]. \quad (\text{C.17})$$

Once one has computed the trace in the previous equation, the discretized update is straightforwardly implemented through, e.g., a leapfrog algorithm [see fig. C.1]. Explicitly writing out all indices for the computation of the force term, one has

$$F_{n'_A n_A}(\phi) = \sum_{n'_r n_r} \sum_{n'_c n_c} \psi_{n'_a n'_r n'_c}^* \mathcal{T}_{n'_r n_r; n'_c n_c}(\phi) \psi_{n_a n_r n_c}, \quad (\text{C.18})$$

$$\mathcal{T}_{n_{r_1} n_{r_{N_T}}; n_{c_1} n_{c_{N_T}}}(\phi) \equiv \prod_{n_t=1}^{N_T-1} \left(\sum_{n_{r_{n_t}} n_{c_{n_t}}} T_{n_{r_{n_t}} n_{r_{n_t+1}}; n_{c_{n_t}} n_{c_{n_t+1}}}^{(1)}(\phi_{n_{r_{n_t}} n_{n_t}}) \right), \quad (\text{C.19})$$

$$T_{n'_r n_r; n'_c n_c}^{(1)}(\phi_{n_r n_t}) = \delta_{n'_r n_r} \delta_{n'_c n_c} - a_T (H_0)_{n'_r n_r} \delta_{n'_c n_c} - \sqrt{a_T c} \phi_{n_r n_t} \delta_{n'_r n_r} \delta_{n'_c n_c}, \quad (\text{C.20})$$

where: $n_t \in \{1, \dots, N_T\}$ — the index for time slice,
 $n_r \in \{1, \dots, N_L^3\}$ — the index for spatial sites,
 $n_a \in \{1, \dots, A\}$ — the index for the nucleon,
 $n_c \in \{\uparrow, \downarrow\} \otimes \{p, n\}$ — the combined spin and isospin index for respective nucleon.

In practice one does not compute the product of the transfer matrix over all time slices as depicted in eq. (C.19), but rather the euclidian time evolve wave function, e.g., one applies the transfer matrix at a given time slice to the wave function and repeats the procedure

$$\overleftarrow{\psi}_{n_{t+1}; n_a n_r n_c} \equiv \sum_{n'_r n'_c} T_{n_r n'_r; n_c n'_c}^{(1)}(a_T, \phi_{n'_r n_t}) \overleftarrow{\psi}_{n_t; n_a n'_r n'_c} \quad (\text{C.21})$$

```

import numpy as np
class LeapfrogIntegrator(object):
    #-----
    def __init__(self, Force, Nvec):
        """Input:
           function Force --- computes the force term for given configuration phi
           int      Nvec  --- size of the configuration vectors
        Usage:
           leapfrog = LeapfrogIntegrator(Force, Nvec)
           phi1, pi1 = leapfrog.integrate(N_M, eps)
           phi2, pi2 = leapfrog.integrate(N_M, eps, phi=phi1)
           phi3, pi3 = leapfrog.integrate(N_M, eps, phi=phi2, pi=-pi2)
        """
        self.Force = Force
        self.Nvec  = Nvec
    #-----
    def _update_pi(self, phi, pi, step_size):
        return pi + step_size*self.Force(phi)
    #-----
    def _update_phi(self, phi, pi, step_size):
        return phi + step_size*pi
    #-----
    def integrate(self, N_M, step_size, phi=None, pi=None):
        """Input:
           int      N_M      --- number of Molecular Dynamics steps
           double  step_size --- step size of Molecular Dynamics steps
           vector  phi, pi   --- configurations (optional)
        """
        if pi is None:
            pi = np.random.normal(size=self.Nvec)
        if phi is None:
            phi = np.random.normal(size=self.Nvec)
        for n in range(N_M):
            phi = self._update_phi(phi, pi, step_size/2)
            pi = self._update_pi(phi, pi, step_size)
            phi = self._update_phi(phi, pi, step_size/2)
        return phi, pi
    
```

Figure C.1: Example for a numerical leapfrog integration implemented in **python**. Input to the integrator is a function **Force** which implements eq. (C.17). The integration depends on the input configuration **phi**, the number of MD steps **N_M** and the respective step size **step_size**. This integrator is reversible, e.g, **phi1==phi3** (up to **Force** precision).

$$\vec{\psi}_{n_t-1; n_a n_r n_c} \equiv \sum_{n'_r n'_c} T_{n_r n'_r; n_c n'_c}^{(1)}(a_T, \phi_{n'_r n_t}) \vec{\psi}_{n_t; n_a n'_r n'_c}, \quad (\text{C.22})$$

where the arrows indicate the direction of evolution, e.g., ‘ \rightarrow ’ corresponds to the trajectory of auxiliary fields $\phi_{n'_t}$ from $n'_t = N_T \rightarrow n'_t = n_t$ and ‘ \leftarrow ’ to $n'_t = 1 \rightarrow n'_t = n_t$ and the boundaries (independent of direction) are as follows $\psi_{N_T; n_a n_r n_c} \equiv \psi_{1; n_a n_r n_c} \equiv \psi_{n_a n_r n_c}$. Note that there is a difference if one evolves the fields from $n_t = 1$ to $N_T/2$ or from

$n_t = N_T$ to $N_T/2$, because the evolution tracks in general depend on different auxiliary fields, e.g. $\phi_{n_r N_T-1} \neq \phi_{n_r 2}$. Thus a matrix matrix multiplication becomes a matrix vector multiplication.

Also, since one has vectors at both ends of the product for computing the fermion matrix, one can update both ends in parallel and compute the fermion matrix eq. (C.18) as a scalar product at any time step n_t in the allowed interval

$$F_{n'_a n_a}(\phi) = \sum_{n_r n_c} \left(\vec{\psi}_{n_t; n'_a n_r n_c} \right)^* \overleftarrow{\psi}_{n_t; n_a n_r n_c}, \quad n_t \in \{1, \dots, N_T\}. \quad (\text{C.23})$$

Finally, the remaining task is the computation of the derivative of the fermion matrix

$$\begin{aligned} \frac{\partial}{\partial \phi_{n_r n_t}} F_{n'_a n_a}(\phi) &= \sum_{n'_r n'_c} \left(\vec{\psi}_{n_t; n'_a n'_r n'_c} \right)^* \left(\frac{\partial}{\partial \phi_{n_r n_t}} \overleftarrow{\psi}_{n_t; n_a n'_r n'_c}(\phi_{n'_r n_t}, \dots) \right) \\ &= \sum_{n'_r n'_c} \left(\vec{\psi}_{n_t; n'_a n'_r n'_c} \right)^* \sum_{\bar{n}'_r \bar{n}'_c} \left(\frac{\partial}{\partial \phi_{n_r n_t}} T_{n'_r \bar{n}'_r; n'_c \bar{n}'_c}^{(1)}(a_T, \phi_{n'_r n_t}) \right) \overleftarrow{\psi}_{n_t-1; n_a \bar{n}'_r \bar{n}'_c} \\ &= \sqrt{a_T c} \sum_{n'_c} \left(\vec{\psi}_{n_t; n'_a n_r n'_c} \right)^* \overleftarrow{\psi}_{n_t-1; n_a n_r n'_c}, \end{aligned} \quad (\text{C.24})$$

where it was first used that only the ‘from the right evolved field’ at $n'_t = n_t$ depends on n_t and the definition of the transfer matrix was used to compute the derivative of the auxiliary field. Finally, to compute the force term needed for the auxiliary field update, one needs the fermion matrix (time independent) and the wave functions at each time step.

C.2.2 Hybrid Monte Carlo workflow

In contrast to Lattice Quantum Chromodynamics (LQCD), in NLEFT the system specific fermion determinant is included in the computation of the ensemble of auxiliary fields and thus the ensemble depends on the nuclear state. It is not worthwhile to export the configurations but rather generate them when needed. Fortunately, the generation of an ensemble is also less expansive than in LQCD computations. For this reason, the wave function and or fermion determinant are more important quantities of the computation.

In this section, the workflow for computing the auxiliary field computations $\phi^{(n_H, n_M)}$, $\pi^{(n_H, n_M)}$ and the wave functions $\psi^{(n_H, n_M)}$ for all time slices is presented. Hereby, $n_H = 1, \dots, N_H$ is the size of the HMC ensemble and $n_M = 1, \dots, N_M$ is the number of MD steps in the intermediate integration. While it is expected that increasing N_H is correlated with decreasing the statistical uncertainty of the result, N_M influences the correlation between different configurations. The workflow is also visualized in fig. C.2 and the following listings correspond to the numbers in the figure.

- (0) To evaluate the wave function from time slice $n_t = 1$ to time slice $n_t = N_T$, one needs the auxiliary field ϕ at the respective time slice. The initial auxiliary field is sampled according to a normal distribution

$$\phi^{(0,0)} \sim N(\mu = 0, \sigma = 1), \quad \pi^{(0,0)} \sim N(\mu = 0, \sigma = 1).$$

Note that this is a bad first approximation for ϕ . For this reason, in the beginning of a sampling procedure, one does several HMC updates $n_H = N_{therm}$ before actually measuring an observable to ensure that our distribution is sufficiently *thermalized*.

- (1) One evaluates the wave function from the first time slice to the last by multiplying with the transfer matrix which depends on the auxiliary field of the respective time slice [see eqs. (C.21) and (C.22)]. This can be done through a pinch update by evaluating the wave function from the left and from the right. Once the wave functions are available at all time slices, one can compute the fermion matrix.
- (2) One computes the Hamiltonian of the system [eq. (C.10)] given by

$$H[\phi^{(n_H, n_M)}, \pi^{(n_H, n_M)}] = \sum_{n_r, n_t} \frac{1}{2} \left(\pi_{n_r n_t}^{(n_H, n_M)} \right)^2 + \frac{1}{2} \left(\phi_{n_r n_t}^{(n_H, n_M)} \right)^2 - \log \left(\det \left| F \left(\phi^{(n_H, n_M)} \right) \right| \right). \quad (\text{C.25})$$

Because all the quantities are already available, this can be completely done in parallel.

- One now enters the HMC workflow. Here all the values $\phi^{(n_H, 0)}$, $\psi^{(n_H, 0)}$ and $H^{(n_H, 0)}$ are stored.
- (A) One executes an HMC step to update $\pi^{(n_H, 0)} \rightarrow \pi^{(n_H+1, 0)}$, $\phi^{(n_H, 0)} \rightarrow \phi^{(n_H+1, 0)}$ and $\psi^{(n_H, 0)} \rightarrow \psi^{(n_H+1, 0)}$.
- One now enters the MD workflow. An initial random field $\pi^{(n_H, 0)}$, according to a normal distribution with $\mu = 0$ and $\sigma = 1$, is sampled.
- (B) One executes an MD step to update $\pi^{(n_H, n_M)} \rightarrow \pi^{(n_H, n_M+1)}$, $\phi^{(n_H, n_M)} \rightarrow \phi^{(n_H, n_M+1)}$ and $\psi^{(n_H, n_M)} \rightarrow \psi^{(n_H, n_M+1)}$.

- (3) One updates $\phi^{(n_H, n_M)}$ according to

$$\phi_{n_r n_t}^{(n_H, n_M+1/2)} = \phi_{n_r n_t}^{(n_H, n_M)} + \frac{\epsilon}{2} \pi_{n_r n_t}^{(n_H, n_M)}, \quad (\text{C.26})$$

where ϵ is the MD step size and the factor of one half is coming from the leapfrog procedure. This changes for different MD integrators.

- * One obtains the updated wave function $\psi^{(n_H, n_M+1/2)}$ depending on the updated auxiliary field $\phi^{(n_H, n_M+1/2)}$ like in (1).

(4) One updates the auxiliary $\boldsymbol{\pi}$ field to $\boldsymbol{\pi}^{(n_H, n_M+1)}$ according to

$$\pi_{n_r n_t}^{(n_H, n_M+1)} = \pi_{n_r n_t}^{(n_H, n_M)} - \epsilon \frac{\partial}{\partial \phi_{n_r n_t}^{(n_H, n_M+1/2)}} H \left(\boldsymbol{\pi}^{(n_H, n_M)}, \boldsymbol{\phi}^{(n_H, n_M+1/2)} \right), \quad (\text{C.27})$$

where the derivative of the fermion determinant is given by eq. (C.24).

* Repeat (3) to obtain $\boldsymbol{\phi}^{(n_H, n_M+1)}$.

* Repeat (1) to obtain $\boldsymbol{\psi}^{(n_H, n_M+1)}$.

– Repeat (B) until $n_M = N_M$.

(5) Measure the Hamiltonian $H^{(n_H, N_M)}$ like in (2) and compare to the stored value of the Hamiltonian $H^{(n_H, 0)}$. Sample a random (uniform) number $0 \leq r \leq 1$ and compare r to the exponential of the difference of these Hamiltonians to decide whether to accept or reject the new configuration [Eq. (C.13)]

$$r \leq \exp \left\{ +H^{(n_H, 0)} - H^{(n_H, N_M)} \right\} \Rightarrow \text{Accept the new configuration.}$$

(6) Store the new configurations [or the old, depending on (5)]

$$\begin{aligned} \text{accept : } & H^{(n_H+1, 0)} = H^{(n_H, N_M)} & \psi^{(n_H+1, 0)} = \psi^{(n_H, N_M)} & \phi^{(n_H+1, 0)} = \phi^{(n_H, N_M)} \\ \text{reject : } & H^{(n_H+1, 0)} = H^{(n_H, 0)} & \psi^{(n_H+1, 0)} = \psi^{(n_H, 0)} & \phi^{(n_H+1, 0)} = \phi^{(n_H, 0)}. \end{aligned}$$

- Repeat (A) until $n_H = N_{therm}$ without measuring the observable $\mathcal{O}(\boldsymbol{\phi}^{(n_H, 0)})$
- Repeat (A) until $n_H = N_H$ and measure the observable $\mathcal{O}(\boldsymbol{\phi}^{(n_H, 0)})$.

C.3 Implementation on GPUs and intermediate results

The code is implemented in **C++**, as it allows the same level of hardware control as **C**, but makes it possible to create more expressive algorithms for a high level description. For example, operator overloading is useful for writing intuitive code. Also, **C++** offers **template metaprogramming** which makes it possible to maintain multiple code versions in a comfortable way. Additionally, **template metaprogramming** offers a rich toolbox for performance tuning of a code: template parameters allow the compiler to evaluate important decisions at compile time and thus produces more efficient code. Example candidates for such compile time parameters are, e.g., the lattice spacings a_L and a_T , or the temporal and spatial numbers of nodes N_T and N_L^3 . Another advantage of **C++** is the direct compatibility with **CUDA**.

In order to structure the application such that sufficient parallelism can be exposed, one needs to analyze the different levels with respect to data dependencies. Dependent data sets make it very hard or even impossible to achieve a reasonable efficiency by

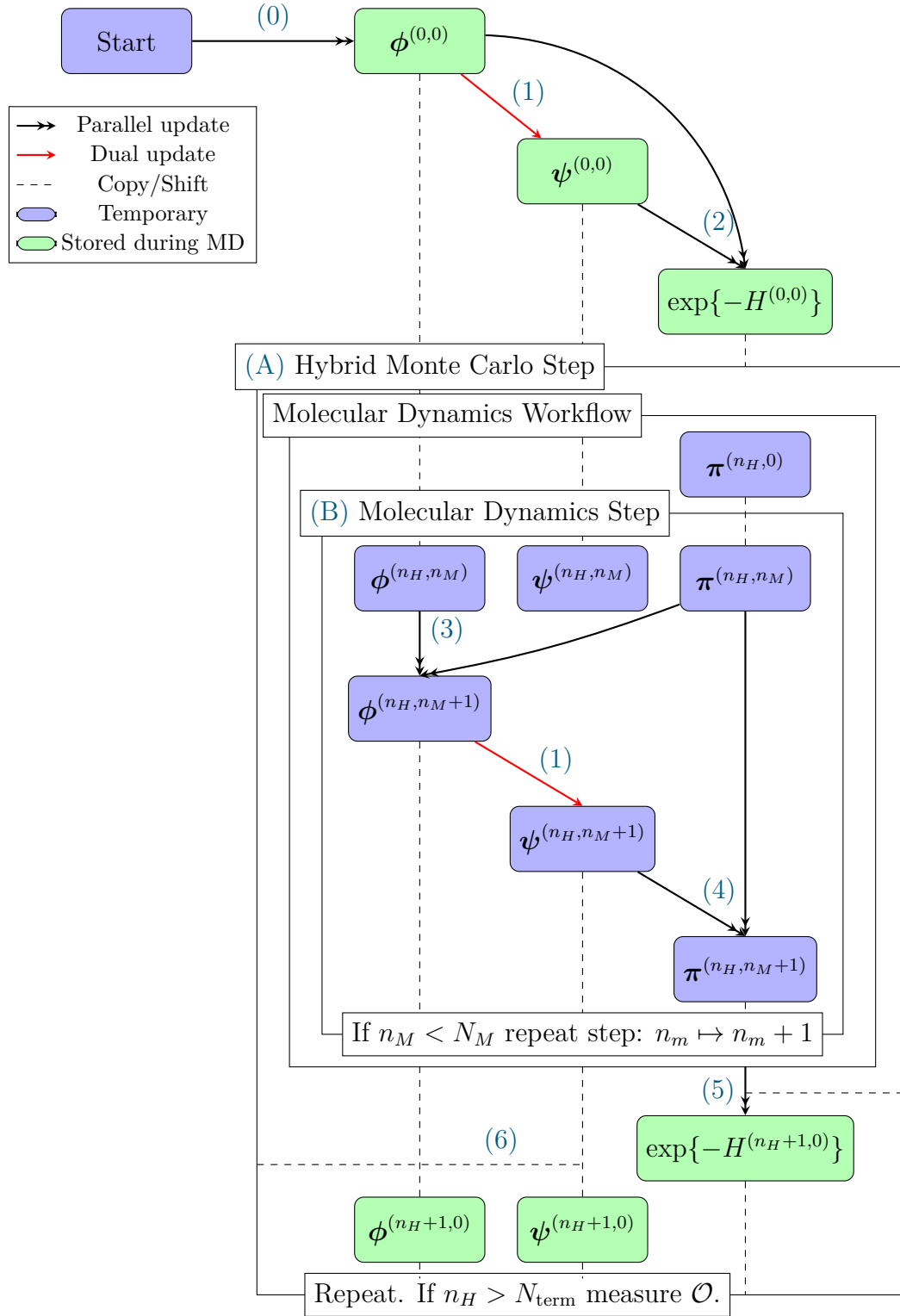


Figure C.2: HMC workflow of the algorithm including the MD updates. For a detailed description see the enumeration in [appendix C.2.2](#). The numbers in the figure correspond to the numbers in the enumeration. For the sake of simplicity, this figure does not show the leapfrog steps where, one updates the ϕ fields in half steps, e.g., $\phi^{(n_H, n_M)} \rightarrow \phi^{(n_H, n_M+1/2)}$.

parallelization. An example for such dependencies is where, e.g., the next computation depends on the previous computations. Levels with dependencies are

- the update of the wave functions at different temporal slices [step (1)],
- the update of any HMC configurations and [step (A)]
- the update of any MD configurations [step (B)].

Levels with exposable parallelism are

- any spacial operation on the N_L^3 lattice sites,
- any operation on the $N_c = 4$ channels,
- any operation on the A nucleons and
- the computation of different streams of HMC trajectories.

This holds true for ψ , ϕ and π . So one could easily distribute work to more than 2 million threads in the extreme case of $N_L=32$ and $A=20$. While different independent HMC trajectories can be farmed on different independent threads, the parallelization in $N_L^3 \times N_c \times A$ is implemented on GPUs. **This additional parallelization in $N_L^3 \times N_c \times A$ is completely new to NLEFT.**

C.3.1 A trial implementation

The first step towards having a completely scalable NLEFT code in the exposable parallelism dimensions is given by the implementation of the kernel operation: the temporal evolution of the wave function (and accordingly the computation of the fermion determinant) [step (1) in the HMC flow]. To do so, we implemented a trial version of the kinetic energy operator in sixth order finite difference discretization ($N_S = 6$) and the potential operator in CUDA for NVIDIA GPUs [P100 GPU]. We computed the action of the transfer matrix on initial wave functions and the computation of the final scalar product to obtain the fermion matrix [eqs. (C.21) and (C.23)].

The chosen data layout for the wave function is `double* Psi[NT][NL*NL*NL][2*A4*Nc]` so the innermost index loops over **Nc** channels. **A4** is the number of nucleons padded to a multiple of 4. The dimension with **[2]** represents the real and imaginary part. **NT=12** time steps are performed before the inner product is evaluated. In order to get meaningful measurements, 343 iterations of the core operations are executed where each iteration performs 5558 floating point operations per nucleon and lattice site. 1536 of these flops are spent in **apply-vij**—the application of the potential operator. Furthermore, there is one inner product that needs to be evaluated after the temporal sweep corresponding to the computation of the fermion matrix. In Fig. C.3, one can observe up to 500GFlop/s as peak performance. This is about 10% of the nominal machine performance of the P100 GPU. Favorable are large lattice sizes and nucleon numbers that are multiples of 8. The corner values for the timings shown in fig. C.3 can be found in table C.1.

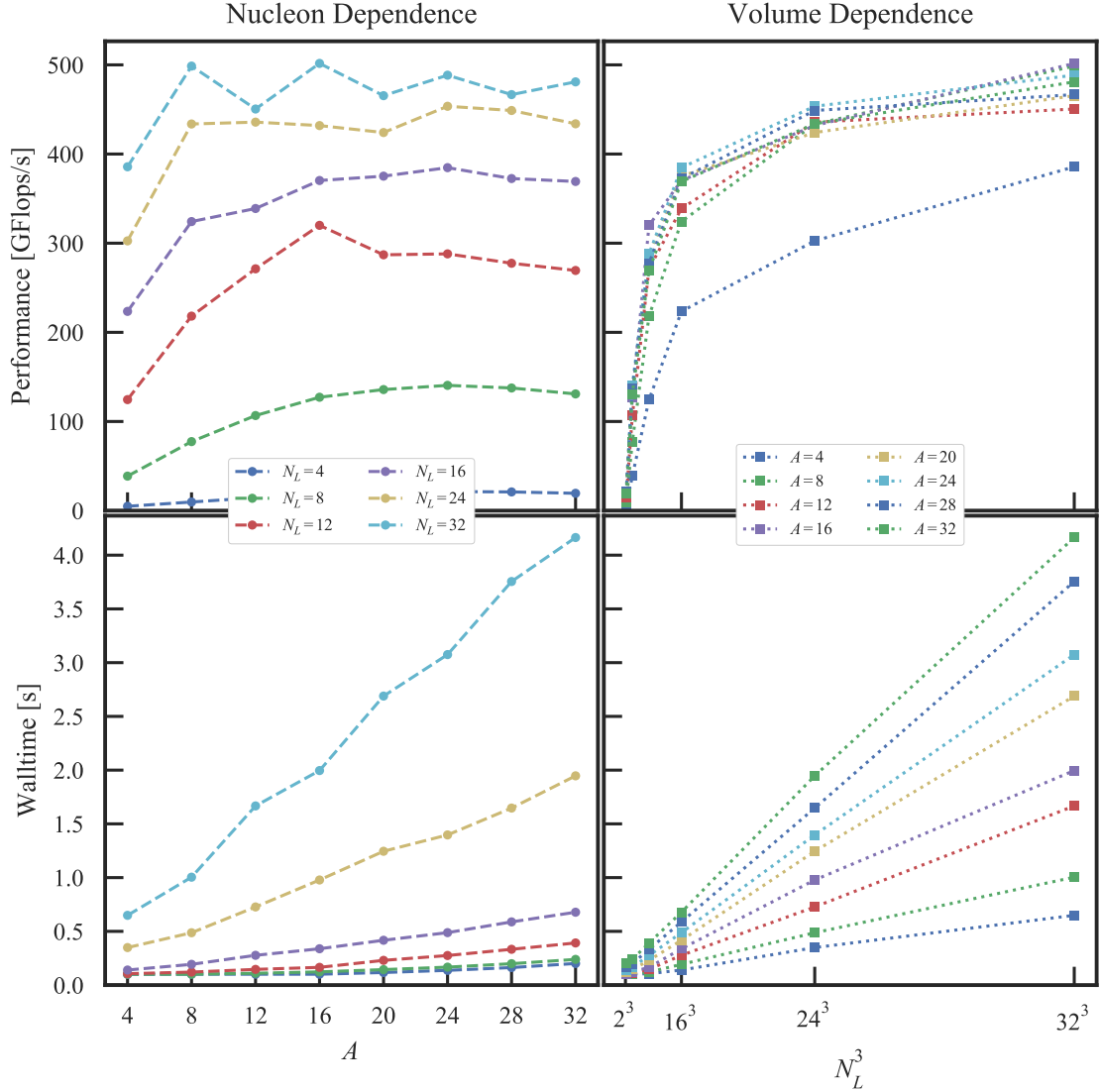


Figure C.3: Benchmark performance results for 343 applications of the transfer matrix. Operation throughput (top) and raw timings (bottom). The left column shows the scaling in the number of nucleons A for different volumes and the right column shows the volume dependence N_L^3 for different nucleon numbers. Larger lattice sizes correspond to longer runtimes but also higher performance values.

Kernel	Scaling	Calls	$A=4$ $N_L=4$	$A=32$ $N_L=4$	$A=4$ $N_L=32$	$A=32$ $N_L=32$
apply-vij	AN_L^3	4116	6.0 12.8%	8.0 4.3%	294.8 43.7%	1335.6 30.6%
Laplace-z	AN_L^3	4116	10.1 21.5%	10.0 5.3%	195.7 29.0%	1541.5 35.3%
Laplace-y	AN_L^3	4116	9.4 20.0%	10.2 5.4%	76.5 11.3%	429.1 9.8%
Laplace-x	AN_L^3	4116	10.3 21.9%	10.1 5.4%	74.7 11.1%	411.7 9.4%
innerprod	$A^2 N_L^3$	343	2.1 4.5%	86.0 45.8%	24.4 3.6%	586.6 13.4%
treereduc	$A^2 \log N_L$	3087	8.6 18.2%	62.9 33.5%	8.0 1.2%	62.9 1.4%

Table C.1: Four selected profiles in milliseconds (and percent) for the six most important kernels.

First results are very promising, e.g., we could verify the expected scaling. Further investigations are intended. As can be seen in [fig. C.3](#), one has not reached the peak performance of the GPU, yet, and thus one can expect that the same scaling continues. It remains to be seen how much the implementation of the HMC workflow will affect the scaling and for which parameters one reaches the memory limit of the GPU. The implementation of the HMC workflow are expected to be worked out soon and results will be published in the near future.

Bibliography

- [1] C. Körber and T. Luu,
Applying Twisted Boundary Conditions for Few-body Nuclear Systems,
Physical Review C **93**, no. 5, 054002 (2015), arXiv: 1511.06598.
- [2] C. Körber, A. Nogga, and J. de Vries,
First-principle calculations of Dark Matter scattering off light nuclei,
Physical Review C **96**, no. 3, 035805 (2017), arXiv: 1704.01150.
- [3] C. Körber, E. Berkowitz, and T. Luu,
Sampling General N-Body Interactions with Auxiliary Fields,
Europhys. Lett. **119**, no. 6, 60006 (2017), arXiv: 1706.06494.
- [4] C. Körber, E. Berkowitz, and T. Luu,
Hubbard-Stratonovich-like Transformations for Few-Body Interactions,
Submitted to PoS (2017), arXiv: 1710.03126.
- [5] E. Berkowitz, C. Körber, S. Krieg, P. Labus, T. A. Lähde, and T. Luu,
Extracting the Single-Particle Gap in Carbon Nanotubes with Lattice Quantum Monte Carlo,
Submitted to PoS (2017), arXiv: 1710.06213.
- [6] C. A. Baker et al.,
An Improved experimental limit on the electric dipole moment of the neutron,
Phys. Rev. Lett. **97**, 131801 (2006), arXiv: hep-ex/0602020 [hep-ex].
- [7] J. de Vries and U.-G. Meißner,
Violations of discrete space-time symmetries in chiral effective field theory,
Int. J. Mod. Phys. E25, no. 05, 1641008 (2016), arXiv: 1509.07331 [hep-ph].
- [8] R. D. Peccei and H. R. Quinn,
CP Conservation in the Presence of Instantons,
Phys. Rev. Lett. **38**, 1440–1443 (25 1977).
- [9] L. Canetti, M. Drewes, and M. Shaposhnikov,
Matter and Antimatter in the Universe, *New J. Phys.* **14**, 095012 (2012),
arXiv: 1204.4186 [hep-ph].
- [10] J. D. Vergados,
The Neutrinoless double beta decay from a modern perspective,
Phys. Rept. **361**, 1–56 (2002), arXiv: hep-ph/0209347 [hep-ph].

- [11] D. S. Akerib et al., LUX Collaboration,
Results from a search for dark matter in the complete LUX exposure,
Phys. Rev. Lett. **118**, no. 2, 021303 (2017), arXiv: 1608.07648 [astro-ph.CO].
- [12] C. Fu et al., PandaX-II Collaboration,
Spin-Dependent Weakly-Interacting-Massive-Particle–Nucleon Cross Section Limits from First Data of PandaX-II Experiment,
Phys. Rev. Lett. **118**, no. 7, 071301 (2017), arXiv: 1611.06553 [hep-ex].
- [13] W. Guo and D. N. McKinsey,
Concept for a dark matter detector using liquid helium-4,
Phys. Rev. D **87**, no. 11, 115001 (2013), arXiv: 1302.0534 [astro-ph.IM].
- [14] K. Schutz and K. M. Zurek,
Detectability of Light Dark Matter with Superfluid Helium,
Phys. Rev. Lett. **117**, 121302 (2016), arXiv: 1604.08206 [hep-ph].
- [15] J. Engel and J. Menéndez,
Status and future of nuclear matrix elements for neutrinoless double-beta decay: a review, *Reports on Progress in Physics* **80**, no. 4, 046301 (2017), arXiv: 1610.06548.
- [16] S. Dell’Oro, S. Marcocci, M. Viel, and F. Vissani,
Neutrinoless Double Beta Decay: 2015 Review,
Advances in High Energy Physics **2016**, 1–37 (2016).
- [17] S. Weinberg,
Phenomenological Lagrangians,
Physica A: Statistical Mechanics and its Applications **96**, no. 1, 327–340 (1979).
- [18] J. Gasser and H. Leutwyler,
Chiral Perturbation Theory to One Loop, *Annals Phys.* **158**, 142 (1984).
- [19] S. Weinberg,
Nuclear forces from chiral Lagrangians, *Phys. Lett.* **B251**, 288–292 (1990).
- [20] C. Ordóñez, L. Ray, and U. van Kolck,
Nucleon-nucleon potential from an effective chiral Lagrangian,
Phys. Rev. Lett. **72**, 1982–1985 (1994).
- [21] V. Bernard, N. Kaiser, and U.-G. Meißner,
Chiral dynamics in nucleons and nuclei, *Int.J.Mod.Phys.* **E4**, 193–346 (1995), arXiv: hep-ph/9501384 [hep-ph].
- [22] E. Epelbaum, H. Krebs, and U.-G. Meißner,
Precision nucleon-nucleon potential at fifth order in the chiral expansion,
Phys. Rev. Lett. **115**, no. 12, 122301 (2015), arXiv: 1412.4623 [nucl-th].
- [23] J. Fan, M. Reece, and L.-T. Wang,
Non-relativistic effective theory of dark matter direct detection,
JCAP **1011**, 042 (2010), arXiv: 1008.1591 [hep-ph].

-
- [24] A. L. Fitzpatrick, W. Haxton, E. Katz, N. Lubbers, and Y. Xu, *The Effective Field Theory of Dark Matter Direct Detection*, *JCAP* 1302, 004 (2013), arXiv: 1203.3542 [hep-ph].
- [25] V. Cirigliano, M. L. Graesser, and G. Ovanessian, *WIMP-nucleus scattering in chiral effective theory*, *JHEP* 10, 025 (2012), arXiv: 1205.2695 [hep-ph].
- [26] P. Klos, J. Menendez, D. Gazit, and A. Schwenk, *Large-scale nuclear structure calculations for spin-dependent WIMP scattering with chiral effective field theory currents*, *Phys. Rev. D* 88, no. 8, 083516 (2013), arXiv: 1304.7684 [nucl-th].
- [27] R. J. Hill and M. P. Solon, *Standard Model anatomy of WIMP dark matter direct detection II: QCD analysis and hadronic matrix elements*, *Phys. Rev. D* 91, 043505 (2015), arXiv: 1409.8290 [hep-ph].
- [28] M. Hoferichter, P. Klos, and A. Schwenk, *Chiral power counting of one- and two-body currents in direct detection of dark matter*, *Phys. Lett. B* 746, 410–416 (2015), arXiv: 1503.04811 [hep-ph].
- [29] F. Bishara, J. Brod, B. Grinstein, and J. Zupan, *Chiral Effective Theory of Dark Matter Direct Detection*, *JCAP* 02, 009 (2017), arXiv: 1611.00368 [hep-ph].
- [30] U.-G. Meißner, *The long and winding road from chiral effective Lagrangians to nuclear structure*, *Phys. Scripta* 91, no. 3, 033005 (2016), arXiv: 1510.03230 [nucl-th].
- [31] C. Gattringer and C. B. Lang, *Quantum chromodynamics on the lattice: An introductory presentation*, Lecture Notes in Physics, Berlin, Heidelberg: Springer Berlin Heidelberg, 2010 1–358, ISBN: 978-3-642-01849-7, arXiv: arXiv:1011.1669v3.
- [32] B. Borasoy, E. Epelbaum, H. Krebs, D. Lee, and U.-G. Meißner, *Lattice simulations for light nuclei: Chiral effective field theory at leading order*, *The European Physical Journal A* 31, no. 1, 105–123 (2007), arXiv: 0611087 [nucl-th].
- [33] D. Lee, *Lattice simulations for few- and many-body systems*, *Prog. Part. Nucl. Phys.* 63, 117–154 (2009), arXiv: 0804.3501 [nucl-th].
- [34] E. Epelbaum, H. Krebs, D. Lee, and U.-G. Meißner, *Ab initio calculation of the Hoyle state*, *Phys. Rev. Lett.* 106, 192501 (2011), arXiv: 1101.2547 [nucl-th].
- [35] E. Epelbaum, H. Krebs, T. A. Lähde, D. Lee, and U.-G. Meißner, *Structure and rotations of the Hoyle state*, *Phys. Rev. Lett.* 109, 252501 (2012), arXiv: 1208.1328 [nucl-th].

- [36] J. M. Alarcón et al.,
Neutron-proton scattering at next-to-next-to-leading order in Nuclear Lattice Effective Field Theory, *Eur. Phys. J. A* **53**, no. 5, 83 (2017),
arXiv: 1702.05319 [nucl-th].
- [37] E. Epelbaum, H. Krebs, T. A. Lähde, D. Lee, U.-G. Meißner, and G. Rupak,
Ab Initio Calculation of the Spectrum and Structure of ^{16}O ,
Phys. Rev. Lett. **112**, no. 10, 102501 (2014), arXiv: 1312.7703 [nucl-th].
- [38] T. A. Lähde, E. Epelbaum, H. Krebs, D. Lee, U.-G. Meißner, and G. Rupak,
Lattice Effective Field Theory for Medium-Mass Nuclei,
Phys. Lett. B **732**, 110–115 (2014), arXiv: 1311.0477 [nucl-th].
- [39] G. Prezeau, A. Kurylov, M. Kamionkowski, and P. Vogel,
New contribution to wimp-nucleus scattering, *Phys. Rev. Lett.* **91**, 231301 (2003),
arXiv: astro-ph/0309115 [astro-ph].
- [40] M. Hoferichter, P. Klos, J. Menendez, and A. Schwenk,
Analysis strategies for general spin-independent WIMP-nucleus scattering,
Phys. Rev. D **94**, no. 6, 063505 (2016), arXiv: 1605.08043 [hep-ph].
- [41] J. Cooley,
Overview of Non-Liquid Noble Direct Detection Dark Matter Experiments,
Physics of the Dark Universe **4**, 92–97 (2014), arXiv: 1410.4960.
- [42] J. Engel, S. Pittel, and P. Vogel,
Nuclear physics of dark matter detection, *Int. J. Mod. Phys. E* **1**, 1–37 (1992).
- [43] E. Behnke et al.,
First dark matter search results from a 4-kg CF_3I bubble chamber operated in a deep underground site, *Phys. Rev. D* **86**, 052001 (5 2012).
- [44] S. Archambault et al.,
Constraints on low-mass WIMP interactions on ^{19}F from PICASSO,
Physics Letters B **711**, no. 2, 153–161 (2012).
- [45] E. Aprile et al., XENON Collaboration,
Physics reach of the XENON1T dark matter experiment,
JCAP **1604**, no. 04, 027 (2016), arXiv: 1512.07501 [physics.ins-det].
- [46] C. E. Aalseth et al.,
CoGeNT: A Search for Low-Mass Dark Matter using p-type Point Contact Germanium Detectors, *Phys. Rev. D* **88**, 012002 (2013),
arXiv: 1208.5737 [astro-ph.CO].
- [47] C. E. Aalseth et al.,
Maximum Likelihood Signal Extraction Method Applied to 3.4 years of CoGeNT Data, (2014), arXiv: 1401.6234 [astro-ph.CO].
- [48] R. Agnese et al.,
Silicon Detector Dark Matter Results from the Final Exposure of CDMS II,
Phys. Rev. Lett. **111**, no. 25, 251301 (2013), arXiv: 1304.4279 [hep-ex].

-
- [49] R. Agnese et al.,
Search for low-mass weakly interacting massive particles using voltage-assisted calorimetric ionization detection in the SuperCDMS experiment,
Physical Review Letters 112, no. 4, 041302 (2014).
- [50] R. Agnese et al.,
Search for low-mass weakly interacting massive particles with SuperCDMS,
Physical Review Letters 112, no. 24, 241302 (2014).
- [51] E. Armengaud et al.,
Search for low-mass WIMPs with EDELWEISS-II heat-and-ionization detectors,
Phys. Rev. D 86, 051701 (5 2012).
- [52] G. Angloher et al.,
Results from 730 kg days of the CRESST-II Dark Matter search,
European Physical Journal C 72, 1971 1971 (2012), arXiv: 1109.0702.
- [53] G. Angloher et al.,
Results on low mass WIMPs using an upgraded CRESST-II detector,
Eur. Phys. J. C 74, no. 12, 3184 (2014), arXiv: 1407.3146 [astro-ph.CO].
- [54] J. Cooley,
Overview of Non-Liquid Noble Direct Detection Dark Matter Experiments,
92–97 (2014), arXiv: 1410.4960v2.
- [55] G. Bertone and D. Hooper,
A History of Dark Matter, (2016), arXiv: 1605.04909 [astro-ph.CO].
- [56] D. S. Akerib et al., LZ Collaboration,
LUX-ZEPLIN (LZ) Conceptual Design Report, (2015),
arXiv: 1509.02910 [physics.ins-det].
- [57] S. R. Beane, S. D. Cohen, W. Detmold, H.-W. Lin, and M. J. Savage,
Nuclear σ terms and scalar-isoscalar WIMP-nucleus interactions from lattice QCD,
Phys. Rev. D 89, 074505 (2014), arXiv: 1306.6939 [hep-ph].
- [58] V. Cirigliano, M. L. Graesser, G. Ovanesyan, and I. M. Shoemaker,
Shining LUX on Isospin-Violating Dark Matter Beyond Leading Order,
Phys. Lett. B 739, 293–301 (2014), arXiv: 1311.5886 [hep-ph].
- [59] S. Profumo,
GeV dark matter searches with the NEWS detector,
Phys. Rev. D 93, no. 5, 055036 (2016), arXiv: 1507.07531 [hep-ph].
- [60] T. Franarin and M. Fairbairn,
Reducing the solar neutrino background in dark matter searches using polarized helium-3,
Phys. Rev. D 94, no. 5, 053004 (2016), arXiv: 1605.08727 [hep-ph].
- [61] D. Gazda, R. Catena, and C. Forssén,
Ab initio nuclear response functions for dark matter searches,
Phys. Rev. D 95, no. 10, 103011 (2017), arXiv: 1612.09165 [hep-ph].

- [62] J. Carlson, S. Gandolfi, F. Pederiva, S. C. Pieper, R. Schiavilla, K. E. Schmidt, and R. B. Wiringa,
Quantum Monte Carlo methods for nuclear physics,
Rev. Mod. Phys. **87**, 1067 (2015), arXiv: 1412.3081 [nucl-th].
- [63] M. A. Shifman, A. I. Vainshtein, and V. I. Zakharov,
Remarks on Higgs Boson Interactions with Nucleons,
Phys. Lett. **B78**, 443–446 (1978).
- [64] M. Hoferichter, J. Ruiz de Elvira, B. Kubis, and U.-G. Meißner,
Matching pion-nucleon Roy-Steiner equations to chiral perturbation theory,
Phys. Rev. Lett. **115**, no. 19, 192301 (2015), arXiv: 1507.07552 [nucl-th].
- [65] K. Olive et al.,
Review of Particle Physics, *Chin. Phys.* **C38**, 090001 (2014).
- [66] A. Crivellin, M. Hoferichter, and M. Procura,
Accurate evaluation of hadronic uncertainties in spin-independent WIMP-nucleon scattering: Disentangling two- and three-flavor effects,
Phys. Rev. **D89**, 054021 (2014), arXiv: 1312.4951 [hep-ph].
- [67] E. Epelbaum, H. Krebs, and U.-G. Meißner,
Improved chiral nucleon-nucleon potential up to next-to-next-to-next-to-leading order, *Eur. Phys. J.* **A51**, no. 5, 53 (2015), arXiv: 1412.0142 [nucl-th].
- [68] A. Crivellin, M. Hoferichter, M. Procura, and L. C. Tunstall,
Light stops, blind spots, and isospin violation in the MSSM,
JHEP **07**, 129 (2015), arXiv: 1503.03478 [hep-ph].
- [69] M. Hoferichter, J. Ruiz de Elvira, B. Kubis, and U.-G. Meißner,
High-Precision Determination of the Pion-Nucleon σ -Term from Roy-Steiner Equations, *Phys. Rev. Lett.* **115**, 092301 (2015), arXiv: 1506.04142 [hep-ph].
- [70] D. A. Brantley, B. Joo, E. V. Mastropas, E. Mereghetti, H. Monge-Camacho, B. C. Tiburzi, and A. Walker-Loud,
Strong isospin violation and chiral logarithms in the baryon spectrum, (2016), arXiv: 1612.07733 [hep-lat].
- [71] S. Dürr et al.,
Lattice computation of the nucleon scalar quark contents at the physical point,
Phys. Rev. Lett. **116**, no. 17, 172001 (2016), arXiv: 1510.08013 [hep-lat].
- [72] M. Hoferichter, C. Ditsche, B. Kubis, and U.-G. Meißner,
Dispersive analysis of the scalar form factor of the nucleon,
JHEP **06**, 063 (2012), arXiv: 1204.6251 [hep-ph].
- [73] M. Hoferichter, *Private communication* (2017).
- [74] N. Fettes, U.-G. Meißner, M. Mojzis, and S. Steininger,
The Chiral effective pion nucleon Lagrangian of order p^4 ,
Annals Phys. **283**, 273–302 (2000), arXiv: hep-ph/0001308 [hep-ph].

-
- [75] P. Junnarkar and A. Walker-Loud,
Scalar strange content of the nucleon from lattice QCD,
Phys.Rev. D87, 114510 (2013), arXiv: 1301.1114 [hep-lat].
- [76] M. Cirelli, E. Del Nobile, and P. Panci,
Tools for model-independent bounds in direct dark matter searches,
JCAP 1310, 019 (2013), arXiv: 1307.5955 [hep-ph].
- [77] M. C. Smith et al.,
The RAVE Survey: Constraining the Local Galactic Escape Speed,
Mon. Not. Roy. Astron. Soc. 379, 755–772 (2007),
arXiv: astro-ph/0611671 [astro-ph].
- [78] R. B. Wiringa, V. G. J. Stoks, and R. Schiavilla,
An Accurate nucleon-nucleon potential with charge independence breaking,
Phys. Rev. C51, 38–51 (1995), arXiv: nucl-th/9408016 [nucl-th].
- [79] R. Machleidt,
The High precision, charge dependent Bonn nucleon-nucleon potential (CD-Bonn),
Phys. Rev. C63, 024001 (2001), arXiv: nucl-th/0006014 [nucl-th].
- [80] C. Van Der Leun and C. Alderliesten,
The deuteron binding energy,
Nucl. Phys. A380, 261–269 (1982).
- [81] A. Huber, T. Udem, B. Gross, J. Reichert, M. Kourogi, K. Pachucki, M. Weitz,
and T. W. Hänsch,
Hydrogen-Deuterium $1S - 2S$ Isotope Shift and the Structure of the Deuteron,
Phys. Rev. Lett. 80, 468–471 (3 1998).
- [82] D. M. Bishop and L. M. Cheung,
Quadrupole moment of the deuteron from a precise calculation of the electric field gradient in D-2,
Phys. Rev. A20, 381–384 (1979).
- [83] I. Borbely, W. Grüebler, V. König, P. A. Schmelzbach, and
A. M. Mukhamedzhanov,
Determination of the deuteron S-state asymptotic normalization by continuation of p-d elastic cross section to the transfer pole,
Phys. Lett. 160B, 17–20 (1985).
- [84] N. L. Rodning and L. D. Knutson,
Asymptotic D-state to S-state ratio of the deuteron,
Phys. Rev. C41, 898–909 (1990).
- [85] S. Weinberg,
Three body interactions among nucleons and pions,
Phys. Lett. B295, 114–121 (1992), arXiv: hep-ph/9209257 [hep-ph].
- [86] M. C. Birse,
Power counting with one-pion exchange,
Phys. Rev. C74, 014003 (2006),
arXiv: nucl-th/0507077 [nucl-th].

- [87] A. Nogga, R. G. E. Timmermans, and U. van Kolck, *Renormalization of one-pion exchange and power counting*, *Phys. Rev. C* **72**, 054006 (2005), arXiv: [nucl-th/0506005](#) [nucl-th].
- [88] M. Pavon Valderrama and E. Ruiz Arriola, *Renormalization of NN interaction with chiral two pion exchange potential. central phases and the deuteron*, *Phys. Rev. C* **74**, 054001 (2006), arXiv: [nucl-th/0506047](#) [nucl-th].
- [89] M. Pavon Valderrama and E. Ruiz Arriola, *Renormalization of NN interaction with chiral two pion exchange potential: Non-central phases*, *Phys. Rev. C* **74**, 064004 (2006), arXiv: [nucl-th/0507075](#) [nucl-th].
- [90] E. Epelbaum and U.-G. Meißner, *On the Renormalization of the One-Pion Exchange Potential and the Consistency of Weinberg's Power Counting*, *Few Body Syst.* **54**, 2175–2190 (2013), arXiv: [nucl-th/0609037](#) [nucl-th].
- [91] M. Pavon Valderrama, *Perturbative Renormalizability of Chiral Two Pion Exchange in Nucleon-Nucleon Scattering: P- and D-waves*, *Phys. Rev. C* **84**, 064002 (2011), arXiv: [1108.0872](#) [nucl-th].
- [92] M. P. Valderrama, *Perturbative renormalizability of chiral two pion exchange in nucleon-nucleon scattering*, *Phys. Rev. C* **83**, 024003 (2011), arXiv: [0912.0699](#) [nucl-th].
- [93] E. Epelbaum and J. Gegelia, *Regularization, renormalization and 'peratization' in effective field theory for two nucleons*, *Eur. Phys. J. A* **41**, 341–354 (2009), arXiv: [0906.3822](#) [nucl-th].
- [94] S. Binder et al., LENPIC Collaboration, *Few-nucleon systems with state-of-the-art chiral nucleon-nucleon forces*, *Phys. Rev. C* **93**, no. 4, 044002 (2016), arXiv: [1505.07218](#) [nucl-th].
- [95] A. Nogga, A. Kievsky, H. Kamada, W. Gloeckle, L. E. Marcucci, S. Rosati, and M. Viviani, *The Three nucleon bound state using realistic potential models*, *Phys. Rev. C* **67**, 034004 (2003), arXiv: [nucl-th/0202037](#) [nucl-th].
- [96] A. Nogga, *Nuclear and hypernuclear three- and four-body bound states*, PhD thesis: Ruhr-Universität Bochum, Germany, 2001.
- [97] G. Audi, M. Wang, A. Wapstra, F. Kondev, M. MacCormick, X. Xu, and B. Pfeiffer, *The Ame2012 atomic mass evaluation*, *Chinese Physics C* **36**, no. 12, 1287 (2012).

-
- [98] M. Wang, G. Audi, A. Wapstra, F. Kondev, M. MacCormick, X. Xu, and B. Pfeiffer,
The Ame2012 atomic mass evaluation,
Chinese Physics C 36, no. 12, 1603 (2012).
- [99] A. Nogga, H. Kamada, W. Gloeckle, and B. R. Barrett,
The Alpha particle based on modern nuclear forces,
Phys. Rev. C 65, 054003 (2002), arXiv: nucl-th/0112026 [nucl-th].
- [100] B. S. Pudliner, V. R. Pandharipande, J. Carlson, S. C. Pieper, and R. B. Wiringa,
Quantum Monte Carlo calculations of nuclei with $A \leq 7$,
Phys. Rev. C 56, 1720–1750 (1997), arXiv: nucl-th/9705009 [nucl-th].
- [101] S. A. Coon and H. K. Han,
Reworking the Tucson-Melbourne three nucleon potential,
Few Body Syst. 30, 131–141 (2001), arXiv: nucl-th/0101003 [nucl-th].
- [102] J. L. Friar, B. F. Gibson, and G. L. Payne,
Coulomb effects in the He-3 ground state, *Phys. Rev. C* 35, 1502–1507 (1987).
- [103] C. R. Ottermann, G. Kobschall, K. Maurer, K. Rohrich, C. Schmitt, and V. H. Walther,
Elastic electron scattering from He-3 and He-4,
Nucl. Phys. A 436, 688–698 (1985).
- [104] A. Baroni, L. Girlanda, S. Pastore, R. Schiavilla, and M. Viviani,
Nuclear Axial Currents in Chiral Effective Field Theory,
Phys. Rev. C 93, no. 1, 015501 (2016), arXiv: 1509.07039 [nucl-th].
- [105] H. Krebs, E. Epelbaum, and U.-G. Meißner,
Nuclear axial current operators to fourth order in chiral effective field theory,
Annals Phys. 378, 317–395 (2017), arXiv: 1610.03569 [nucl-th].
- [106] C. McCabe,
The Astrophysical Uncertainties Of Dark Matter Direct Detection Experiments,
Phys. Rev. D 82, 023530 (2010), arXiv: 1005.0579 [hep-ph].
- [107] S. Liebig, V. Baru, F. Ballout, C. Hanhart, and A. Nogga,
Towards a high precision calculation for the pion-nucleus scattering lengths,
Eur. Phys. J. A 47, 69 (2011), arXiv: 1003.3826 [nucl-th].
- [108] V. Baru, C. Hanhart, M. Hoferichter, B. Kubis, A. Nogga, and D. R. Phillips,
Precision calculation of threshold $\pi^- d$ scattering, πN scattering lengths, and the GMO sum rule, *Nucl. Phys. A* 872, 69–116 (2011), arXiv: 1107.5509 [nucl-th].
- [109] R. H. Helm,
Inelastic and Elastic Scattering of 187-Mev Electrons from Selected Even-Even Nuclei, *Phys. Rev.* 104, 1466–1475 (5 1956).

- [110] J. D. Lewin and P. F. Smith,
Review of mathematics, numerical factors, and corrections for dark matter experiments based on elastic nuclear recoil,
Astroparticle Physics 6, no. 1, 87–112 (1996).
- [111] A. Lovato, S. Gandolfi, J. Carlson, S. C. Pieper, and R. Schiavilla,
Neutral weak current two-body contributions in inclusive scattering from ^{12}C ,
Phys. Rev. Lett. 112, no. 18, 182502 (2014), arXiv: 1401.2605 [nucl-th].
- [112] J. L. Feng, J. Kumar, D. Marfatia, and D. Sanford,
Isospin-Violating Dark Matter, *Phys. Lett. B* 703, 124–127 (2011),
arXiv: 1102.4331 [hep-ph].
- [113] S. Liebig, U.-G. Meißner, and A. Nogga,
Jacobi no-core shell model for p -shell nuclei,
Eur. Phys. J. A 52, no. 4, 103 (2016), arXiv: 1510.06070 [nucl-th].
- [114] L. D. Faddeev,
Scattering theory for a three particle system,
Sov. Phys. JETP 12, 1014–1019 (1961).
- [115] O. A. Yakubovsky,
On the Integral equations in the theory of N particle scattering,
Sov. J. Nucl. Phys. 5, 937 (1967).
- [116] G. Hagen, T. Papenbrock, M. Hjorth-Jensen, and D. J. Dean,
Coupled-cluster computations of atomic nuclei,
Rept. Prog. Phys. 77, no. 9, 096302 (2014), arXiv: 1312.7872 [nucl-th].
- [117] P. Navratil, S. Quaglioni, I. Stetcu, and B. R. Barrett,
Recent developments in no-core shell-model calculations,
J. Phys. G 36, 083101 (2009), arXiv: 0904.0463 [nucl-th].
- [118] H. Hergert, S. K. Bogner, T. D. Morris, A. Schwenk, and K. Tsukiyama,
The In-Medium Similarity Renormalization Group: A Novel Ab Initio Method for Nuclei,
Phys. Rept. 621, 165–222 (2016), arXiv: 1512.06956 [nucl-th].
- [119] E. Caurier, G. Martinez-Pinedo, F. Nowacki, A. Poves, and A. P. Zuker,
The Shell model as unified view of nuclear structure,
Rev. Mod. Phys. 77, 427–488 (2005), arXiv: nucl-th/0402046 [nucl-th].
- [120] C. Fiolhais, F. Nogueira, and M. A. Marques,
A primer in density functional theory, Springer Science & Business Media, 2003.
- [121] M. Creutz,
Global Monte Carlo algorithms for many-fermion systems,
Phys. Rev. D 38, 1228–1238 (4 1988).
- [122] R. L. Stratonovich,
On a method of calculating quantum distribution functions,
Doklady Akad. Nauk S.S.S.R. 115, 1097 (1957).

-
- [123] J. Hubbard,
Calculation of Partition Functions,
Physical Review Letters 3, no. 2, 77–78 (1959).
- [124] J. Gubernatis, N. Kawashima, and P. Werner,
Quantum Monte Carlo Methods: Algorithms for Lattice Models,
Cambridge University Press, 2016, ISBN: 978-1-316-48312-1.
- [125] H. Kleinert,
Hubbard-Stratonovich Transformation: Successes, Failure, and Cure,
Electron. J. Theor. Phys. 8, no. 25, 57–64 (2011),
arXiv: [1104.5161](#) [cond-mat.quant-gas].
- [126] E. Epelbaum, H. Krebs, D. Lee, and U.-G. Meißner,
Lattice effective field theory calculations for $A = 3, 4, 6, 12$ nuclei,
Phys. Rev. Lett. 104, 142501 (2010), arXiv: [0912.4195](#) [nucl-th].
- [127] E. Epelbaum, H.-W. Hammer, and U.-G. Meißner,
Modern Theory of Nuclear Forces, *Rev. Mod. Phys.* 81, 1773–1825 (2009),
arXiv: [0811.1338](#) [nucl-th].
- [128] P. Kopietz,
Bosonization of Interacting Fermions in Arbitrary Dimensions,
Lecture Notes in Physics Monographs, Springer Berlin Heidelberg, 2008,
ISBN: 978-3-540-68495-4.
- [129] H. Reinhardt,
Path integral approach for fermi systems with N -body interactions,
Phys. Lett. B 208, 15–18 (1988).
- [130] H. P. Büchler, A. Micheli, and P. Zoller,
Three-body interactions with cold polar molecules,
Nat Phys 3, no. 10, 726–731 (2007).
- [131] L. Bonnes, H. Büchler, and S. Wessel,
Polar molecules with three-body interactions on the honeycomb lattice,
New J. Phys. 12, 053027 (2010).
- [132] Faà di Bruno,
Sullo sviluppo della funzione,
Ann. di Scienze Mathem. et Fisiche di Tortoloni 6, 479–480 (1855).
- [133] V. M. Adamyan, J. Alcober, and I. M. Tkachenko,
Reconstruction of distributions by their moments and local constraints,
Applied Mathematics Research eXpress 2003, no. 2, 33–70 (2003).
- [134] J.-W. Chen, D. Lee, and T. Schäfer,
Inequalities for light nuclei in the Wigner symmetry limit,
Phys. Rev. Lett. 93, 242302 (2004), arXiv: [nucl-th/0408043](#) [nucl-th].
- [135] C. Körber *et al.* (in preparation).

- [136] R. Brower, C. Rebbi, and D. Schaich,
Hybrid Monte Carlo simulation on the graphene hexagonal lattice,
PoS LATTICE2011, 056 (2011), arXiv: [1204.5424 \[hep-lat\]](#).
- [137] T. Luu and T. A. Lähde,
Quantum Monte Carlo Calculations for Carbon Nanotubes,
Phys. Rev. B **93**, no. 15, 155106 (2016), arXiv: [1511.04918 \[cond-mat.str-el\]](#).
- [138] J. E. Drut, R. J. Furnstahl, and L. Platter,
Toward ab initio density functional theory for nuclei,
Prog. Part. Nucl. Phys. **64**, 120–168 (2010), arXiv: [0906.1463 \[nucl-th\]](#).
- [139] E. Braaten and H.-W. Hammer,
Efimov Physics in Cold Atoms, *Annals Phys.* **322**, 120–163 (2007),
arXiv: [cond-mat/0612123 \[cond-mat\]](#).
- [140] P. Naidon and S. Endo,
Efimov Physics: a review, *Rept. Prog. Phys.* **80**, no. 5, 056001 (2017),
arXiv: [1610.09805 \[quant-ph\]](#).
- [141] G. Rupak and D. Lee,
Radiative capture reactions in lattice effective field theory,
Physical Review Letters **111**, no. 3, 1–4 (2013), arXiv: [1302.4158](#).
- [142] M. Lüscher,
Volume Dependence of the Energy Spectrum in Massive Quantum Field Theories. 2. Scattering States, *Commun. Math. Phys.* **105**, 153–188 (1986).
- [143] M. Lüscher,
Two particle states on a torus and their relation to the scattering matrix,
Nucl. Phys. **B354**, 531–578 (1991).
- [144] S. König, D. Lee, and H.-W. Hammer,
Non-relativistic bound states in a finite volume,
Annals Phys. **327**, 1450–1471 (2012), arXiv: [1109.4577 \[hep-lat\]](#).
- [145] S. König,
Effective quantum theories with short- and long-range forces,
PhD thesis: University of Bonn, 2013.
- [146] S. Elhatisari, D. Lee, G. Rupak, E. Epelbaum, H. Krebs, T. A. Lähde, T. Luu,
and U.-G. Meißner,
Ab initio alpha-alpha scattering, *Nature* **528**, 111 (2015),
arXiv: [1506.03513 \[nucl-th\]](#).
- [147] R. A. Briceño, Z. Davoudi, T. C. Luu, and M. J. Savage,
Two-Baryon Systems with Twisted Boundary Conditions,
Phys. Rev. D **89**, no. 7, 074509 (2014), arXiv: [1311.7686 \[hep-lat\]](#).

-
- [148] S. R. Beane et al.,
Light Nuclei and Hypernuclei from Quantum Chromodynamics in the Limit of $SU(3)$ Flavor Symmetry, *Phys. Rev. D* **87**, no. 3, 034506 (2013),
arXiv: 1206.5219 [hep-lat].
- [149] S. R. Beane et al.,
Hyperon-Nucleon Interactions and the Composition of Dense Nuclear Matter from Quantum Chromodynamics, *Phys. Rev. Lett.* **109**, 172001 (2012),
arXiv: 1204.3606 [hep-lat].
- [150] S. R. Beane et al.,
Evidence for a Bound H -dibaryon from Lattice QCD,
Phys. Rev. Lett. **106**, 162001 (2011), arXiv: 1012.3812 [hep-lat].
- [151] K. Orginos, A. Parreño, M. J. Savage, S. R. Beane, E. Chang, and W. Detmold,
Two Nucleon Systems at $m_\pi \sim 450$ MeV from Lattice QCD, (2015),
arXiv: 1508.07583 [hep-lat].
- [152] F. Etminan et al.,
Spin-2 $N\Omega$ dibaryon from Lattice QCD, *Nucl. Phys.* **A928**, 89–98 (2014),
arXiv: 1403.7284 [hep-lat].
- [153] T. Inoue et al.,
Two-Baryon Potentials and H -Dibaryon from 3-flavor Lattice QCD Simulations,
Nucl. Phys. **A881**, 28–43 (2012), arXiv: 1112.5926 [hep-lat].
- [154] T. Yamazaki, K.-i. Ishikawa, Y. Kuramashi, and A. Ukawa,
Study of quark mass dependence of binding energy for light nuclei in 2+1 flavor lattice QCD, *Phys. Rev. D* **92**, no. 1, 014501 (2015), arXiv: 1502.04182 [hep-lat].
- [155] T. Yamazaki, K.-i. Ishikawa, Y. Kuramashi, and A. Ukawa,
Helium nuclei, deuteron and dineutron in 2+1 flavor lattice QCD,
Phys. Rev. D **86**, 074514 (2012), arXiv: 1207.4277 [hep-lat].
- [156] E. Epelbaum, H. Krebs, T. A. Lähde, D. Lee, and U.-G. Meißner,
Viability of Carbon-Based Life as a Function of the Light Quark Mass,
Phys. Rev. Lett. **110**, no. 11, 112502 (2013), arXiv: 1212.4181 [nucl-th].
- [157] T. A. Lähde, T. Luu, D. Lee, U.-G. Meißner, E. Epelbaum, H. Krebs, and G. Rupak,
Nuclear Lattice Simulations using Symmetry-Sign Extrapolation,
Eur. Phys. J. **A51**, no. 7, 92 (2015), arXiv: 1502.06787 [nucl-th].
- [158] S. R. Beane, P. F. Bedaque, A. Parreño, and M. J. Savage,
Two nucleons on a lattice, *Phys. Lett.* **B585**, 106–114 (2004),
arXiv: hep-lat/0312004 [hep-lat].
- [159] U.-G. Meißner, G. Ríos, and A. Rusetsky,
Spectrum of three-body bound states in a finite volume,
Phys. Rev. Lett. **114**, no. 9, 091602 (2015), arXiv: 1412.4969 [hep-lat].

- [160] N. Byers and C. N. Yang,
Theoretical Considerations Concerning Quantized Magnetic Flux in Superconducting Cylinders, *Phys. Rev. Lett.* **7**, 46–49 (1961).
- [161] M. Guagnelli, K. Jansen, F. Palombi, R. Petronzio, A. Shindler, and I. Wetzorke,
Continuous external momenta in nonperturbative lattice simulations: A Computation of renormalization factors, *Nucl. Phys.* **B664**, 276–298 (2003),
arXiv: [hep-lat/0303012](#) [hep-lat].
- [162] P. F. Bedaque and J.-W. Chen,
Twisted valence quarks and hadron interactions on the lattice,
Phys. Lett. **B616**, 208–214 (2005), arXiv: [hep-lat/0412023](#) [hep-lat].
- [163] C. Lin, F. H. Zong, and D. M. Ceperley,
Twist-averaged boundary conditions in continuum quantum Monte Carlo,
Phys. Rev. **E64**, 016702 (2001), arXiv: [cond-mat/0101339](#) [cond-mat.stat-mech].
- [164] C. Lehner and T. Izubuchi,
Towards the large volume limit - A method for lattice QCD + QED simulations,
PoS LATTICE2014, 164 (2015), arXiv: [1503.04395](#) [hep-lat].
- [165] B. Schuetrumpf and W. Nazarewicz,
Twist-averaged boundary conditions for nuclear pasta Hartree-Fock calculations,
(2015), arXiv: [1508.06611](#) [nucl-th].
- [166] M. Lüscher,
Volume Dependence of the Energy Spectrum in Massive Quantum Field Theories. 1. Stable Particle States, *Commun. Math. Phys.* **104**, 177 (1986).
- [167] S. Bour, S. König, D. Lee, H.-W. Hammer, and U.-G. Meißner,
Topological phases for bound states moving in a finite volume,
Phys. Rev. **D84**, 091503 (2011), arXiv: [1107.1272](#) [nucl-th].
- [168] S. König, D. Lee, and H.-W. Hammer,
Volume Dependence of Bound States with Angular Momentum,
Phys. Rev. Lett. **107**, 112001 (2011), arXiv: [1103.4468](#) [hep-lat].
- [169] C. Körber (in preparation).
- [170] D. Griffiths,
Introduction to Elementary Particles, Weinheim Germany: Wiley, 2008,
ISBN: 978-3-527-40601-2.
- [171] M. E. Peskin and D. V. Schroeder,
An introduction to quantum field theory,
Boulder (Colo.): Westview Press Reading (Mass.), 1995, ISBN: 0-201-50934-2.
- [172] E. Epelbaum,
Nuclear Forces from Chiral Effective Field Theory: A Primer, 2010,
arXiv: [1001.3229](#) [nucl-th].

- [173] D. M. Brink and G. Satchler,
Angular Momentum, London: Clarendon Press, 1994 192,
ISBN: 978-0-19-851759-7.
- [174] N. Metropolis, A. W. Rosenbluth, M. N. Rosenbluth, A. H. Teller, and E. Teller,
Equation of State Calculations by Fast Computing Machines,
The Journal of Chemical Physics 21, no. 6, 1087–1092 (1953),
arXiv: 5744249209.
- [175] W. K. Hastings,
Monte carlo sampling methods using Markov chains and their applications,
Biometrika 57, no. 1, 97–109 (1970), arXiv: 5744249209.
- [176] S. Duane, A. D. Kennedy, B. J. Pendleton, and D. Roweth,
Hybrid Monte Carlo, *Physics Letters B* 195, no. 2, 216–222 (1987).

Acknowledgements

Reflecting on the past three years, I realize that I was given an enormous chance. I believe the possibility of developing myself in numerous ways, pursuing my own scientific goals while having direct access to the available expertise and resources at any time cannot be taken for granted. And for this, I am grateful.

However, I also believe that I would not have been able to take this chance if it was not for all the support I have received. I am grateful to Manfred Müller and specifically Frank Schümann for their exceptional teaching efforts and helping me to decide to study physics. I would like to thank Martina Havenith-Newen, Hans-Paul Bürkner and the Bonn-Cologne Graduate School of Physics and Astronomy for encouraging me to give my best. And I would like to thank Evgeny Epelbaum and Dean J. Lee for mentoring me during my period as a graduate student and enabling my semester abroad at the North Carolina State University.

In addition to the academic support I have received, I could always rely on my family and friends. I believe that this support had a paramount impact on my motivation and thus my effort to pursue this path. And for this, I would like to express my gratitude.

I am grateful to you, Mama and Papa, for supporting me and providing a home I can always come back to. And especially, I am grateful to you, Mone, for being with me at any point and for backing me up in any aspect on this way. Thank you for everything!

I have had the luck to work with members of the Institut für Kernphysik and Institute for Advanced Simulations in Jülich. I believe that one of the outstanding qualities of these groups are the tremendous and instant amount of information and feedback one receives on request. There has not been a time where I have felt left alone with problems I could not solve by myself. Throughout this period, I have significantly benefited from this exchange and therefore would like to thank my colleagues. In particular, I would like to thank my collaborators Paul F. Baumeister, Evan Berkowitz, Jordy de Vries, Christoph Hanhart, Inka Hammer, Andreas Nogga and Jan-Lukas Wynen.

And, in addition to the gratitude for the support I have received, I would like to thank Thomas Luu and Ulf-G. Meißner for giving me this chance and investing in me.

Finally, I would like to express my deep gratitude to you, Tom. You have been an outstanding mentor and friend along this way. I believe that your continuous support and encouragement, as well as your patient and aware guidance, have significantly influenced my growth as a scientist and as a person. And for this, I would like to thank you.

Acronyms

- $0\nu\beta\beta$ -decay** Neutrinoless Double β Decay. 1, 2, 5, 120
- χ EFT** Chiral Effective Field Theory. 8, 11, 12, 15, 20, 36, 47, 118
- χ PT** Chiral Perturbation Theory. iii, 3, 5, 14–17, 20, 21, 48, 117
- aPBC** anti-Periodic Boundary Condition. 88, 103, 105
- AV18** Argonne v18. 25–28, 37, 141
- BSM** Beyond the Standard Model. iii, iv, 1–5, 8, 47, 117, 119, 120
- CDB** CD-Bonn. 25–28, 37, 141
- CM** Center of Mass. 91, 92, 96, 99, 103, 109, 114
- CP** Charge-Parity. iii, 1
- DM** Dark Matter. iii, 1, 2, 4–6, 8, 11–24, 26, 29, 31, 33, 35, 36, 38–44, 47, 55, 69, 117–120, 123–125, 129–132, 136, 138, 140
- EDM** Electric Dipole Moment. iii, 1, 2
- EFT** Effective Field Theory. iii, 2–4, 12–14, 43, 44, 47, 48
- EM** Electromagnetic. 26
- FT** Fourier Transformation. 75–77
- FV** Finite-Volume. iv, 3, 70, 72, 76–80, 83, 84, 87–90, 93–97, 99–115, 119
- GPU** Graphics Processing Unit. 84, 119, 143, 154, 156
- HMC** Hybrid Monte Carlo. iii, 84, 143, 146, 150, 151, 153, 154, 156
- HPC** High Performance Computing. 143
- HS** Hubbard-Stratonovitch. 8, 49, 53–55, 60, 64, 66, 67, 118, 143, 148

- iPBC** i-Periodic Boundary Condition. 103–105, 110–115
- LEC** Low-Energy Constant. 14–17, 20, 21, 24, 38, 49
- LO** Leading Order. 15, 17, 23, 25, 28, 29, 33, 71, 87–89, 93–98, 101, 106–115, 117, 141
- LQCD** Lattice Quantum Chromodynamics. iii, 2, 3, 19, 20, 37, 47, 50, 84, 88, 89, 91, 100, 115, 119, 150
- MC** Markov Chain. 145
- MD** Molecular Dynamics. 146, 147, 149–151, 153, 154
- N²LO** Next-to-Next-to-Leading Order. 13, 15, 25, 28, 32–37, 39–42, 55, 96, 105, 141
- N³LO** Next-to-Next-to-Next-to-Leading Order. 21, 25, 28, 29, 33–37, 41, 42, 44, 118, 141
- N⁴LO** Next-to-Next-to-Next-to-Next-to-Leading Order. 15, 25, 28, 29, 33–37, 141
- NLEFT** Nuclear Lattice Effective Field Theory. iii, iv, 3, 5, 8, 13, 48–52, 54, 68, 70, 71, 84, 87–89, 91, 97, 100, 114, 115, 118–120, 143, 147, 150, 154
- NLO** Next-to-Leading Order. iii, 8, 15, 17, 20, 25, 28, 29, 31–35, 37, 80, 96, 101–108, 117, 138, 141
- NME** Nuclear Matrix-Element. iii, iv, 2, 8, 47, 55, 69, 72, 75, 79, 83, 84, 117, 119, 120, 133
- OPE** One-Pion Exchange. 15
- PBC** Periodic Boundary Condition. 88, 90, 93, 103, 105, 106, 115
- QCD** Quantum Chromodynamics. iii, 1, 3, 14, 15, 21
- SM** Standard Model. iii, 1, 2, 4, 12, 14, 47, 117
- TBC** Twisted Boundary Condition. 8, 84, 87, 88, 90, 91, 93, 95, 97, 99, 107, 113–115, 119
- TM** Tucson-Melbourne. 27, 28, 141
- TNF** Three-Nucleon Force. 13, 15, 27, 36, 37, 55, 118
- TPE** Two-Pion Exchange. 15
- URB IX** Urbana IX. 27, 28, 141
- WIMP** Weakly Interacting Massive Particle. iii, 1, 7